EUROPEAN MECHANICAL SCIENCE

TRDİZİN

Indexed / Abstracted in:

TR-Dizin, EXALY Full-Text Search Engine, Index Copernicus, Root Indexing, Google Scholar, Harvard University Library, Scilit, journaltocs, Sobiad Fatcat, Cite Factor

Aims and Scopes

European Mechanical Science (EMS) is an international, peer reviewed journal which publishes full length original research papers, reviews related to all areas of Mechanical Engineering such as: Solid Mechanics, Materials Engineering, Automotive Engineering, Fluid Mechanics, Thermal Engineering, Engine and Power Engineering, Dynamics & Control, Robotics & Mechatronics, Transportation Engineering, Computational Mechanics, Design, Systems, Manufacturing, Bio-Medical Engineering; Process Engineering, Aerospace Engineering. No charges are required from the Authors to publish the articles.EMS is a quarterly published journal operating an online submission and peer review system. It allows authors to submit articles online and track their progress via its web interface.

https://dergipark.org.tr/ems

Contents

– *Research Articles*

Investigating the biomechanics of the biceps brachii muscle during dumbbell curl exercise: A comprehensive approach

Hamid Asadi Dereshgi[1*]

[1]Department of Biomedical Engineering, Istanbul Arel University, 34537 Istanbul, Turkey

ORCID: H. Asadi Dereshgi (0000-0002-8500-6625)

Abstract: Investigation of the mechanical behavior of the biceps brachii (BB) muscle at different dynamic forces is essential to improve training techniques, prevent sports injuries and optimize rehabilitation results. In previous studies, researchers studied mechanical changes during muscle contraction using various mathematical methods and simulation models. The models adopted by the majority of these studies assumed a constant value for muscle force. However, variable muscle force has different effects on muscle mechanics. In this study, an inverse dynamic simulation model was initially utilized to determine the dynamic muscle forces generated in the BB while performing the dumbbell curl exercise with 5 kg and 10 kg weights. Subsequently, the finite element method (FEM) was used to calculate the stress and strain changes experienced by BB as a consequence of the applied forces. Moreover, simultaneous analysis through electromyography (EMG) was carried out to investigate muscle contraction during the dumbbell curl exercise. Consequently, it was concluded that the average BB force during the dumbbell curl exercise with 5 kg and 10 kg weights was 433.9 N and 695.0 N, respectively. The maximum stresses in the BB during exercise were calculated to be 960.5 Pa and 1484.9 Pa, respectively. Additionally, the maximum displacements were determined to be 102.30 μm and 158.28 μm, respectively. According to the findings of muscle force 100% increase in dumbbell weight increases the maximum muscle force by 83.13% and the average muscle force by 60.17%. Therefore, it is understood that there was no linear correlation between weight gain and muscle force.

Keywords: Joint moment, Biceps Brachii muscle force, musculoskeletal model, elbow joint, EMG

1. Introduction

The biceps brachii (BB) is a skeletal muscle located in the upper arm, composed of a long and short head that originate from the scapula and is inserted on the radius bone [1]. It is responsible for flexing the elbow joint, supinating the forearm, and is innervated by the musculocutaneous nerve [2]. The muscle is made up of both fast-twitch and slow-twitch muscle fibers, allowing for both explosive power and sustained contraction [3]. The muscle is also considered a synergist for other muscles involved in elbow flexion, such as the brachialis and brachioradialis muscles [4]. In general, the BB muscle plays an important role in many aspects of upper body movement and is a key muscle for daily activities as well as athletic performance [5, 6]. Therefore, strengthening the BB muscle can provide numerous benefits, including improved arm strength, better aesthetics, and improved grip strength [7]. There are several effective methods to strengthen the BB muscle, including resistance training [8, 9], isometric training [10], plyometric training [11], and eccentric training [12]. Resistance training involves using weights or resistance bands to perform exercises that target the

BB muscle [13], whereas isometric training involves holding a static contraction of the muscle without any joint movement [14]. Plyometric training involves performing explosive movements that involve rapid stretching and contracting of the muscle [15], and eccentric training involves focusing on the lowering phase of a movement [16]. The literature surveyed indicates that resistance training is a highly effective way to strengthen the BB muscle, and has several advantages over other types of exercise for achieving this goal [17, 18]. By providing specificity, progressive overload, high muscle activation, and flexibility, resistance training is a key tool for building strength and hypertrophy in the BB muscle [19, 20]. It is worth mentioning that dumbbell curls are a common exercise in resistance training programs aimed at strengthening and hypertrophying the BB muscle, and can be performed as part of a full-body workout or as a targeted exercise in isolation [21, 22]. Therefore, researchers are studying the effects of dumbbell curls on the BB muscle to understand the mechanisms of muscle hypertrophy, improve athletic performance, and potentially develop rehabilitation programs for individuals recovering from injury or surgery

[23, 24]. Additionally, insights into the optimal training strategies for enhancing bicep strength may be useful for individuals with musculoskeletal disorders [25, 26].

The effect of dumbbell curls exercise on the BB muscle has been investigated through the use of different methodologies in various studies. These include electromyography (EMG) [27] to assess muscle activation levels, muscle biopsies [28] to analyze changes in muscle fiber size and composition, ultrasound imaging [29] to measure muscle thickness and cross-sectional area, and strength testing [30] to evaluate changes in muscular strength and endurance. Additionally, some studies have utilized different variations of the dumbbell curl exercise, such as altering the resistance [31], range of motion [32], and grip type [33], to investigate the effects of these factors on BB muscle activation and hypertrophy. In general, these diverse methods provide a comprehensive understanding of the physiological [34] and biomechanical [35] responses of the BB muscle to dumbbell curls exercise. In the open literature, several studies have been conducted to investigate the biomechanical modifications occurring in the BB muscle during different forms of physical exercise. For example, Watanabe et al. (2015) studied EMG changes in the BB muscle during resistance training and detraining in 10 male subjects. They performed 6 weeks of resistance training on one arm followed by 8 weeks of detraining, measuring EMG using a 64-channel surface system during dumbbell curls. The researchers found that EMG amplitude increased during training, but returned to baseline during detraining. However, the spatial distribution of EMG potentials did not significantly change during either phase [36]. Hwang et al. (2016) developed a new method for predicting muscle fatigue and force during isokinetic dumbbell curl exercise using EMG signals. The method involved investigating the relationship between biceps fatigue and EMG signals at different maximum voluntary contraction levels and co-plotting them in a global EMG index map. An algorithm based on this map was developed to predict muscle fatigue and force in real-time EMG signals with arbitrary maximum voluntary contraction levels [37]. Fu et al. (2018) investigated the impact of exercise intensity on electrical impedance changes of biceps tissue during a fatiguing isotonic exercise. Resistance and reactance measurements were collected from 18 participants before and after execution of a fatiguing protocol at two different intensities. This study found that exercise intensity did not significantly affect changes in electrical impedance of biceps tissue during a fatiguing isotonic exercise. This has important implications for the use of electrical impedance measurements in monitoring exercise-related changes and injury [38]. Li et al. (2020) utilized numerical and experimental methods to investigate the local muscle fatigue of the BB during dynamic and static contractions. Firstly, the electromechanical behavior of the human upper arm's skin, fat, muscle, and bone layers was investigated using the finite element method (FEM) to construct a three-dimensional model. Secondly, local muscle fatigue was evaluated using a non-invasive electrical impedance myography

system on ten volunteers. Finally, the study revealed that there is a linear correlation between resistance and muscle fatigue [39]. Coratella et al. (2023) investigated the impact of different handgrip positions on the activation of the BB and brachioradialis muscles during dumbbell curl exercises. EMG measurements in 10 resistance-trained male subjects revealed that the supinated grip resulted in higher BB activation, while the pronated grip yielded greater brachioradialis activation [40]. Typically, the techniques utilized for investigating the mechanical behavior of the BB muscle are contingent upon the particular kind of physical information that researchers seek to acquire. The open literature includes several investigations that primarily examine the mechanical behavior of the BB muscle during different exercises and movements, but there are no studies supporting each other.

The purpose of this study was to investigate the influence of different dumbbell weights on the BB muscle during dumbbell curl exercises, with a particular emphasis on the assessment of the associated dynamic forces. In this context, a multifaceted methodology was utilized, encompassing motion analysis, FEM, and EMG techniques, to unveil the concealed biomechanical intricacies governing muscle behavior during the dumbbell curl exercise. The initial approach entailed motion analysis, which encompassed the utilization of cameras and markers to monitor the kinematics of the link during exercise. This facilitated the quantification of link angle, angular velocity, and acceleration, thereby affording insight into the muscle's biomechanical activity during exercise. The subsequent approach utilized force and torque measurement, which enabled the determination of the magnitudes of forces and torques evoked during exercise. This data was critical for assessing the muscle's load and work output, consequently affording valuable insight into the resultant mechanical stresses on the muscle. The tertiary methodology comprised FEM, which entailed utilizing computerized models to emulate the dynamics of the musculotendinous-bony complex during exercise. This method allowed for the prediction of the stresses and strains placed on the muscle, tendons, and bones during exercise, providing a way to analyze the internal stresses and strains that occur in the muscle during exercise. Finally, the acquisition of EMG signals during exercise was utilized. EMG involved measuring the electrical activity in the muscle during exercise, providing insight into the activation patterns of the muscle during exercise and how the muscle functioned during activity. Together, these methods provided a comprehensive understanding of the changes that occur in the BB muscle during dumbbell curl exercises with different weights. These techniques provided complementary information on the mechanical stresses placed on the muscle, the internal stresses and strains occurring within the muscle, and the activation patterns of the muscle during exercise.

This study is potentially novel in the field of biomechanics as it combines several methods to examine changes in the BB muscle during dumbbell curl exercise. In general,

the study has the potential to provide valuable insights into the biomechanics of dumbbell curl exercise and could contribute to the development of more effective exercise programs for individuals looking to strengthen their BB muscle. These methodologies can also be applied to effectively engage the BB muscle during rehabilitation processes and monitor the recovery progress. Therefore, this research holds the potential to offer benefits in the biomedical and healthcare domains. The organization of the paper is as follows. The methods of the study are described in Section 2. In Section 3, the results of motion analysis, muscle force, FEM simulations, and EMG analysis are presented and discussed. Finally, the concluding remarks are reviewed in Section 4.

2. Materials and Methods

Investigating the effects of the dumbbell curl exercise on the BB muscle using a combination of motion analysis, FEM, and EMG signals was the central focus of this study. A simulation model was created to encompass the forearm, upper arm, elbow joint, and shoulder joint for this purpose. The mass properties of the body segments were adapted from previous studies, and the motion analysis of the dumbbell curl exercise was performed with a male participant. The Link Segment Model (LSM) and body mass properties were modeled with MATLAB Simscape Multibody block diagrams, and the dumbbell curl exercise was simulated using motion analysis data with the Simscape Multibody model. In addition, EMG signals were used to measure the electrical activity of the muscle during the exercise. The following sections provide a detailed description of these methods and their application in this study.

2.1. Biomechanical Model of the Dumbbell Curl Movement

The LSM consisting of the forearm, upper arm, elbow joint, shoulder joint, BB, and dumbbells is shown in Figure 1. It was determined that the forearm and upper arm were solid bodies. The movement of the shoulder and wrist joints remained constant since no examination was conducted on them. In accordance with the Hill muscle model, the BB was modeled using spring and damping elements [41]. The composition of this model consists of a contractile element (CE), a series element (SE), and a parallel element (PE). CE is surrounded by passive connective tissue. In this model, PE refers to connective tissues, and SE refers to the force produced by tendons.

The maximum contraction force of the BB according to the Hill muscle model could be expressed in Equation 1.

$$[\vec{F}(x) + a][\vec{v}(t) + b] = [\vec{F}(x)_{max} + a]b \tag{1}$$

where, F was the muscle force, v was the muscle contraction velocity, F_{max} was the maximum isometric force, t was the time, x was the muscle strain, a and b were the contraction constants. The moment generated on the elbow joint during the dumbbell curl exercise due to the force exerted on the BB is mathematically represented by Equation 2.

$$\vec{M}(t) = \vec{F}(t) \cdot d \tag{2}$$

The moment of reaction, denoted as M, was exerted at the elbow joint while the distance between the connection point of the BB and the forearm and the elbow joint's center of rotation was represented by d in Equation 2. Because Equation 1 was structured non-linearly [41], determining muscle force from joint moment was more straightforward.

Based on previous studies, the mass, moment of inertia, length of the segment, center of mass location, BB stiffness, damping constant, and distance from bone attachment point to joint center (d) were determined. Additionally, the male participant's weight and height (70 kg, 174 cm) were measured and utilized as parameters for the motion analysis study. It is important to note that the male participant included in the analysis had no reported health issues and had a background in sports activities. The anthropometric characteristics of the LSM are listed in Table. It is worth noting that 5 kg and 10 kg dumbbells were modeled as thin discs in this study.

2.2. Motion Analysis

The characteristics of a male participant mentioned in the previous section were subjected to motion analysis. In this regard, passive markers were placed on the shoul-
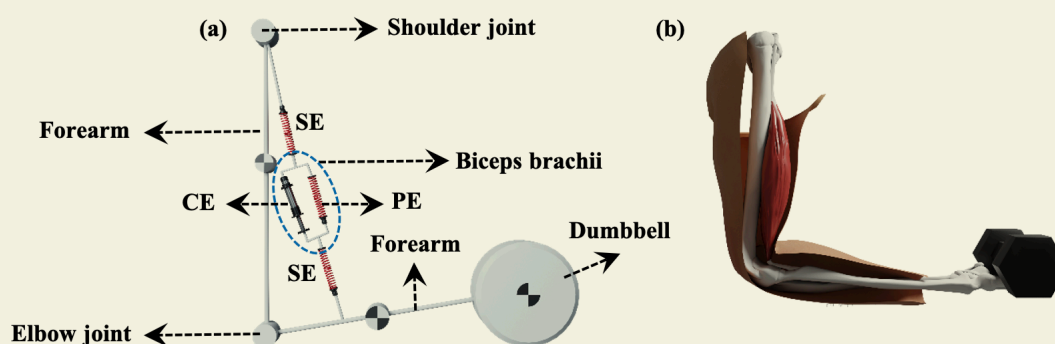

Figure 1. Musculoskeletal model of the dumbbell curl exercise. a) LSM, and b) physiological model.

der joint, the elbow joint, and the dumbbell. The participant performed the exercise using 5 kg and 10 kg dumbbells. The motion analysis was initiated with the forearm placed parallel to the ground, followed by a curling motion of the forearm, and terminated with the forearm assuming its original position, completing the analysis process. The participant stood and moved at the self-selected speed during the motion analysis. Meanwhile, the images were captured using a digital video camera that recorded 30 frames per second. The calculation of the angular displacement of the elbow joint was carried out using camera images, with the assistance of the Open Source Physics video analysis software.

2.3. MATLAB Simscape Structure of the LSM

In this study, the Simscape Multibody tool was used to prepare the joint model, as presented in Figure 2. Simscape Multibody is a robust and versatile simulation environment within MATLAB, specifically designed

for modeling and simulating multi-domain physical systems. The elbow joint was actuated by the "Joint Actuator" block. The values obtained as a result of motion analysis were transferred to the model from the file named 'R1' (displacement, velocity, acceleration, time) in MATLAB Workspace. The solution of the Simscape Multibody model was done with the inverse dynamics method (fixed-step, sample time: 0.033) [47]. The moment of reaction that occurred in the elbow joint was calculated using the 'Joint Sensor' block. Subsequently, muscle force was calculated according to Equation 2.

2.4. EMG Analysis of BB

In this study, EMG was utilized to assess the biomechanical effects of dumbbell curl exercise on the BB muscle. EMG measurement [48] was performed to determine the level of muscle contraction during exercises with different dumbbell weights. The Delsys Bagnoli amplifier, manufactured by Delsys Inc. and featuring 8 channels

Table. Anthropometric properties. k; spring stiffness, b; damping constant, l; BB length.						
Segment Parameters						
Body	Length (cm) [42]	Mass (kg) [42]	Moment of inertia (g·cm²) [43]			Centre of mass from proximal end (cm) [42]
			I_{xx}	I_{yy}	I_{zz}	
Upper arm	30.52	1.965	$132×10^3$	$22×10^3$	$133×10^3$	13.3
Forearm	26.3	1.123	$64.5×10^3$	$88.8×10^3$	$66.9×10^3$	11.31
BB parameters						
k = 196 N/m [44]	b = 49 Ns/m [41]		l = 25 cm [41]			d; variable [45, 46]
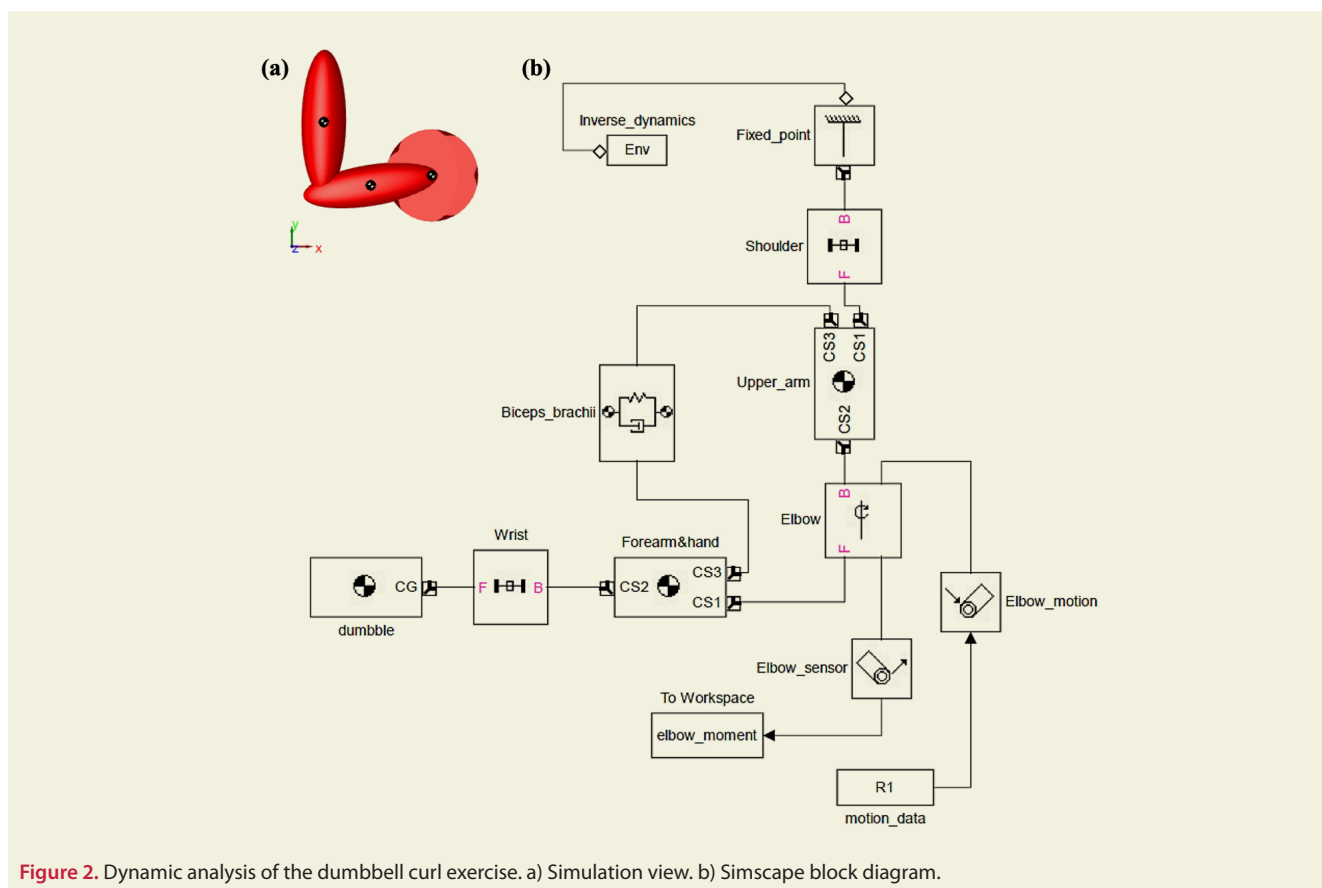
Figure 2. Dynamic analysis of the dumbbell curl exercise. a) Simulation view. b) Simscape block diagram.

Figure 3. Representation of dumbbell curl exercise and EMG measurement.

with a total gain of 1000, was used for the measurement. A Delsys DE surface electrode was placed on the BB muscle belly on the anterior surface of the upper arm. The reference electrode is placed in the elbow area of the upper arm. Figure 3 illustrates the placement of the reference electrode in the elbow area of the upper arm. During the measurements, the participant was prevented from following the EMG measur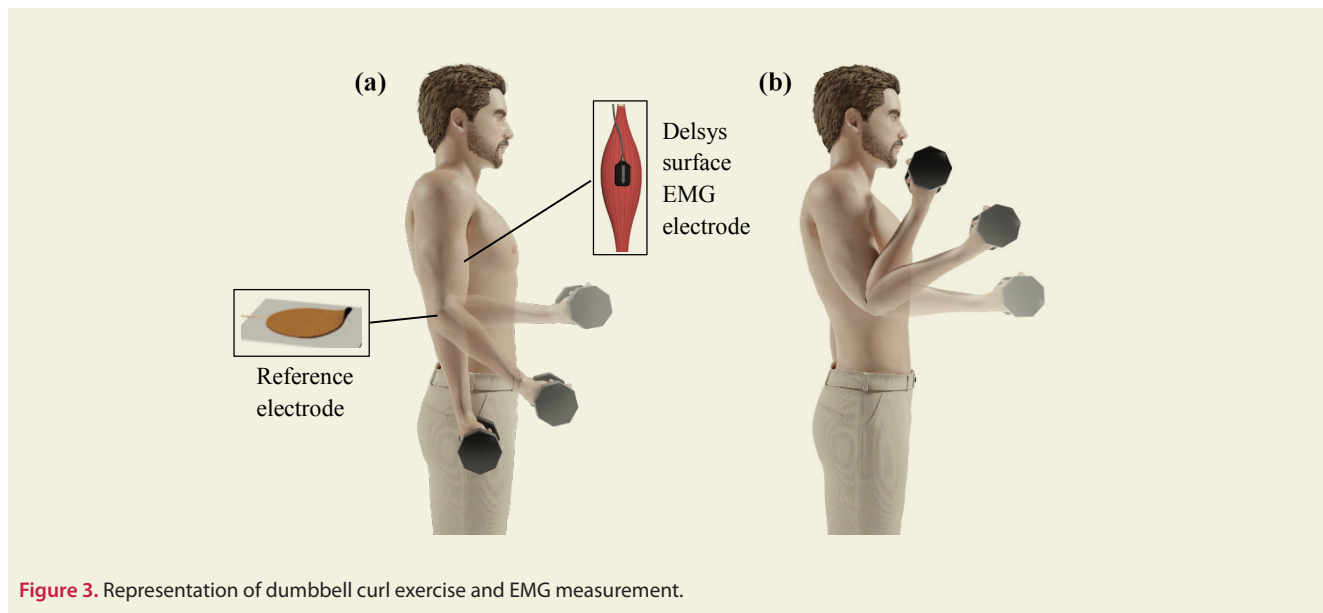ement screen in order to focus only on the exercise movements. The EMG signals recorded during exercises performed with 5 kg and 10 kg dumbbells were analyzed using Delsys EMG-Works software. In general, this study utilized state-of-the-art EMG techniques to provide a detailed and accurate assessment of muscle activation during dumbbell curl exercises, which could be useful in designing effective exercise programs for individuals seeking to improve biceps strength and hypertrophy. In section 3, a detailed analysis and evaluation of the EMG results was presented.

2.5. Finite Element Modelling

In this particular study, the FEM was utilized to simulate the displacement, stress, and strain parameters in the BB muscle during the performance of dumbbell curl exercise. The construction of the model was accomplished through the utilization of COMSOL Multiphysics 5.5 software, a prevalent tool for finite element analysis. It is significant to note that the complex anatomical configuration of the elbow joint was modeled in three dimensions using simple geometries reported in the literature [49]. The boundary components proposed for this joint are depicted in Figure 4. In the presented model, the cubes (bone) were interconnected via two small cylinders (tendons) and a central large cylinder (BB muscle), thereby establishing an integrated system. In the analyses, the representative BB muscle, bone, and tendon displayed respective densities of 1056 kg/m³, 2570 kg/m³, and 1670 kg/m³. Their respective Young's modulus were 1.162×10^6 Pa, 1.0×10^{10} Pa, and 1.6×10^6 Pa, while their respective poison ratios were 0.4, 0.3, and 0.497 [49]. The elasticity and damping constant values of the BB muscle, like many

other biological tissues, can vary depending on factors such as age, fitness level, and individual variability. However, in this study, the elastic constant value for the BB muscle, as presented in the open literature for numerical analyses, was assumed to be 3535 N/m, and the damping constant was taken as 6916 Ns/m [50].
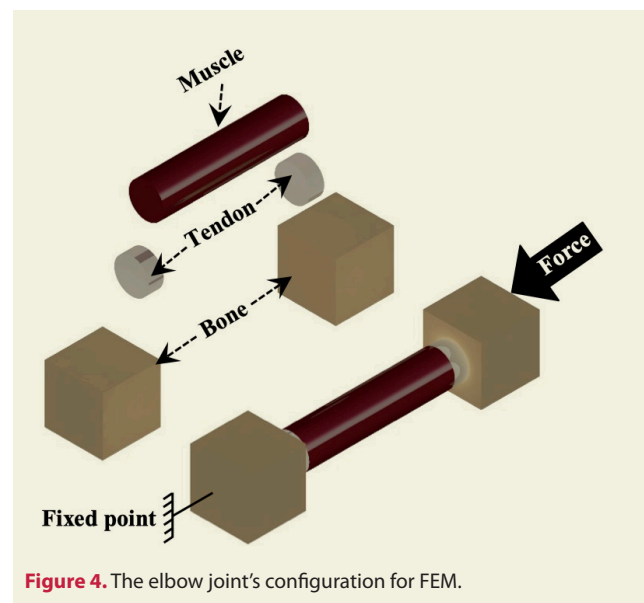
Figure 4. The elbow joint's configuration for FEM.

It is important to point out that the accuracy and validity of analysis depend on the quality of three-dimensional model, material properties, and appropriate finite element selection. In numerical analysis, the proper choice of finite element type is critical as the elements have varying capabilities and limitations. Therefore, it is important to choose the appropriate element type as it can significantly affect the accuracy and efficiency of the analysis. It is worth mentioning that the four-node tetrahedron type hyperelastic element is widely utilized by researchers in simulations of biological soft tissues, such as muscles [51-53]. The geometric shape of the element is a tetrahedron, which consists of four vertices and four

triangular faces. In order to approximate the behavior of a small volume of the muscle being analyzed, the element is utilized, and nodal values are used to calculate the stresses and strains within that volume. Thus, this study extensively investigated the nonlinear behavior of the BB muscle using a four-node tetrahedron-type hyperelastic element, which is a nonlinear, continuum-based method. Furthermore, antecedent to commencing the exhaustive analysis, the mesh convergence method was judiciously applied to ascertain the most suitable element and node quantities. Consequently, 3574 and 14296 were identified as the optimal element and node numbers, respectively. Subsequent to the delineation of pivotal parameters, FEM simulations were meticulously executed with a precision threshold of 0.001. By this method, it is possible to investigate any parameter such as displacement, strain, and stress. The results of the mechanical behavior of the LSM are presented in Section 3.

3. Results and Discussions

In our previous study, the elbow joint moment was quantified via Simscape simulation, followed by the computation of the corresponding muscle force that took into account the change in muscle moment arm [8]. The moment arm distance of BB was adapted from Delp et al. [45] in accordance with the angular changes of the elbow joint. The elbow moment and muscle force of the BB during exercise with 5 and 10 kg dumbbells were shown in Figures 5 and 6. It appeared that muscle force occurred more at the beginning and end of the exercise. In the dumbbell curl exercise with 5 kg dumbbells, 925 N of force occurred at the beginning of the exercise, while with 10 kg dumbbells, 1579 N of force occurred at the beginning. The force at the end of the exercise with 5 kg dumbbells was 1103 N, and at the end of the 10 kg exercise, a force of 2020 N had occurred. In addition, the average muscle force during exercise was evaluated, revealing average forces of 433.9 N and 695.0 N for training with 5 kg and 10 kg dumbbells, respectively.

Figure 6. BB muscle force during the dumbbell curl exercise [8].

The results of the EMG measurement, as depicted in Figure 7, indicated that the maximum amplitude of the BB muscle during the forearm dumbbell curl exercise increased with an increase in exercise load. Specifically, the maximum amplitude of the BB muscle in the exercise performed with a 5 kg dumbbell was 0.795×10^{-5} V, and the maximum amplitude increased to 1.30×10^{-5} V when the exercise was performed with a 10 kg dumbbell. Even though the exercise weight increased by 100%, the maximum EMG amplitude increased by 63.5%. Additionally, the minimum EMG amplitude during exercises performed with different dumbbells was measured as 0.513×10^{-5} V and 0.754×10^{-5} V, respectively. There was a 46.9% increase in the minimum EMG amplitude. The results suggested that as the exercise weight increased, the muscle activity also increased, which may have been related to the muscle's ability to generate more force to overcome the resistance. However, this increase appeared to be non-linear in comparison to the increase in exercise weight.

Figure 5. Elbow moment during the dumbbell curl exercise.
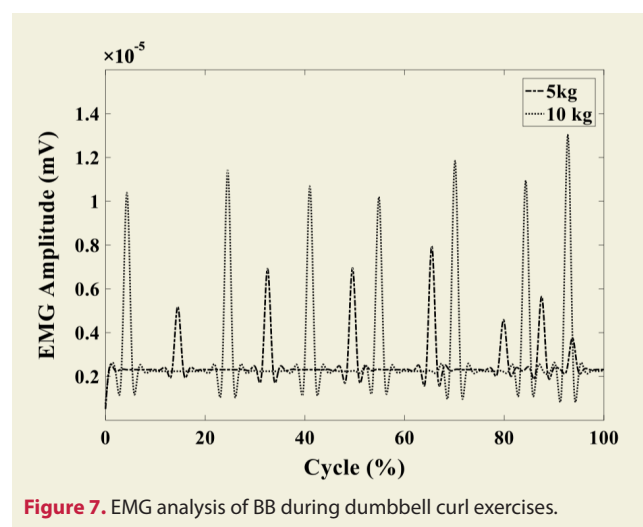
Figure 7. EMG analysis of BB during dumbbell curl exercises.

In the FEM analysis that was conducted (see Figure 8), the difference in the Young's modulus of bone (1×10^{10} Pa), tendon (1.6×10^{6} Pa), and muscle (1.162×10^{6} Pa) tissues

caused the maximum displacement to occur at the midline of the muscle and the junction surface of the tendon and bone. The concentration of displacement, stress, and strain values observed at the midline were the result of a complex interaction between tissue properties and mechanical loading. Nonetheless, the purpose of this study was to analyze the modifications in the mechanical behavior of the BB. Therefore, the effect of forces was investigated by determining a surface in the midline of the BB.

The results of the numerical analysis revealed that at 2020.80 N (see Figure 9), the maximum displacement, strain, and stress on the midline surface of the BB were 158.28 μm, 1.27×10^{-3} and 1484.97 Pa, respectively. The muscle force-induced displacement in BB was demonstrated in Figure 9a. The average displacement during exercise with 5 kg dumbbells was 34.51 μm, compared to 55.86 μm during exercise with 10 kg dumbbells. Moreover, the maximum displacements achieved were 102.30 μm and 158.28 μm, respectively. In Figure 9b, the stress-strain change in BB was illustrated, and the maximum stresses experienced during exercise movements were calculated to be 960.5 Pa and 1484.9 Pa, respectively.

3.1. Mechanical Considerations of LSM

In this study, the mechanical effects of different dumbbell weights on the BB were investigated. The muscle force was determined by means of the MATLAB Multibody tool. Although the MATLAB Multibody tools are developed for mechanical analysis of solid bodies, musculoskeletal systems can be examined in terms of mechanical aspects [54, 55]. Subsequently, the finite element model developed in the COMSOL Multiphysics 5.5 was utilized to study the stress-strain behavior of the BB, depending on muscle force. The muscle force findings showed that doubling the dumbbell weight resulted in an 83.13% increase in maximum muscle force and a 60.17% increase in average muscle force. The maximum and minimum EMG amplitudes experienced an increase of 63.5% and 46.9%, respectively, mirroring the pattern observed in muscle force. Therefore, it was understood that there was no linear relationship between weight gain and muscle force. This situation arose because the muscle moment arm distance was dependent on the angle of the joint. It can be concluded from these findings that further increases in exercise weight would not result in a similar effect on muscle contraction. The research
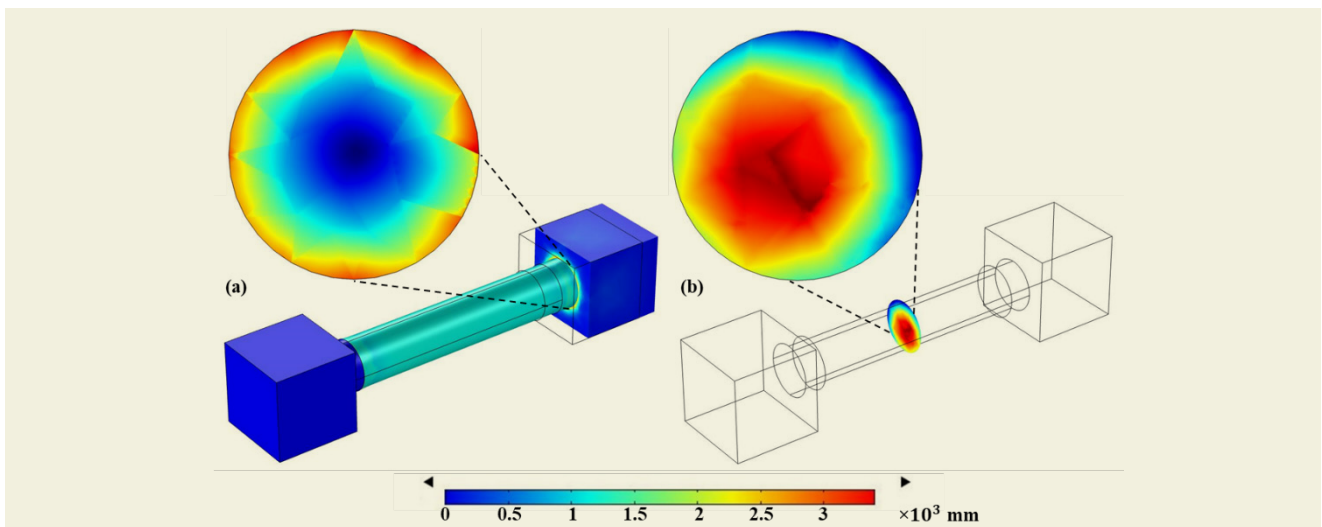

Figure 8. Displacement analysis of LSM at a) the junction surface of the bone-tendon tissues, and b) the midline of the BB.
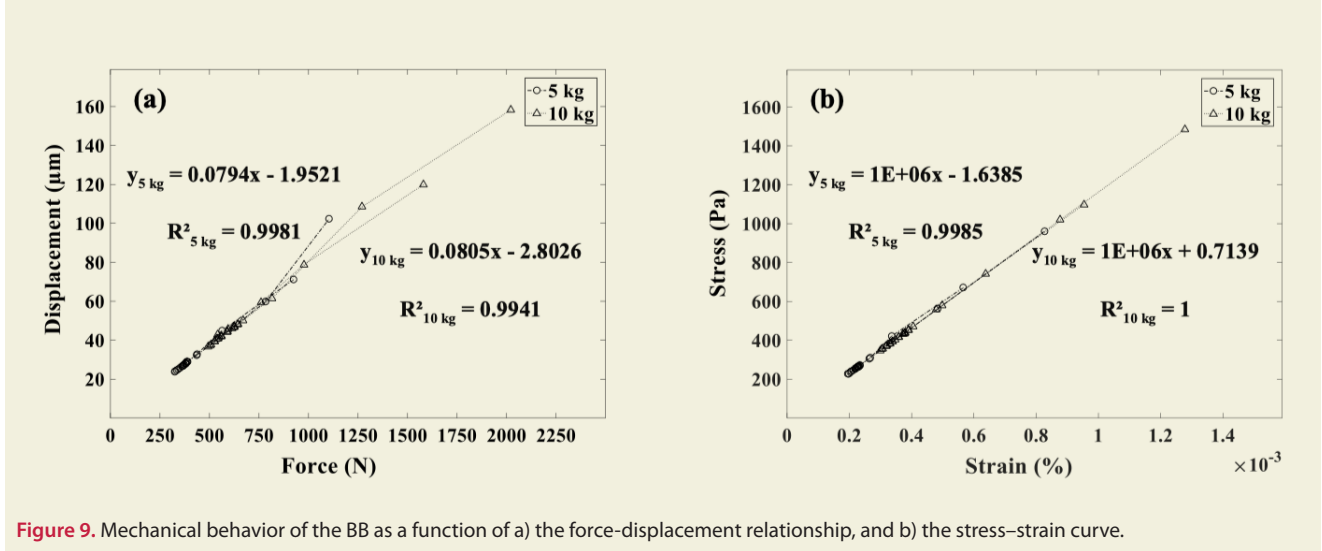

Figure 9. Mechanical behavior of the BB as a function of a) the force-displacement relationship, and b) the stress–strain curve.

conducted by Bryanton et al. [56] on Scott demonstrated that increasing barbell load had no discernible impact on muscle effort with measuring EMG. The results of our study mirrored this finding.

In light of the pressure and strain findings, it was determined that the maximum displacement and maximum strain had increased by 54.72% and 54.59%, respectively, upon doubling the weight of the dumbbell. Once again, it is observed that weight gain and the search for pressure and strain are not linearly related. Nevertheless, an escalation in strain led to an increase in muscle tension. The research conducted by Leedham and Dowling [57] showed that stretching the arm from the BB area resulted in an increase in the maximum muscle force. These results were also supported by our findings. The finite element analysis results indicated that the tendon underwent more substantial changes, primarily because of the unique material properties of the tendon tissue.

This study utilized MATLAB R2018b and COMSOL Multiphysics 5.5 to holistically model muscle, tendon, and bone tissues. The analyses were carried out with a sensitivity of 0.001s. The changes that occur at each point of the model as a result of applying random dynamic forces were investigated. Consequently, it was evident that the FEM analysis conducted in this study yielded accurate mechanical behaviors of LSM, which were consistent with the findings of previous studies.

3.2. Comparison with the State of the Art

In accordance with the investigation, the mechanical behavior of the BB muscle could be compared with those described in other research that utilized different methodologies. In previous research, the biomechanical effects of exercise on the BB muscle were studied using techniques such as EMG [58, 59], ultrasound imaging [60, 61], and magnetic resonance imaging (MRI) [62]. In comparison to EMG analysis, the study provided a more complete understanding of the mechanical behavior of the BB muscle during dumbbell curl exercise by utilizing joint motion analysis and finite element analysis. In contrast to EMG analysis, joint motion analysis and finite element analysis provided extensive insights into muscle force, moment, and activation patterns. The supplementary data can assist researchers in comprehending the interaction between the BB muscle with other muscles and joints during exercise. Similarly, ultrasound imaging and MRI were useful for evaluating muscle structure and activation patterns. However, these techniques were often expensive and time-consuming compared to joint motion analysis and finite element analysis. Additionally, ultrasound imaging and MRI did not provide information on muscle force and moment, which were critical in understanding the biomechanics of muscle function during exercise. Therefore, the joint motion analysis and finite element analysis methods used in the study provided several advantages over other techniques in terms of comprehensively evaluating the biomechanical effects of exercise on the BB muscle. These methods offered a

cost-effective and time-efficient way to examine muscle force, moment, and activation patterns, which were essential for understanding muscle function during exercise. In our previously referenced study [8], these techniques were applied to a single fiber of the BB muscle, resulting in significant findings. Furthermore, in the present investigation, an additional EMG approach was incorporated to scrutinize the biomechanical dynamics exhibited by the entirety of the BB muscle. Finally, the study provided valuable insights into the mechanical behavior of the BB muscle during dumbbell curl exercise, and the joint motion analysis and finite element analysis methods used in the research offered several advantages over other techniques used in previous studies.

4. Conclusion

It is necessary to perform continuous exercises and strengthen muscles to achieve high performance levels in different types of sports. The BB muscle can also grow with different exercises depending on the position of the forearm. The BB muscle is a long muscle that sits anteriorly to the humerus, characterized by an easily palpable, oval-shaped bump. It is one of the flexor group muscles of the forearm and, as the only flexor of the arm, it extends from the shoulder joint to the elbow joint and acts on both joints. Therefore, it is particularly important to strengthen this muscle based on the correct principles. This is because BB injury is associated with pain and inflammation and causes limitations in daily activities. An important point to make is that injuries and pain in this muscle are usually caused by excessive pressure and overuse. The techniques used in this paper are crucial for addressing BB muscle injuries and pain because they provide a comprehensive understanding of the underlying biomechanics. Moreover, the conclusions of this study have found that the mechanical behavior of dynamic muscle force generated during a dumbbell curl exercise was investigated using MATLAB R2018b and COMSOL Multiphysics 5.5. It was evident from that research that specialized software programs like Open-Sim, AnyBody, and LifeModeler, developed exclusively for muscle mechanics analysis, were not mandatory for carrying out muscle mechanics studies. The findings of the study were consistent with the previous literature, as revealed by the results. Additionally, it was found that the correlation between muscle force increase and muscle contraction is not linear and that the proposed model can be easily expanded and applied to other muscles and exercise movements. This research can help to improve our understanding of muscles' response to different loads and can aid in exercise prescription, muscle training, and injury prevention. Therefore, the methodologies used in the study show promise for applications in the biomedical and healthcare fields. These approaches can be adapted to design more effective rehabilitation programs, monitor progress, and contribute to the overall well-being of individuals with specific muscle-related conditions.

It is important to acknowledge certain limitations in this

study. Firstly, this study involved tests on a single participant, who was a healthy individual without any preexisting medical conditions. Future studies could explore the applicability of findings to a broader population, including individuals with various fitness levels and clinical conditions. Secondly, the study focused solely on the BB muscle, and future research could extend its scope to other muscle groups involved in similar exercises to provide a more comprehensive understanding of exercise biomechanics. Additionally, this study primarily examined short-term effects, and longitudinal investigations could elucidate the long-term adaptations of the BB muscle to different training regimens. Furthermore, technological advancements may offer new avenues for more precise data collection and analysis.

References

[1] Jarmey, C. (2018). The concise book of muscles. North Atlantic Books.

[2] Benes, M., Kachlik, D., Lev, D., & Kunc, V. (2022). Accessory heads of the biceps brachii muscle: A systematic review and meta-analysis. Journal of Anatomy, 241(2): 461-477. doi:10.1111/joa.13666.

[3] Eberstein, A. R. T. H. U. R., & Goodgold, J. O. S. E. P. H. (1968). Slow and fast twitch fibers in human skeletal muscle. American Journal of Physiology-Legacy Content, 215(3): 535-541. doi:10.1152/ajplegacy.1968.215.3.535.

[4] Allen, G. M., McKenzie, D. K., & Gandevia, S. C. (1998). Twitch interpolation of the elbow flexor muscles at high forces. Muscle & Nerve: Official Journal of the American Association of Electrodiagnostic Medicine, 21(3): 318-328. doi:10.1002/(SICI)1097-4598(199803)21:3%3C318::AID-MUS5%3E3.0.CO;2-D.

[5] McGinnis, P. M. (2013). Biomechanics of sport and exercise. Human Kinetics.

[6] Bussey, M. (2002). Sports biomechanics: Reducing injury and improving performance. Routledge.

[7] Landin, D., Thompson, M., & Jackson, M. R. (2017). Actions of the biceps brachii at the shoulder: a review. Journal of Clinical Medicine Research, 9(8): 667. doi:10.14740/jocmr2901w.

[8] Asadi Dereshgi, H., Serbest, K., Balik, B., Sahin, S. N. (2022). Stress-strain response of muscle fibers in biceps brachii under dynamic force: An analysis of biceps curl exercise. Journal of Polytechnic, 25: 1777–1783. doi:10.2339/politeknik.1025328.

[9] Asadi Dereshgi, H., Serbest, K., Şahin, S. N., Balik, B. (2022). A mechanical model and stress-strain response of the biceps brachii under static load. European Mechanical Science, 6: 27–31. doi:10.26701/ems.1015772.

[10] Lovecchio, N., Maiorano, C., Naddeo, F., Sforza, C. (2010). Biceps brachii muscle fatigue during isometric contraction: Is antagonist muscle fatigue a key factor?. The Open Sports Medicine Journal, 6: 1–8. doi:10.2174/1874387001307010001.

[11] Sgroi, T. A. (2021). Post-operative Rehabilitation: Biceps Tenodesis. The Management of Biceps Pathology: A Clinical Guide from the Shoulder to the Elbow, 235-241. doi:10.1007/978-3-030-63019-5_19.

[12] Jhan, T., Zutshi, K., & Sethi, A. (2021). Effect of Vibration on Delayed Onset Muscle Soreness before and after the Eccentric Exercise in Biceps Brachii Muscle of Females. International Journal of Preventive Cardiology, 1(1): 4-12.

[13] Fleck, S. J., & Kraemer, W. (2014). Designing resistance training programs, 4E. Human Kinetics.

[14] Davies, J., Parker, D. F., Rutherford, O. M., & Jones, D. A. (1988). Changes in strength and cross sectional area of the elbow flexors as a result of isometric strength training. European journal of applied physiology and occupational physiology, 57: 667-670. doi:10.1007/bf01075986.

[15] Lundin, P. (1985). Plyometrics: A review of plyometric training. Strength & Conditioning Journal, 7(3): 69-76.

[16] Mike, J., Kerksick, C. M., & Kravitz, L. (2015). How to incorporate eccentric training into a resistance training program. Strength & Conditioning Journal, 37(1): 5-17. doi:10.1519/ssc.0000000000000114.

[17] Peterson, M., Rhea, M., Alvar, B. (2004). Maximizing strength development in athletes. Journal of Strength and Conditioning Research, 18: 377–382. doi:10.1519/00124278-200405000-00031.

[18] Schoenfeld, B. J., Peterson, M. D., Ogborn, D., Contreras, B., & Sonmez, G. T. (2015). Effects of low-vs. high-load resistance training on muscle strength and hypertrophy in well-trained men. The Journal of Strength & Conditioning Research, 29(10): 2954-2963. doi:10.1519/jsc.0000000000000958.

[19] Schoenfeld, B. J., Contreras, B., Krieger, J., Grgic, J., Delcastillo, K., Belliard, R., & Alto, A. (2019). Resistance training volume enhances muscle hypertrophy but not strength in trained men. Medicine and science in sports and exercise, 51(1): 94. doi:10.1249/mss.0000000000001764.

[20] Steele, J., Fisher, J., Giessing, J., & Gentil, P. (2017). Clarity in reporting terminology and definitions of set endpoints in resistance training. Muscle & nerve, 56(3): 368-374. doi:10.1002/mus.25557.

[21] Wakahara, T., Miyamoto, N., Sugisaki, N., Murata, K., Kanehisa, H., Kawakami, Y., ... & Yanai, T. (2012). Association between regional differences in muscle activation in one session of resistance exercise and in muscle hypertrophy after resistance training. European journal of applied physiology, 112: 1569-1576. doi:10.1007/s00421-011-2121-y.

[22] Wilk, M., Stastny, P., Golas, A., Nawrocka, M., Jelen, K., Zajac, A., & Tufano, J. (2018). Physiological responses to different neuromuscular movement task during eccentric bench press. Neuroendocrinology Letters, 39(1): 26-32.

[23] Campos, G. E., Luecke, T. J., Wendeln, H. K., Toma, K., Hagerman, F. C., Murray, T. F., ... & Staron, R. S. (2002). Muscular adaptations in response to three different resistance-training

regimens: specificity of repetition maximum training zones. European journal of applied physiology, 88: 50-60. doi:10.1007/s00421-002-0681-6.

[24] Folland, J. P., & Williams, A. G. (2007). Morphological and neurological contributions to increased strength. Sports medicine, 37: 145-168. doi: 10.2165/00007256-200737020-00004.

[25] Romiti, M., Finch, C. F., & Gabbe, B. (2008). A prospective cohort study of the incidence of injuries among junior Australian football players: evidence for an effect of playing-age level. British journal of sports medicine, 42(6): 441-446. doi:10.1136/bjsm.2008.051417.

[26] Wernbom, M., Augustsson, J., & Thomeé, R. (2007). The influence of frequency, intensity, volume and mode of strength training on whole muscle cross-sectional area in humans. Sports medicine, 37: 225-264. doi:10.2165/00007256-200737030-00004.

[27] Liao, F., Zhang, X., Cao, C., Hung, I. Y. J., Chen, Y., & Jan, Y. K. (2021). Effects of muscle fatigue and recovery on complexity of surface electromyography of Biceps Brachii. Entropy, 23(8): 1036. doi:10.3390/e23081036.

[28] Mattiello-Sverzut, A. C., & Martins, E. J. (2023). Does the early phase of aging affect the morphology of biceps brachii and torque and total work of elbow flexors in healthy volunteers?. Brazilian Journal of Medical and Biological Research, 56. doi:10.1590/1414-431x2023e12202.

[29] Li, S., Li, H., Hu, Y., Zhu, S., Xu, Z., Zhang, Q., ... & Xu, J. (2020). Ultrasound for measuring the cross-sectional area of biceps brachii muscle in sarcopenia. International Journal of Medical Sciences, 17(18): 2947. doi:10.7150/ijms.49637.

[30] Nuzzo, J. L. (2023). Narrative review of sex differences in muscle strength, endurance, activation, size, fiber type, and strength training participation rates, preferences, motivations, injuries, and neuromuscular adaptations. Journal of strength and conditioning research, 37(2): 494-536. doi:10.1519/jsc.0000000000004329.

[31] Barakat, C., Barroso, R., Alvarez, M., Rauch, J., Miller, N., Bou-Sliman, A., & De Souza, E. O. (2019). The effects of varying glenohumeral joint angle on acute volume load, muscle activation, swelling, and echo-intensity on the biceps brachii in resistance-trained individuals. Sports, 7(9): 204. doi:10.3390/sports7090204.

[32] Pedrosa, G. F., Simões, M. G., Figueiredo, M. O., Lacerda, L. T., Schoenfeld, B. J., Lima, F. V., ... & Diniz, R. C. (2023). Training in the initial range of motion promotes greater muscle adaptations than at Final in the arm curl. Sports, 11(2): 39. doi:10.3390/sports11020039.

[33] Bagchi, A., & Raizada, S. (2019). A comparative electromyographical analysis of biceps brachii and brachioradialis during eight different types of biceps curl. Indian Journal of Public Health, 10(5): 730-735. doi:10.5958/0976-5506.2019.01098.2.

[34] Girard, O., Mariotti-Nesurini, L., & Malatesta, D. (2022). Acute performance and physiological responses to upper-limb multi-set exercise to failure: Effects of external resistance and systemic hypoxia. European Journal of Sport Science, 22(12): 1877-1888. doi:10.1080/17461391.2021.2002951.

[35] Serbest, K. (2022). A biomechanical analysis of dumbbell curl and investigation of the effects of increasing loads on biceps brachii using a finite element model. doi: 10.21203/rs.3.rs-1263844/v1.

[36] Watanabe, K., Kouzaki, M., & Moritani, T. (2015). Spatial EMG potential distribution of biceps brachii muscle during resistance training and detraining. European journal of applied physiology, 115: 2661-2670. doi:10.1007/s00421-015-3237-2.

[37] Hwang, H. J., Chung, W. H., Song, J. H., Lim, J. K., & Kim, H. S. (2016). Prediction of biceps muscle fatigue and force using electromyography signal analysis for repeated isokinetic dumbbell curl exercise. Journal of Mechanical Science and Technology, 30: 5329-5336. doi:10.1007/s12206-016-1053-1.

[38] Fu, B., & Freeborn, T. J. (2018). Biceps tissue bioimpedance changes from isotonic exercise-induced fatigue at different intensities. Biomedical Physics & Engineering Express, 4(2): 025037. doi:10.1088/2057-1976/aaabed.

[39] Li, D., Huang, L., Wen, Y., Gao, Y., Vasić, Ž. L., Cifrek, M., & Du, M. (2020). Analysis of electrical impedance myography electrodes configuration for local muscle fatigue evaluation based on finite element method. IEEE Access, 8: 172233-172243. doi:10.1109/access.2020.3025150.

[40] Coratella, G., Tornatore, G., Longo, S., Toninelli, N., Padovan, R., Esposito, F., & Cè, E. (2023). Biceps Brachii and Brachioradialis Excitation in Biceps Curl Exercise: Different Handgrips, Different Synergy. Sports, 11(3): 64. doi:10.3390/sports11030064.

[41] Winters, J. M., & Woo, S. L. (Eds.). (2012). Multiple muscle systems: biomechanics and movement organization. Springer Science & Business Media.

[42] Gordon, D., Robertson, E., Caldwell, G. E., Hamill, J., Kamen, G., Whittlesey, S. N. (2004). Research methods in biomechanics. Human Kinetics, Champaign.

[43] Chandler, R. F., Clauser, C. E., McConville, J. T., Reynolds, H. M., Young, J. W. (1975). Investigation of inertial properties of the human body. Aerospace Medical Research Laboratory, Technical Report.

[44] Agyapong-Badu, S., Warner, M., Samuel, D., Stokes, M. (2016). Measurement of ageing effects on muscle tone and mechanical properties of rectus femoris and biceps brachii in healthy males and females using a novel hand-held myometric device. Archives of Gerontology and Geriatrics, 62: 59-67. doi:10.1016/j.archger.2015.09.011.

[45] Delp, S. L., Anderson, F. C., Arnold, A. S., Loan, P., Habib, A., John, C., Guendelman, E., Thelen, E. D. G. (2007). OpenSim: Open-Source Software to Create and Analyze Dynamis Simulations of Movement. IEEE Transactions on Biomedical Engineering, 54: 1940-1950. doi:10.1109/TBME.2007.901024.

[46] Tozeren, A. (2000). Human Body Dynamics Classical Mechanics and Human Movement. New York: Springer-Verlag.

[47] Jamshidi, N., Rostami, M., Najarian, S., Menjah, M. B., Saadatnia, M., Firooz, S. (2009). Modelling of human walking to optimise the function of ankle-foot orthosis in Guillan-Barre patients with drop foot. Singapore Med J, 50(4): 412–417.

[48] Khushaba, R. N., Kodagoda, S., Takruri, M., & Dissanayake, G. (2012). Toward improved control of prosthetic fingers using surface electromyogram (EMG) signals. Expert Systems with Applications, 39(12): 10731-10738. doi: 10.1016/j.eswa.2012.02.192.

[49] Ford, J. M. (2013). Skeletal Muscle Contraction Simulation: A Comparison in Modeling. Ph.D. thesis, University of South Florida.

[50] Gherasim, D. M., Arghir, M. (2021). Study of the Free Vibrations Over the Muscular System of the Human Body. Part I: Mechanical Characteristics of the Left Deltoid. Acta Technica Napocensis-Series: Applied Mathematics, Mechanics, and Engineering, 64(1): 123-128.

[51] Modi, V., Fulton, L., Jacobson, A., Sueda, S., Levin, D. I. W. (2020). EMU: Efficient muscle simulation in deformation space. Computer Graphics Forum, 40: 234–248. doi:10.1111/cgf.14185.

[52] Teran, J., Blemker, S., Hing, V. N. T., Fedkiw, R. (2003, July). Finite volume methods for the simulation of skeletal muscle. In Proceedings of the 2003 ACM SIGGRAPH/Eurographics symposium on Computer animation (pp. 68-74).

[53] Asadi Dereshgi, H., Serbest, K. (2022). A finite element model of the deltoid muscle and biomechanical analysis of the standing dumbbell fly for shoulder exercises. Journal of the Brazilian Society of Mechanical Sciences and Engineering, 44: 439. doi:10.1007/s40430-022-03745-y.

[54] Cilli, M., Serbest, K., Kayaoglu, E. (2021). The effect of body weight on joint torques in teenagers: Investigation of sit-to-stand movement. Clinical Biomechanics, 83: 1-6. doi:10.1016/j.clinbiomech.2021.105288.

[55] Serbest, K., Berisha, M., Cilli, M. (2018). Dynamic analysis of three different high bar dismounts in the Simmechanıcs environment. Journal of Mechanics in Medicine and Biology, 18: 1-11. doi:10.1142/S0219519418500306.

[56] Bryanton, M. A., Kennedy, M. D., Carey, J. P., Chiu, L. Z. F. (2012). Effect of Squat Depth and Barbell Load on Relative Muscular Effort in Squatting. Journal of Strength and Conditioning Research, 26: 2820–2828. doi:10.1519/jsc.0b013e31826791a7.

[57] Leedham, J. S., Dowling, J. J. (1995). Force-length, torque-angle and EMG-joint angle relationships of the human in vivo biceps brachii. European Journal of Applied Physiology and Occupational Physiology, 70: 421–426. doi:10.1007/bf00618493.

[58] Chatfield, L. T., Pretty, C. G., Fortune, B. C., McKenzie, L. R., Whitwham, G. H., & Hayes, M. P. (2021). Estimating voluntary elbow torque from biceps brachii electromyography using a particle filter. Biomedical Signal Processing and Control, 66: 102475. doi:10.1016/j.bspc.2021.102475.

[59] Bailey, C. A., Yoon, S., & Côté, J. N. (2021). Relative variability in muscle activation amplitude, muscle oxygenation, and muscle thickness: Changes with dynamic low-load elbow flexion fatigue and relationships in young and older females. Journal of Electromyography and Kinesiology, 59: 102553. doi:10.1016/j.jelekin.2021.102553.

[60] Mechtenberg, M., Grimmelsmann, N., Meyer, H. G., & Schneider, A. (2022). Manual and semi-automatic determination of elbow angle-independent parameters for a model of the biceps brachii distal tendon based on ultrasonic imaging. Plos one, 17(10): e0275128. doi:10.1371/journal.pone.0275128.

[61] Stragier, S., Baudry, S., Carpentier, A., & Duchateau, J. (2019). Efficacy of a new strength training design: the 3/7 method. European journal of applied physiology, 119: 1093-1104. doi:10.1007/s00421-019-04099-5.

[62] Stokes, T., Tripp, T. R., Murphy, K., Morton, R. W., Oikawa, S. Y., Lam Choi, H., ... & Phillips, S. M. (2021). Methodological considerations for and validation of the ultrasonographic determination of human skeletal muscle hypertrophy and atrophy. Physiological reports, 9(1): e14683. doi:10.14814/phy2.14683.

Investigation of alternative vehicle applications for reducing greenhouse gas emissions in urban public transport: The case of Adana province

Çağrı Ün[1*]

[1]Survey and Projects Department, Adana Metropolitan Municipality, Adana, Türkiye

Orcid: C. Un (0000-0002-7925-5000)

Abstract: Passenger cars, trucks, commercial airplanes, and railways all contribute to greenhouse gas emissions as part of the transportation sector. The usage of fossil fuels such as gasoline and diesel emits exhaust gases commonly referred to as greenhouse gases (GHGs) into the atmosphere. The buildup of these greenhouse gases in the atmosphere is responsible for global warming, a phenomenon that is becoming increasingly pronounced in today's climate. In response to the GHG problem, cities have started setting targets to reduce their emission values. Adana is one of the cities that has set reduction targets. In all of the studies forming the basis of this research, the potential for transitioning buses and minibuses used in public transportation in Adana to alternative vehicles is investigated, with a focus on reducing greenhouse gas emissions. This study includes a comparison between electric, compressed natural gas (CNG), hydrogen and conventional vehicles, considering various parameters such as fuel economy estimates, vehicle size, and emission calculations. The research delves into greenhouse gas emission calculations specific to the Adana province, along with potential alternative applications in public transportation. Within the province, the transportation sector accounts for 27% of the total city inventory's emissions. This study shows that converting the existing urban public transport fleet to alternative buses can lead an impressive reduction in greenhouse gas emissions as 81.93% with electric car, while hydrogen vehicles achieve a commendable 57.37% decrease. This underscores the substantial potential of electric and hydrogen-powered vehicles to lead to a significant reduction in transportation-related carbon emissions in the city. Consequently, the research places significant emphasis on addressing the transportation sector, which stands out as a primary contributor to emissions.

Keywords: Electric vehicle, CNG, hydrogen, diesel, greenhouse gas.

1. Introduction

Climate change refers to alterations in weather patterns, primarily stemming from the release of greenhouse gases by natural processes such as forest fires, earthquakes, oceanic activity, permanent ice melting, wetland dynamics, and volcanic eruptions [1], as well as human-driven actions, including energy production, industrial operations, and land use modifications [2,3]. Climate change stands as one of the foremost contemporary environmental challenges [4]. It poses several issues, including amplified global warming, heightened energy demands [5,6,7]. At the same time, cities play a pivotal role in worsening climate change, as urban activities act as substantial sources of greenhouse gas emissions. Estimates indicate that urban areas are responsible for approximately 75% of the world's CO_2 emissions, with transportation and buildings being the primary contributors to this substantial footprint. [8]. Simultaneously, cities serve as epicenters of creativity, innovation, and education, wielding the potential to drive substantial systemic changes across various critical environmental issues. With their local governments, cities are often the most capable entities to take proactive measures to address and resolve environmental challenges. Throughout history, municipalities have played pivotal roles in enhancing waste management, wastewater treatment, water resource management, public transportation, and urban land use through integrated urban planning strategies. In the present day, cities have taken on an increasingly central role in the realms of climate change mitigation and adaptation, the preservation and restoration of ecosystems, and the promotion of circular economies. Furthermore, the presence of easily accessible, high-quality green spaces within cities promotes physical and mental health, as well as social well-being [9].

Achieving triumph requires a synchronized strategy and execution at the global, regional, national, and local tiers. Hence, it is imperative to integrate cities as a fundamental component of the resolution to combat climate

change. Numerous cities are already taking substantial actions by employing renewable energy sources, adopting cleaner production methods, and instituting regulations or incentives to cap industrial discharges. The mitigation of emissions will also lead to a decrease in localized pollution stemming from industries and transportation, thereby enhancing the quality of urban air and the well-being of urban inhabitants [8].

The Ministry of Trade in the Republic of Türkiye published Green Reconciliation Action Plan in July 2021. This action plan includes objectives, tactics, and educational initiatives aimed at various aspects, such as border carbon regulations, fostering a green and circular economy, promoting green finance, ensuring a clean, efficient, and secure energy supply, advancing sustainable agriculture, facilitating sustainable smart transportation, addressing climate change mitigation, diplomatic efforts, and aligning with the European Green Deal [10].

Some outputs of Türkiye's Green Deal Action Plan are as follows;

- ✓ *Carbon at the Border:* Harmonization of standards and certification activities within the scope of the EU's border carbon regulation,
- ✓ *Green and Circular Economy:* Preparation of needs and impact analysis reports on the basis of priority sectors,
- ✓ *Green Finance:* Preparation of draft legislation to develop the ecosystem that will enable the development of green finance in Türkiye,
- ✓ *Clean and Reliable Energy Supply:* 1 GW capacity increase per year until 2027 for new solar and wind power plant developments,
- ✓ *Sustainable and Smart Transportation:* Determining the requirements and standards needed for the installation, operation and equipment of electric vehicle charging stations,
- ✓ *Combating Climate Change:* Preparation of Türkiye Climate Change Mitigation Report [11].

In the sense of following these steps taken at the national level, also local mechanisms have started to demonstrate their desire to reduce urban emissions by setting targets for themselves. At this point; the Global Covenant of Mayors on Climate and Energy (GCoM) is a structure in which governing bodies at the local level set targets for future generations by making commitments on climate and energy actions. Cities that are party to the GCoM support a common vision for 2050. This vision involves uniting a global coalition of numerous cities and local governments, and it can be characterized as a long-term commitment to promote voluntary actions aimed at addressing climate change and establishing a resilient, low-emission society. The commitment of the cities participating in the GCoM is to take the necessary measures within the framework of a 30%-40% greenhouse gas reduction target by 2030 and to act supporting the adoption of a common approach to combating climate

change[12]. Among the commitments of GCoM member cities are the following items;

- ✓ Preparation of a city-scale "Greenhouse Gas Emission Inventory" in accordance with the Sustainable Energy and Climate Action Plan (SECAP) guide,
- ✓ Assessment of climate risks and vulnerabilities,
- ✓ Setting ambitious, measurable and time-bound targets to reduce/prevent greenhouse gas emissions,
- ✓ Determination of ambitious climate adaptation vision and targets, based on numerical and scientific evidence as much as possible, in order to increase local resilience against climate change,
- ✓ Setting an ambitious and equitable target to improve access to safe, sustainable and affordable energy,
- ✓ Formulating formally endorsed strategies to tackle climate change mitigation/low emission development, enhance climate resilience and adaptation efforts, and ensure availability of sustainable energy [12].

Cities engaged in the GCoM have additionally embraced the SECAP, a strategic and policy dossier delineating the primary steps they intend to implement within a span of two years subsequent to the municipal council's resolution to translate their political pledges into tangible actions and initiatives.

1.1. Greenhouse Gas Emission in Transportation Sector

With the increasing world population over the years, people's need for transportation has also increased. Both passenger and freight transport play an important role. As a result of the need for transportation, the amount of CO_2 emissions has also increased. These emissions, which have increased over the years, will reach 12 Gt CO_2e/year in 2050 [13]. In 2021, carbon dioxide emissions from the transportation sector constituted 38% of energy-related emissions in the United States, making it the most significant contributor among all sectors of the economy [14].

In 2022, the recovery in both passenger and cargo transportation activities following the aftermath of the Covid-19 pandemic resulted in a 3% uptick in carbon dioxide (CO_2) emissions from the transport sector compared to the preceding year. Over the period spanning from 1990 to 2022, transport-related emissions exhibited an average annual growth rate of 1.7%, surpassing all other end-use sectors except for industry, which also experienced a similar growth rate of around 1.7%. In order to align with the Net Zero Emissions (NZE) target for 2050, it is imperative that CO_2 emissions stemming from the transportation sector witness an annual reduction of more than 3% by 2030. Achieving these reductions will necessitate the implementation of robust regulatory measures, fiscal incentives, and substantial investments in infrastructure to facilitate the operation of low- and

zero-emission vehicles [15]. Achieving substantial cuts in CO_2 emissions within the transportation domain will prove to be a formidable challenge, given the deceleration in the pace of emission reduction. Present forecasts indicate a mere 22% reduction in transportation-related emissions by 2050, trailing significantly behind prevailing aspirations. With the introduction of road vehicles with carbon-free clean energy into our lives, greenhouse gas emissions can be reduced by 11.9% [16]. In 2019, transportation-based emissions in European countries remained a significant contributor to overall greenhouse gas emissions, with many nations implementing various measures to address and reduce their carbon footprint in this sector (Figure 1) [35]. Emissions stemming from the transportation sector involve a spectrum of greenhouse gases, encompassing carbon dioxide (CO_2), methane (CH_4), nitrous oxide (NO), and various hydrofluorocarbons (HFCs). The automotive industry is strongly committed to mitigating these emissions and enhancing fuel efficiency. On an average basis, a passenger car releases roughly 4.6 metric tons of carbon dioxide into the atmosphere each year. This amount may fluctuate based on factors like the vehicle's fuel type, fuel economy, and annual mileage [17]. However, it would be overly simplistic to anticipate that merely reducing fossil fuel consumption would constitute a globally effective strategy. The transportation sector dynamics are intricate and multifaceted, implying that achieving changes and advancements requires a multifaceted approach. Consequently, attaining anticipated efficiency gains in greenhouse gas reduction necessitates the implementation of multiple preventative measures.

Figure 1. Transportation based emissions in the European countries, 2019 [35]
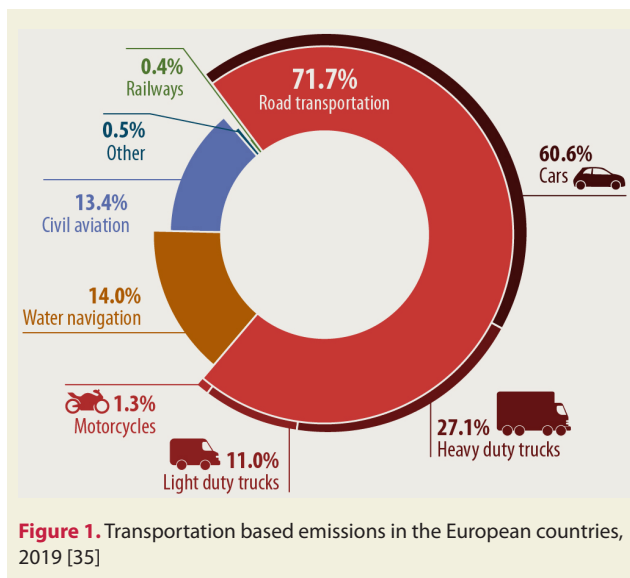
The literature presents seven key focal points for achieving sustainable transportation with reduced greenhouse gas emissions. These encompass the adoption of alternative fuels, the promotion of fuel-efficient vehicles, curbing vehicle usage, reducing transportation infrastructure footprints, fostering smart transportation systems, integrating transportation networks, and ultimately curtailing travel frequency [18]. It is widely recognized that

the majority, if not all, of the environmental impacts and challenges arising from the transportation sector are a result of the excessive use of fossil fuels. [19]. Fuel consumption and associated greenhouse gas emissions within the transportation sector are categorized based on fuel type and transportation modes. Similarly, emissions within municipal operations are classified according to the fleet types employed by local governments for transportation activities, and these figures are integrated into emission inventory projections [20].

The United Nations Environment Program (UNEP) has introduced the eMob calculator, a tool facilitating the assessment of energy consumption, CO_2 emissions, air pollutants, and potential cost reductions linked to electric and low-emission buses (including Euro 6 and CNG buses). This initiative has showcased that the shift towards zero and low-emission vehicles, encompassing battery electric, hybrid, and compressed natural gas (CNG) buses, holds the potential to prevent roughly 1.4 billion tons of CO_2 emissions and approximately 30 million tons of particulate matter from 2020 to 2050. In 2020, the transportation sector was responsible for emitting 80.7 million tons of CO_2 equivalent, making up 15.4% of the total greenhouse gas emissions [21].

Electric vehicles (EVs) replace the traditional gasoline tank with a battery and substitute the internal combustion engine with an electric motor. Conversely, plug-in hybrid electric vehicles (PHEVs) integrate both gasoline and electric components, including a battery, an electric motor, a gasoline tank, and an internal combustion engine. PHEVs utilize both gasoline and electricity as sources of energy.

The shift towards electric vehicles (EVs) arose from concerns about depleting crude oil reserves and a growing societal awareness of the environmental impacts linked to fossil fuel combustion. The escalating energy demand resulting from industrial growth in emerging and established nations further accentuates these countries' reliance on imported oil. Consequently, nations dependent on foreign oil allocation must earmark significant portions of their domestic revenues for petroleum imports [22]. Figure 2 displays the emissions for different vehicle categories, while Figure 3 illustrates hydrogen's exceptional energy density in comparison to alternative technologies.

The emerging advancements in the fuels industry are positioning hydrogen and CNG as highly suitable options for sizeable vehicles such as buses. These vehicles are gaining increasing popularity among the general populace, thanks to their substantial potential as an energy source with minimal harm to the environment. These gases are regarded as eco-friendly and environmentally conscious fuels, primarily derived from sustainable sources. This trend is opening up fresh possibilities within the fuel market [37,38].

Highways are the most frequently used mode of transportation. Therefore, the characteristics of the fuel burned play a significant role in determining emission values. CO_2 emissions per liter of used fuels vary depending on the fuel type. CO_2 emissions corresponding to each fuel type are provided in Table 1.

Table 1. Carbon dioxide emissions due to fuel consumption per liter fuel type CO_2 emissions [24]

Fuel Type	CO_2 Emission (g of CO_2 per liter)
Diesel	2,700
Gasoline	2,500
LPG	1,600

In Türkiye, the greenhouse gas inventory findings indicated that in 2021, the total greenhouse gas (GHG) emissions, measured in terms of CO_2 equivalent (eq.), increased by 7.7% compared to the preceding year, reaching a total of 564.4 million tonnes (Mt). On a per capita basis, the total GHG emissions were 6.3 tonnes of CO_2 eq. in 2020 and 6.7 tonnes of CO_2 eq. in 2021. The share of transport-related emissions in total greenhouse gas emissions was 15.3% in 2019. According to Turkish Statistical Institute's (TURKSTAT) greenhouse gas emission inventory data for 2020; 94.9% of the CO_2 emissions originating from transportation originate from the road, 2.7% from the airway, 1.6% from the seaway, 0.4% from the railway and 0.4% from other modes of transport [25].

As part of the Sustainable Energy Action Plan (SEAP), a comprehensive analysis of Antalya's 2019 emissions was determined. Including industrial contributions, reveals that the total energy consumption in the province amounted to 28,623,531 MWh, resulting in greenhouse gas emissions totaling 10,683,551 tCO_2e. Notably, the transportation sector accounts for 30.2% of these emissions [26]. As detailed in the Izmir SECAP report for 2018, the current greenhouse gas emissions in the transportation sector constitute 23.1% of the municipality's total emissions, equivalent to 5,780,293 tCO_2e. The primary culprits within the transportation sector are private vehicles, including cars, minibuses, buses,
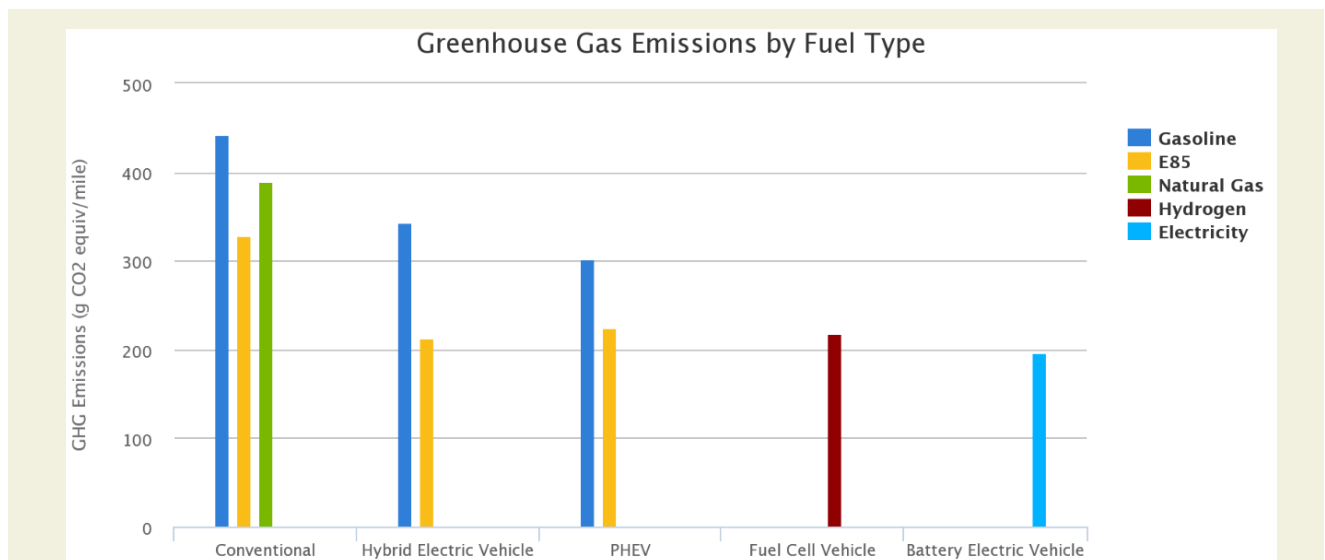
Figure 2. A comparison among different models of vehicles in terms of greenhouse gas emissions [23]
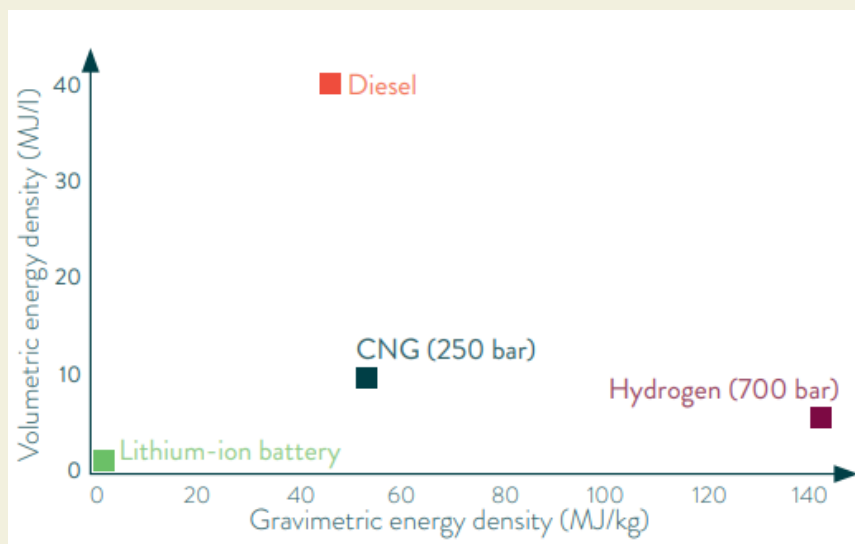
Figure 3. Hydrogen's high energy density compared to other technologies [36]

trucks, pick-up trucks, and motorcycles, accounting for 19.9% of these emissions. Notably, a significant portion of these private vehicles are quite old, with an average age exceeding 13 years, and they predominantly rely on fossil fuels for power. To be precise, approximately 46% of these vehicles use diesel fuel, contributing not only to greenhouse gas emissions but also to the release of other harmful gases, thereby negatively impacting air quality [27]. In contrast, the greenhouse gas emissions in Ankara, calculated using the GPC BASIC approach for 2019, amount to 22,884,636 tCO_2e (the breakdown of these emissions, with 72% stemming from 'Scope 1 - Direct Emissions' and 28% from 'Scope 2 - Indirect Emissions.) Stationary energy sources contribute the highest proportion at 39%, followed by transportation at 28%, and waste management at 2% [28]. In accordance with the GPC BASIC Standards for Stationary Energy, Transportation, and Waste sectors, the total greenhouse gas emissions at Istanbul for 2019, amount to 50,888,653 tCO_2e. Of this total, the sector with the most substantial share is stationary energy, accounting for 63%, followed by transportation at 28%, and waste at 9% [29]. The greenhouse gas emission total for the province of Adana in 2020 was determined to be 9.7 metric tons of CO_2 equivalent (tCO_2e), with a per capita carbon footprint calculated at 4.3 tCO_2e. [20].

1.2. SECAP studies in Adana Province

The Mediterranean Region, where Adana City is located, faces significant climate change impacts, including rising temperatures, droughts, reduced water availability, and extreme weather events. Adana, like many other provinces, is already experiencing these effects. In 2021, the Adana Metropolitan Municipality (AMM) joined the Global Covenant of Mayors (GCoM) with a goal to reduce emissions by 40% by 2030 compared to 2020 levels. AMM conducted a thorough greenhouse gas emissions assessment and identified strategies for achieving this reduction. They also conducted a Risk and Vulnerability Analysis to pinpoint climate-related hazards and vulnerabilities in the city, resulting in an adaptation strategy and measures to address these risks. Adana faces challenges like prolonged heatwaves, increased droughts, urban flooding, and forest fires. Key priorities include expanding carbon sink zones, improving waste management, enhancing transportation, and promoting renewable energy. Rainwater harvesting and wastewater recovery are also essential parts of AMM's agenda.[30].

Adana's Sustainable Energy and Climate Action Plan (SECAP) envisions the city becoming a low-carbon urban hub, integrating measures to meet reduction targets with existing strategies. The goal is an energy-efficient city with reliable access to sustainable energy sources, enhancing resilience against climate change. The SECAP is a strategic blueprint for Adana, outlining both mitigation and adaptation actions, setting timelines, and responsibilities. It focuses on boosting energy efficiency and renewable energy adoption to reduce urban emissions. The plan aligns with existing frameworks and

governance structures and includes recommendations for their strengthening. It's a flexible document meant to adapt to evolving circumstances and insights, ensuring ongoing climate action. Adaptation measures consider current conditions, educational insights, references, and extreme weather events. [20].

2. Methodology

The approach used in this study for reporting greenhouse gas emissions adheres to the Global Protocol on Community Scale Greenhouse Gas Emissions Inventories (GPC), a standard endorsed by the Global Covenant of Mayors for Climate and Energy (GCoM). This protocol is based on the 2006 Guidelines from the Intergovernmental Panel on Climate Change (IPCC) for National Greenhouse Gas Inventories [12]. In the context of Adana City, projections for greenhouse gas emissions in 2030 were calculated by using the greenhouse gas emission inventory data from the baseline year of 2020. This inventory encompasses the assessment of carbon dioxide (CO_2), methane (CH_4), and nitrogen oxides (N_2O) as the primary greenhouse gases of interest. These gases are particularly significant in terms of emissions arising from energy consumption within the city's boundaries, as well as activities extending beyond energy use. To clarify, CO_2 constitutes the majority of emissions, while CH_4 and N_2O originate from different sources. In the calculations, we have included the carbon dioxide equivalent (tCO_2e) of emissions from CH_4 and N_2O, utilizing the global warming potentials specified in the IPCC 5th Assessment Report (AR5) [31].

In this study, we also incorporated the Kaya Identity (KI) model in the computation of greenhouse gas emission projections. The KI model serves as a crucial foundation for estimating greenhouse gas emissions, identifying emission-intensive areas, and formulating relevant policies. The preeminent method employed for estimating greenhouse gas emissions is the Kaya Identity equation, originally formulated by the Japanese energy economist Yoichi Kaya [32]. The Kaya Identity, utilized for forecasting greenhouse gas emissions by both the Intergovernmental Panel on Climate Change (IPCC) and the C40 Cities Climate Leadership Group, recognizes that greenhouse gas emissions are directly influenced by four primary factors. These factors include:

- ✓ Population
- ✓ Economic Output (Gross Domestic Product)
- ✓ Energy Efficiency of the Economy
- ✓ Carbon Efficiency of the Economy

At the Kaya Identity equation;

CO_2 emissions are defined as; Population × (Gross Domestic Product/Population) × (Energy/Gross Domestic Product) × (CO_2/Energy) and constitute an equality in terms of population, economy, politics, energy [33]. This equivalence provides a new perspective on how

each country emits greenhouse gases by including carbon emission factors within itself. The population projections for Türkiye and Adana for the period spanning from 2020 to 2030 were integrated into the Kaya Identity Model. These projections were sourced from official references provided by TURKSTAT, including TURKSTAT's Population Data for Provinces from 2018 to 2025, Türkiye's Population Projections from 2018 to 2080, Results derived from the Address-Based Population Registration System spanning from 2007 to 2021 [34] In addition, for the population projection after 2025, the population growth rates predicted by TURKSTAT for the years 2018-2025 for Türkiye and Adana Province, and the population growth rate predicted for Türkiye until 2080, were taken into account. The difference between the population growth rates of Türkiye and Adana Province 2018-2025 has been used for the post-2025 population projection of Adana Province.

GDP per capita is another critical factor considered in greenhouse gas emission projections. The GDP values utilized in these calculations were obtained from the "Gross Domestic Product on Province Basis, 2004-2020" report published by TURKSTAT [34]. Between 2004 and 2020, the per capita GDP growth in Adana in US$ units was calculated as 1.80% per year on average. In the emission projections, it is assumed that the GDP per capita will experience an annual growth rate of 1.80% for the period from 2020 to 2030.

In the context of carbon intensity and energy intensity for Türkiye between 2010 and 2016, it is assumed that there will be an annual decrease of 2.6% in carbon intensity and 1.98% in energy intensity from 2020 to 2030. This assumption forms the basis for calculating annual carbon intensity and energy intensity values, which are subsequently used in greenhouse gas emission projections for Adana Province.

To calculate greenhouse gas emissions for a specific year in a particular region according to the Kaya Identity, the following formula is employed:

CO_2 equivalent (GHG) emissions = Population × (GDP/Population) × (Energy/GDP) × (CO_2/Energy)

The "CO_2/Energy" factor in the formula can be calculated as follows:

CO_2/Energy = (Carbon Intensity of Economy/Energy Intensity of Economy)

Based on the provided values for carbon intensity and energy intensity, the "CO_2/Energy" factor has been calculated as "0.994." This factor is crucial for estimating greenhouse gas emissions in Adana Province for each year within the 2020-2030 timeframe.

The calculation method for estimating greenhouse gas emissions for the year 2020 and subsequent years in Adana Province, based on the Kaya Identity formula, is described as follows:

2020 CO_2 equivalent (GHG) emissions = [2019 CO_2 equivalent (GHG) emissions × (2020 Adana Province Population/2019 Adana Province Population) × (2020 GDP Per Capita/ 2019 GDP Per Capita)] × (CO_2/Energy)

This formula allows for the projection of greenhouse gas emissions for 2020 and beyond by considering population growth, changes in GDP per capita, and the CO_2/Energy factor, as described above.

In the context of efforts to address climate change, an assessment of Adana City's transportation sector was carried out by conducting a Strengths, Weaknesses, Opportunities, and Threats (SWOT) analysis. To assess the Adana City transportation sector's role in addressing climate change, information from the Sustainable Energy and Climate Action Plan, a collaborative effort among various institutions, served as the primary data source [20]. These data resources encompassed details regarding Adana's transportation infrastructure, encompassing vehicle categories, traffic patterns, and utilization statistics. Environmental impact evaluations and climate change assessments were referenced to ascertain the sector's influence on greenhouse gas emissions and air quality, assisting in the identification of environmental strengths and weaknesses. Valuable insights into the public's perception of the transportation system's effectiveness were gleaned from public opinion surveys. The analysis also delved into ongoing and prospective transportation projects, governmental policies, and regulatory frameworks to pinpoint opportunities and threats, with a particular emphasis on reducing carbon emissions. Additionally, an examination of economic and financial data, technological advancements, and the resilience of transportation infrastructure to climate-related risks were integral components of the study. This analysis provided a

Table 2. The current data on Adana City transportation in the year 2020 [20]

Data Name	Value	Unit
Number of Diesel Buses (Public Transport)	324	units
Number of Diesel Buses (Private Transport)	419	units
Distance Covered per Bus (Public Transport)	71,603	km/year
Distance Covered per Bus (Private Transport)	59,236	km/year
Distance per Bus (Average)	64,629	km/year
Diesel Bus Fuel Consumption (Public Transport)	0.48	lt/km
Diesel Bus Fuel Consumption (Private Transport)	0.35	lt/km
Diesel Bus Consumption (Average)	0,41	lt/km
Average Electric Vehicle Electricity Consumption	0.85	kWh/km
Number of Diesel Bus Passengers (Public Transport)	52,288	passengers/year
Number of Diesel Bus Passengers (Private Transport)	64,629	passengers/year

methodical framework for evaluating the present state and potential enhancements within Adana's transportation sector concerning climate change mitigation, offering a comprehensive viewpoint on the determinants of the sector's success or challenges. In this research, it was focused on public and private transportation vehicles, which hold a significant position in urban emission sources. Public buses, as mentioned Table 2., pertain to the municipal-owned vehicles, while private buses refer to smaller-sized vehicles commonly recognized as minibuses. All these vehicles utilize diesel fuel, and our study aims to explore the potential impact of alternative fuel system conversions on emission levels. The current data on Adana City transportation in the year 2020 are in Table 2. below;

3. Results

3.1. Adana City Transportation Sector SWOT Analysis

The results of the SWOT analysis of transportation sector are given below;

Strengths:

- ✓ Pursuing the strategic objective of efficient transportation service management, aiming to deliver economical, secure, and convenient services across all corners of the city,

- ✓ Ongoing development of the Transportation Master Plan study,

- ✓ Enlarging the rail system network to enhance connectivity,

- ✓ Launching an extensive citywide bicycle path project aimed at promoting active transportation throughout the urban area,

- ✓ Introducing intelligent transportation systems to enhance transportation efficiency and effectiveness,

- ✓ Undertaking citywide road and infrastructure maintenance and restoration projects to ensure their long-term sustainability.

Weaknesses:

- ✓ Limited integration among diverse transportation modes,

- ✓ Urban design prioritizing motor vehicle usage,

- ✓ Insufficient awareness regarding active transportation.

Opportunities:

- ✓ The potential to curtail private car reliance

through mobility management and optimization of the road network,

- ✓ Opportunities for adopting electric vehicles as a part of the transportation system,

- ✓ Possibilities to encourage stakeholder engagement in the planning, implementation, and oversight of transportation initiatives.

Threats:

- ✓ Difficulties in organizing the road network,
- ✓ Public transportation and practices that support active transportation are not adopted by the citizens.

To compare the greenhouse gas (GHG) emissions of diesel buses and electric vehicles (EVs), 2.602 kg CO_2e per liter fuel consumption data for diesel buses and the electricity consumption data for EVs were used. The GHG emissions from electric vehicles depend on the carbon intensity of the electricity generation source. This is an estimate and may vary based on the specific geographical region and the percentage of renewable energy sources integrated into the grid.

Emissions from hydrogen vary significantly depending on the production method employed. There are three common types of hydrogen: gray, blue, and green hydrogen. The carbon intensity for hydrogen production ranges from 850 to 71 g CO_2/km [39]. For this study; the average of these was determined as 0,460 kg CO_2/km.

The carbon dioxide equivalent (CO_2e) emissions for CNG can vary depending on various factors such as the source of the natural gas and the efficiency of the CNG production and distribution process. On average, CNG is considered to have lower CO_2e emissions compared to traditional gasoline or diesel fuels. Performance value for CNG was given 0.833 kg CO_2/km. at the literature [40].

3.2. GHG Projections and Reduction Results

Within the scope of this study, greenhouse gas emission projections for the 2020-2030 period were prepared
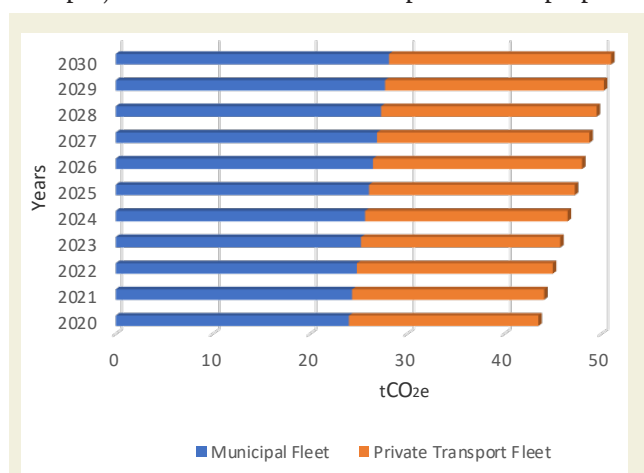

Figure 3. Amount of greenhouse gas in case of without mitigation studies (2020-2030 term)

based on the 2020 greenhouse gas emission inventory has been prepared. It was prepared with the KI methodology. The greenhouse gas emission projections for Adana City for the period of 2020- 2030, which have been developed within this framework, are elaborated in Figure 3 below.

The GHG emissions for both different vehicles are given below in Table 3.

Table 3. GHG Emissions for different vehicle types

Vehicle Type	GHG Emissions (kg CO$_2$e/km)	Bus Fleet (743 bus) (kg CO$_2$e/km)
Public-Private Transport Diesel Bus (average)	1.079	801.697
Electric Vehicle	0.195	144.885
Hydrogen	0.460	341.78
CNG	0.833	618.919

When comparing greenhouse gas (GHG) emissions of different vehicle types to the average diesel bus emissions, several key insights emerge. In contrast, electric vehicles demonstrate a remarkable environmental advantage, showcasing a significant 81.93% decrease in GHG emissions. Hydrogen-powered vehicles also offer a notable reduction of approximately 57.37% compared to diesel buses. Compressed Natural Gas (CNG) vehicles provide a moderate decrease of around 22.77%. These percentages underscore the potential for electric and hydrogen vehicles to substantially contribute to lowering carbon emissions in the transportation sector, while CNG serves as an intermediate step toward cleaner mobility solutions.

Even with the revised diesel emissions factor, it is clear that electric vehicles maintain a notably lower greenhouse gas emissions profile when compared to both public and private diesel buses in the transportation sector. The shift toward electric vehicles still presents substantial environmental advantages in terms of mitigating carbon emissions.

Based on the results of the greenhouse gas transportation emission inventory for the 2020 base year in Adana City, it was determined that emissions accounted for 27% of the total. Originating from public transportation and municipal fleet vehicles was determined as 19,500 tCO$_2$e and 24.003 tCO$_2$e, respectively. In addition, the greenhouse gas emission projections until 2030 are given below; if a greenhouse gas reduction study is not carried out, it has been calculated that the greenhouse gas emission value from public transportation and municipal fleet vehicles in 2030 could be 22,859 tCO$_2$e and 28.137 tCO$_2$e respectively.

To address this challenge and reduce GHG emissions, transitioning to electric bus alternatives is a viable solution. Electric buses produce significantly lower or zero tailpipe emissions when compared to their internal combustion engine counterparts. Electric buses oper-

ate without burning fossil fuels, leading to lower or zero emissions of pollutants and GHGs during operation. This directly contributes to lowering the transportation sector's carbon footprint. Electric buses produce fewer pollutants like nitrogen oxides and particulate matter, leading to improved air quality. This has positive implications for public health and environmental well-being. In summary, the data underscores the importance of addressing emissions from diesel buses, both in the public and private transport sectors. The transition to electric buses not only offers a promising solution for reducing carbon emissions but also has the potential to enhance the sustainability and environmental quality of urban transportation. Additionally, the substantial passenger capacity of these buses highlights their critical role in providing mobility services to the community, making the move toward electric buses even more impactful from both environmental and societal perspectives.

4. Conclusions

The engineering and technical aspects of electric buses represent a pivotal and transformative force in the ongoing efforts to significantly reduce greenhouse gas (GHG) emissions. Their remarkable efficiency serves as a beacon of hope in the fight against climate change, delivering a significant 81.5% reduction in emissions when contrasted with the average diesel-powered bus. This noteworthy reduction not only lessens the burden on our environment but also results in tangible benefits for the air quality in our cities, as electric buses produce zero tailpipe pollutants. However, the genuine environmental impact of electric buses becomes even more profound when taking into account the potential for seamless integration with renewable energy sources in their charging infrastructure. When these buses are powered by clean energy grids, they can achieve a staggering 100% reduction in emissions, making them a shining example of sustainable transportation.

One of the key enablers of the electric bus revolution is the continuous advancement in battery technology. These innovations have significantly extended the operational range of electric buses while enhancing their overall efficiency. As a result, electric buses have become a highly viable and environmentally friendly choice for public transportation, offering a sustainable alternative to traditional fossil fuel-powered vehicles. It's important to note that the transition to electric vehicles, including buses, is not confined to the public transportation sector alone. Efforts to combat climate change extend to both private vehicles and public transportation, with a primary emphasis on shifting from fossil fuel-powered vehicles to low-emission alternatives, such as electric vehicles. In this context, electric buses play a crucial role in setting an example for the broader transportation industry. To quantify the significant advantages of embracing electric buses, our analysis relied on both primary data collected from authoritative sources such as AMM and secondary data sourced from reputable national and international

organizations. This approach allowed us to provide robust estimates of the emissions reductions achievable through the widespread adoption of electric buses. In comparing various vehicle types to the average diesel bus emissions, electric vehicles demonstrate a significant 81.93% reduction in GHG emissions, while hydrogen vehicles achieve a notable 57.37% decrease. These findings highlight the substantial potential of electric and hydrogen-powered vehicles in reducing carbon emissions in transportation. This progressive trajectory not only promises to revolutionize public transportation systems but also to establish a more sustainable and greener transportation landscape that surpasses the current scenario. By doing so, it contributes to the well-being of our planet and ensures a healthier environment for future generations. By embracing electric buses and the associated advancements in clean energy, we take a significant step forward in building a more sustainable future for all.

References

[1] Yue, X. L., Gao, Q. X. (2018). Contributions of natural systems and human activity to greenhouse gas emissions. Advances in Climate Change Research, 9(4), 243-252. doi: 10.1016/j.accre.2018.12.003.

[2] Fawzy, S., Osman, A. I., Doran, J., Rooney, D. W. (2020). Strategies for mitigation of climate change: A review. Environmental Chemistry Letters, 18, 2069-2094. doi: 10.1007/s10311-020-01059-w.

[3] Valizadeh, N., Esfandiyari Bayat, S., Bijani, M., Hayati, D., Viira, A.-H., Tanaskovik, V., Kurban, A., Azadi, H. (2021). Understanding Farmers' Intention towards the Management and Conservation of Wetlands. Land, 10(8), 860. doi: 10.3390/land10080860.

[4] Jacquemont, J., Blasiak, R., Le Cam, C., Le Gouellec, M., Claudet, J. (2022). Ocean conservation boosts climate change mitigation and adaptation. One Earth, 5(10), 1126-1138. doi: 10.1016/j.oneear.2022.09.002.

[5] Watts, N., Amann, M., Arnell, N., Ayeb-Karlsson, S., Belesova, K., Boykoff, M., ... & Montgomery, H. (2019). The 2019 report of The Lancet Countdown on health and climate change: ensuring that the health of a child born today is not defined by a changing climate. The Lancet, 394(10211), 1836-1878.

[6] Pourjavid, S., Poursaeed, A., Mirdamadi, S. M. (2020). Modeling the effectiveness of urban agriculture education courses. Urban Ecosystem, 23, 927–932. doi: 10.1007/s11252-020-00955-x.

[7] Ogunbode, C. A., Doran, R., Hanss, D., Ojala, M., Salmela-Aro, K., van den Broek, K. L., ... & Karasu, M. (2022). Climate anxiety, wellbeing and pro-environmental action: Correlates of negative emotional responses to climate change in 32 countries. Journal of Environmental Psychology, 84, 101887.

[8] UNEP. (accessed date 17 October 2023). https://www.unep.org/explore-topics/resource-efficiency/what-we-do/cities/cities-and-climate-change.

[9] European Energy Agency. (accessed date 17 October 2023). https://www.eea.europa.eu/en/topics/in-depth/urban-sustainability.

[10] Aşıcı, A. A., Acar, S. (2022). Channels of cooperation between the EU and Turkey on green transformation. Ankara Avrupa Çalışmaları Dergisi, 21, 43-67. doi: 10.32450/aacd.1148598.

[11] Ministry of Trade: Republic of Türkiye. (accessed date 17 October 2023). https://climate-laws.org/documents/green-deal-action-plan-approved-by-presidential-circular-2021-15_b8d4?id=green-deal-action-plan-approved-by-presidential-circular-2021-15_946c.

[12] CDP-ICLEI Track Guidance. (accessed date 17 October 2023). https://cdn.cdp.net/cdp-production/cms/guidance_docs/pdfs/000/003/476/original/Reporting-Guidance-for-GCoM-EN.pdf?1649177827.

[13] Edenhofer, O., Pichs-Madruga, R., Sokona, Y., Farahani, E., Kadner, S., Seyboth, K., Adler, A., Baum, I., Brunner, S., Eickemeier, P., Kriemann, B., Savolainen, J., Schlömer, S., von Stechow, C., Zwickel, T., Minx, J.C. (Eds.). (2014). Climate Change 2014: Mitigation of Climate Change. Contribution of Working Group III to the Fifth Assessment Report of the Intergovernmental Panel on Climate Change. Cambridge University Press, Cambridge, United Kingdom and New York, NY, USA.

[14] Emissions of Carbon Dioxide in the Transportation Sector. (accessed date 17 October 2023). https://www.cbo.gov/publication/58861.

[15] IEA. (accessed date 17 October 2023). https://www.iea.org/reports/tracking-clean-energy-progress-2023.

[16] CO₂ and Greenhouse Gas Emissions. (accessed date 17 October 2023). https://ourworldindata.org/co2-and-greenhouse-gas-emissions.

[17] U.S. Environmental Protection Agency. (2023). Tailpipe Greenhouse Gas Emissions From a Typical Passenger Vehicle Report (EPA 420-F-23-014).

[18] Peng, Z., Shen, S., Lu, Q., Kutz, M. (Eds.) (2010). Climate Change and Transportation. In Handbook of Transportation Engineering Volume II. McGraw Hill, New York.

[19] Greene, D., L. (1997). Sustainable Transport. Journal of Transport Geography, 5, 177-190. doi: 10.1016/S0966-6923(97)00013-6.

[20] Ministry of Environment, Urbanization and Climate Change, Adana Metropolitan Municipality, World Bank, Sustainable Cities, ILBANK, EU, ARUP Publications. (2022). Sustainable Energy and Climate Action Plan (SECAP) of Adana City, Republic of Türkiye.

[21] UNEP. (accessed date 17 October 2023). https://www.unep.org/resources/toolkits-manuals-and-guides/emob-calculator.

[22] Tüccar, G., Tosun, E., Özcanlı, M., Aydın, K. (2013). Possibility of Turkey to transit Electric Vehicle-based transportation / Transit Elektrikli Araç Tabanlı Ulaşıma Türkiye'nin imkânı. International Journal of Automotive Engineering and Technologies, 2(2), 64-69. Retrieved from https://dergipark.org.tr/en/pub/ijaet/issue/7964/104559.

[23] Energy Education, GHGs for AFVs. (accessed date 17 October 2023). https://energyeducation.ca/encyclopedia/GHGs_for_AFVs#cite_note-DOE-2.

[24] Synák, F., Gaňa, J., Rievaj, V., Mokričková, L. (2019). Ways of reducing carbon dioxide from road transport. The Archives of Automotive Engineering – Archiwum Motoryzacji, 4, 41-54. doi: 10.14669/AM.VOL86.ART3.

[25] TURKSTAT Greenhouse Gas Emission Statistics. (2023). 1990-2021, Report No: 49672.

[26] Antalya Metropolitan Municipality. (2021). Sustainable Energy Action Plan.

[27] European Bank for Reconstruction and Development, Izmir Metropolitan Municipality, AECOM, and Green Engineering.

(2020). Izmir Green City Action Plan.

[28] Ankara Metropolitan Municipality. (2022). Ankara Climate Change Action Plan.

[29] Istanbul Metropolitan Municipality, Environmental Protection and Control Department & Climate Change Department. (2022). Climate Monitoring Report, Istanbul.

[30] Ün, Ç. (2022). Investigation and mitigation studies of transportation-based greenhouse gas emissions in Adana city. Guldal, S. (Eds.), Sustainability of Natural Resources' Efficiency. Iksad Publications. ISBN: 978-625-8213-08-9.

[31] Pachauri, R. K., Meyer, L. A. (Eds.). (2014). IPCC: 2014 Climate Change Synthesis Report, Fifth Assessment Report of the Intergovernmental Panel on Climate Change. IPCC, Geneva, Switzerland.

[32] Kaya, Y. (1990). Impact of Carbon Dioxide Emission Control on GNP Growth: Interpretation of Proposed Scenarios. Paper presented to the IPCC Energy and Industry Subgroup, Response Strategies Working Group, Paris. Mimeo.

[33] Wang, Z., Jing, D., Lu, Z. (2011). Decomposition of factors impacting on carbon emission for China based on LMDI. International Journal of Nonlinear Science, 12, 80-85.

[34] TUIK. (accessed date 17 October 2023). https://data.tuik.gov.tr/.

[35] Transport and Environment Report. (2022). Decarbonising road transport — the role of vehicles, fuels, and transport demand. EEA Report No 02/2022, European Environment Agency, Luxembourg: Publications Office of the European Union.

[36] Fuel Cell Buses: Best Practices and Commercialization Approaches. (accessed date 17 October 2023). https://cms.uitp.org/wp/wp-content/uploads/2020/07/Knowledge-Brief-Fuel-Cell-Buses_web.pdf.

[37] Kaplan, R., Kopacz, M. (2020). Economic Conditions for Developing Hydrogen Production Based on Coal Gasification with Carbon Capture and Storage in Poland. Energies, 13(19), 5074. doi: 10.3390/en13195074.

[38] Brzezińska, D., Januszewski, J. (2022). Enclosure Safety in a Case of Hydrogen, CNG, or LNG Accidental Release from a Bus Tank. Chemical Engineering Transactions, 90, 349-354. doi: 10.3303/CET2290059.

[39] Hensher, D. A., Wei, E., Balbontin, C. (2022). Comparative assessment of zero emission electric and hydrogen buses in Australia. Transportation Research Part D: Transport and Environment, 102, 103130. doi: 10.1016/j.trd.2021.103130.

[40] Topal, O., Nakir, İ. (2018). Total Cost of Ownership Based Economic Analysis of Diesel, CNG, and Electric Bus Concepts for Public Transport in Istanbul City. Energies, 11(9), 2369. doi: 10.3390/en11092369.

Metaheuristic algorithm-based cascade PID controller design for fixed wing unmanned aerial vehicle

Mehmet Durmaz[1], Kenan Cici[1], Muhammet Sarıkaya[1], Mesut Bilici[1], Hasan Huseyin Bilgic[1*]

[1]Necmettin Erbakan University, Faculty of Aviation and Space Sciences, Aeronautical Engineering Department, Konya, 42140, Türkiye

Orcid: M. Durmaz (0000-0003-1145-7244), K. Cici (0000-0001-9211-4678), M. Sarıkaya (0000-0001-8217-1353), M. Bilici (0000-0002-0016-1600), H. H. Bilgic (0000-0001-6006-8056)

Abstract: In this study, the nonlinear model of the longitudinal and lateral motions of a fixed-wing Unmanned Aerial Vehicle (UAV) with assured geometrical features and aerodynamic parameters is linearized under certain conditions. A cascade proportional integral differential controller is designed on the linear model. The controller coefficients that applied to the model of the UAV were optimized with a metaheuristic algorithm, which is based on a metaheuristic search algorithm. The four different controller gains in the system are optimized using four different objective functions. Controller performances were tested in a simulation environment for unit step input responses. Considering the longitudinal dynamics of the aircraft, among the ITAE, ISE, MSE and IAE fitness functions, IAE can be shown as the optimum result for altitude control.

Keywords: Cascade PID, UAV, ABC Algorithm, Optimisation.

1. Introduction

Nowadays, when it comes to remotely controlled vehicles, the first thing that comes to mind is undoubtedly UAVs. Historically, UAVs were first used for military purposes. Tracking, surveillance and attack capabilities are among the most important features of UAVs according to their usage areas [1-4]. Compared to other aircraft, its costs are cheaper and easier to use, making it possible for civilians to use it as well. Therefore, using of UAVs has increased significantly, especially in areas such as search and rescue, logistics and real-time monitoring [5-6].

UAVs should provide certain features while performing their duties. Some of those features are high maneuverability, fast response of the system in case of any disturbance, high accuracy trajectory tracking, altitude control, etc. However, in order to meet these criteria, the controllers of the UAV must be reliable and respond quickly. Undoubtedly, the biggest challenge in controller design is the optimization process. Several methods have been derived for the optimization of the controller parameters used to obtain the properties that affect the performance, such as a fast response of the system, minimum steady-state error, minimum overshoot [7-9].

The control of fixed-wing UAVs has recently become a common subject of study. The absence of the human factor in it requires more trust in controllers while performing their duties. A reliable controller is critical to mission safety and cost. Route estimation and its planning are of vital importance for the unit to be tasked. In the literature, many solutions are presented to nonlinear equations and uncertainty situations in order to perform a task. In their study, Hervas et al. designed a nonlinear controller for the landing of a fixed-wing drone on the ship's deck with a Kalman filter using a scholastic downwind laser sensor. At the end of their studies, they showed that they gave successful results even at high angles of attack [10]. Autopilot design using a controller is widely used, especially in small-sized and commercial fixed-wing unmanned aerial vehicles. Stastny et al. applied speed and path control to a small model unmanned aerial vehicle with a 'high level Nonlinear Model Predictive Controller'. As a result of their work, predicts that are quite similar to simulation answers and real-time answers have been provided [11]. Yan and Wang, on the other hand, designed a 'low gain' controller for swarm UAVs and made speed control [12]. Zhen et al. compared 'the trained reinforcement learning (RL)' controller designed for a fixed-wing UAV with a Proportional-Integral-Derivative (PID) controller. They showed that RL gives better results in the simulations than PID in disturbances, such as wind and turbulence. They also stated that PID gains should be tuned according to different flight conditions [13]. Poksawat et

al. designed a 'gain scheduled' controller for a fixed-wing mini-UAV. They tested the PID coefficients according to different conditions by measuring the instantaneous velocity with a Pitot tube. The results were validated in the wind tunnel under different conditions. As a result, they revealed that their proposed method creates less deviation in height compared to the traditional method [14]. Mammarella et al. designed an autopilot for a nonlinear model using the 'sample-based stochastic model predictive control (SMPC)' method. They performed a traction control of a mini UAV and verified it with simulations. As a result, they stated that the SMPC architecture is less affected by disturbances than the classical Model Predictive Control (MPC) architecture [15].

In this study, the longitudinal PID controller parameters applied to the dynamically modeled fixed-wing unmanned aerial vehicle were optimized with the metaheuristic search algorithm. The nonlinear RQ-2 Pioneer model, which was modeled mathematically, was linearized, and the controller was designed under certain trim conditions. Tuning of PID parameters of multi-degree-of-freedom systems takes a long time with trial and error methods. In most cases, the desired results are not achieved. For this reason, ABC optimization, one of the metaheuristic algorithms, is proposed in this study. In the PID controller design, the PID parameters for the control of each of the UAV's pitch speed, pitch angle, altitude and true air speed (TAS) were found with the Artificial Bee Colony (ABC) approach, which is a metaheuristic search algorithm technique. The reason for this can be shown as the poor performance of traditional tuning methods when the systems are not linear [16]. With the development of metaheuristic algorithms, their use in controller design has become widespread and has become more efficient to find the optimum PID parameter values [17].

In section 2, the introduction of fixed-wing UAVs and metaheuristic search algorithms are mentioned under the title of materials and methods. Research findings, algorithm block diagram and system response for objective function are presented in section 3. Finally, in section 4, the results of the system output are interpreted and discussed.

2. Materials and Methods

2.1. AAI RQ-2 Pioneer Fixed Wing Unmanned Aerial Vehicle

The RQ-2 Pioneer is an unmanned aerial vehicle used at sea and on land from 1986 to 2007 by the United States Navy, Marine Corps and Army. Initially placed on Iowa-class battleships to provide artillery detection, its mission has evolved primarily into reconnaissance and surveillance for amphibious forces. In addition to this, many experimental and academic studies have been done on it in the literature [18]. Aerodynamic coefficients, mass and geometric properties taken from the wind tunnel test in Robert Bray's master's thesis, which is one of these

studies, were used in this study [19]. Table 1 presents the technical specifications of the AAI RQ-2 Pioneer.

Table 1. Specifications of AAI RQ-2 Pioneer [19]

Property	Description	Value	Unit
I_x	Moment of Inertia along X_B axis	47.2258	kgm^2
I_y	Moment of Inertia along Y_B axis	90.9482	kgm^2
I_z	Moment of Inertia along Z_B axis	111.4753	kgm^2
I_{xy}	Product of Inertia along $X_B Y_B$ axis	0.0	kgm^2
I_{xz}	Product of Inertia along $X_B Z_B$ axis	-6.6462	kgm^2
I_{yz}	Product of Inertia along $Y_B Z_B$ axis	0.0	kgm^2
S	Wing area	2.8261	m^2
$\bar{c}$	Mean aerodynamic chord	0.54864	m
b	Wing span	5.15	m
m	Mass of UAV	190.5088	kg

2.2. Dynamic Model of AAI RQ-2 UAV

Creating a dynamic model of the aircraft is quite complex. Therefore, some assumptions have been made. These are given below [20].

- The UAV is considered a rigid body.

- The inertial mass of UAVs is constant and is the initial flight state value.

- The UAV has a constant gravitational acceleration.

- The Earth is treated as a stationary plane in inertial space.

- The angular momentum changes due to rotating subsystems are neglected.

- The angular momentum changes due to fuel sloshing, the motion of hinged parts and elastic deformation are neglected.

Newton's 2nd law is applied by taking the above assumptions [20].

$$F_t = m \frac{d(v)}{dt} \tag{1}$$

$$G_t = \frac{d(h)}{dt} \tag{2}$$

F_t, G_t and h are the total external force, total external moment and angular momentum respectively

$$h_B = I_B \omega_B \tag{3}$$

I_B and ω_B are moment of inertia and angular momentum, respectively. In this case, the two products of inertia, I_{xy} and I_{yz} are zero.

$$I_B = \begin{bmatrix} I_x & -I_{xy} & -I_{xz} \\ -I_{xy} & I_y & -I_{yz} \\ -I_{zx} & I_{zy} & I_z \end{bmatrix}$$

$$I_B = \begin{bmatrix} I_x & -I_{xy} & -I_{xz} \\ -I_{xy} & I_y & -I_{yz} \\ -I_{zx} & I_{zy} & I_z \end{bmatrix}$$

and

$$\omega_B = \begin{bmatrix} p & q & r \end{bmatrix}^T \tag{4}$$

B subscript indicates the body fixed frame those vectors describe on them. The nonlinear equations are attained by utilizing Newton's second law and the assumptions.

$$X - mg\sin\theta = m(\dot{u} + qw - rv) \tag{5}$$
$$Y - mg\cos\theta\sin\phi = m(\dot{v} + ru - pw) \tag{6}$$
$$Z - mg\cos\theta\cos\phi = m(\dot{w} + pv - qu) \tag{7}$$
$$L = I_x\dot{p} - I_{zx}\dot{r} + qr(I_z - I_v) - I_{zx}pq \tag{8}$$
$$M = I_v\dot{q} + rp(I_x - I_z) - I_{zx}(p^2 - r^2) \tag{9}$$
$$N = I_x\dot{r} - I_{zx}\dot{p} + pq(I_v - I_x) - I_{zx}qr \tag{10}$$

$$p = \phi - \dot{\varphi}\sin\theta \tag{11}$$
$$q = \phi\cos\phi + \dot{\varphi}\cos\theta\sin\phi \tag{12}$$
$$r = \dot{\varphi}\cos\theta\cos\phi - \theta\sin\phi \tag{13}$$

$$\phi = p + (q\sin\phi + r\cos\phi)\tan\theta \tag{14}$$
$$\theta = q\cos\phi - r\sin\phi \tag{15}$$
$$\dot{\varphi} = (q\sin\phi + r\cos\phi)\sec\theta \tag{16}$$

$$\dot{x}_E = u^E\cos\theta\cos\varphi + v^E(\sin\phi\sin\theta\cos\varphi - \cos\phi\sin\varphi)$$
$$+ w^E(\cos\phi\sin\theta\cos\varphi - \sin\phi\sin\varphi) \tag{17}$$
$$\dot{y}_E = u^E\cos\theta\sin\varphi + v^E(\sin\phi\sin\theta\sin\varphi - \cos\phi\cos\varphi)$$
$$+ w^E(\cos\phi\sin\theta\sin\varphi - \sin\phi\cos\varphi) \tag{18}$$

$$\dot{z}_E = -u^E\sin\theta + v^E\sin\phi\cos\theta + w^E\cos\phi\cos\theta \tag{19}$$
$$u^E = u + W_x \tag{20}$$
$$v^E = v + W_v \tag{21}$$
$$w^E = w + W_z \tag{22}$$

15 nonlinear ordinary differential equations in the independent variable time (t) and three algebraic equations are obtained. 3 of the differential equations are not independent, thus there are 12 independent equations.

X, Y, and Z represent aerodynamic forces, and L, M and N are moments components of UAV on the body axes. Moments and forces depend on linear velocities (u, v, w), angular velocities (p, q, r), and one control vector.

2.3. PID Controller Design
PID controller stands for Proportional-Integral-Derivative and regulates different parameters, such as pressure, temperature and speed at desired values. As in many sectors, its use in aviation is quite common. As in this study, it was used in aircraft for longitudinal motion (altitude and velocity) control. In systems with PID controller feedback, the error value of the output signal is calculat-

ed according to the input signal, and the cycle continues until this value is minimum.

Proportional-Integral-Derivative controllers each contain advantages and disadvantages. The purpose of the PID controller is to complete the deficiency of each other by using three controllers simultaneously. The PID controller provides a reasonable system response by eliminating the steady state error and reducing the settlement time. The PID controller equation used in the study is presented with equation 23.

$$u(t) = Kpe(t) + Kd\frac{e(t)}{dt} + Ki\int e(t)\,dt \tag{23}$$

Today, the advanced version of the classical PID control systems with feedback is the cascade control structure, which can also be applied to multi-degree-of-freedom systems [21-23]. Cascade controller structure, in short, means that a control variable is controlled gradually when there is more than one measurement. In the cascade control system, first, the parameters of the inner loop controller are determined and then the parameters of the outer loop controller are obtained [24]. A metaheuristic algorithm-based search algorithm was used to find internal and external controller parameters simultaneously in this study.

2.4. Artificial Bee Colony Algorithm
Metaheuristic algorithms are defined by several different classes according to their characteristic structures. In one of these classes, the bio-inspired metaheuristic algorithm, as the name suggests, is a form of optimization created by examining the life instincts of various living things based on swarm intelligence, such as humans, animals, cells, etc. There are various variations, such as particle swarm optimization, ant colony optimization, Artificial Bee Colony optimization, bat algorithm optimization, etc. [25-26]. The Artificial Bee Colony search algorithm used in this article was first introduced by Karaboğa in 2005 by making an analogy with honey bees based on their foraging instincts [27].

The ABC algorithm model consists of three groups of bees. The first group, the worker bee group, looks for productive food sources around the hive and is responsible for keeping their location and nectar information in mind and conveying them to the other bees in the hive with a 'waggle dance' in the dance area. Onlooker bees, following the information brought by the worker bees in the dance area, try to determine the most efficient food source in direct proportion to the productivity with the 'greedy selection' method [28]. As a result of this selection, the scouts gravitate towards productive food sources. Only one worker bee or onlooker bee is assigned for each food source. Worker bees, found in other food sources that are insufficient, leave the food source they have exploited and turn into scout bees and disperse in the search space to find more efficient food sources. When applied to real-life problems, nectar productivity in food sources represents the optimized system. The implementation of this algorithm becomes an iterative

process that continues until the requirements of system optimization are achieved. This iterative cycle continues until the most efficient resource is found, and system performance is improved [27]. Figure 1 presents the flow-chart of the ABC algorithm.
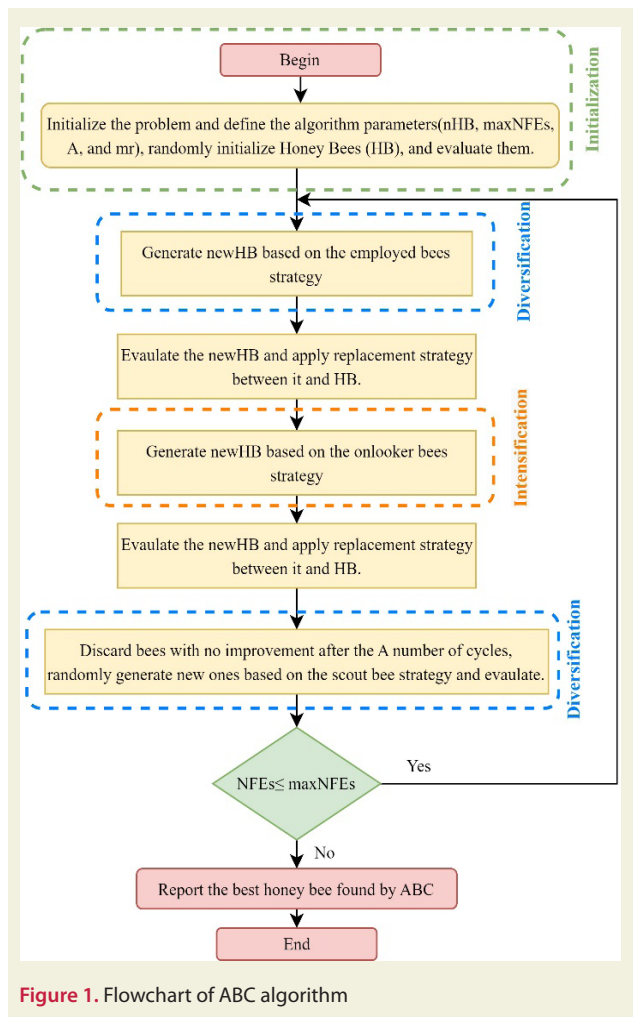

Figure 1. Flowchart of ABC algorithm

3. Results and Discussion

6 DOF model and 3 DOF control of the Pioneer RQ-2 UAV were created in the Matlab/Simulink environment. The flow diagram of the control system is shown in Figure 2.

As seen in the Figure 2, the altitude, speed, pitch angle and pitch rate values are controlled with a cascade structure. Controller parameters are optimized with the ABC algorithm. During the optimization process, four different fitness functions were used. The designed objective

All objective functions successfully followed the 450 meters altitude requirements, which were given as step input to the 5th second of the flight simulation. Among the answers, the objective function with the least oscillation, overshoot and least steady-state error was found to be IAE. Also, IAE is almost as successful as ITAE when the UAV's pitch angle increased for the desired altitude

functions consist of MSE (Mean Square Error), ITAE (Integral Time Absolute Error), ISE (Integral Square Error) and IAE (Integral Absolute Error) fitness functions that are frequently used in the literature [29-31]. The determined objective functions are presented in equations 28-31.

$$error_h = Altitude_{ref} - Altitude \qquad (24)$$

$$error_\theta = Theta_{ref} - Theta \qquad (25)$$

$$error_q = q_{ref} - q \qquad (26)$$

$$error_{TAS} = TAS_{ref} - TAS \qquad (27)$$

$$J_{ISE} = \sum_{t=0}^{40} error_h(t)^2 + error_\theta(t)^2$$
$$+ error_q(t)^2 + error_{TAS}(t)^2 \qquad (28)$$

$$J_{IAE} = \sum_{t=0}^{40} |error_h(t)| + |error_\theta(t)|$$
$$+ |error_q(t)| + |error_{TAS}(t)| \qquad (29)$$

$$J_{ITAE} = \sum_{t=0}^{40} t(|error_h(t)| + |error_\theta(t)|$$
$$+ |error_q(t)| + |error_{TAS}(t)| \qquad (30)$$

$$J_{MSE} = \frac{1}{40} \sum_{t=0}^{40} t(error_h(t)^2 + error_\theta(t)^2$$
$$+ error_q(t)^2 + error_{TAS}(t)^2 \qquad (31)$$

The optimization process consisting of a maximum of 100 iterations and 40 seconds was performed for the four objective functions. The scatter graphs obtained are presented in Figure 3.

For each algorithm, the lower and upper limits of the PID gains were selected the same, and the optimization process was carried out for the same conditions. The best PID coefficients found for each objective function are given in Table 2.

The performance analyzes of the controllers designed with different objective functions were evaluated for 40 seconds during the cruise flight at 100 meters altitude, and the results are shown in Figure 4.

response. Additionally, all aircraft have a pitch rate limit. Sudden changes in the control surface increase the load on the hinge point of the elevator and strained the entire control surface system. For this reason, the pitch rate of the UAV could not provide as good a result as the altitude and pitch angle against the 450 meters altitude requirements. Notwithstanding, it has been found the best gains
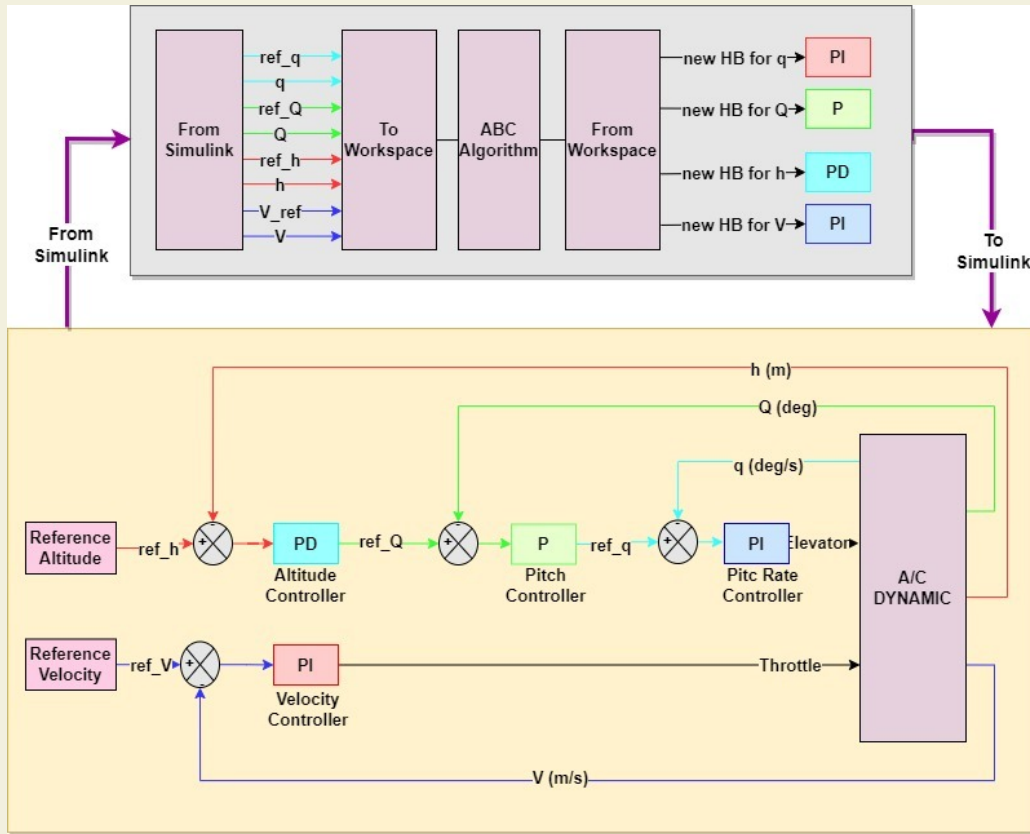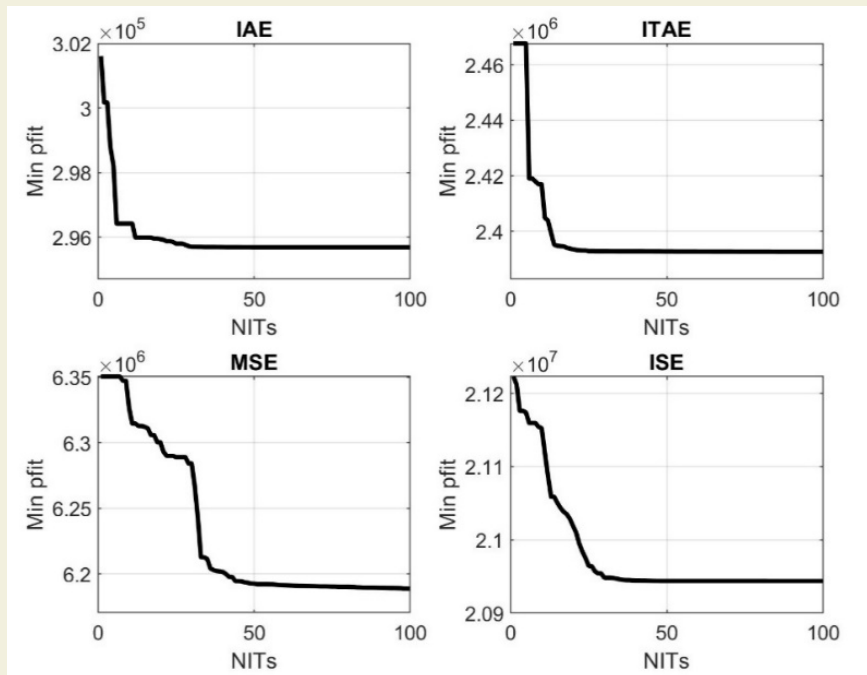
Figure 2. Cascade PID Control Flow Diagram

Figure 3. Scatter graphs for IAE, ITAE, MSE and ISE Objective Functions

Table 2. PID Gains of Objective Functions

	Pitch Rate		Theta	Altitude		TAS	
	P	I	P	P	D	P	I
J_{ISE}	-1	-36.384	1.42292	1.033536	0.522843	0	200
J_{IAE}	-50	-200	1.573113	1.990487	1.618973	195.4142	200
J_{ITAE}	-1.71825	-1	1.321292	1.340334	1.276471	199.7004	198.5689
J_{MSE}	-49.9994	-200	14.37209	1.96579	0.760183	195.4503	199.9767

that give the most stable response for pitch rate. Finally, the objective function that makes the least change for the true airspeed (TAS) of the UAV is prescribed as MSE. True airspeeds for all objective functions show that varied with low intervals.

The time response characteristics of the designed control system are presented in Table 3. According to these results, while the objective function with the lowest overshoot was J_{IAE}, the objective function with the lowest settling time was J_{MSE}. Although all objective functions exhibit successful system behavior, J_{IAE} stands out with these features, especially since the overshoot and peak values are expected to be low in the pitching movements of UAVs.

In spite of altitude requirements and responses, there is no reference input for speed and the UAV tends to maintain its true airspeed. For any altitude input, a change in velocity will occur, as kinetic energy will momentarily transform into potential energy. However, this change is brought closer to the equilibrium state by the speed controller. The closer this speed is to the trim speed, the better the velocity controller is. Therefore, the best result for cruise true airspeed is seen as the J_{MSE} objective function.

4. Conclusion

In this study, the nonlinear model of an unmanned aerial vehicle was linearized, and the longitudinal controller was designed on the linear model. In the controller design, besides the altitude control of the UAV, the speed control is also performed using a cascade PID controller. Seven gains of four different controllers are optimized
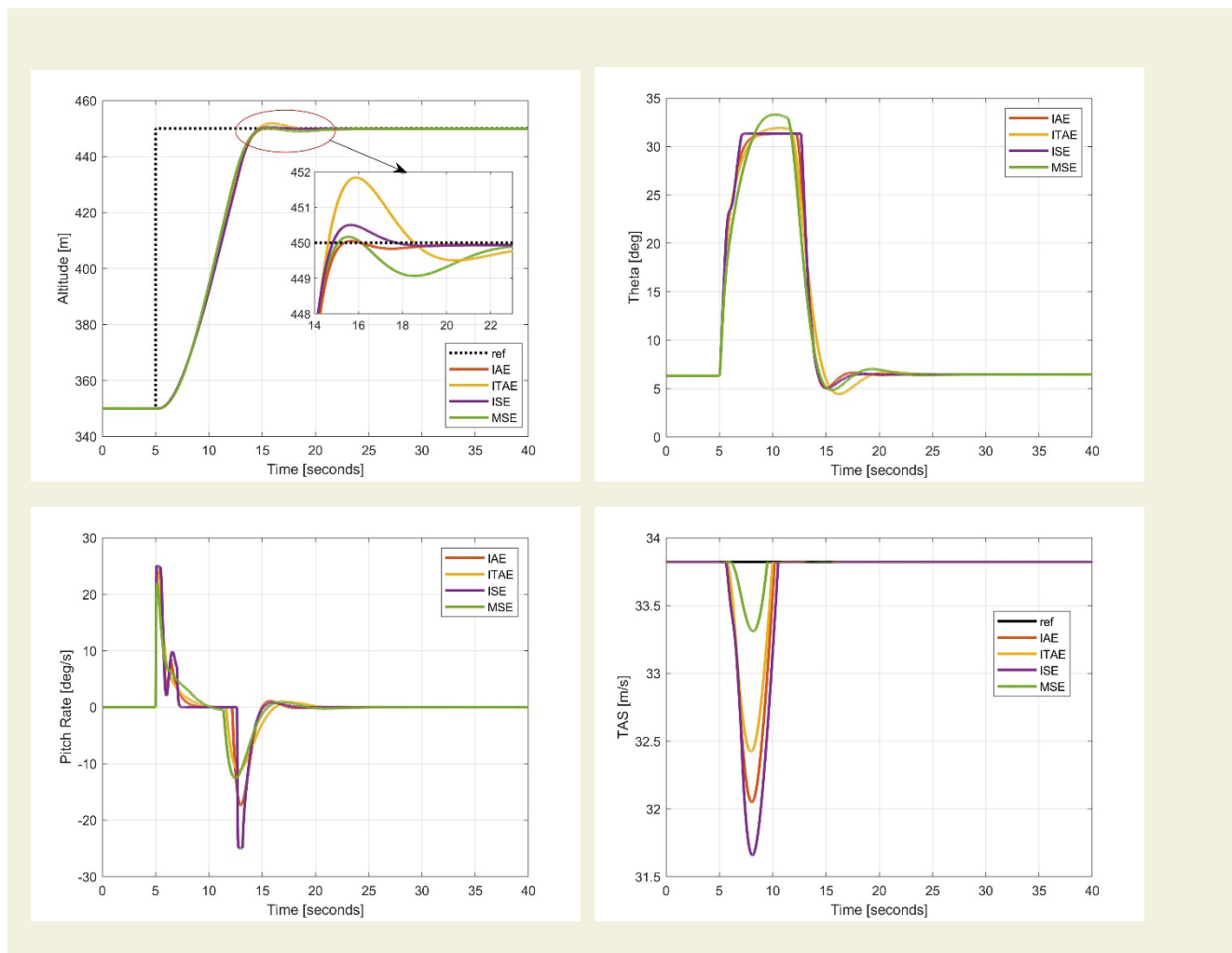
Figure 4. System Responses of a) Altitude b)Theta c) Pitch Rate d) TAS (True Air Speed)

Table 3. Time domain specifications.

	Rise Time	Settling Time	Settling Min	Settling Max	Overshoot	Undershoot	Peak	Peak Time
J_{ISE}	5.935	14.243	440.001	451.989	0.44	0	452	15.986
J_{IAE}	5.880	14.252	440.016	450.047	0.01	0	450	15.66
J_{ITAE}	5.881	14.163	440.021	450.503	0.11	0	450.5	15.642
J_{MSE}	5.632	14.153	440.002	450.169	0.04	0	450.2	15.538

with the ABC algorithm. In the optimization process, ITAE, ISE, MSE and IAE functions are used in the design of the objective function, which are the fitness functions whose effectiveness has been proven in the literature. Objective function; It is created with the fitness functions of altitude, pitch angle, pitch rate, and true airspeed. The system responses obtained as a result of the optimization are presented with tables and graphics. When the results were examined, it was revealed that the longitudinal con-

trol of the UAV gave the best result, with a 0.01 maximum overshoot of the J_{IAE} objective function. It is foreseen that the proposed optimization approach can be a guide in the control of multi-degree-of-freedom systems.

5. Conflict of Interest

The authors declare that there is no conflict of interest regarding the publication of this paper.

References

[1] Han, T., Xiao, B., Zhan, X. S., Wu, J., & Gao, H. (2019). Time-optimal control of multiple unmanned aerial vehicles with human control input. International Journal of Intelligent Computing and Cybernetics, 12(1), 138-152.

[2] Alladi, T., Chamola, V., & Kumar, N. (2020). PARTH: A two-stage lightweight mutual authentication protocol for UAV surveillance networks. Computer Communications, 160, 81-90.

[3] Xia, C., Yongtai, L., Liyuan, Y., & Lijie, Q. (2020). Cooperative task assignment and track planning for multi-UAV attack mobile targets. Journal of Intelligent & Robotic Systems, 100(3), 1383-1400.

[4] Bilici, M., Karılı, M., (2022) Modeling and Control of a Fixed-Wing High-Speed UAV. International Journal of Aviation Science and Technology, 3(01), 35-44.

[5] Altan, A. (2020, October). Performance of metaheuristic optimization algorithms based on swarm intelligence in attitude and altitude control of unmanned aerial vehicle for path following. In 2020 4th International Symposium on Multidisciplinary Studies and Innovative Technologies (ISMSIT) (pp. 1-6). IEEE.

[6] Ilango, H. S., & Ramanathan, R. (2020). A Performance Study of Bio-Inspired Algorithms in Autonomous Landing of Unmanned Aerial Vehicle. Procedia Computer Science, 171, 1449-1458.

[7] Mobarez, E. N., Sarhan, A., & Ashry, M. M. (2019, December). Robust PID Flight Controller for Ultrastick-25e UAV. In 2019 15th International Computer Engineering Conference (ICENCO) (pp. 150-156). IEEE.

[8] Kaba, A. (2021). Improved PID rate control of a quadrotor with a convexity-based surrogated model. Aircraft Engineering and Aerospace Technology. 93, 1287–1301.

[9] Amarat, S. B., & Zong, P. (2019). 3D path planning, routing algorithms and routing protocols for unmanned air vehicles: a review. Aircraft engineering and aerospace technology.

[10] Hervas, J. R., Reyhanoglu, M., Tang, H., & Kayacan, E. (2016). Nonlinear control of fixed-wing UAVs in presence of stochastic winds. Communications in Nonlinear Science and Numerical Simulation, 33, 57-69.

[11] Stastny, T., & Siegwart, R. (2018, June). Nonlinear model predictive guidance for fixed-wing UAVs using identified control augmented dynamics. In 2018 International Conference on Unmanned Aircraft Systems (ICUAS) (pp. 432-442). IEEE.

[12] Yan, J., Yu, Y., & Wang, X. (2022). Distance-based formation control for fixed-wing UAVs with input constraints: A low gain method. Drones, 6(7), 159.

[13] Zhen, Y., Hao, M., & Sun, W. (2020, November). Deep reinforcement learning attitude control of fixed-wing UAVs. In 2020 3rd International Conference on Unmanned Systems (ICUS) (pp. 239-244). IEEE.

[14] Poksawat, P., Wang, L., & Mohamed, A. (2017). Gain scheduled attitude control of fixed-wing UAV with automatic controller tuning. IEEE Transactions on Control Systems Technology, 26(4), 1192-1203.

[15] Mammarella, M., Capello, E., Dabbene, F., & Guglieri, G. (2018). Sample-based SMPC for tracking control of fixed-wing UAV. IEEE control systems letters, 2(4), 611-616.

[16] Abachizadeh, M., Yazdi, M. R. H., & Yousefi-Koma, A. (2010, July). Optimal tuning of PID controllers using artificial bee colony algorithm. In 2010 IEEE/ASME International Conference on Advanced Intelligent Mechatronics (pp. 379-384). IEEE.

[17] Coban, S., Bilgic, H.H., Akan, E. (2020). Improving autonomous performance of a passive morphing fixed wing UAV. Information Technology and Control. 49 (1), pp. 28-35.

[18] McCafferty, J. P., Woodward, D. A., Ray, G., Bachelani, A., & Kim, B. (2014). Investigation of an autonomous landing sensor for unmanned aerial systems. In AIAA Guidance, Navigation, and Control Conference (p. 0979).

[19] Bray, R. M. (1991). A wind tunnel study of the Pioneer remotely piloted vehicle. NAVAL POSTGRADUATE SCHOOL, MONTEREY CA.

[20] Etkin, B., & Reid, L. D. (1995). Dynamics of flight: stability and control. John Wiley & Sons.

[21] Johnson, M. A., & Moradi, M. H. (2005). PID control. London, UK: Springer-Verlag London Limited.

[22] Kada, B., & Ghazzawi, Y. (2011, October). Robust PID controller design for an UAV flight control system. In Proceedings of the World congress on Engineering and Computer Science (Vol. 2, No. 1-6, pp. 1-6).

[23] Andrade, F. A., Guedes, I. P., Carvalho, G. F., Zachi, A. R., Haddad, D. B., Almeida, L. F., ... & Pinto, M. F. (2021). Unmanned Aerial Vehicles Motion Control with Fuzzy Tuning of Cascaded-PID Gains. Machines, 10(1), 12.

[24] Bilgiç, H. H., Tutumlu, M. S., & Conker, Ç. (2021). Top ve çubuk sistemi için kaskad denetleyici parametrelerinin meta-sezgisel algoritmalarla optimizasyonu. Dokuz Eylül Üniversitesi Mühendislik Fakültesi Fen ve Mühendislik Dergisi, 23(67), 157-167.

[25] Bilgic, H. H., Sen, M. A., Yapici, A., Yavuz, H., & Kalyoncu, M. (2021). Meta-heuristic tuning of the LQR weighting matrices using various objective functions on an experimental flexible arm under the effects of disturbance. Arabian Journal for Science and Engineering, 46(8), 7323-7336.

[26] Guvenc, M. A., Bilgic, H. H., Cakir, M., & Mistikoglu, S. (2022). The prediction of surface roughness and tool vibration by using metaheuristic-based ANFIS during dry turning of Al alloy (AA6013). Journal of the Brazilian Society of Mechanical Sciences and Engineering, 44(10), 1-14.

[27] Karaboga, D. (2005). An idea based on honey bee swarm for

numerical optimization (Vol. 200, pp. 1-10). Technical report-tr06, Erciyes university, engineering faculty, computer engineering department.

[28] Akay, B., & Karaboga, D. (2012). Artificial bee colony algorithm for large-scale problems and engineering design optimization. Journal of intelligent manufacturing, 23(4), 1001-1014.

[29] Hekimoğlu, B. (2019). Optimal tuning of fractional order PID controller for DC motor speed control via chaotic atom search optimization algorithm. IEEE Access, 7, 38100-38114.

[30] Shagor, M. R. K., Nishat, M. M., Faisal, F., Mithun, M. H., & Khan, M. A. (2021, December). Firefly algorithm based optimized PID controller for stability analysis of DC-DC SEPIC converter. In 2021 IEEE 12th Annual Ubiquitous Computing, Electronics & Mobile Communication Conference (UEMCON) (pp. 0957-0963). IEEE.

[31] Maghfiroh, H., Saputro, J. S., Hermanu, C., Ibrahim, M. H., & Sujono, A. (2021, March). Performance Evaluation of Different Objective Function in PID Tuned by PSO in DC-Motor Speed Control. In IOP Conference Series: Materials Science and Engineering (Vol. 1096, No. 1, p. 012061). IOP Publishing.

Effect of nano hybrid additives on low velocity impact responses of aramid composite plates: example of CNT and ZrO₂

Mehmet Kayrici¹, Yusuf Uzun²*, Huseyin Arikan¹, Ahmet Karavelioğlu¹

¹Necmettin Erbakan University, Seydisehir Ahmet Cengiz Faculty of Engineering, Department of Mechanical Engineering, 42370, Konya, Turkey
²Necmettin Erbakan University, Seydisehir Ahmet Cengiz Faculty of Engineering, Department of Computer Engineering, 42370, Konya, Turkey

Orcid: M. Kayrici (0000-0003-1178-5168), Y. Uzun (0000-0002-7061-8784), H. Arikan (0000-0003-1266-4982), A. Karaveli (0000-0001-5044-1929)

Abstract: Aramid reinforced composites are advanced materials that are widely used in many industrial applications thanks to their combination of high strength and lightness. Nano additives are of great importance for improving the mechanical properties of aramid reinforced composites and reducing costs. In this paper, multi-walled Carbon Nanotube (CNT) and Zirconia (ZrO₂) nano hybrid additives were used to determine the effect on the mechanical characterization of aramid composite plates. Therefore, low velocity impact responses of aramid fiber reinforced composites were investigated by adding ZrO₂ and CNT nano hybrid additives to the Polives 701 polymer vinylester resin matrix. Low velocity impact tests were carried out at 10 J and 15 J. As a result of the experiments, the effects of nano hybrid additives on the impact absorption properties of aramid composite plates were determined. By determining the maximum force, displacement and time values, the effect of CNT and ZrO₂ nano hybrid additives on the impact resistance of the composite plates was analyzed. In addition, it contributed to the development of composite materials used in industrial applications by providing information on increasing the performance of composite materials by using nano additives. As a result of this study, it was determined that the strength of the composite material increased proportionally when the CNT additive was used, and the material became embrittled when the ZrO₂ additive was used.

Keywords: aramid fiber, carbon nanotube, low velocity impact, zirconia.

1. Introduction

Fiber-reinforced composite materials are widely used in many industrial applications due to their advantages such as high strength, low weight, and good corrosion resistance [1]. Such composites consist of a combination of fiber reinforcement and polymer matrix and are usually produced using matrix resin. However, continuous research is carried out to further improve the mechanical properties of these materials and reduce their costs. In recent years, nano additives have been found to be a potential solution to improve the properties of fiber-reinforced composite materials. Nano additives are composed of particles on the nanometer scale and can significantly affect the mechanical, thermal, and electrical properties of composite materials. Therefore, nano additives have been an important research area for optimizing the properties of composite materials and for a wider range of applications. In recent years, significant progress has been made in improving the mechanical properties of fiber-reinforced composites with nano additives and reducing costs. For example, has been observed

that graphene oxide additives increase the mechanical strength of composite plates and at the same time reduce their weight. Mahesh V.P. et al. has been stated that polymer matrix composites are the best choice in terms of properties such as thermal conductivity, protection against moisture and good strength at the same time [2]. Brabazon mentioned that polymer matrix composites are used in applications such as aerospace and water treatment systems that contain external factors that will adversely affect the material [3]. The study by Esmaeilzadeh et al. shows that when multi-walled CNT are added to the material at a certain rate, they increase the hardness and fracture resistance of the material, and when the additive ratio increases, mechanical properties such as hardness are negatively affected [4]. Bocanegra et al. found high fracture toughness and short dimensional cracks relative to single-walled CNT when they added double-walled CNT in their experiments that sintered the ZrO₂-saturated alumina composite for one hour at 1520 °C [5]. Shadakshari et al. found that the electrical and thermal conductivity decreased as a result of increasing the weight

of multi-walled CNT, and they observed with SEM, XRD, EDS and TEM tools that the decrease in thermal conductivity was due to inter-nanotube bending due to high temperature as a result of sintering and heat treatment [6]. Li R. et al. concluded that when ZrO_2, which is known for its biocompatibility in dental applications, is added to the composite to increase the shear bond strength, it is very beneficial in the maintenance and repair stages in the sector, and the silaning process as a bonding agent has played an important role in increasing this bond strength and durability [7]. Muthusamy et al. determined that vinylester resins are an ideal resin type with better erosion performance than other polymer resins in this type of studies due to their affordability, properties and easy availability [8]. Thooyan et al. discussed that the use of basalt fiber as a reinforcing element in vinylester matrix composites indicates poor adhesion, and as a result, low mechanical properties occur, to prevent this negative by adding a filler additive containing nano- and micro-level SiC composition [9]. When Bonsu et al. investigated the mechanical behavior of a polymer matrix composite in an artificial seawater environment, they preferred vinylester resin because it was in the middle of epoxy and polyester in terms of moisture resistance and price [10].

There are many studies investigating the mechanical behavior of composites against low-velocity impact. Mantena et al. observed that the effect of low-velocity impact with weight reduction in composites is much lower than that of high-velocity impact, and the process is quasi-static [11]. Hongkarnjanakul et al. performed a very low velocity impact test using a three-point bending tester to examine matrix failure and defects such as matrix cracks opening and a small percentage of self-closing [12]. Mahdian et al. discussed that the damage can be examined more realistically and non-destructively in the low-speed impact test with acoustic emission sensor weight reduction, which is planned to be used in a similar impact test [13]. Chandekar et al. showed comparatively that realistic results can be obtained with low speed impact test analysis using LS-DYNA program on the data obtained by computer aided simulation and finite element analysis method [14]. Sevkat et al. found that the symmetrical plate with different fold directions showed the best resistance to impact [15]. It was also observed that the delamination energy due to local deformation at the contact point increased with increasing laminate thickness [16]. During impact, it complicates the simulation of impact as damage modes such as fiber breakage, delamination, matrix cracking and crushing can occur simultaneously [17]. Linking the onset of damage to a single parameter is unrealistic and also increases the margin of error of simulations. While microscopic damages represent the effects of distributed defects in terms of internal state variables, damage detection is done at the macroscopic level in some way with continuous damage mechanics. It was concluded that woven composites were superior to unidirectional composites in low-speed impact tests [18]. Bhatnagar et al., using the impact output results, found the force formed by the mass/spring mechanism and

the energy conservation law, and revealed that this force could later be used to calculate the contact time [19]. Hanif et al. performed bending tests on a multi-walled carbon nanotube reinforced epoxy/aramid composite homogenized by sonication under different forces according to ASTM D5045 standard [20]. Evci et al. argued that damage criteria can be revealed by determining the impact response, and in this context, they performed three-point bending tests to compare the dynamic structure with the static structure [18]. Wang et al. improved the matrix-fiber interface adhesion by treating bamboo-reinforced epoxy resin matrix composites produced by the resin transfer molding (RTM) process with NaOH solution in addition [21]. Increasing production temperature also plays a role in the adhesion of the composite matrix-fiber interface [22]. Wu et al., by changing the order of the chemical bonds between the layers, obtained different adhesion interfaces when additives were added according to the bonds [23]. It has been found that the use of chopped fibers between flat laminates improves the delamination strength of composites [24]. Gupta et al. concluded that epoxy resin is the matrix that uses the absorbed energy most efficiently by making the matrix epoxy or vinylester in layered composites [25]. Meyer et al. have solved this problem by reducing the molding gap after concluding that pressing at high speeds distorts the position of the stacks, but resin flow could not occur [26]. Abiodun et al., using the central composite design method, concluded that mixing should be done for 30 minutes at 643 °C and 423 rpm in order to obtain optimum results in the production of $mTiO_2p/Al$ 7075 composite [27].

The aim of this study is to investigate the effect of CNT and ZrO_2 nano-hybrid additives on low velocity impact responses of aramid composite plates. Maximum force, displacement and time values were determined by performing low speed impact tests. The obtained results were analyzed to determine the effect of nano hybrid additives on the impact absorption properties of aramid composite plates. In this study, hybrid interactions of additive ratios in 4 different composite plates, one of which was produced by using vacuum infusion method and autoclave curing, one pure resin / aramid and the other 3 using different nano additive ratios, were considered and it was aimed to find the most suitable hybridization ratio in terms of impact resistance in layered composites. The results of this study will contribute to the development of composite materials used in industrial applications by providing information on increasing the mechanical performance of composite materials with nano additives. In future studies, it is aimed to complete the studies on hybridization rates and transfer them to artificial intelligence applications by adding higher ratios of CNT and ZrO_2 to the vinylester resin / aramid composite produced with the central composite design methodology.

2. Material and Methods

Ballistic para-aramid fabric with product code Kevlar 29 CT736 was used as fiber reinforcement material in the

study. Aramid fiber fabric basket type is 2x2 braided, 0.62 mm thick, 410 g/m² density and 150 cm wide. Vinylester Polives 701 was used as matrix material. Multi-walled CNT and ZrO₂ nanopowders were used as nano additives. The properties of nano additives are shown in Table 1.

Table 1. Properties of CNT and ZrO₂

Nano materials	Properties	Values
CNT	Purity	92%
	Intensity	2.4
	Outer diameter	8-10 nm
	Inner diameter	5-15 nm
	Electrical conductivity	98 S/cm
ZrO₂	Size	20 nm
	Purity	99.8%
	Morphology	Spherical
	Surface area	20-60
	Intensity	5.89

Aramid fabric was cut with special scissors in dimensions of 400 mm x 400 mm. New production vinylester resin hardener 0.2% by weight and 6% cobalt accelerator 0.02% by weight were prepared for hand lay-up. Six layers of nano-additive-free fabric were laid on the vacuum nylon and impregnated with a resin roller brush with hardener and accelerator between each layer. Trial studies were carried out with the resin to wet six layers of fabric and the amount that completely wetted the fabrics was determined as 280 g. In order to prevent any gelation of the vinylester resin during the process with a hardener and accelerator with a roller brush, the airflows in the workshop were turned off and the work was carried out at 20 °C (ambient temperature). After the material was placed in a vacuum bag in a vacuum of -0.6 Bar and placed in a press heated at 30 °C, the temperature was increased to 70 °C, and it was left to cure under 5 Bar pressure for 2 hours and left to cool naturally for 24 hours after the press was closed. After cleaning the sample, it was prepared for impact test by cutting with water jet in 100 mm x 150 mm dimensions according to ASTM D-7136 standard. In the sample with additives, it was first mixed into the CNT resin and cooled intermittently up to 40 °C by mixing for 15 minutes in the mechanical mixer and for 10 minutes in 2 periods in the ultrasonic mixer, for a total of 20 minutes. Then, ZrO₂ was added and mixed for 15 minutes in the mechanical mixer and in 2 periods of 10 minutes in the ultrasonic mixer, for a total of 20 minutes, and it was prepared by cooling to 40 °C. Hardener and accelerator were added to the prepared resin and applied on the aramid fabric. In this way, homogeneous dispersion of nano materials into the resin is ensured. All production processes were applied separately to the fabrics for each nano parameter (3 different parameters) as stated above, and nano-doped samples were obtained and made ready for the experiment. Sample preparation is shown in Figure 1.
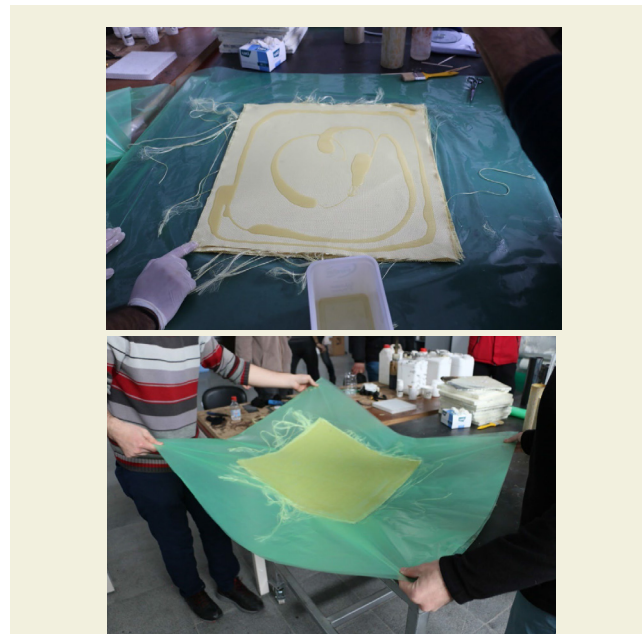
Figure 1. Sample preparation

Impact tests were performed with free weight drop. The impactor has a hemispherical barrel with a diameter of 12 mm and a mass of 5.6 kg. Force changes were obtained with a millivolt piezo electrical sensor. Sensor signals were acquired via a computer-mounted data acquisition card. The variation of the interaction force between the impactor and the samples over time was obtained with the NI Labview Signal Express (Figure 2) software. The sampling rate of the data acquisition system is 25 kHz. The tests were applied separately from three samples with the same parameter to samples with four different parameters at two different speeds, 10 J and 15 J, and a total of 24 results were obtained. The force data received were calculated as described in the ASTM D-7136 standard. The velocity with the first integration of acceleration and the displacement values with the second integration are obtained [28]. When the impactor hits the samples, its kinetic energy is partially transferred to the material and the remaining kinetic energy is recovered as recoil energy. The impact test unit has a rebound mechanism to catch the impactor after the initial impact is complete.

Figure 2. Impact testing device

2.1. Data Analysis and Preprocessing

Data analysis involves the process of examining, modeling and interpreting data. Data preprocessing is the process of making raw data suitable for analysis. In this process, steps such as data cleaning, transformation and feature engineering are performed. The data set obtained from experimental studies consists of CNT, ZRO_2, time, applied energy, displacement, obtained energy and force features. A number of adjustments were made using the data pre-processing method for the missing and erroneous data that occurred on the data of these features. Feature statistics of the dataset are shown in Table 2.

3. Results and Discussion

Figures were obtained using force-time data under 10 J and 15 J energy levels. The interactions of low-rate CNT and ZrO_2 nano additives on the strength of the composite were discussed. Comparisons at 10 J and 15 J energy levels were made with reference to the undoped sample. The undoped vinylester resin/aramid composite sample was taken as the reference material. When the force/time graph obtained from the experimental study performed at 10 J energy level was examined, it showed a normal distribution in the form of a bell curve to the impact response of the undoped vinylester resin/aramid composite plates.

It was observed that the force increased rapidly in a short time and reached its maximum value (Figure 3). The oscillations observed in all graphs showed that the damage started with delaminations and matrix fractures in the impact region. With the addition of 0.5% ZrO_2, a decrease in maximum force and an increase in pulse duration were observed. It was determined that the damage was in the form of delaminations and partial fiber fractures. When 0.5% CNT was added, it was observed that the maximum strength of the material increased partially, and the damage occurred in the form of high rates of delamination and fiber breaks. When 0.5% CNT / 0.5% ZrO_2 was added, it was determined that the damage was severely intensified with fiber breaks and delaminations because of the increase in the maximum force.

These results emphasized that CNT and ZrO_2 nano additives have significant effects on the impact strength of aramid composite plates and that nano additives contribute to the potential to improve the impact strength of
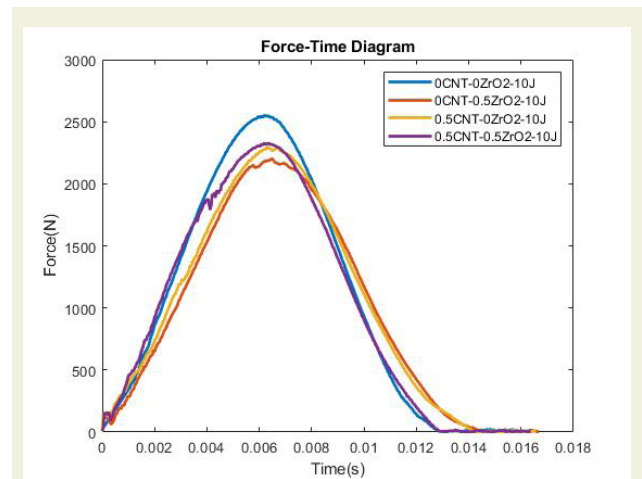

Figure 3. Force-time diagram under 10 J energy

composite materials.

While similar properties to the reference material were observed with only 0.5% ZrO_2 contribution at 15 J energy level (Figure 4), fiber fractures intensified in the impact region and damage developed early and the material exhibited brittle behavior. Since nano material agglomeration occurred in the sample with only 0.5% CNT addition, sudden strength drops were observed. It was observed that fiber fractures intensified, and layer separation occurred in the 0.5% CNT / 0.5% ZrO_2 added sample. The results highlighted that different nano doping ratios can trigger different damage mechanisms and the importance of an optimized additive composition selection.
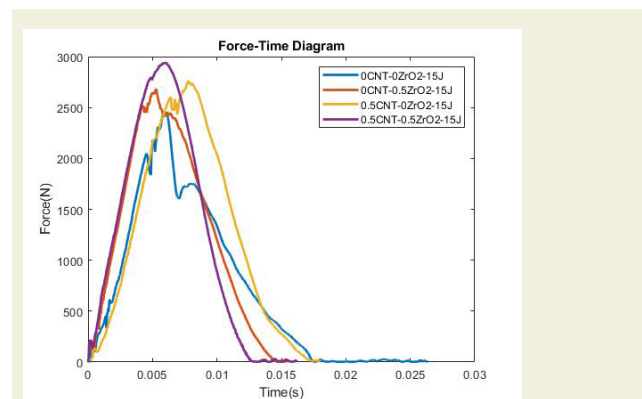

Figure 4. Force-time diagram under 15 J energy

Table2. Feature statistics of the dataset

Feature	Mode	Mean	Median	Dispersion	Min.	Max.	Missing
CNT	0.5	0.268	0.5	0.928	0	0.5	0
ZRO_2	0.5	0.258	0.5	0.964	0	0.5	0
Time	0.004	0.011	0.011	0.505	0.00001	0.041	0
Applied Energy	15	12.720	15	0.195	10	15	0
Displacement	7.55e-08	0.016	0.015	0.549	7.55e-08	0.047	0
Obtained Energy	4.21e-10	6.099	7.161	0.846	4.21e-010	15.332	0
Force	2.755	1058.41	904.711	0.869	2.755	2941.03	0

Figures were obtained using force-displacement data under 10 J and 15 J energy levels. Comparisons at 10 J and 15 J energy levels were made with reference to the undoped sample. In the sample containing only 0.5% ZrO_2 at 10 J energy level, the maximum force decreased while the amount of displacement increased. Maximum force and displacement value of the material increased only in 0.5% CNT added sample. A more balanced situation was observed with 0.5% CNT / 0.5% ZrO_2 additives, and there was no significant difference in force and displacement ratios. Graphs of force-displacement values is shown in Figure 5.
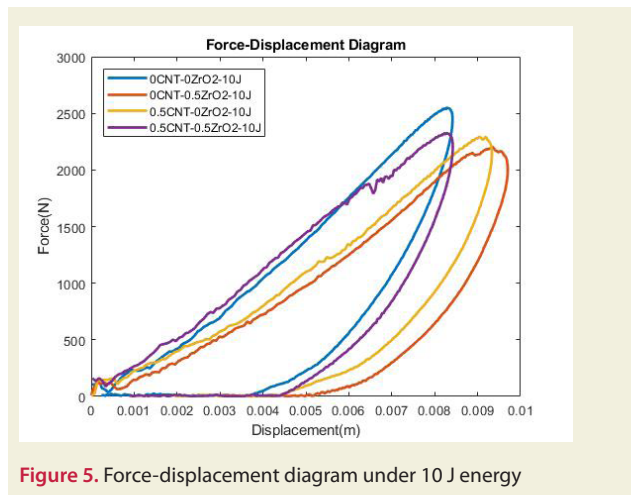
Figure 5. Force-displacement diagram under 10 J energy

Serious damage modes occurred at the 15 J energy level in the pure sample, and the irregularity in the material rebound in the graph is thought to have occured due to nano agglomeration has been detected. This shows that the impact strength of the undoped sample is limited, and its mechanical performance needs to be optimized. It was determined that only 0.5% ZrO_2 added sample material reached the maximum strength and serious fiber damage occurred with low displacement rate in the impact region. These results showed that the ZrO_2 additive increased the impact strength of the material, and the material became brittle when the damage intensified. It was observed that the impact force and displacement amount of the material were maximized in the sample with only 0.5% CNT additive, but the amount of energy consumed was reduced. These results showed that the CNT additive increased the energy absorption capacity of the material and the deformation caused by the impact was absorbed more effectively. With 0.5 CNT / 0.5 ZrO_2 additives, it has been determined that the material maintains the maximum force ratio and the amount of displacement is at the lowest level. It has been shown that the use of CNT and ZrO_2 additives together increases the impact resistance of the material and controls the amount of displacement. Graphs of force-displacement values is shown in Figure 6.

Figure 7 and Figure 8 were obtained using energy-time data at 10 J and 15 J energy levels, and comparisons were made with reference to the undoped sample. At the 10 J energy level, the pure sample gave back 60% of the energy
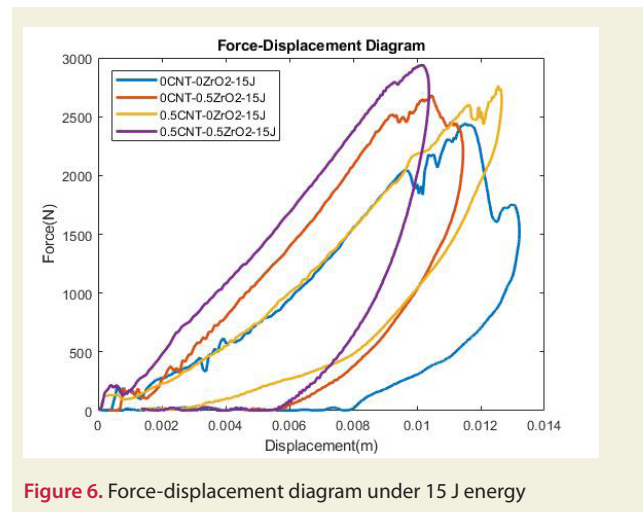

Figure 6. Force-displacement diagram under 15 J energy

as recoil energy and absorbed the rest. The recoil energy increased only in the 0.5% ZrO_2 added sample. As a result, the material was less damaged and partially ductile. It was concluded that only 0.5% CNT additive delayed the recoil energy and increased the energy absorption in the sample. With 0.5% CNT / 0.5% ZrO_2 additives, it did not cause any increase in the energy absorption ability of the sample.
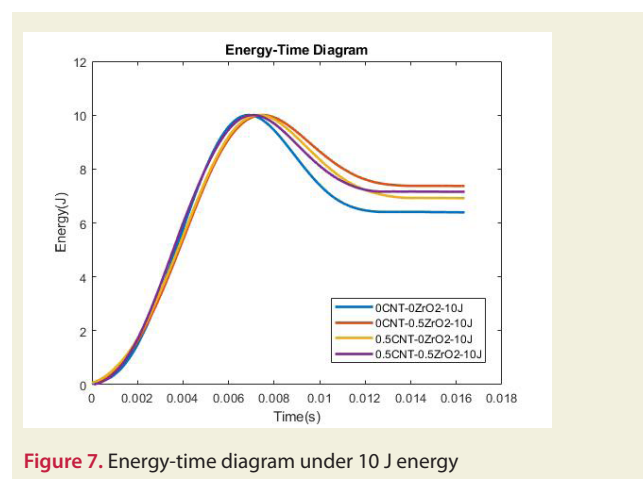

Figure 7. Energy-time diagram under 10 J energy

It was observed that 0.5% CNT / 0.5% ZrO_2 additive at the 15 J level provided a slight increase in the energy absorbing ability of the material. This gives an idea about the low rates of nano additives. The effect of energy increase at this level is clearly visible. The return energy level in the undoped material increased, but the return energy in the 0.5% ZrO_2 doped sample decreased. This can be explained by the fact that as the energy level increases, the material's ability to absorb energy increases. It can be concluded that with the effect of only 0.5% CNT additive, the recoil energy decreases, absorbs more energy, and increases the impact strength.

When the damage images in Figures 9 and 10 were examined, partial delamination's at 10 J energy level and fiber fractures in the first layer were detected in all samples. At 15 J energy level, it was observed that the amount of delamination increased, and fiber fractures occurred in
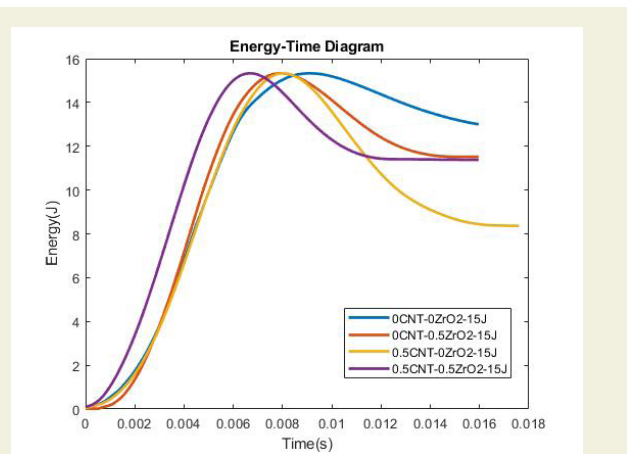
Figure 8. Energy-time diagram under 15 J energy

a wider region. As the energy level increases, the level of these damages should be expected to increase.

It was determined that the 0.5% CNT and 0% ZrO_2 doped sample developed at 10 J energy level in the opposite di-

rection of the impact force, and the delamination's developed towards the layer separation and the material damage occurred in the thickness direction. When the energy level was increased to 15 J, the damages were more intense in the first layers. Although a small number of partial delamination and fiber fractures occurred at 10 J energy level in the 0% CNT and 0.5% ZrO_2 doped sample, the damages increased and intensified due to the embrittlement effect of the ZrO_2 addition.

In the 0.5% CNT and 0.5% ZrO_2 doped sample, it was observed that delamination's resulted in layer separation at 10 J energy level and fiber fractures increased towards the layer depth. At the 15 J energy level, damage occurred due to the separation of the middle layer and the intensification of fiber fractures in the middle layer. It was concluded that the additives of CNT and ZrO_2 at these rates made the material embrittle.

4. Conclusion

In this study, the effect of different amounts of CNT and

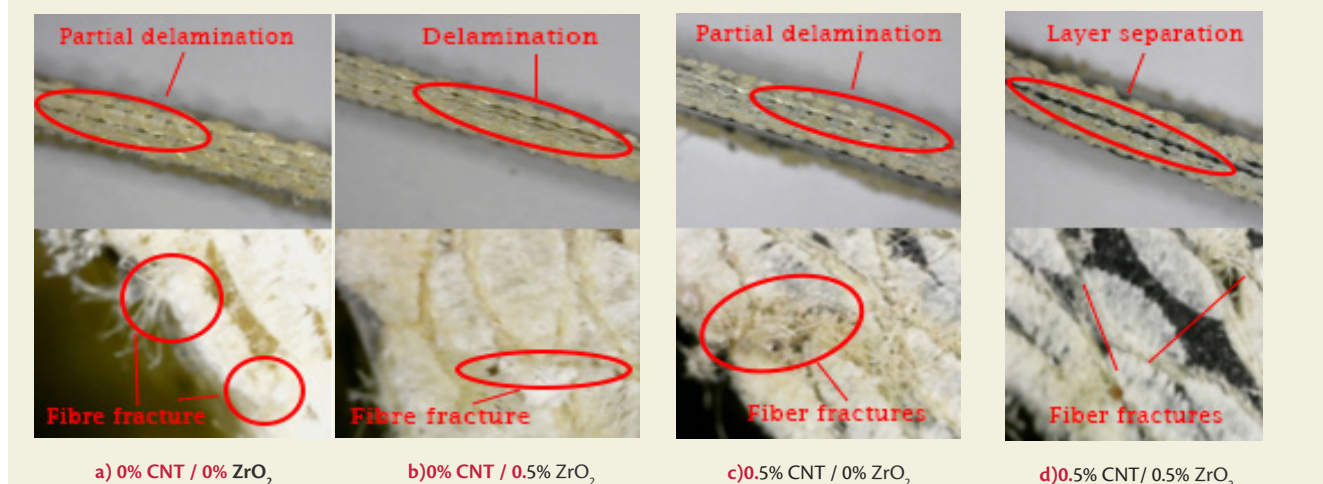**Figure 9.** Impact zone damage mechanisms at 10 J energy level

Figure 10. Impact zone damage mechanisms at 15 J energy level

ZrO_2 additives on the mechanical properties of aramid composite plates was investigated. As a result of the experimental studies and analyzes, the following results were obtained:

- Impact force and displacement amount were homogeneous in unadulterated samples. However, significant damage modes and nano-agglomeration were observed. The maximum force/displacement ratio was determined at a low level.

- Only 0.5% ZrO_2 addition enabled the material to reach its maximum strength level and serious fiber damage occurred in the impact zone. The amount of displacement was realized at a lower level. This indicates a decrease in material flexibility.

- Only 0.5% CNT addition increased the impact force and displacement amount of the material. This shows that the durability of the material has increased. However, sudden force drops due to nanomaterial agglomeration were observed.

- The 0.5% CNT / 0.5% ZrO_2 additive preserved the maximum force ratio of the material and kept the displacement amount at the lowest level. This showed that the use of CNT and ZrO_2 additives together increases the durability of the material and controls the displacement. This shows that the use of CNT and ZrO_2 additives together can affect the mechanical properties of the material in a balanced way. This information is of great value for the design and application of composite materials.

The results showed that suitable nano doping ratios can increase the impact resistance of the material and provide an optimized structure for the desired mechanical properties. In future studies, the determination of the optimum additive ratio by using higher nano additive ratios and the application of artificial intelligence using the data we have, and the mechanical effects of different ratio nano additives on the composite material will be focused on in more detail.

References

[1] Gibson, RF. (2016). Principles of Composite Material Mechanics. 4 ed. CRC Press.

[2] Mahesh, V.P., Patel, S., Gumaste, A., et al. (2021). Joining of Polymer Matrix Composites Through Friction Stir Processes.

[3] Brabazon, D. (2021). Introduction: Polymer Matrix Composite Materials.

[4] Esmaeilzadeh, R., Zamani, C., Reinhardt, H., et al. (2020). Improved mechanical properties of NbC-M2 high speed steel-based cemented carbide by addition of multi-walled carbon nanotubes. International Journal of Refractory Metals and Hard Materials, 93: 105346, DOI: https://doi.org/10.1016/j.ijrmhm.2020.105346.

[5] Bocanegra-Bernal MH, Echeberria J, Ollo J, et al. (2011). A comparison of the effects of multi-wall and single-wall carbon nanotube additions on the properties of zirconia toughened alumina composites. Carbon, 49: 1599-1607. DOI: https://doi.org/10.1016/j.carbon.2010.12.042.

[6] Shadakshari, R., Niranjan, HB. and Pakkirappa, H. (2022). Investigation of mechanical properties, thermal and electrical conductivity of multi-walled carbon nanotubes reinforced with Al2024 nanocomposites. Materials Today: Proceedings, 56: 135-142. DOI: https://doi.org/10.1016/j.matpr.2021.12.567.

[7] li, R., Wang, C., Ma, SQ., et al. (2020). High bonding strength between zirconia and composite resin based on combined surface treatment for dental restorations. Journal of Applied Biomaterials & Functional Materials, 18: 2280800020928655. DOI: 10.1177/2280800020928655.

[8] Muthusamy, AR., Thiagamani, SMK., Krishnaswamy, S, et al. (2022). Erosion performance of natural fiber reinforced vinyl ester hybrid composites: Effect of layering sequences. Materials Today: Proceedings, 64: 200-206. DOI: https://doi.org/10.1016/j.matpr.2022.04.365.

[9] Thooyavan, Y., Kumaraswamidhas, LA., Edwin Raj, R., et al. (2022) Failure analysis of basalt bidirectional mat reinforced micro/nano Sic particle filled vinyl ester polymer composites. Engineering Failure Analysis, 136: 106227. DOI: https://doi.org/10.1016/j.engfailanal.2022.106227.

[10] Osei Bonsu, A., Liang, W., Mensah, C., et al. (2022). Assessing the mechanical behavior of glass and basalt reinforced vinyl ester composite under artificial seawater environment. Structures, 38: 961-978. DOI: https://doi.org/10.1016/j.istruc.2022.02.053.

[11] Mantena, PR., Mann, R. and Nori, C. (2001). Low-Velocity Impact Response and Dynamic Characteristics of Glass-Resin Composites. Journal of Reinforced Plastics and Composites, 20: 513-534. DOI: 10.1177/073168401772678689.

[12] Hongkarnjanakul, N., Rivallant, S., Bouvet, C., et al. (2014). Permanent indentation characterization for low-velocity impact modelling using three-point bending test. Journal of Composite Materials, 48: 2441-2454. DOI: 10.1177/0021998313499197.

[13] Mahdian, A., Yousefi, J., Nazmdar, M., et al. (2017). Damage evaluation of laminated composites under low-velocity impact tests using acoustic emission method. Journal of Composite Materials, 51: 479-490. DOI: 10.1177/0021998316648228.

[14] Chandekar, GS., Thatte, BS. and Kelkar, AD. (2010) On the Behavior of Fiberglass Epoxy Composites under Low Velocity Impact Loading. Advances in Mechanical Engineering, 2: 621406. DOI: 10.1155/2010/621406.

[15] Sevkat, E., Liaw, B., Delale, F., et al. (2010). Effect of repeated impacts on the response of plain-woven hybrid composites. Composites Part B: Engineering, 41: 403-413. DOI: https://doi.org/10.1016/j.compositesb.2010.01.001.

[16] Caprino, G., Lopresto, V., Scarponi, C., et al. (1999). Influence of material thickness on the response of carbon-fabric/epoxy panels to low velocity impact. Composites Science and Technology, 59: 2279-2286. DOI: https://doi.org/10.1016/S0266-3538(99)00079-2.

[17] Yang, L., Yan, Y. and Kuang, N. (2013). Experimental and numerical investigation of aramid fibre reinforced laminates subjected to low velocity impact. Polymer Testing, 32: 1163-1173. DOI: https://doi.org/10.1016/j.polymertesting.2013.07.010.

[18] Evci, C. and Gülgeç, M. (2012). An experimental investigation

on the impact response of composite materials. International Journal of Impact Engineering, 43: 40-51. DOI: https://doi.org/10.1016/j.ijimpeng.2011.11.009.

[19] Bhatnagar, AS., Gupta, A., Arora, G., et al. (2021). Mean-field homogenization coupled low-velocity impact analysis of nano fibre reinforced composites. Materials Today Communications, 26: 102089. DOI: https://doi.org/10.1016/j.mtcomm.2021.102089.

[20] Hanif, WYW., Risby, MS. and Noor, MM. (2015). Influence of Carbon Nanotube Inclusion on the Fracture Toughness and Ballistic Resistance of Twaron/Epoxy Composite Panels. Procedia Engineering, 114: 118-123. DOI: https://doi.org/10.1016/j.proeng.2015.08.049.

[21] Wang, D., Bai, T., Cheng, W., et al. (2019). Surface Modification of Bamboo Fibers to Enhance the Interfacial Adhesion of Epoxy Resin-Based Composites Prepared by Resin Transfer Molding. Polymers, 11: 2107.

[22] Dai, Z., Zhang, B., Shi, F., et al. (2011). Effect of heat treatment on carbon fiber surface properties and fibers/epoxy interfacial adhesion. Applied Surface Science, 257: 8457-8461. DOI: https://doi.org/10.1016/j.apsusc.2011.04.129.

[23] Wu, Q., He, J., Wang, F., et al. (2020). Comparative study on effects of covalent-covalent, covalent-ionic and ionic-ionic bonding of carbon fibers with polyether amine/GO on the interfacial adhesion of epoxy composites. Applied Surface Science, 532: 147359. DOI: https://doi.org/10.1016/j.apsusc.2020.147359.

[24] Singh, TJ. and Samanta, S. (2015). Characterization of Kevlar Fiber and Its Composites: A Review. Materials Today: Proceedings, 2: 1381-1387. DOI: https://doi.org/10.1016/j.matpr.2015.07.057.

[25] Gupta, J., Reynolds, N., Chiciudean, T., et al. (2020). A comparative study between epoxy and vinyl ester CF-SMC for high volume automotive composite crash structures. Composite Structures, 244: 112299. DOI: https://doi.org/10.1016/j.compstruct.2020.112299.

[26] Meyer, N., Schöttl, L., Bretz, L., et al. (2020). Direct Bundle Simulation approach for the compression molding process of Sheet Molding Compound. Composites Part A: Applied Science and Manufacturing, 132: 105809. DOI: https://doi.org/10.1016/j.compositesa.2020.105809.

[27] Abiodun Balogun, O., Adewale Akinwande, A., Adebayo Ogunsanya, O., et al. (2022). Central composite design and optimization of selected stir casting parameters on flexural strength and fracture toughness mTiO2p/Al 7075 composites. Materials Today: Proceedings, 62: 4574-4583. DOI: https://doi.org/10.1016/j.matpr.2022.05.315.

[28] Gemi, L., Kayrıcı, M., Uludağ, M., et al. (2018). Experimental and statistical analysis of low velocity impact response of filament wound composite pipes. Composites Part B: Engineering, 149: 38-48. DOI: https://doi.org/10.1016/j.compositesb.2018.05.006.

Single-pulse MIG welded Perform 700 steel joints with various welding parameters

Fatih Özen[1*]

[1]Welding Programme Division, Department of Machine and Metals, Beşiri Industrial Organized Zone Vocational College, Batman University, 72100, Batman, Türkiye

Orcid: F. Özen (0000-0002-2915-8456)

Abstract: In this work, Perform 700 steel sheets with a 5-mm thickness were welded with a single-pulse MIG welding method with different welding currents and welding speeds. The welded specimens were subjected to tensile tests, hardness measurements, and microstructural observations. According to the results, the heat input played a significant role in the tensile strength of the joint. The maximum tensile strength was obtained as 594.75 MPa at 140A welding current and 450 mm/min welding speed. The tensile specimens consistently separated between the fusion zone and the heat-affected zone. The heat-affected zones have exhibited tempered martensitic structure. The tempering effect increased the sizes of the martensitic structure; therefore, the hardness was significantly increased. However, the fusion zone, which consisted of a bainitic structure inside the ferrite matrix, exhibited soft and ductile behavior. The boundary of the soft fusion zone and hard heat-affected zone formed the weakest point in the joint.

Keywords: welding, joining, mechanical properties, perform steel, S700MC, single-pulse, MIG weld

1. Introduction

Limited fossil fuels, the global warming effect induced by carbon emissions, and increasing the level of safety standards have caused a dramatic change in steel technology [1,2]. However, steel is abundant, easy to produce, rigid, and cheaper than non-ferrous metals, making it an inevitably useful material in various industries. The key motivation is to decrease the weight of a design by increasing its strength without compromising safety, allowing for flexible and light design structures [3]. Although developed steels are not cheaper than conventional steels, they offer lower consumption of the steels, decreasing both carbon emissions and material expenses [4].

With these motivations, numerous steel types have been developed. Among these steels, high-strength low alloy (HSLA) and advanced high-strength steel (AHSS) families have drawn attention in various industries including automotive, transportation, marine, and construction [5–8]. Especially, HSLA steels have been commonly employed in structural applications such as highway barriers, bridge cables, car frames, truck bodies, electrical transmission structures, street light posts, etc. [9].

PERFORM steels are an important member of HSLA steels, which is a trademark of ThyssenKrupp AG (Germany). Among the PERFORM steels, PERFORM 700, which

is also known as S700MC, is one of the most employed steel grades [10]. Due to its popularity, much work has been done on welding similar and dissimilar joints [11-20].

Petronis et al. [11] investigated the hybrid laser-arc weldability of S700MC joints with different thicknesses. They reported that although full penetration was obtained at a laser power of 6 kW, horizontal and vertical positions have exhibited poor weldability at high speeds of the weld. Silva et al. [12] studied MAG welding of S700MC with a low arc technique. It was found that usage of the blowtorch has decreased both the weld energy consumption and splinters while retaining the mechanical performance of the welded joint. Szymczak et al. [13] examined the effect of the welding operation on the mechanical performance of S700MC joints subjected to various types of tests. They noted that S700MC steel is sensitive to the heat input applied by the welding operation in terms of mechanical properties. Ferdinandov et al. [14] studied the mechanical performance of submerged arc-welded S700MC joints with various weld gaps. They reported a limited reduction in the yield strength since most of the plastic deformation is formed in both the heat-affected and fusion zones. Moravec et al. [15] studied the fatigue life performance of MAG-welded S700MC. They reported that the application of the double-sided fillets adversely influenced fatigue life. Tomków et al. [16] investigated the underwater welding of S700MC with rutile

---

electrodes and described that the maximum hardness in the heat affected did not exceed the critical threshold. Eva et al. [17] simulated the welded S700MC joint by joule heating effect and carried out various mechanical tests. They pointed out that the transformations taking place in the heat-affected zone have a profound influence on the fracture response of the welded joint. Kik et al. [18,19] studied a numerical verification analysis of cyclic thermal application and the effect of annealing temperature on the residual stress level, respectively. They noted that S700MC is overly sensitive to the applied temperature in terms of both stress levels and phase transitions. Sebestova et al. [20] investigated the fatigue properties of hybrid laser-TIG welded S700MC and S460MC steels. They stated that the fatigue cracks frequently initiate from the interface between the fusion zone and the heat-affected zone.

The works regarding the Perform steels emphasize the sensitivity against the exposure of the heat application, especially in welding processes. Therefore, applying low-heat inputs in the welding of Perform steels is of foremost importance. In this study, investigating the single-pulse MIG welding technique in the welding of Perform 700 steels is of high importance. Although a great deal of studies have been conducted in these steel grades, single-pulse MIG welding has not been thoroughly investigated. The microstructural and mechanical properties are investigated using microstructural observation, hardness measurements, and tensile tests with various welding parameters.

2. Materials and Method

The Perform 700 steel sheets with 4-mm thickness were acquired by the local dealers. The sheets were sliced to 150x120-mm dimensions. The weld surfaces of the specimens were cleaned with acetone to remove oil and dirt. Figure 1 shows the welding tractor manipulator and welding setup for the experiments. The welding tractor manipulator was employed to attain sound and reliable weld joints. The tractor manipulator was also used to adjust the welding speeds.

A Magmaweld IDS 320MM Pulse welding machine was employed in the experiments. The shielding gas consisted of 86% Ar, 12% CO_2, and 2% O. SG-2 weld wire was employed in the experiments. The chemical compositions of the Perform 700 steel and SG-2 wire are presented in Table 1. Standard arc distance was kept between weld filler wire and BM.

Table 2 illustrates the welding experiment design for single-pulse MAG welding. Two main motivations were planned. First, hold the welding speed while increasing the current intensity, second, stabilizing the current intensity while increasing the welding speed. To obtain this goal, welding speeds were kept constant in the first three experiments while welding currents were fixed in experiment numbers 4, 5, and 6. The welded specimen was sliced with a 25-mm width. Three of them were used for tensile tests, and the last specimen was employed in hardness and microstructural observations. The weld start and end distances with 25 mm were thrown to obtain sound welds,

Table 1. Chemical compositions of the Perform 700 and SG-2 filler metal wire.

Material	Elements (wt.%)											
	C	Mn	Si	Mo	Ni	P	S	Al	Ti	Nb	V	Fe
Perform 700	0.047	1.966	0.205	0.156	0.161	0.005	0.006	0.034	0.058	0.066	0.061	Rest
SG-2 wire	0.075	1.516	0.851	-	-	-	-	-	-	-	-	Rest
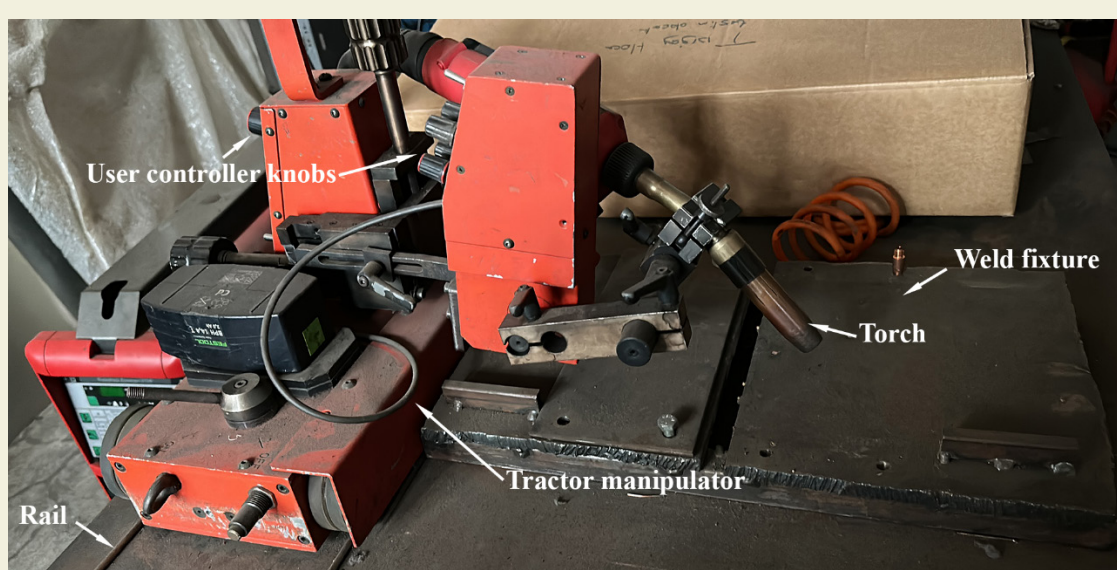
Figure 1. Welding setup for experiments

ensuring consistent welding parameters.

**Table 2.** Applied welding parameters for the experiments.

Experiment no.	Current (A)	Voltage (V)	Welding speed (mm/min)	Gas flow rate (l)
1	120	16.2	350	
2	140	17.5	350	
3	160	19.3	350	10
4	140	17.8	300	
5	140	17.8	400	
6	140	17.8	450	

Tensile tests were carried out with a universal testing device. Tensile speed was 10 mm/min. The average results were employed in the graphs. For the metallographic examination, conventional specimen preparation techniques were adopted. The final pass of polishing was executed with 1 μm Alumina suspension. The polished surfaces were etched with 4% Nital solution. The microstructures were examined by a Nikon L150A light microscope. Wilson hardness tester with Vickers indentation was used for line hardness measurements.

3. Results and Discussion

Since heat input is of high importance, the welding speeds and welding current were carefully designed. The heat input can be calculated using (1) [21]. Here, H is the heat input (kJ/mm), Ƞ is efficiency, I is the current density (A), E is the applied voltage (V) and S is the welding speed (mm/min).

$$H = \frac{I.V.60}{S.1000} Ƞ \qquad (1)$$
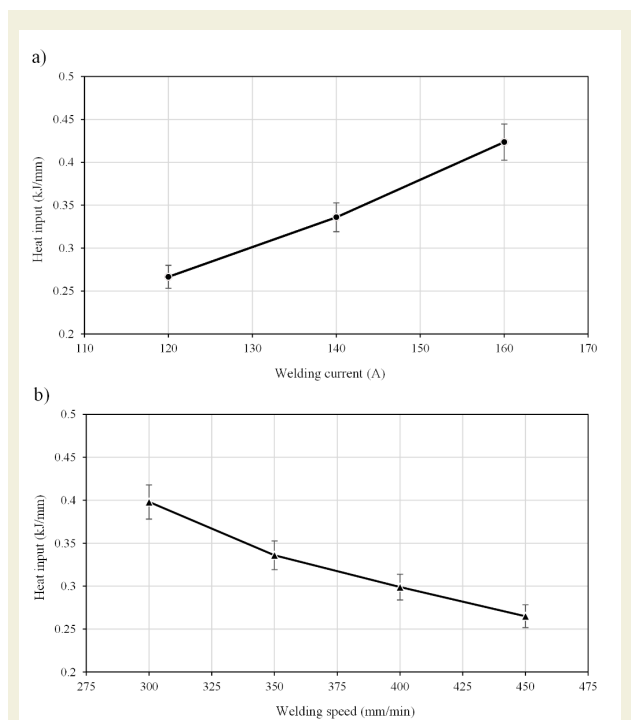
Figure 2. Calculated heat input in terms of a) various welding currents under a constant welding speed of 300 mm/min, and b) different welding speeds under a constant welding current of 140A

Figures 2a and 2. b illustrate calculated heat inputs both under a constant welding speed of 300 mm/min and under a constant welding current of 140A, respectively. As the applied welding current is increased, the heat input increases. The welding speed has opposite characteristics, the heat input decreases as the welding speed increases. This can be attributed to the accumulation of the applied heat during welding.
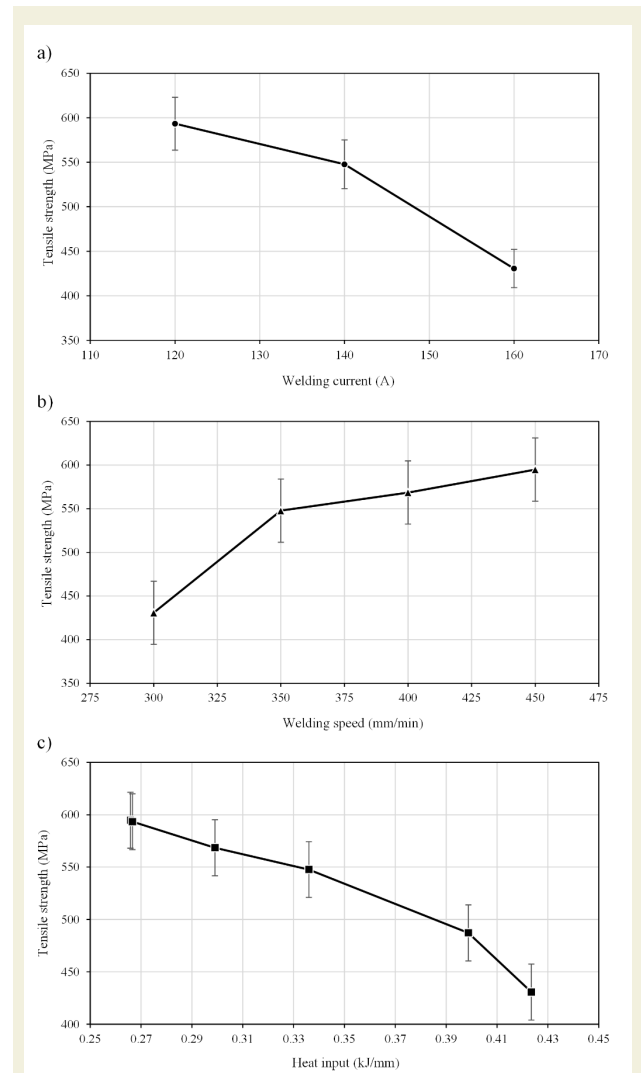

Figure 3. Tensile strength of the MIG welded joint in terms of a) Welding current, b) Welding speed, and c) Heat input.

The effect of welding current, welding velocity, and heat input on tensile strength of the single-pulse MIG welded Perform 700 joint is presented in Figure 3. a-c, respectively. The welding current and the welding velocity exhibit an inverse characteristic. This significant variation can be attributed to the heat input during welding. Elevated welding currents increase the heat input at the weld joint, and a slowdown in welding speed causes the accumulation of heat as well. The lowest tensile strength was obtained at a high welding speed and the maximum welding current, which is measured as 300 mm/min welding speed and 160A welding current, respectively. The maximum tensile strength was measured as 594.75 MPa at 140A welding current and 450mm/min welding speed.

Figure 4a-f shows the microstructure of single-pulse MIG welded joints with various magnifications. The weld microstructure can be divided into three sections: base metal (BM), heat-affected zone (HAZ), and fusion zone (FZ). The BM of the joint consists mostly of bainite and ferrite islands, with small fractions of martensite as well. Figure 5 shows line hardness measurements of the single-pulse MIG-welded joint. The BM of the Perform 700 exhibited an average hardness of 285±5 Hv10. Then, the hardness increased in the HAZ, reaching the peak point, measured as 381Hv10. As seen in Figure 4. e, the bainite transformed into tempered martensite. The grain sizes also increased in the HAZ. The hardness variation in the

HAZ does not have linear consistency. These hardness differences are attributed to coarse polygonal ferrites [22]. However, high hardness is yielded near the FZ/HAZ junction. Although the ferrite grains are softer than tempered martensite, the ferrite grains are not bigger than Vickers indentation, thereby measuring indentation has always touched not only ferrites but also the tempered martensite [16].

The hardness line from HAZ to FZ suddenly decreases. Although the hardness increased to a limited extent near the HAZ/FZ interface, the hardness decreased to 283±5 Hv10, similar to that of BM. The hardness at the center-
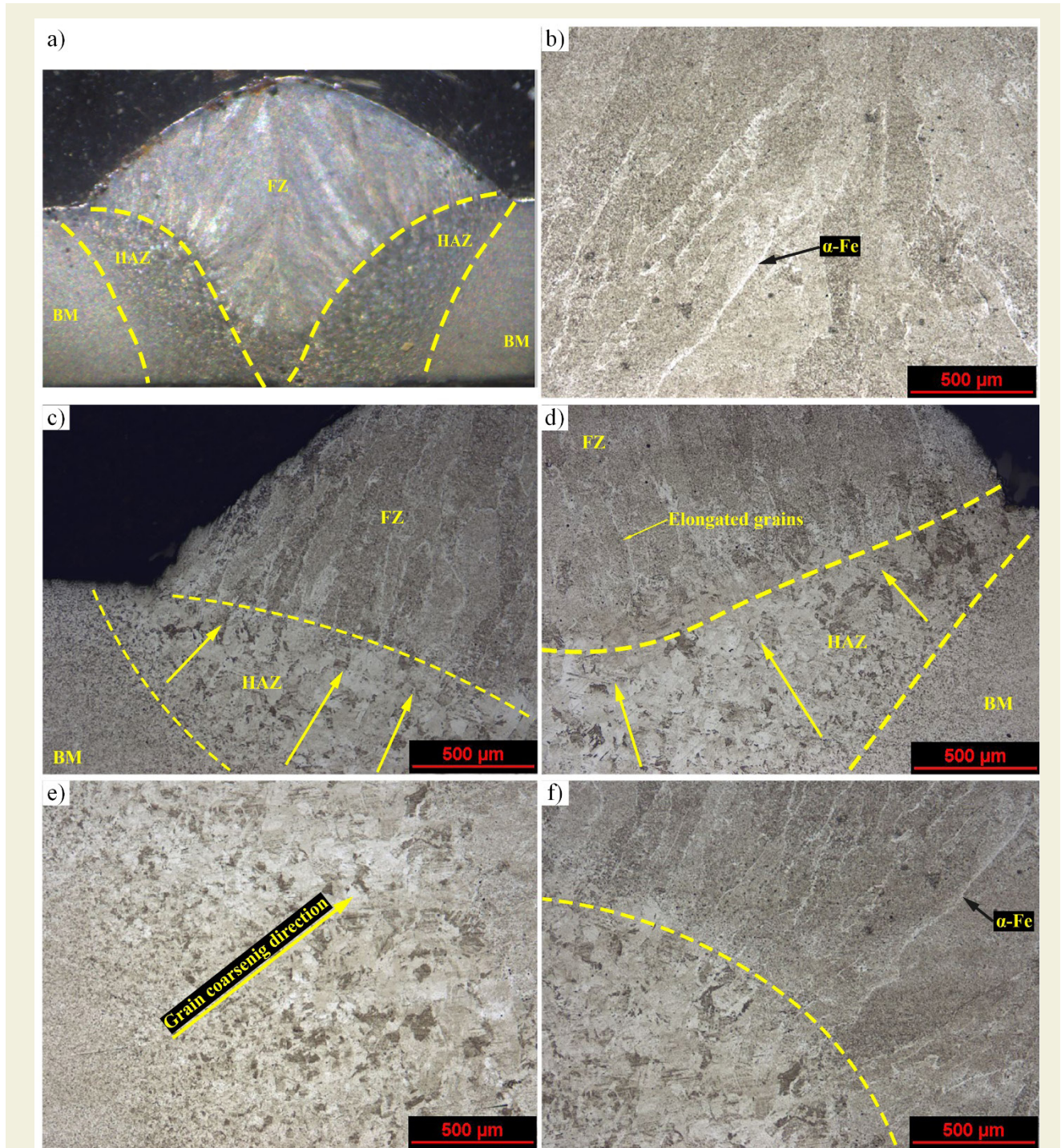
Figure 4. Micrographs of single-pulse MIG welded joints from different regions from; a) the whole joint macro image, b) FZ, c) Weld joint from left side, d) Weld joint from right side, e) HAZ, and f) HAZ/FZ interface
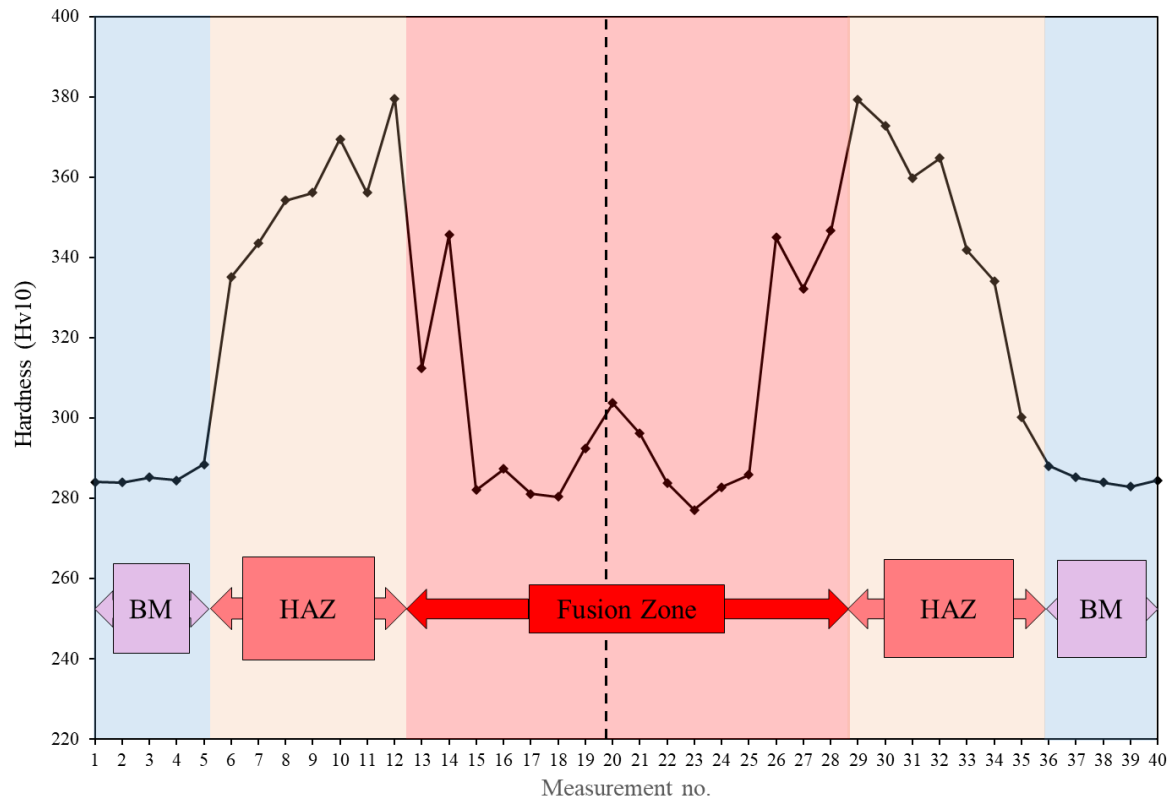
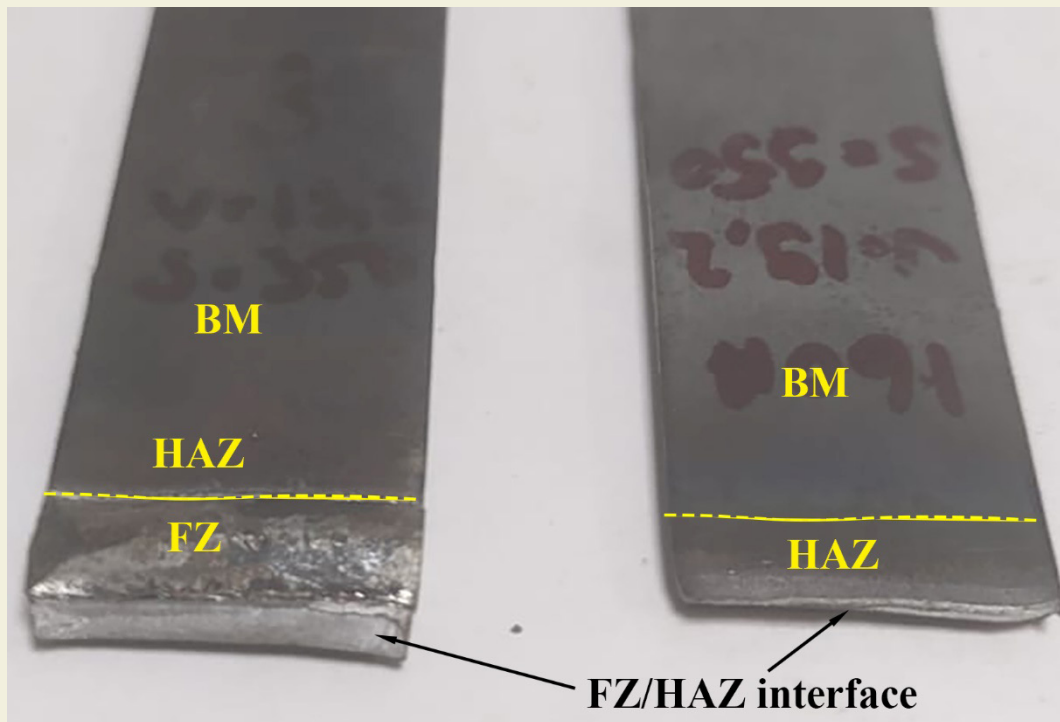**Figure 5.** Line hardness measurement of the single-pulse MIG welded joint.

Figure 6. Rupture surface of single-pulse MIG welded tensile specimen.

line of the FZ increased to 306 Hv10 due to the orientation of the grains. The grains formed in the FZ have followed the cooling path and formed a neutral axis in the middle of the FZ. The grains have joined through the neutral centerline.

The FZ consists of mostly bainitic and ferritic grains. The boundary of the grains is enveloped by α-ferrite as seen in Figure 4b. The bainitic formations are scattered through the α-ferrite matrix. Near the HAZ in FZ, the grains are refined, marking the boundary of the FZ. These refined grains increased the hardness at this location. Then, the hardness decreased in the FZ and exhibited a ductile structure due to scattered bainitic formations in the

ferrite matrix.

Figure 6 illustrates the rupture surface of a single-pulse MIG welded tensile specimen. The tensile specimens consistently separate from the FZ/HAZ interface. In other words, the FZ/HAZ interface represents the weakest point in the welded joint. This failure can be evaluated in terms of two factors. First, a significant hardness difference between the FZ/HAZ interface, creating a natural boundary between ductile and brittle structures. Second, the solidified grains follow the cooling direction, and the boundaries of the grains, surrounded by a soft α-ferrite, form a pathway for separation. Consequently, the entire welded tensile specimens become detached from the FZ/HAZ interface.

4. Conclusions

The Perform 700 steel sheets were successfully welded using single-pulse MIG method with SG-2 wire. The heat input has played a crucial role in determining the tensile strength. The main affecting factor is the degree of the heat input. The heat input degraded the bainitic BM into tempered martensite. The FZ/HAZ interface functioned as a boundary between hard highly tempered martensite and soft granular bainitic within the ferritic matrix. As a result, this natural boundary compromised the weakest point for the single-pulse welded joint. The locations of ruptures on the separation surfaces also confirm this weakness. The abrupt decrease in hardness from HAZ to FZ contributed to FZ/HAZ separations.

References

[1] Park, G.W., Park, M., Kim, B.J., Shin, S., Kim, H.C., Park, I.W., et al., (2022). Microstructure and mechanical properties of a gas-tungsten-arc-welded Fe-24Mn-3.5Cr-0.4C high manganese steel pipe using a Fe-22Mn-2.34Ni-0.38C welding wire. Materials Characterization. 194(11): 1–12. doi: 10.1016/j.matchar.2022.112469.

[2] Onar, V., (2022). Mechanical and Microstructural Characterizations of Resistance Spot Welded Dissimilar TWIP/304L Stainless Steel. Transactions of the Indian Institute of Metals. 75: 1731–1739. doi: 10.1007/s12666-021-02446-9.

[3] Kekik, M., Özen, F., Onar, V., Aslanlar, S., (2022). Investigation effect of resistance spot welding parameters on dissimilar DP-1000HF/CP800 steel joints. Sadhana - Academy Proceedings in Engineering Sciences. 47(4): 1–17. doi: 10.1007/s12046-022-01977-1.

[4] Bjorhovde, R., (2004). Development and use of high-performance steel. Journal of Constructional Steel Research. 60(3–5): 393–400. doi: 10.1016/S0143-974X(03)00118-4.

[5] Özsaraç, U., Onar, V., Özen, F., Aslanlar, Y.S., Akkaş, N., (2019). Effect of current and welding time on tensile-peel strength of resistance spot welded TWIP 1000 and martensitic steels. Indian Journal of Chemical Technology. 26(4): 248–51.

[6] Özsaraç, U., Onar, V., Özen, F., Aslanlar, Y.S., Akkaş, N., (2019). Effect of welding time on tensile-shear load in resistance spot welded TRIP 800 and microalloyed steels. Indian Journal of Chemical Technology. 26(4): 355–7.

[7] Lun, N., Saha, D.C., Macwan, A., Pan, H., Wang, L., Goodwin, F., et al., (2017). Microstructure and mechanical properties of fiber laser welded medium manganese TRIP steel. Materials and Design. 131: 450–9. doi: 10.1016/j.matdes.2017.06.037.

[8] Hong, S.-H., Eo, D.-R., Lee, S., Cho, J.-W., Kim, S.-J., (2023). Strong resistance to Zn-assisted liquid metal embrittlement of austenitic-TWIP/martensitic-HSLA multi-layered steel sheets additively manufactured by laser cladding. Acta Materialia. 258(March): 119224. doi: 10.1016/j.actamat.2023.119224.

[9] Shreyas, P., Panda, B., Vishwanatha, A.D., (2021). Embrittlement of hot-dip galvanized steel: A review. AIP Conference Proceedings, vol. 2317. p. 1–15.

[10] Phung, T.A., (2022). Experimental study on mechanical properties and microstructure of PERFORM 700 steel butt-welding joints using in high load-bearing structures. Journal of Science and Technique. 17(1): 53–63. doi: 10.56651/lqdtu.jst.v17.n01.301.

[11] Petronis, E., Cerwenka, G., Emmelmann, C., (2017). Hybrid laser-arc welding of steel S700MC butt joints under different sheet thickness.

[12] Silva, A., Szczucka-Lasota, B., Węgrzyn, T., Jurek, A., (2019). MAG welding of S700MC steel used in transport means with the operation of low arc welding method. Welding Technology Review. 91(3): 23–8. doi: 10.26628/wtr.v91i3.1043.

[13] Szymczak, T., Makowska, K., Kowalewski, Z.L., (2020). Influence of the welding process on the mechanical characteristics and fracture of the s700mc high strength steel under various types of loading. Materials. 13(22): 1–17. doi: 10.3390/ma13225249.

[14] Ferdinandov, N., Gospodinov, D., Ilieva, M., Radev, R., (2021). Influence of Weld Joint Preparation on the Mechanical Properties of High Strength Steel S700Mc Weldments. METAL 2021 - 30th Anniversary International Conference on Metallurgy and Materials, Conference Proceedings.: 441–6. doi: 10.37904/metal.2021.4149.

[15] Moravec, J., Sobotka, J., Novakova, I., Bukovska, S., (2021). Assessment the partial welding influences on fatigue life of s700mc steel fillet welds. Metals. 11(2): 1–16. doi: 10.3390/met11020334.

[16] Tomków, J., Świerczyńska, A., Landowski, M., Wolski, A., Rogalski, G., (2021). Bead-on-Plate Underwater Wet Welding on S700MC Steel. Advances in Science and Technology Research Journal. 15(3): 288–96. doi: 10.12913/22998624/140223.

[17] Schmidová, E., Bozkurt, F., Culek, B., Kumar, S., Kucharíková, L., Uhríčik, M., (2019). Influence of Welding on Dynamic Fracture Toughness of Strenx 700MC Steel. Metals. 9(5): 494. doi: 10.3390/met9050494.

[18] Kik, T., Górka, J., Kotarska, A., Poloczek, T., (2020). Numerical Verification of Tests on the Influence of the Imposed Thermal Cycles on the Structure and Properties of the S700MC Heat-Affected Zone. Metals. 10(7): 974. doi: 10.3390/met10070974.

[19] Kik, T., Moravec, J., Švec, M., (2020). Experiments and Numerical Simulations of the Annealing Temperature Influence on the Residual Stresses Level in S700MC Steel Welded Elements. Materials. 13(22): 5289. doi: 10.3390/ma13225289.

[20] Šebestová, H., Horník, P., Mrňa, L., Jambor, M., Horník, V., Pokorný, P., et al., (2020). Fatigue properties of laser and hybrid laser-TIG welds of thermo-mechanically rolled steels. Materials Science and Engineering: A. 772(December 2019): 138780. doi: 10.1016/j.msea.2019.138780.

[21] ONAR, V., (2020). Robotik MAG Kaynak Metodunda XAR 500 Serisi Çeliklerin Mikrosertliğine Farklı Kaynak Akımlarının ve

Hızlarının Etkisi. Düzce Üniversitesi Bilim ve Teknoloji Dergisi. 8(1): 1193–203. doi: 10.29130/dubited.646727.

[22] Fayazi Khanigi, A., Farnia, A., Ardestani, M., Torkamany, M.J., (2020). Microstructure and mechanical properties of low power pulsed Nd:YAG laser welded S700MC steel. Sadhana - Academy Proceedings in Engineering Sciences. 45(1): 1–13. doi: 10.1007/s12046-020-1279-6.

Baby cry-sensitive armband design for parents with hearing loss

Mustafa Kaan Baltacıoğlu [1*], Mustafa Tunahan Başar[2,3], Volkan Akdoğan[4], Muharrem Karaaslan[4], Emre Arda İlçigen[1]

[1]İskenderun Technical University, Engineering and Natural Sciences Faculty, Department of Mechatronics Engineering, Hatay, Türkiye
[2]İskenderun Technical University, Engineering and Natural Sciences Faculty, Department of Mechanical Engineering, Hatay, Türkiye
[3]Amasya University, Vocational School of Taşova Yüksel Akın, Department of Motor Vehicles and Transportation Technologies, Amasya, Türkiye
[4]İskenderun Technical University, Engineering and Natural Sciences Faculty, Department of Electrical Electronic Engineering, Hatay, Türkiye

Orcid: M. K. Baltacıoğlu (0000-0002-4082-902x), M. T. Başar (0000-0002-3108-8995), M. Karaaslan (0000-0003-0923-1959), V. Akdoğan (0000-0003-2219-2317), E. A. İlçigen (0009-0006-2883-6135)

Abstract: This study was carried out to design an armband for parents with hearing impairment or hearing loss. The study's main purpose is to design a warning system by taking advantage of the distribution of sounds at different intensity values and analyzing the quiet environment, speech sounds, and baby crying sounds in the propagation area. Sound analysis is carried out by collecting the data within the scope of the study and a vibration warning system is developed based on the analysis. Data is sent from the radio in the baby's room to the parent's armband via radio frequencies. The changes in sound data for a total of 20 seconds were analyzed. Based on these changes, it was determined that the amplitude of the silent environment was 600 delta, the speech sound environment was in the range of 1300-1600 delta and the baby crying sound could reach up to 1650 delta and above. It is seen that the speech sounds exhibit an increase of approximately 75% compared to the silent environment, while the changes in the baby crying sound increase by 102.5% compared to the silent environment. These increases indicate that the system can work effectively in wearable technologies.

Keywords: Hearing loss, healthy living, delta value, amplitude, wearable technology, vibration

1. Introduction

In today's world, wearable technologies have an important potential in critical issues such as providing instant patient follow-up, administering treatments, and minimizing misdiagnosis errors [1]. Over the years, the number of people with disabilities has increased with the increasing population. Out of every 1000 newborn children, 5.6 are born with hearing loss [2]. Depending on the living environment and environmental factors, this rate increases over time with the advancing age of individuals, leading to an increase in problems such as decreased hearing percentage, hearing loss, and severe hearing. In Turkey, more than 10 % of the population is thought to have hearing-related disorders [3]. Various technological devices such as listening and speech-to-text devices have been produced to minimize hearing problems[4]. On the user side, interest in wearable technology is increasing, especially in health, entertainment, and sports. In order to meet this interest, companies attach importance to wearable technology in their production. The wearable technology market is increasing day by day in line with the demands [5]. On the other hand, it is seen that the continuous use of these products by users is not wide-spread due to high costs. However, it is reported that if hearing impairment is not resolved, it will be a major economic problem in society. [6].¬Wearable technology is a circuit or software integrated into a piece of clothing or an accessory that an individual wears. Wearable technology ranges from hearing aids to smartwatches and wristbands. It can also be expressed as a kind of technology field that emerged and became widespread due to the desire of doctors to monitor the conditions of their patients for a long time [7]. As a result, wearable technology is the integration of technology with clothes that a person can wear or items that can be used as accessories. The common feature of wearable technology products is that they can process the data obtained from the external environment in a compact structure and transmit them in an ergonomic way. [8]. Foreseeing that wearable technology will become more important in the coming years, many research centers or manufacturers support polymer chemists, physicists, and textile engineers to produce new technologies related to the subject and to continue their studies. In addition, these studies enable the spread of e-medicine technology [9]. Wearable technology in the health sector sometimes causes

* Corresponding author.
Email: mkaan.baltacioglu@iste.edu.tr

difficulties on the patient side. Information such as how patients should use the device, what they should pay attention to, and what routine maintenance, if any, should be provided. Otherwise, there may be disruptions in the treatment processes of patients [10]. In this case, it shows the importance of integrating innovations in treatment methods with the developing technology for a healthy life. In this case, it reveals the necessity of realizing the designs of products that users are familiar with and can easily get used to over time.

With its increasing popularity in the fields of health and medicine, wearable technology is of great importance not only in terms of medical diagnosis but also in terms of treatment follow-up and management. Thanks to the developing wearable technology, data on patient health or condition can be monitored and analyzed in real-time. This also applies to the quality of life of the hearing impaired. Hearing aids, wearable devices, transcription of speech, and environmental sounds with different sensory inputs such as vibrations or light signals [11]. One of the main benefits of using wearable devices is to create devices that can enhance environmental sounds or create personalized sound profiles for the hearing impaired to understand speech more easily [12]. Researchers working on behalf of hearing-impaired individuals believe that vibrating wearable devices can be an important tool for hearing-impaired individuals. These devices enable the user to encode the incoming sound signals with different vibration patterns. According to the research, vibration on the user side leads to the most accurate results in terms of functionality and usability [13]. Various applications and technological devices are being developed to improve the quality of life of hearing-impaired individuals and to ensure their participation in social life. Such devices include hearing aids, cochlear implants, vibrating alarm clocks, fire alarm clocks, etc. Technological devices are also used in the education of hearing-impaired individuals. Video-telephone systems, sign language interpreters, and software-based hearing aids are among the main devices. These devices improve the quality of life of individuals and facilitate their participation in education and social life [14]. The aim of this study is to realize the design of an armband with an excitation system for hearing-impaired individuals by revealing the differences in sound depending on the characteristics of intensity and propagation changes. The detected sound is first divided into sound frames. Then, delta (spread) and decibel values are obtained from the obtained sound signal. After various amplification processes on the sound, the differences between the sound emissions are detected. It is reported that if a detected sound repeats, it can be checked whether there is a match with the sounds in the database [15-16]. The focus is on the development of a functional warning mechanism by sending a warning to the armband according to the sound characteristics obtained. In addition, the fact that sound signals are converted into a mechanical effect and thus offer a feasible and economical solution to a critical health problem such as hearing loss reveals the unique nature of the study.

2. Materials and Methods

In the study, an independent receiver circuit and a transmitter circuit design are realized and the ground is prepared for the sound signals to form the excitation signals. The calculations are analyzed in decibels of the perceived sound and the delta value is calculated from the changes between the maximum and minimum sound intensities in the environment instantaneously. Here, the delta values of the sound in the same time periods are examined when the ambient sounds in the environment are silent, in the environment with speech sound, and in the environment with baby crying sound. In the study, a transmitter (radio) environment and a receiver (armband) are defined. The general aim of the study is to create an excitation mechanism by converting the difference obtained from sound signals into a physical effect. However, the vibration motors preferred as the excitation mechanism here are very small and produce a vibration effect at levels that do not cause discomfort. The operation of the two vibration motors is directly proportional to the sound intensity. While a single vibration motor gives a warning at low-intensity baby crying (1650-1800 delta), double motors are activated at higher levels of baby crying (1800 delta and above), increasing the effect of vibration. In order for the radio and armband data transmission to be effective, the system aims to increase the interaction between the baby and the parent by creating vibration in direct proportion to the intensity of the sound level in both single and dual motors. Thus, the receiver-side stimulation process is successfully realized. No vibration effect occurs in the quiet environment defined in the system. However, one of the vibration motors is activated when speech or small sounds are detected. Finally, when the baby cries, both vibration motors are activated depending on the propagation range of the sound, and the receiver-side excitation process is clearly realized.

As shown in Figure 1, it is aimed to initiate wireless communication with the baby's crying among the sounds that the microphone detects from the environment, and if the baby is crying, with a low or loud cry. Then, if the baby is not crying, the microphone will continue to analyze the data of the sounds in the room. If the baby is crying, the vibration motors in the armband are activated depending on whether it is low or loud. In this way, the parent is notified that their baby is crying. In addition, the system can operate full-time thanks to the continuous data reading of the microphone.

In the study, wireless communication is provided with radio frequencies. In these criteria, the nRf24L01 module was preferred as the communication module. Depending on the frequency and thickness of the obstacles between the transmitter and receiver, data transmission can be provided in the range of 20-200 meters. It can operate with 3.3V and 4mA. In short, it is a module with very low power consumption. The transmitter module provides frequency transmission at 2.4GHz. The working principle of radio frequencies is that the frequency sent from
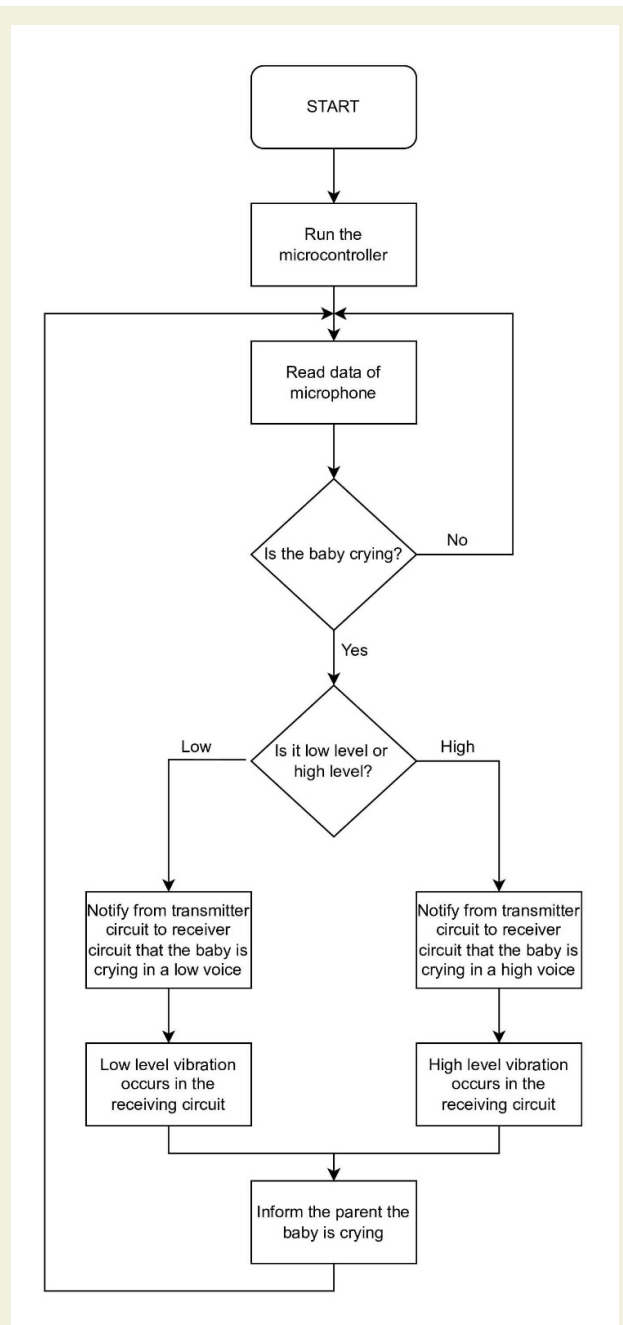
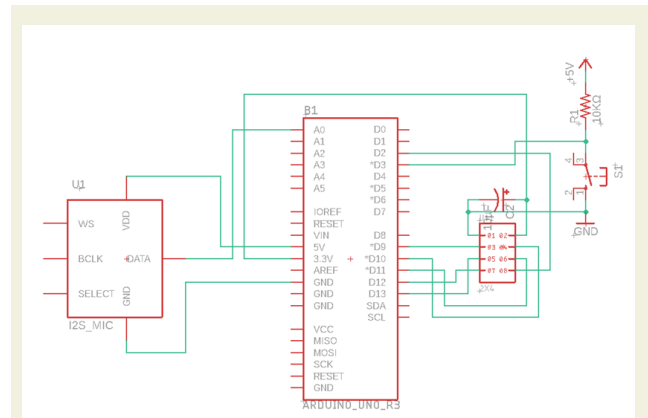**Figure 1.** Flow algorithm of the research

Figure 2. Transmitter circuit diagram

materials were emphasized in the design of the armband so that it can be worn and removed, battery replacement is easy and it has a size suitable for each person. In addition, the schematic representation of the electronically receiving circuit is shown in Figure 3. A 100 µF capacitor ensures that the receiver module works properly without fluctuations. 2 BJT type NPN transistors (BC547) are used to operate the vibration motors. Motor control is provided with the microcontroller triggering the transistors. The 5mm LED in the system is used for testing whether there is communication between the transmitter and receiver. In order to minimize interference during data transfer in the system, the system is mostly prepared by soldering instead of cable.
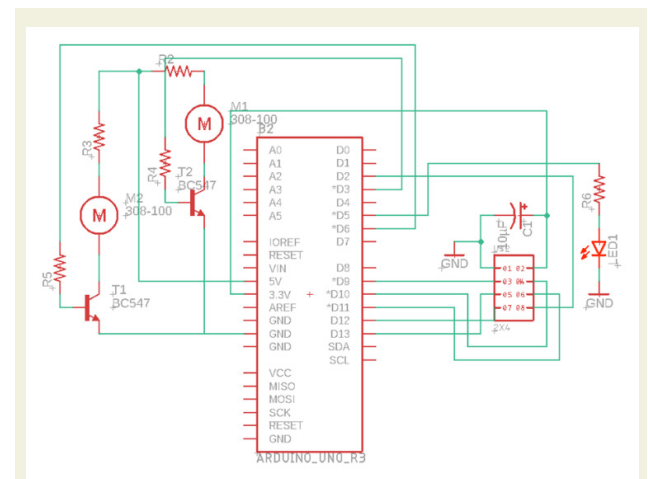

Figure 3. Receiver circuit diagram

the transmitter module is detected by the receiving module and the data is imported. In SPI protocol, the microcontroller performs serial communication over a single bus. The protocol works synchronously.

The circuit diagram of the transmitter medium is shown in Figure 2. A capacitor with a value of 100 µF is used for the transmitter module to receive a clean voltage without ripple. In order to minimize interference in data transmission, the system is generally prepared by soldering instead of wires. The stages of data transfer can be controlled by the button on the radio.

The small size of the modules will make it easier to integrate them into the receiving circuit (armband), and the weight of a few grams allows for ergonomic use. Elastic

Lithium-ion batteries are used to power the armband so that it does not run out of charge in a short time. A lithium-ion battery is 3.7V and the peak voltage can reach up to 4.2V. A 2500MAh battery was chosen for long-term charging of the armband. Thanks to the 2 lithium-ion batteries used in the series, it can easily supply the microcontroller, vibration motors, and nRF24L01.

There are various types of wireless communication. They have their own prominent features such as data transfer speed, range, and volume. In this study, the nRF24L01

module, which provides communication in SPI (serial peripheral interface) protocol with radio frequencies using a fast and cost-effective transceiver module within the domestic boundaries, was preferred. In addition to the economic advantages of this module, it is also advantageous in terms of ease of application.
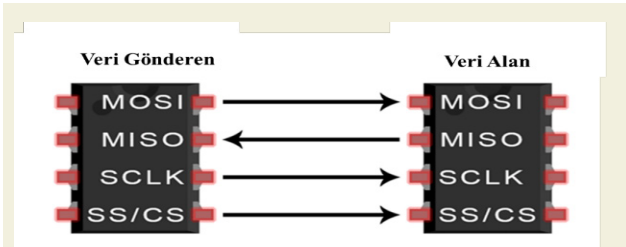

Figure 4. Pins and connections that enable communication between data sender and receiver

The module, which has 2 types with an internal antenna and an external antenna, can transfer data at a range of 20-25 meters inside the house in the tests performed. The 2.4 GHz frequency band wireless communication module requires only 3.3V voltage to operate. It provides 2 megabytes of data transfer per second. SPI protocol works as a transceiver (Figure 4).

As seen in Figure 5, the system basically consists of two components: the radio in the transmitting environment and the armband in the receiving environment. Here, the housing shell designs of the circuit designs were obtained using a 3D printer. Additionally, a design for the armband was made from materials (spandex) suitable for elastic wearable technology. The entire weight of the design attached to the arm here is 260 grams. This weight value aims to prevent fatigue or uncomfortable situations during long-term use. Finally, the vibration motors are integrated and fed simultaneously with the signals coming from the receiver circuit. In this way, it is aimed that one or two motors will work as a sleep mechanism depending on different environmental sounds.

3. Results and Discussion

After the designs determined within the scope of the study were realized, experimental studies were continued. Since the use of elastic materials is preferred in its

production, it is a successful output in terms of physical dimensions that a design that can adapt to arm sizes in different tolerances has been put forward. On the other hand, if cost analysis is performed, it seems that the high cost of device designs for sound perception in individuals with hearing impairment can be solved by developing physically stimulated systems.
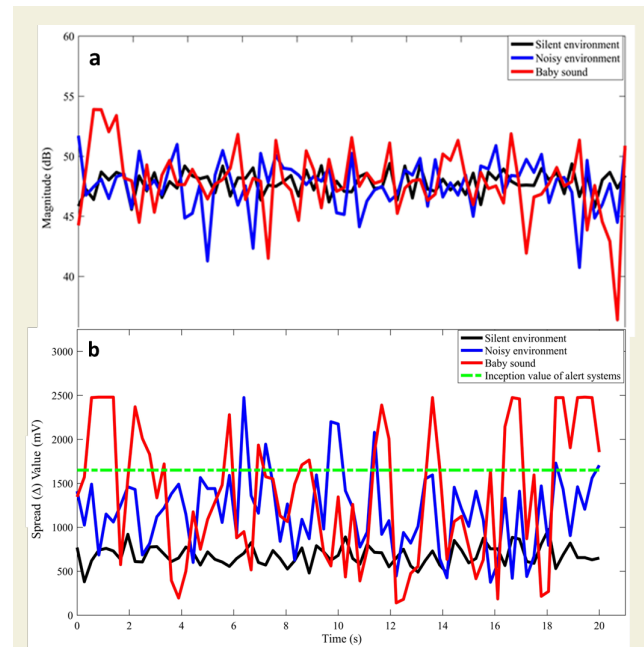

Figure 6. From different environments a) intensities b) propagation changes of sounds

Figure 6a shows the intensities of sound data from different environments. As can be seen here, the intensity range of the data obtained from the quiet environment is in the range of (45-48) dB. When the intensities of the noise values obtained from speech sounds are examined, it is seen that they increase up to 52 dB values. Finally, when the data obtained for baby crying are examined, it is determined that this value reaches even higher limits. It is also stated that these sound intensities are within reasonable ranges [17]. The microphone is located 50 cm from the sound source. Depending on this distance, it is thought that an increase in intensity values and differences between different ambient conditions may occur as it gets closer. In addition, it can be said that sufficient

Figure 5. Components of the designed armband

Mustafa Kaan Baltacıoğlu, Mustafa Tunahan Başar, Volkan Akdoğan, Muharrem Karaaslan, Emre Arda İlçigen

separation can be achieved for these measurement results to be an input in the excitation mechanism. In this context, a study investigating the ability of hearing-impaired individuals to listen to and understand music, it is aimed to develop systems with tactile vibration stimulation for the perception of the disabled individual by examining the frequency characteristics of different types of songs. It is stated here that these processes can be achieved up to certain limit values in the frequency range where sound effects can be transformed into vibration effects [18]. Similarly, in this study, the noise levels of sound effects were recorded within certain ranges. As can be seen, vibration effects can be transferred to the user depending on the sound exceeding certain intensity levels. The differences in sound intensities over the whole time interval show a regular pattern. Figure 6. b shows the variation between the maximum and minimum values of the sound values obtained from the propagation differences for detailed analysis. Sound measurements were taken at 20-second intervals in environments where sound continuity is maintained. In this context, the differences between the maximum and minimum values of the sound data are determined and presented in the graph obtained in Figure 6b. It is clearly seen that the quiet environment has the lowest change amplitude. However, it can be stated that speech sounds exhibit an increase of approximately 75% compared to the quiet environment. In addition, the changes in the baby crying sound show an increase of 102.5% compared to the quiet environment. When the change in the baby crying sound over time is analyzed, momentary silence phases are observed in the baby crying sound at 4 s, 12 s, 16 s, and 18 s values. It is noteworthy that dialog tones at time intervals of 6.3 s and 10 s produce noise at the same levels as the baby crying sounds. Considering that the sensor systems are in the environment where the baby is present, this shows that an excitation mechanism can be developed in the excitation system not only against crying sounds but also against other ambient noises. These changes show that differences can be transformed into reactive results by creating a warning system. In this context, the initial value of the alarm system designed is determined as 1650 millivolts as the limit value (the green line in the graph shows this limit value). When the detected sound value exceeds this limit value, the first vibration motor in the armband activates and gives a warning. When this level increases to 1800 milli volts, the second vibration motor is activated and the excitation mechanism is supported. In this way, in abnormal noise values that occur in the environment where the baby is located, solution approaches are put forward, especially for parents who have hearing problems. It is clearly seen that the proposed method can work successfully, especially at night or in the sleep sections as the quiet hours of the day.

4. Conclusion

The results obtained within the scope of the study prove that excitation mechanisms can be successfully devel-

oped by converting audio signals into mechanical effects. In this context, the transformation of sound data into a mechanical effect in an economical form expresses the original and innovative aspect of the study. Considering the elastic material design, a production that is quite suitable for daily use has been realized. If the cost analysis of the materials used is carried out, it seems possible to develop effectively and serve existing users. When the results obtained by analyzing the sound types are analyzed, it is seen that the baby crying sound provides approximately twice the amplitude increase compared to the quiet environment. It was determined that the baby's crying sound increased by 15.5% compared to the speech sound. In addition, the amount of increase in sound intensities also supports this situation. In addition to baby crying sounds, speech sounds near the baby, outdoor noises, etc. can be detected in accordance with the proposed method. Considering the cost analysis of the designs realized within the scope of the study, it is thought that 50% improvements can be achieved compared to their existing counterparts. In this case, it is necessary to develop similar studies to increase the widespread use of wearable technology products. In addition, in today's technology, where remote monitoring technologies in the health sector have increased so much, it is envisaged that information with different functional features can be provided to the user from the external environment. There is a need to develop studies that transform sound signals into vibratory stimulation mechanisms to solve the problems of disabled individuals. This study constitutes an example of how stimulation systems can be designed at very low economic costs, especially compared to similar applications. In fact, it is stated that it is important for wearable technology devices to be usable and accessible as well as being developed [19]. It is thought that the results obtained in this study can eliminate this deficiency if they are improved in terms of both providing economic conditions and being familiar to the user. It is stated that technologies with wearable vibration sources can be beneficial for hearing-impaired individuals, that products designed as prototypes can be converted into ergonomic use in line with certain development processes, and that the discrimination between society and disabled individuals can be reduced [20]. Therefore, the use of wearable vibration-stimulated systems may be beneficial for disabled individuals to complete their deficiencies in seeing their own needs, and it also has a very important potential in terms of their adaptation to social life. With the proposed method, a different perspective on mitigating the effects of a critical problem such as hearing impairment has been tried to be brought to the literature.

5. Acknowledgment

References

[1] Bonato, P. (2010). Advances in wearable technology and its medical applications. Annual International Conference of the IEEE Engineering in Medicine and Biology, Buenos Aires, Argentina, 2010, pp. 2021-2024, https://doi.org/10.1109/IEMBS.2010.5628037.

[2] Nagapoornima, P., Ramesh, A., Srilakshmi et al. Universal hearing screening. The Indian Journal of Pediatrics, 74, 545–549 (2007). https://doi.org/10.1007/s12098-007-0105-z

[3] Babaroğlu, A. (2017). Hearing Impaired Children in Turkey and Their Education. US-China Education Review, 7(1), 32-37. doi: 10.17265/2161-6248/2017.01.004

[4] Karmel, A., Sharma, A., & Garg, D. (2019). IoT based assistive device for deaf, dumb and blind people. Procedia Computer Science, 165, 259-269. https://doi.org/10.1016/j.procs.2020.01.080

[5] Kılıç, H. Ö. (2017). Giyilebilir teknoloji ürünleri pazarı ve kullanım alanları. Aksaray Üniversitesi İktisadi ve İdari Bilimler Fakültesi Dergisi, 9(4), 99-112.

[6] McDaid, D., Park, A. L., & Chadha, S. (2021). Estimating the global costs of hearing loss. International journal of audiology, 60(3), 162-170. https://doi.org/10.1080/14992027.2021.1883197

[7] Demirci, Ş. (2018). Giyilebilir Teknolojilerin Sağlık Hizmetlerine ve Sağlık Hizmet Kullanıcılarına Etkileri. Anemon Muş Alparslan Üniversitesi Sosyal Bilimler Dergisi, 6 (6), 985-992.

[8] Ajami, S., & Teimouri, F. (2015). Features and application of wearable biosensors in medical care. Journal of research in medical sciences: the official journal of Isfahan University of Medical Sciences, 20(12), 1208. https://doi.org/10.4103/1735-1995.172991.

[9] Yalçınkaya, B., & Yılmaz, D. (2011). Elektronik Tekstillerin, Tekstil Endüstrisindeki Yeri ve Giyilebilir Tekstilde Kullanılan İletken Lifler. Tekstil Teknolojileri Elektronik Dergisi, 5(1), 61-71.

[10] Koştı, G., Burmaoğlu, S. & Kıdak, L. B. (2021). Sağlık 4.0: sanayide öngörülen gelişimin sağlık sektörüne yansımaları. Hacettepe Sağlık İdaresi Dergisi, 24(3), 483-506 .

[11] Yağanoğlu, M., & Köse, C. (2018). Real-time detection of important sounds with a wearable vibration based device for hearing-impaired people. Electronics, 7(4), 50. https://doi.org/10.3390/electronics7040050

[12] Çiçek, M. (2015). Wearable technologies and its future applications. International Journal of Electrical, Electronics and Data Communication, 3(4), 45-50.

[13] Ebong, A., Chen, N., Unsur, V., Chowdhury, A., & Damiani, B. (2016). Innovative front grid design, four-streets and five-busbars (4S-5BB), for high efficiency industrial Al-BSF silicon solar cell. IEEE Electron Device Letters, 37(4), 459-462. https://doi.org/10.1109/LED.2016.2528048

[14] Yoon, C. H., Choi, S. H., Lee, H. J., Kang, H. J., & Kim, M. K. (2019). Predictive biomarkers for graft rejection in pig-to-non-human primate corneal xenotransplantation. Xenotransplantation, 26(4), e12515. https://doi.org/10.1111/xen.12515

[15] Zhang, Y., Shao, L., & Snoek, C. G. (2021). Repetitive activity counting by sight and sound. In Proceedings of the IEEE/CVF Conference on Computer Vision and Pattern Recognition, 14070-14079.

[16] Mouawad, P., Dubnov, T., & Dubnov, S. (2021). Robust detection of COVID-19 in cough sounds: using recurrence dynamics and variable Markov model. SN Computer Science, 2(1), 34. https://doi.org/10.1007/s42979-020-00422-6

[17] Doğan, H. & Çataltepe, Ö. A. (2018). Gürültünün İnsan Sağlığı Üzerine Etkileri. Sağlık ve Spor Bilimleri Dergisi, 1 (1) , 29-38.

[18] Alves Araujo, F., Lima Brasil, F., Candido Lima Santos, A., de Sousa Batista Junior, L., Pereira Fonseca Dutra, S., & Eduardo Coelho Freire Batista, C. (2017). Auris system: Providing vibrotactile feedback for hearing impaired population. BioMed research international, 2017. https://doi.org/10.1155/2017/2181380

[19] Moon, N. W., Baker, P. M., & Goughnour, K. (2019). Designing wearable technologies for users with disabilities: Accessibility, usability, and connectivity factors. Journal of Rehabilitation and Assistive Technologies Engineering, 6, 2055668319862137. https://doi.org/10.1177/2055668319862137

[20] Cavdir, D. (2022, June 9). Touch, Listen, (Re)Act: Co-designing Vibrotactile Wearable Instruments for Deaf and Hard of Hearing. NIME 2022. https://doi.org/10.21428/92fbeb44.b24043e8

Research Article

Determination of effects of some alcohol blends on performance, emission, mechanical vibration and noise in diesel engines

Nurullah Gültekin[1*], Halil Erdi Gülcan[2], Murat Ciniviz[2]

[1]Automotive Technology Program, Karamanoğlu Mehmetbey University, Türkiye
[2]Department of Mechanical Engineering, Selcuk University, Türkiye

Orcid: N. Gültekin (0000-0002-0139-1352), H. E. Gülcan (0000-0002-2328-5809), M. Ciniviz (0000-0003-3512-6730)

Abstract: The use of alcohol-derived fuels produced from renewable resources is an effective method to reduce dependence on petroleum. However, alcohols can improve the combustion process by changing the fuel chemistry. In this way, performance, emission, mechanical vibration and noise values can be improved in diesel engines. In this study; new fuel forms (D90E10, D90IB10, D80E10IB10, D77.5E10IB10DEE2.5, 75E10IB10DEE5) were formed by mixing ethanol, isobutanol and diethyl ether alcohols with diesel fuel in certain proportions. The fuels generated was used in experiments. The studies were conducted with four different loads (%25, 50, 75, and 100) at a constant speed (2800 rpm). The optimum fuel mixture was determined by examining the engine performance, exhaust emissions, mechanical vibrations and noise data obtained in the experiments. When the most important data output of the test results is evaluated; because D75E10IB10DEE5 fuel has a lot of oxygen in it and diethyl ether makes the cetane number go up, it was found that at full load, smoke emissions went down by 24.6% and mechanical vibrations went down by 14.2% compared to standard diesel fuel.

Keywords: Diesel engine, alcohol blends, performance, emissions, mechanical vibrations, noise.

1. Introduction

The majority of vehicles, which are indispensable to adapt to the fast flow of life, use petroleum-derived fuel. However, the limited amount of oil in the world threatens the future of vehicles. As a result, industries and academics are focusing on finding alternate energy sources. [1, 2]. This focus has led to a rise in the manufacture of electric vehicles in recent years. However, the inability to solve problems such as charging time, battery, and infrastructure of these vehicles stands as an obstacle to the transition to electric vehicles. Since it will take time to get over these challenges, internal combustion engines will be used for quite some time. [3-6]. Continuing the use of internal combustion engines requires solving the problems of these engines such as fuel, exhaust emissions, noise and vibration [7, 8]. The utilization of renewable biofuels, which can replace petroleum in internal combustion engines, is crucial for the resolution of these issues [9, 10]. The use of biodiesel, which is at the top of the biofuels, is widely used in diesel engines [11, 12]. In spark-ignition engines, the use of alcohol has become prominent. In addition, it is feasible to blend alcohols with diesel fuel and use the resulting mixture in diesel engines. This option is quite economical as it does not require significant modifications in diesel engines [13, 14].

When alcohols are introduced to diesel fuel, the fuel is changed, which has an impact on the combustion process. Improvements in engine performance, exhaust emissions, mechanical vibrations and noise emissions seem possible with the right choice of fuel mixtures [15]. Qudais et al. [16] investigated the impact of ethanol-diesel combination on engine performance and emissions. They determined that the optimum ethanol mixture is 20%. The researchers found a 7.5% increase in thermal efficiency and a 32% decrease in soot emissions with the ethanol mixture in the study. In another similar study, Bilgin et al. [17], conducted tests by adding ethanol to diesel fuel at volumetric ratios of 2%, 4%, and 6%. The trials revealed that 4% ethanol added to diesel fuel improved the engine's performance and efficiency. Mofijur et al.[18], in a review study on biodiesel-diesel-ethanol blends, stated that ethanol added to biodiesel-diesel blends reduced hydrocarbon, particulate matter, nitrogen oxide (HC, PM, NOx) and smoke emissions but slightly increased fuel consumption. In another experimental study examining alcohol blends, it was determined that the biodiesel-alcohol-diesel blend increased specific fuel consumption compared to pure diesel fuel. Additionally, it was found in the study that increasing the fuel's alcohol level increased the carbon dioxide (CO_2) and HC emis-

sions while lowering the NO emissions. Lujaji et al. [19] found in their study with croton oil-butanol-diesel fuel blends that mixtures containing butanol exhibited higher in-cylinder heat and pressure release rate. Datta and Mandalı [20], in their study with croton oil-butanol-diesel fuel mixtures, they found that mixtures containing butanol exhibited higher in-cylinder pressure and heat release rate. In the study, determined that the addition of ethanol and methanol improved engine efficiency. The maximum in-cylinder pressure and heat release rate increased when butanol-ethanol-methanol mixtures were used with diesel fuel, according to Emiroğlu and Şen [21]. Additionally, they found that the addition of alcohol reduced smoke and CO emissions while increasing NO emissions. In a numerical study similar to this study, Temizer et al. [38] They examined the effects of ethanol and diethyl ether added fuel on performance and emissions at different speeds. In the study, it was determined that NO emissions decreased with alcohol additives. Overall, when the studies were evaluated, it can be concluded that using alcohols in combination with diesel fuel affects exhaust emissions. Especially, the high oxygen content in alcohols contributes to a more efficient combustion process, leading to reduced emissions.

Another important problem of diesel engines is mechanical vibrations and noise emissions [22-24]. These problems negatively affect driving comfort and harm people and the environment [25, 26]. When examining the literature studies in this regard, it is evident that research on biodiesel fuels generally predominates. The research on fuels made of alcohol and diesel has been found to be sparse. Focusing on this issue, Taghizadeh-Alisaraei and Rezaei-Asl [27] looked examined the impact of various ethanol mixture ratios on engine performance and vibration. According to the study, the addition of ethanol caused an increase in engine torque and vibration. Morgul [28], who examined the effect of butanol-diesel

mixture on engine noise and vibration, determined that noise emissions decreased by 2-3 dBA and vibration values increased in his experiments with 10% butanol mixture. According to Karagöz [29], who investigated how introducing nanoparticles to the diesel-methanol combination affected engine vibration and noise, there was an increase in vibration and noise.

The main purpose of this research is to investigate the effects of alcohol fuels on the performance, emissions, mechanical vibration and noise emissions of the diesel engine. In line with this goal, an experimental study was carried out by applying different alcohol mixtures to diesel fuel. In the study; pure diesel (D100), 10% ethanol added diesel (D90E10), 10% isobutanol added diesel (D90IB10), 10% ethanol 10% isobutanol added diesel (D80E10IB10), 10% ethanol 10% isobutanol 2.5% diethyl ether added diesel (D77.5E10IB10DEE2.5) and 10% ethanol 10% isobutanol 5% diethyl ether added diesel (D75E10IB10DEE5) fuels were tested. The experiments were carried out at four different loads (25, 50, 75 and 100) and at a constant speed of 2800 rpm, which is the revolution at which the maximum torque occurs. In the tests, engine performance, exhaust emissions, mechanical vibrations and noise data were recorded and analyzed.

2. Material and Method

Figure 1 depicts the constructed system's schematic view. In the system; ANTOR AD320 model single-cylinder diesel engine, 49.3 kW ABB brand dynamometer for loading the engine, Bosch BEA 60-70 emission devices for emission measurements, fuel measurement system, PCE-VD3 vibration device was used to measure mechanical vibrations and GERATECH DT 8820 model noise device was used to measure engine noise values. The computer was wired to the vibration device, which was mounted to the engine's cylinder head. The device is capable of measuring
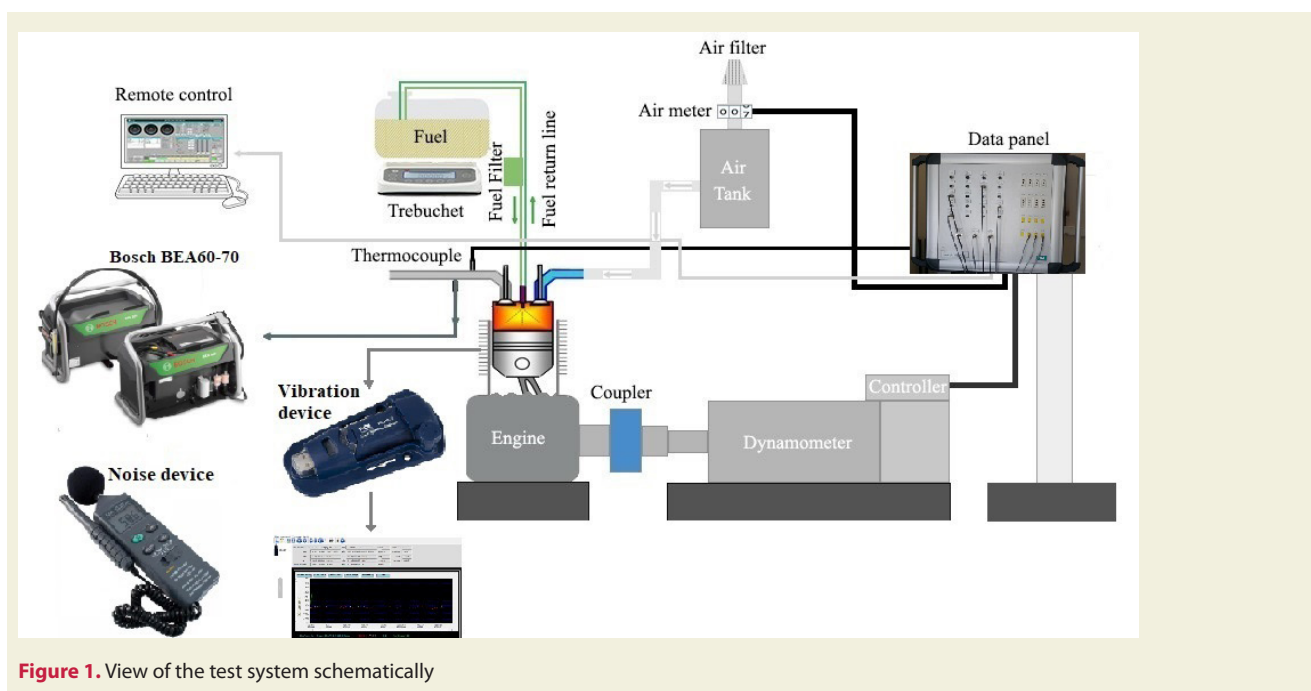

Figure 1. View of the test system schematically

in 3 axes (x, y, z) and can record data at 500 ms intervals through the computer interface, enabling the calculation of average values. The noise device determines values in decibels dB(A). Noise measurements were recorded according to ISO 362-1:2007 standard at a distance of 1.0 meter from the noise source [23].

2.1. Test Fuels

Table 1 lists the physical and chemical characteristics of the fuels utilized in the studies. The volumetric mixing ratios of the fuels are shown in Table 2. Mixture ratios of ethanol and isobutanol were determined based on literature review. However, the study of diethyl ether additive addition of these fuels is limited in the literature.

Table 1. Test fuels physical and chemical specialties [30, 31, 43-45].

Properties	Diesel	Ethanol	Isobutanol	Diethyl ether
Mol. formula	C_nH_m	C_2H_5OH	C_4H_9OH	$C_4H_{10}O$
Mol. wt. (Kg/kmol)	185-212	46.06	74.1	74.12
Density (kg/m³)	830-840	788	800-810	713
Cetane num.	45-52	5-15	-	128
Lower heating value (kJ/kg)	42500	26400	33000	36850
Viscosity at 40°C (m/s²)	0.0027	0.00012	0.0022	0.00023

Table 2. Volumetric fuel mixture ratios.

Fuel	Diesel (%)	Ethanol (%)	Isobutanol (%)	Diethyl ether (%)
D100	100	-	-	-
D90E10	90	10	-	-
D90IB10	90	-	10	-
D80E10IB10	80	10	10	-
D77.5E10IB10DEE2.5	77.5	10	10	2.5
D75E10IB10DEE5	75	10	10	5

Table 3 lists the experimental parameters. The tests were carried out at a constant speed of 2800 rpm with four different loads (2.7, 5.4, 8.1, and 10.8 Nm).

The full load (100%) of the AD320 model engine with mechanical fuel injector is determined to be 10.8 Nm. In preliminary tests, the motor can slightly exceed this load. However, due to the engine being air-cooled and considering the long duration of the experiments, 10.8 Nm load is set as the full load. Other loads are scaled based on this value. Prior to the experiments, preliminary tests were conducted to bring the engine to suitable operating conditions. During the operation, the engine was supported with a fan to maintain its temperature balance. Each test was repeated three times to reduce the error rates in the trials and the difference between the values remained below 3%.

Table 3. Experimental test procedure.

Engine Speed (rpm)	Engine Load (%)	Fuels
2800	25	D100
		D90E10
		D90IB10
		D80E10IB10
		D77.5E10IB10DEE2.5
		D75E10IB10DEE5
	50	D100
		D90E10
		D90IB10
		D80E10IB10
		D77.5E10IB10DEE2.5
		D75E10IB10DEE5
	75	D100
		D90E10
		D90IB10
		D80E10IB10
		D77.5E10IB10DEE2.5
		D75E10IB10DEE5
	100	D100
		D90E10
		D90IB10
		D80E10IB10
		D77.5E10IB10DEE2.5
		D75E10IB10DEE5

2.2. Test Engine

To perform the fuel tests, Figure 2 ANTOR AD 320 model single-cylinder CI engine, shown in. and technical specifications given in Table 4., was used.

Table 4. Engine specifications [34].

Brand/Model	ANTOR / AD 320
Number of cylinders	1
Cylinder volume	315 cm³
Cylinder diameter	78 mm
Stroke	66 mm
Compression ratio	17,5/1
Engine speed	3600 rpm
Max. torque	13.8 @2800 rpm
Crankcase oil capacity	1,2 lt
Injection timing	20 [°CA bTDC]
Injection pressure	220 [Bar]

2.3. Uncertainty analysis

The methods developed by Kline and McClintock have been widely employed for doing uncertainty analysis on test results due to their ability to yield more exact out-

Figure 2. Test Engine.

comes. The uncertainty analyses of the calculated parameters were established by employing equation (1), as presented below [39,40]

$$W_R = \left[\left(\frac{\partial R}{\partial x_1} w_1 \right)^2 + \left(\frac{\partial R}{\partial x_2} w_2 \right)^2 + \left(\frac{\partial R}{\partial x_3} w_3 \right)^2 + \cdots + \left(\frac{\partial R}{\partial x_n} w_n \right)^2 \right]^{1/2} \quad (1)$$

Here; R represents the size to be measured or calculated, $x_1, x_2, x_3 \ldots x_n$ represents n independent variables affecting the size, $w_1, w_1, w_1, \ldots w_n$ represents the error rates for each independent variable, and W_R represents the total uncertainty of the magnitude of R.

3. Result and Discussion

3.1. Break thermal efficiency (BTE)

In internal combustion engines, thermal efficiency is an important evaluation criterion. The most significant factors affecting thermal efficiency are engine design and fuel chemistry. Changes in engine design require time and cost, whereas fuel changes are simpler. The thermal efficiencies of the fuels formed in Figure 3 at four different loads are given.
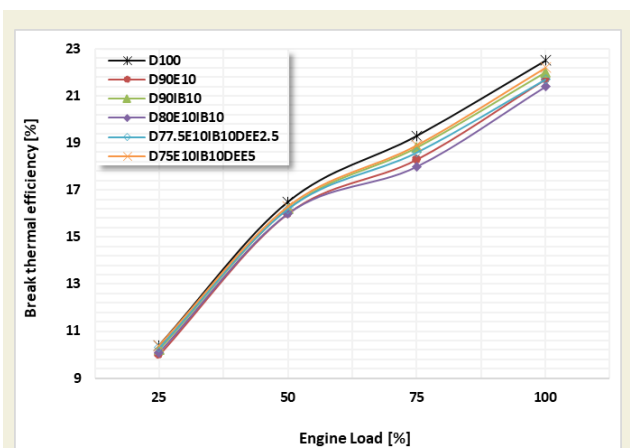
Figure 3. The calculated thermal efficiencies of fuels at 2800 rpm and various loads.

In parallel with the increase in load, the quality of com-

bustion increased and increased the thermal efficiency. However, it was discovered that increasing the ethanol and isobutanol component of the fuel reduces the thermal efficiency. The main reason for this situation is that the heating values of alcohols are lower than diesel fuel. It was also found that the addition of diethyl ether caused a slight increase in thermal efficiency. With the addition of diethyl ether, the cetane number of the fuel increased, positively affecting the combustion efficiency.

3.2. Brake specific fuel consumption (BSFC)

A reduction in Brake Specific Fuel Consumption (BSFC) is desirable in internal combustion engines. However, especially in diesel engines, exhaust emissions have become more crucial than fuel consumption in recent years. Figure 4 shows the BSFC of the fuels at different loads. Table 4 illustrates the comparison of the used fuels with the standard diesel fuel, presented as a percentage. An upward arrow indicates an increase, while a downward arrow indicates a decrease.
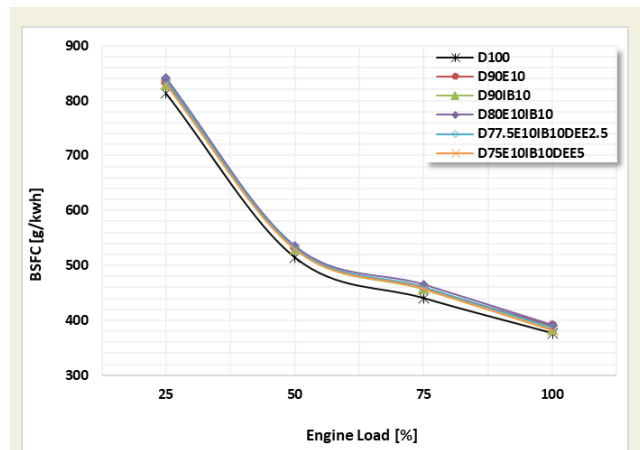

Figure 4. BSFC of fuels used at 2800 rpm and different loads.

As can be clearly seen in Table 6, the addition of ethanol and isobutanol increased the BSFC. The addition of diethyl ether to the mixture prevented the increase of BSFC somewhat. The reason for the increase in BSFC with increasing alcohol content in the fuel is the lower heating value of alcohols.

3.3. HC emissions

The basic fuel of internal combustion engines consists of hydrogen and carbon atoms. For this reason, incomplete combustion causes these atoms to be ejected from the exhaust without burning. Reducing HC emissions is an indication that fuel energy is used more efficiently [41]. Figure 5 shows the HC values of the fuels used at different loads. Table 7 shows the comparison of standard diesel and fuels used.

As seen in Table 7, HC emissions increased by 20% at full load when using D80E10IB10 fuel. In the use of D75E10IB10DEE5 fuel at the same load, there was a 5% increase in HC emissions compared to pure diesel fuel. In line with these results, it can be concluded that the ad-
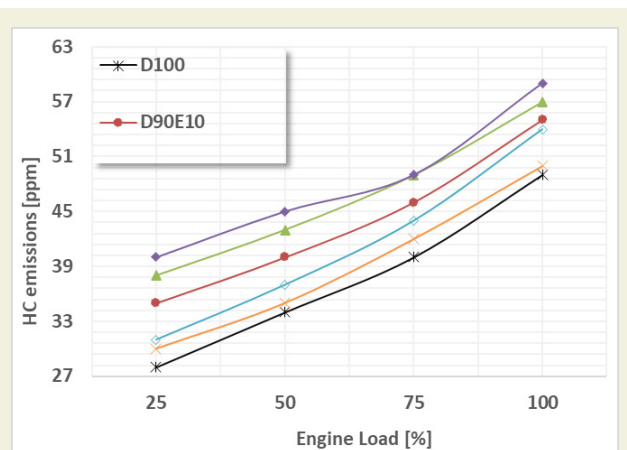
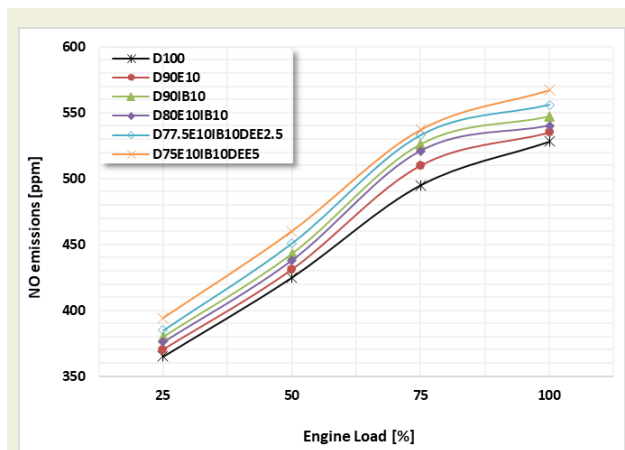**Figure 5.** HC emissions measured at 2800 rpm and different loads

Figure 6. NO emissions measured at 2800 rpm and different loads

dition of ethanol and isobutanol increases HC emissions. it was also determined that the addition of diethyl ether decreased the HC emissions. The high cetane number of diethyl ether increases the cetane number of the mixture and causes a decrease in HC emissions.

3.4. NO emissions

In diesel engines, one of the significant emission issues is NO emissions [42]. Additional systems are being implemented in diesel engines to reduce these emissions. These systems negatively affect the engine performance and cannot work well for a long time. Figure 6 shows the NO values of the fuels used at different loads. Table 8 shows the comparison of the fuels used with the standard diesel.

As seen in Table 8, NO emissions rose as the alcohol concentration of the fuel increased. These experimental re-

sults are consistent with findings to other studies in the literature [32, 33]. The main reason for the increase in NO emissions is the low calorific value of alcohols. This increases the amount of fuel delivered to the cylinder as well as the temperature inside the cylinder. As a result, BSFC and NO emissions increase.

3.5. Smoke emissions

In diesel engines, another important emission is smoke emissions. Therefore, exhaust emission measurements focus on smoke emissions. The main cause of smoke emissions is the carbon atoms present in the fuel. Alcohols, due to their lower carbon atom count and the presence of oxygen, result in more efficient combustion, leading to a reduction in smoke emissions. Figure 7 illustrates the measured smoke emissions in the experiments. Table 9 shows the comparison of alcohol-blended fuels with the standard diesel fuel.

Table 6. BSFC change rates of the generated fuels compared to standard diesel.

Engine speed	Engine load (%)	D100 (g/kwh)	D90E10	D90IB10	D80E10IB10	D77.5E10IB10DEE2.5	D75E10IB10DEE5
2800 rpm	25	813	2.45%	1.97%	3.44%	2.83%	1.97%
	50	514	3.5%	3.11%	4%	3.5%	2.92%
	75	440	4.3%	3.86%	5.68%	4.55%	3.86%
	100	376	3.7%	2.12%	3.99%	2.66%	1.33%

Table 7. HC change rates of generated fuels compared to standard diesel

Engine speed	Engine load (%)	D100 (ppm)	D90E10	D90IB10	D80E10IB10	D77.5E10IB10DEE2.5	D75E10IB10DEE5
2800 rpm	25	28	25%	35%	42%	10%	7%
	50	34	17%	26%	32%	8%	3%
	75	40	15%	22%	22%	10%	5%
	100	49	12%	3.6%	20%	10%	2%

Table 8. NO change rates of generated fuels compared to standard diesel

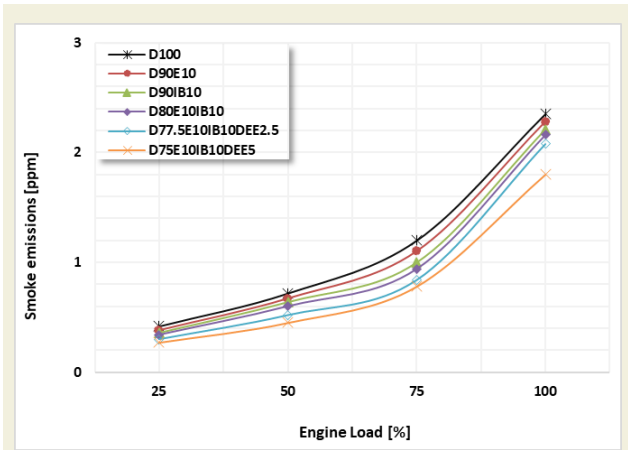| Engine speed	Engine load (%)	D100 (ppm)	D90E10	D90IB10	D80E10IB10	D77.5E10IB10DEE2.5	D75E10IB10DEE5
2800 rpm	25	365	1.37%	4.1%	3%	5.48%	7.94%
	50	425	1.41%	4.23%	3%	6.1%	8.23%
	75	495	3%	6.26%	5.25%	7.67%	8.48%
	100	528	1.32%	3.6%	2.27%	5.3%	7.38%

Figure 7. Smoke emissions measured at 2800 rpm and different loads

The addition of ethanol and isobutanol has resulted in a decrease in smoke emissions. Furthermore, the addition of diethyl ether has further contributed to the reduction of smoke emissions. The high-octane number of diethyl ether is the primary reason for this effect.

3.6. Mechanical vibrations

Since diesel engines have a high compression ratio, their end-of-combustion pressures are higher than those of spark-ignition engines. This causes diesel engines to generate a higher vibration. High vibration is undesirable for users and the engine. In Figure 8, the average vibration values occurring in the tests of fuels are shown as g (m/s^2). Table 10 shows the comparison of the generated fuel blends' vibration values with the standard diesel fuel.

The addition of ethanol and isobutanol has resulted in an average decrease of 4.4% in vibration values. Increasing the proportion of diethyl ether has been effective in

reducing vibrations, providing a 12.2% decrease at full load. The high setan number of diethyl ether allowed the D75E10IB10DEE5 fuel to achieve minimum vibration values.
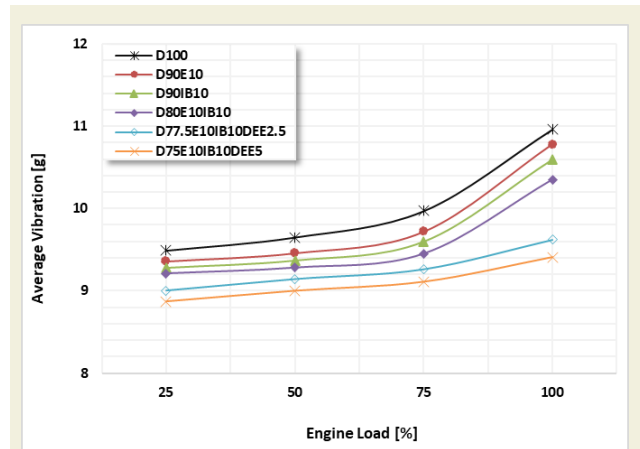
Figure 8. Mechanical vibrations measured at 2800 rpm and different loads

3.7. Noise

In diesel engines, noise caused by high cylinder pressure is an undesirable condition due to its negative effects. Furthermore, noise emissions must be restricted due to their negative influence on the environment and human health. Figure 9 shows the noise values obtained during the tests. Table 11 compares the noise levels of alcohol-blended fuels with the standard diesel fuel.

It was discovered that as the alcohol component in the fuel mixture increased, the noise levels decreased. It was determined that the addition of ethanol and isobutanol

Table 9. Smoke emissions change rates of generated fuels compared to standard diesel

Engine speed	Engine load (%)	D100 (ppm)	D90E10	D90IB10	D80E10IB10	D77.5E10IB10DEE2.5	D75E10IB10DEE5
2800 rpm	25	0.42	9.53%	14.3%	19%	28.5%	36%
	50	0.72	7%	10.12%	17%	27.8%	37.5%
	75	1.2	8.4%	16.7%	22%	30%	35%
	100	2.35	3%	6%	8%	21.5%	24.6%

Table 10. Change rates of mechanical vibrations of the generated fuels according to the standard diesel

Engine speed	Engine load (%)	D100 (g)	D90E10	D90IB10	D80E10IB10	D77.5E10IB10DEE2.5	D75E10IB10DEE5
2800 rpm	25	9.49	1.4%	2.8%	3%	5.2%	6.55%
	50	9.65	2%	3%	3.85%	5.3%	6.5%
	75	9.97	2.5%	3.7%	5.2%	7.2%	8.7%
	100	10.96	1.65%	3.3%	5.7%	12.3%	14.2%

Table 11. Noise change rates of the generated fuels compared to standard diesel

Engine speed	Engine load (%)	D100 (dBA)	D90E10	D90IB10	D77.5E10IB10DEE2.5	D75E10IB10DEE5
2800 rpm	25	100.9	0.2	0.3	1.1	1.4
	50	101.1	0.1	0.3	1	1.3
	75	101.3	0.2	0.3	1.1	1.4
	100	101.9	0.2	0.4	1.3	1.6

reduced noise emissions by 0.7 dBA at full load. In addition, although the diethyl ether ratio is low, it has been found to be more successful in reducing noise values. It was determined that the noise emissions were reduced by 1.7 dBA with the addition of 5% diethyl ether at full load. Increasing the cetane number of the fuel with diethyl ether additive reduced the knocking process and reduced vibration and noise emissions.
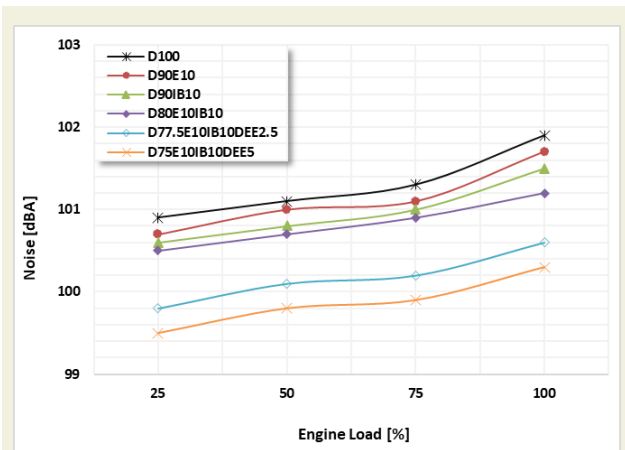

Figure 9. Noise measured at 2800 rpm and different loads

4. Conclusion

Different alcohol mixtures; When the data obtained in this study, which examined the effects on engine performance, exhaust emissions, mechanical vibrations and noise, the following results were determined.

- The increase in alcohol rates reduced thermal efficiency. This drop has been determined to be less at low loads and more at high loads.
- An increase in the alcohol blending ratio has reduced the thermal efficiency. However, the addition of diethyl ether has somewhat mitigated this decrease in thermal efficiency.
- NO emissions obtained from alcohol-blended fuel tests are higher than those from standard diesel fuel. This is due to the higher fuel injection resulting from the lower calorific values of the blends. The experimental results are in line with the studies in the literature [37,38].
- It has been found that alcohols are effective in reducing smoke emissions. At half load (50%), D75E10IB10DEE5 fuel has shown a 37.5% reduction in soot emissions compared to standard diesel. These results are supported by studies in the literature [35,36].
- Increasing the alcohol percentage effectively reduces mechanical vibrations. When compared to ethanol and isobutanol blends, the addition of diethyl ether was found to be more successful in minimizing mechanical vibrations.
- The use of alcohols has been effective in reducing noise emissions. It has been determined that diethyl ether is the most effective alcohol in reducing noise emissions.
- Future research could contribute to the usage of alcohols in diesel engines by exploring the effects of different alcohol blends and motor changes on engine performance.

5. Acknowledgment

References

[1] Gültekin, N., Mayda, M., & Kilit, M. (2017). Benzin ve Dizel Motorlarda Devir Sayısının Titreşime Olan Etkisinin İncelenmesi. Bitlis Eren Üniversitesi Fen Bilimleri Dergisi, 6(2), 39-43.

[2] Gürbüz, H., & Demirtürk, S. (2020). Investigation of dual-fuel combustion by different port injection fuels (Neat Ethanol and E85) in a DE95 diesel/ethanol blend fueled compression ignition engine. Journal of Energy Resources Technology, 142(12), 122306.

[3] Shafiee, S., & Topal, E. (2008, June). An overview of fossil fuel reserve depletion time. In 31st IAEE International Conference, Istanbul (pp. 18-20).

[4] Ediger, V. Ş. (2019). An integrated review and analysis of multi-energy transition from fossil fuels to renewables. Energy Procedia, 156, 2-6.

[5] Cook, P. J. (2022). Resources and reserves in a carbon-constrained world. Mineral Economics, 35(3-4), 361-371.

[6] Yang, Y., Liu, Z., Saydaliev, H. B., & Iqbal, S. (2022). Economic impact of crude oil supply disruption on social welfare losses and strategic petroleum reserves. Resources Policy, 77, 102689.

[7] Gurbuz, H. (2020). The effect of H2 purity on the combustion, performance, emissions and energy costs in an SI engine. Thermal Science, 24(1 Part A), 37-49.

[8] Cinar, C., Uyumaz, A., Solmaz, H., Sahin, F., Polat, S., & Yilmaz, E. (2015). Effects of intake air temperature on combustion, performance and emission characteristics of a HCCI engine fueled with the blends of 20% n-heptane and 80% isooctane fuels. Fuel Processing Technology, 130, 275-281.

[9] Agarwal, A. K. (2007). Biofuels (alcohols and biodiesel) applications as fuels for internal combustion engines. Progress in energy and combustion science, 33(3), 233-271.

[10] Vergel, O. A., Cárdenas, D., García-Contreras, R., & Mata, C. (2020). Bioethanol-Diesel Blends Used in Diesel Engines and Vehicles under Transient Operation. Bioethanol Technologies.

[11] Örs, İ., Sarıkoç, S., Atabani, A. E., & Ünalan, S. (2019). Experimental investigation of effects on performance, emissions and combustion parameters of biodiesel–diesel–butanol blends in a direct-injection CI engine. Biofuels.

[12] Örs, I., Sarıkoç, S., Atabani, A. E., Ünalan, S., & Akansu, S. O. (2018). The effects on performance, combustion and emission characteristics of DICI engine fuelled with TiO2 nanoparticles addition in diesel/biodiesel/n-butanol blends. Fuel, 234, 177-188.

[13] Chao, M. R., Lin, T. C., Chao, H. R., Chang, F. H., & Chen, C. B. (2001). Effects of methanol-containing additive on emission characteristics from a heavy-duty diesel engine. Science of the

Total Environment, 279(1-3), 167-179.

[14] Yilmaz, N., & Davis, S. M. (2016). Polycyclic aromatic hydrocarbon (PAH) formation in a diesel engine fueled with diesel, biodiesel and biodiesel/n-butanol blends. Fuel, 181, 729-740.

[15] Yao, C., Cheung, C. S., Cheng, C., Wang, Y., Chan, T. L., & Lee, S. C. (2008). Effect of diesel/methanol compound combustion on diesel engine combustion and emissions. Energy conversion and management, 49(6), 1696-1704.

[16] Abu-Qudais, M., Haddad, O., & Qudaisat, M. (2000). The effect of alcohol fumigation on diesel engine performance and emissions. Energy conversion and management, 41(4), 389-399.

[17] Bilgin, A., Durgun, O., & Sahin, Z. (2002). The effects of diesel-ethanol blends on diesel engine performance. Energy sources, 24(5), 431-440.

[18] Mofijur, M., Rasul, M. G., & Hyde, J. J. P. E. (2015). Recent developments on internal combustion engine performance and emissions fuelled with biodiesel-diesel-ethanol blends. Procedia Engineering, 105, 658-664.

[19] Lujaji, F., Kristóf, L., Bereczky, A., & Mbarawa, M. (2011). Experimental investigation of fuel properties, engine performance, combustion and emissions of blends containing croton oil, butanol, and diesel on a CI engine. Fuel, 90(2), 505-510.

[20] Datta, A., & Mandal, B. K. (2016). Impact of alcohol addition to diesel on the performance combustion and emissions of a compression ignition engine. Applied thermal engineering, 98, 670-682.

[21] Emiroğlu, A. O., & Şen, M. (2018). Combustion, performance and emission characteristics of various alcohol blends in a single cylinder diesel engine. Fuel, 212, 34-40.

[22] Redel-Macías, M. D., Pinzi, S., Babaie, M., Zare, A., Cubero-Atienza, A., & Dorado, M. P. (2021). Bibliometric studies on emissions from diesel engines running on alcohol/diesel fuel blends. A case study about noise emissions. Processes, 9(4), 623.

[23] Zaman, Ç., Topgül, T., & Sarıdemir, S. (2022). İçten Yanmalı Motorlu Bir Taşıtta Titreşim ve Gürültünün Deneysel Olarak Belirlenmesi. Gazi University Journal of Science Part C: Design and Technology, 10(2), 230-241.

[24] Topgül, T. O. L. G. A., SARIDEMİR, S., & Zaman, Ç. (2020). Tek Nokta Enjeksiyonlu Buji ile Ateşlemeli Bir Motorda Motor Devri ve Yükünün Motor Titreşimleri ve Gürültüye Etkisinin Deneysel İncelenmesi. Düzce Üniversitesi Bilim ve Teknoloji Dergisi, 8(3), 1948-1956.

[25] Sharma, N., Patel, C., Tiwari, N., & Agarwal, A. K. (2019). Experimental investigations of noise and vibration characteristics of gasoline-methanol blend fuelled gasoline direct injection engine and their relationship with combustion characteristics. Applied Thermal Engineering, 158, 113754.

[26] Taghizadeh-Alisaraei, A., Ghobadian, B., Tavakoli-Hashjin, T., & Mohtasebi, S. S. (2012). Vibration analysis of a diesel engine using biodiesel and petrodiesel fuel blends. fuel, 102, 414-422.

[27] Taghizadeh-Alisaraei, A., & Rezaei-Asl, A. (2016). The effect of added ethanol to diesel fuel on performance, vibration, combustion and knocking of a CI engine. Fuel, 185, 718-733.

[28] Morgul, O. K. (2021). Experimental analysis for assessing noise and vibration of the diesel engine fuelled with a butanol–diesel blend under different injection pressures and engine speeds. International Journal of Environmental Science and Technology, 18(7), 2019-2030.

[29] Karagöz, M. (2020). Dizel-Metanol-Nanopartikül ile Çalışan Bir Dizel Motorda Titreşim ve Gürültü Değişimlerinin İncelenmesi. Düzce Üniversitesi Bilim ve Teknoloji Dergisi, 8(3), 1995-2004.

[30] Kumar, B. R., & Saravanan, S. (2016). Use of higher alcohol biofuels in diesel engines: A review. Renewable and Sustainable Energy Reviews, 60, 84-115.

[31] Zheng, Z., Li, C., Liu, H., Zhang, Y., Zhong, X., & Yao, M. (2015). Experimental study on diesel conventional and low temperature combustion by fueling four isomers of butanol. Fuel, 141, 109-119.

[32] Kolhe, A. V., Malwe, P. D., Chopkar, Y., Panchal, H., Ağbulut, Ü., Mubarak, N. M., ... & Amesho, K. T. (2023). Performance analysis of biofuel–ethanol blends in diesel engine and its validation with computational fluid dynamics. Environmental Science and Pollution Research, 1-21.

[33] Krishnan, M. G., Rajkumar, S., Thangaraja, J., & Devarajan, Y. (2023). Exploring the synergistic potential of higher alcohols and biodiesel in blended and dual fuel combustion modes in diesel engines: A comprehensive review. Sustainable Chemistry and Pharmacy, 35, 101180.

[34] https://anadolumotor.com/uploads/teknik-olculer/antor-ad-320.pdf

[35] Qi, D. H., Chen, H., Geng, L. M., & Bian, Y. Z. (2011). Effect of diethyl ether and ethanol additives on the combustion and emission characteristics of biodiesel-diesel blended fuel engine. Renewable energy, 36(4), 1252-1258.

[35] Patnaik, P. P., Jena, S. P., Acharya, S. K., & Das, H. C. (2017). Effect of FeCl3 and diethyl ether as additives on compression ignition engine emissions. Sustainable Environment Research, 27(3), 154-161.

[36] Banapurmath, N. R., Khandal, S. V., Swamy, R. L., & Chandrashekar, T. (2015). Alcohol (ethanol and diethyl ethyl ether)-diesel blended fuels for diesel engine applications-a feasible solution. Advances in Automobile Engineering, 4(1), 1-8.

[37] Paul, A., Bose, P. K., Panua, R., & Debroy, D. (2015). Study of performance and emission characteristics of a single cylinder CI engine using diethyl ether and ethanol blends. Journal of the energy institute, 88(1), 1-10.

[38] Temizer, I., Gücer, F., & Cihan, Ö. (2022). A numerical approach in the investigation of the effects of diethyl ether and ethanol mixtures on combustion characteristics and NO emissions in a DI diesel engine. European Mechanical Science, 6(2), 110-118.

[39] FIRAT, M., Altun, Ş., Mutlu, O. K. C. U., & Varol, Y. (2021). Bir RCCI motorun yanma ve egzoz emisyon karakteristikleri üzerinde benzin ön karışım oranı ve motor yükünün etkisinin incelenmesi. Gazi Üniversitesi Mühendislik Mimarlık Fakültesi Dergisi, 37(1), 541-554.

[40] Gülcan, H. E., & Ciniviz, M. (2023). The effect of pure methane energy fraction on combustion performance, energy analysis and environmental-economic cost indicators in a single-cylinder common rail methane-diesel dual fuel engine. Applied Thermal Engineering, 230, 120712.

[41] Gulcan, H. E., & Ciniviz, M. (2023). Experimental study on the effect of piston bowl geometry on the combustion performance and pollutant emissions of methane-diesel common rail dual-fuel engine. Fuel, 345, 128175.

[42] Gülcan, H. E., Gültekin, N., & Ciniviz, M. (2022). The Effect of Methanol-Dodecanol Addition on Performance and Smoke Emission in a CI Engine with Diesel Fuel. International Journal of Automotive Science And Technology, 6(2), 207-213.

[43] Kumar, B. R., & Saravanan, S. (2016). Use of higher alcohol biofuels in diesel engines: A review. Renewable and Sustainable

Energy Reviews, 60, 84-115.

[44] Karabektas, M., & Hosoz, M. (2009). Performance and emission characteristics of a diesel engine using isobutanol–diesel fuel blends. Renewable Energy, 34(6), 1554-1559.

[45] Ibrahim, A. (2016). Investigating the effect of using diethyl ether as a fuel additive on diesel engine performance and combustion. Applied Thermal Engineering, 107, 853-862.

Stress concentration factor based design curves for cylinder-cylinder connections in pressure vessels

Murat Bozkurt[1]*, David Nash[2]

[1]Department of Mechanical Engineering, İstanbul University – Cerrahpaşa
[2]Department of Mechanical and Aerospace Engineering, University of Strathclyde

Abstract: The results of the parametric analysis of the cylinder-cylinder intersections in pressure vessels, performed in both elastic and plastic regions, are discussed in this study. Besides, the outcomes that contribute to the development of classical solutions in the literature are addressed as design curves depending on stress concentration factors (SCF). To begin with, the maximum stresses for cylinder-cylinder connections were calculated by finite element analysis, and SCF values were obtained. In these calculations, external local loads acting on the nozzle center and internal pressure are the main variables for loading conditions. Following that, different parametric approaches and loading conditions are presented to develop design curves for cylinder/cylinder connections by changing the main geometric parameters, such as cylinder and nozzle radii, and their thicknesses. A new approach is presented using these new curves thus allowing industrial designers to calculate maximum nozzle stresses without the need to undertake a thorough finite element analysis.

Keywords: Pressure Vessel, Stress Concentration Factors, Nozzle, FEA, Design Curves

1. Introduction

There is a significant difference in difficulty between analyzing sphere/cylinder intersections and cylinder/cylinder geometry in pressure vessel problems. The literature presents a number of theoretical solutions; however, until now, none have been implemented into an industrial code of practice, since these contain assumptions and restrictions that can impose severe limitations on the solutions. For instance, when it is desired to calculate the SCF for a cylindrical vessel-nozzle connection, the existing calculation approach for the spherical vessel-nozzle connection could be used. [1]. There are some applications where sphere/cylinder models are used to determine hoop stresses in cylinder/cylinder models. In one approach, it is ensured that the remote membrane stress occurring on the sphere is equalized to the cylindrical container hoop stress. Another approach states that the radius of the cylindrical container should be 1.5 times smaller than the radius of the spherical container [2]. Stress distributions in cylinder/nozzle connections, however, are quite different from those obtained for sphere/nozzle connections once detailed stress distributions are obtained. Taking all this into account, it is considered necessary to provide designers with stress concentration factor design curves that contain several geometric parameters that can be easily accessed and directly provide physically representative solutions in the analysis of cylinder/cylinder problems.

Kharat et al. [3] obtained stress concentration factors originating from nozzle combinations in their study. The authors, using the finite element method to find the SCF, have used different computational approaches in the literature for the reliability of the results. A comparison case study is presented by changing parameters such as radius and wall thickness for the nozzle-vessel junction under constant internal pressure. As a result, it was observed that the results of FEA and the results obtained from the experimental data largely overlapped. Apart from that, this study also discusses how conservative the equations developed by Money [4], Moffat [5,6], Mershone [7], Peterson, Lind [8], and Decock [9] are in calculating SCF.

Kihiu et al. [10], worked on cylinders with cross holes to calculate the SCF values. The main parameter considered here was the chamfer angle and length. In addition, the authors examined the thickness and radius ratios that created SCF values for these various combinations. As a result, the authors presented optimum chamfer angle values, which is helpful in those cases.

Mukhtar [11], on the other hand, carried out a comprehensive SCF assessment for 150 cases in nozzle-vessel connections. The authors developed a functional dimensionless expression for basic geometry ratios. In this way, they provided an improvement for the traditional empirical expression derivation. In addition, the limitations of

---

the widely used *p*-SCF charts and their significant differences in certain points according to the cases examined are noted.

Besides, Gerdeen [12] used thin-walled vessels with side holes and crossholes to calculate the SCF. The main parameters for the SCF in the study were the ratio of the outside diameter to the hole diameter (outside diameter-to-bore diameter) and the ratio of the hole diameter to the bore diameter-to-sidehole diameter. This study is also useful as it includes shear effects in the solutions, which were neglected in previous studies. The obtained results were confirmed by comparing them with the experimental data in the literature.

In his study, Moffat [5] conducted a study to develop an equation for calculating the effective stress factor (ESF). Therefore, existing design curves are combined with experimental data, internal pressure loading, and external moment loading. Here the author used the term ESF to avoid confusion, as the term stress intensity factor (SIF) has a different definition, especially in piping systems and fracture mechanics. The results obtained are in accordance with ASME III rules, FEA results, and additional test results. In their other study [6], Moffat et al. tried to generate a correlation equation on the ESF results for cylinder-cylinder connections under internal pressure. The produced Effective Stress Factor magnitudes are well above the values obtained from the Finite Element Analysis calculation, and therefore ESF obtained can only be used with some confidence for the stress magnitudes of the crotch corner.

Nziu and Masu [13] tried to optimally determine the position of circular cross holes in thick-walled vessels. For this purpose, cross-drilled vessels for variable offset positions were examined. Thickness ratios were kept between 1.4 – 3.0. The results clearly demonstrate the variation of SCF with an offset of circular holes. With these SCF values, it is stated that the optimum offset value will be 0.9 for the specified ranges.

Moreover, Makulsawatudom et al.[14] reveal SCF values for thick cylindrical containers with circular and elliptical cross holes in their work. The main problem here is the way the holes intersect (plain, chamfered, and blend radiused).

In addition to these studies, Kharat and Kulkarni[15] categorize the studies on the stress intensity factors occurring in the pressure vessel openings and put forward a review article for the literature. Although the studies discussed are limited in number, they have been a guide for researchers who want to have information about the literature.

In this study, SCF values for a β coefficient determined depending on the problem type were obtained according to the parameters t/T, dm/Dm, D/T, di/Di, and Dp/dm. These curves for internal pressure, external loading, and pad reinforcement serve as an alternative guide for researchers [16].

2. The Curve-Generating Process For Nozzle-Cylinder Connection Problems

The estimation of the maximum stress is the most crucial stage in determining the stress concentration variables. The opening where the nozzle is penetrated is the area where the stress concentration is most intense. Therefore, in the nozzle/cylinder junction areas, the inner crotch wall is where potentially the highest stress is expected under internal pressure loading conditions. On the other hand, estimations cannot be made about the maximum stress location and stress distributions for nozzle/cylinder connections without determining the direction and magnitude of the applied force at nozzle centripetal external loadings. In their earlier work [16, 17, 18], the authors validated the finite element model linked to the aforementioned scenarios. Due to this, solutions from finite element analysis are used in this section to compute the maximum stress belonging to external local loads and inner pressure. Also, the results are taken into account independent of the stress locations such as crotch corner or nozzle wall, etc. Outcomes are provided in the following SCFs:

SCF = (Maximum calculated stress in cylinder) / (membrane stress).

The membrane stress is PD/2T for internal pressure loading and V/2πrt for external local loading. The maximum stress values are taken from the FEA results.

At first, internal pressure loading conditions in nozzle-cylinder connections are examined under various parameters, and design curves are created. Reinforcement plate application will not be included in this section. The effect of the pad reinforcement is then looked at thereafter. Design curves for external local loads are generated in the third stage. Using the proper attachment parameter - *β*, all of these SCF data are shown.

Bijlaard's work will be taken as basis for attachment parameter-β. Basically, appropriate geometric parameters are recommended for nozzle and cylindrical connections according to the nozzle type (Round Attachment, Square Attachment). Since the subject of this study is cylinder-cylinder connections, the Round Attachment parameter was used. The most important parameters affecting the maximum stress in cylinder-cylinder intersection problems are the radii of the main cylinder and the nozzle. For this reason, the ratio of these two expressions provides the designer with the opportunity to easily examine the SCF with a dimensionless geometric parameter. In this context, in the following subheadings, SCF values will be calculated according to the appropriate β parameter and design curves will be created.

2.1. Design Curve Generation for Nozzle-Cylinder Junction Under Internal Pressure Loading

In that section, a cylinder of a prescribed finite size is taken into account. In other words, the cylinder diameter and wall thickness remain constant through all analyses. Nozzle thickness and diameter are variables in this analysis.

As can be seen in Figure 1, curves for 13 different di/Di ratios are plotted. The curves consist of SCF results for ten different t/T ratios. t/T values start from 0.2 and continue up to 2.0 with a constant increment of 0.2 units. The lowest t/T is also associated with the highest SCF. Some points for t/T variations are marked on the di/Di=0.728 curve in Figure 1. Additionally, since the diameter of the cylinder is fixed and the diameter of the nozzle is variable, the Attachment Parameter is represented as in the equation.

$$\beta = \frac{0.875 d_o}{D_m} \qquad \textbf{Equation 1}$$

When Figure 1 is examined, it will be seen that the increase in di/Di causes an increase in SCF for the same t/T ratios. In addition, when each curve is evaluated within itself, it is noteworthy that the increase in t/T values follows a parabolic decrease in SCF. When the di/Di ratio drops below 0.25, this parabolic downtrend becomes a more linear downtrend.

Another scenario that has been considered uses t/T as the primary variable. The proposed curves range from t/T = 0.25 to 2.50 and advance by 0.25 steps for each curve. Each point on the curves indicates the change in di/Di in this case when Di and T values are fixed. SCF values were acquired for a total of 11 separate di/Di ratios throughout the creation of each curve, with a 0.05 rise in the ratios at each point. In Figure 2, generated curves are displayed.

As shown in Figure 2, di/Di values start from 0.1 and continue up to 0.6 in increments of 0.05. Considering that the shell diameter remains constant, an increase in nozzle diameter also causes an increase in SCF values. Otherwise, SCF values decrease when t/T increases because the increased nozzle wall thickness has a positive effect on strength.

In the third case, different parameters are used to regulate the t/T change. In any case, the dm/Dm value is equivalent to the t/T value. A total of 9 different t/T cases are considered in this case. It should also be noted that the shell wall thickness (T) is constant, and variations are created to change the nozzle wall thickness (t). The SCF data from 5 distinct analyses are used to draw each curve. Each of these points represents the scenario where D/T starts from 10 and continues up to 50 in 10 increments. The outcomes are displayed in Figure 3.

According to Figure 3, each case's SCF curves follow the same general trend. However, as t/T grows, dm/Dm will expand at the same pace, resulting in a nozzle opening that nearly exceeds the 0.5 shell's diameter. Since the maximum stress will rise as a result, S.C.F values also have a tendency to rise dramatically.
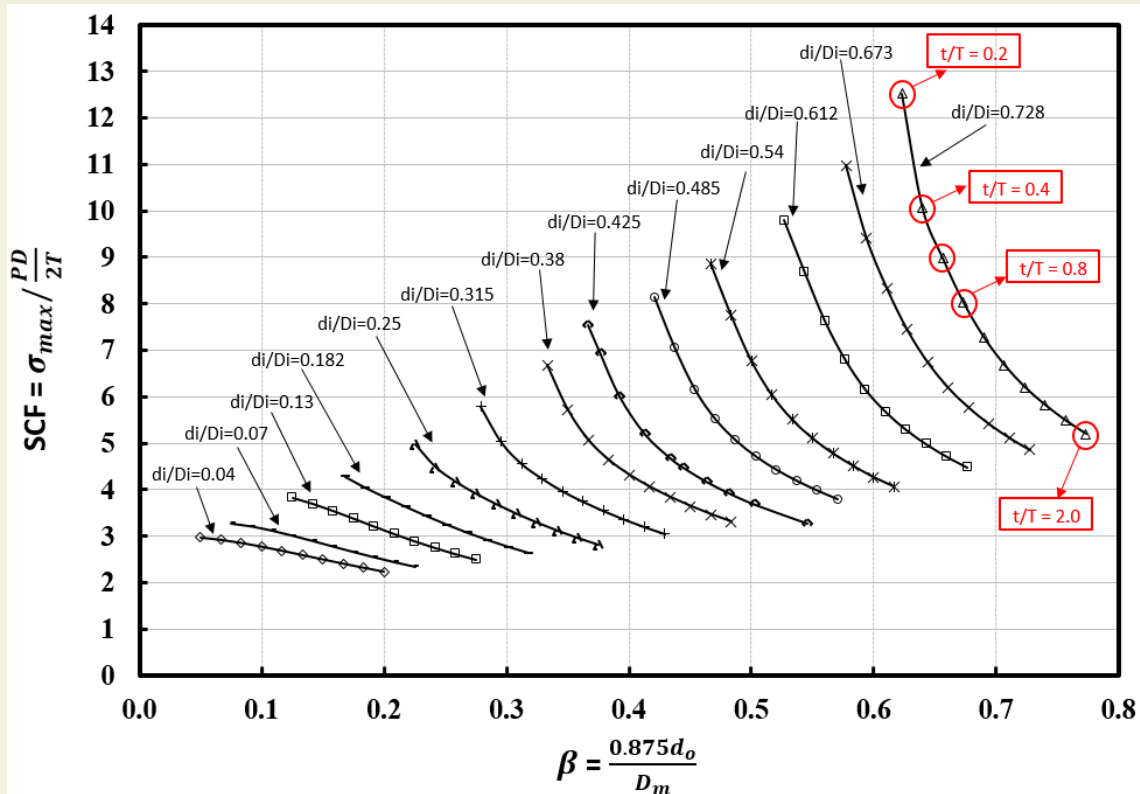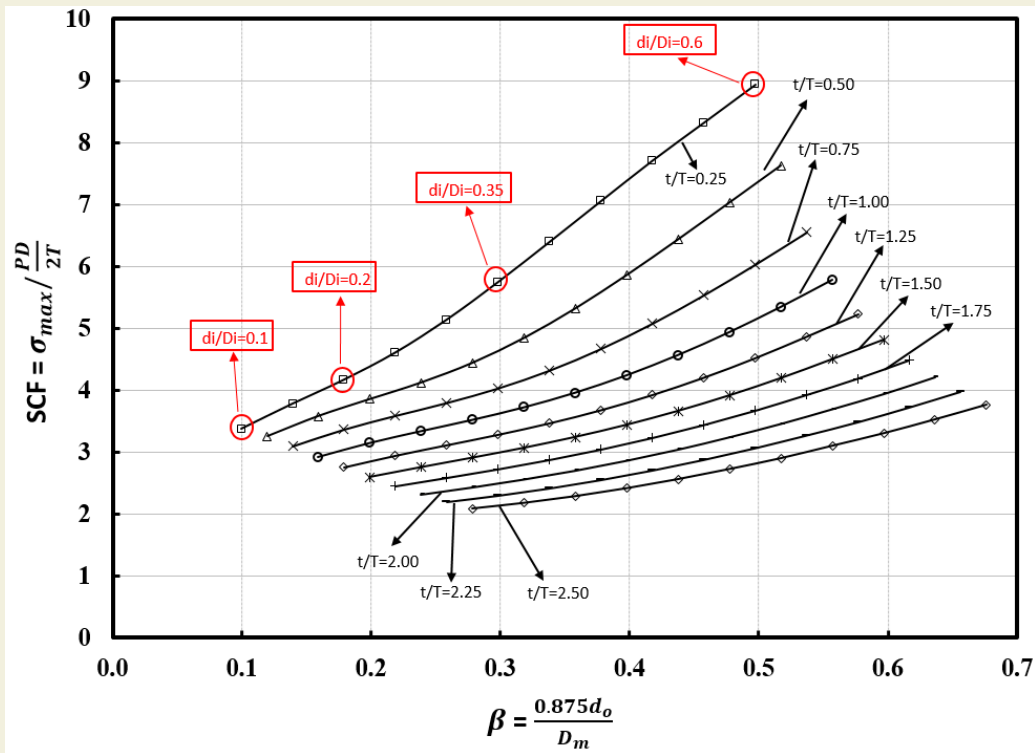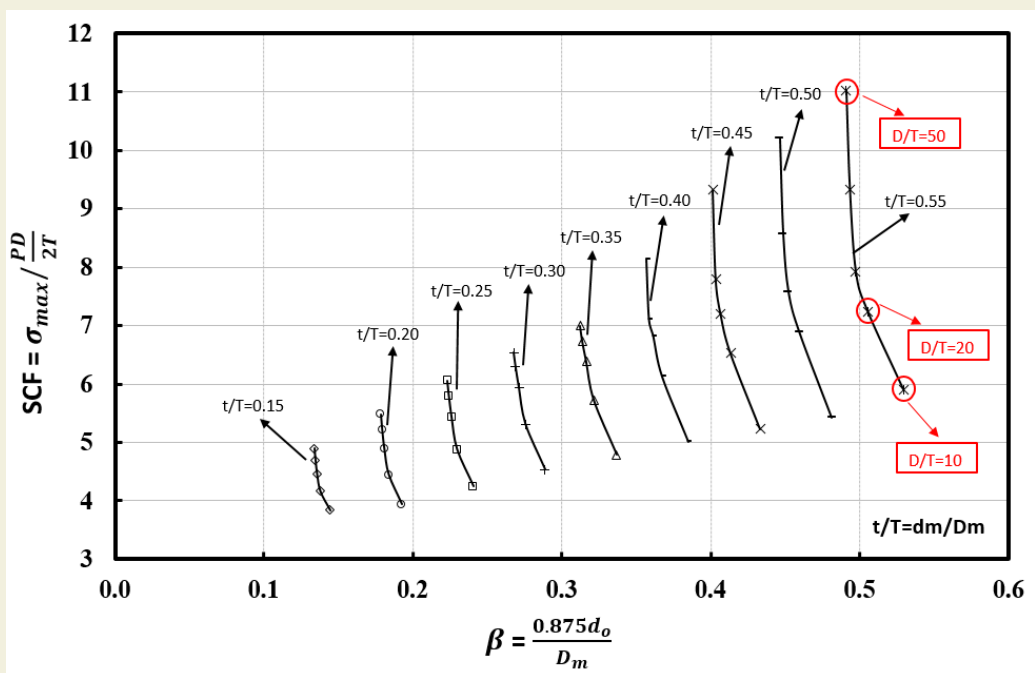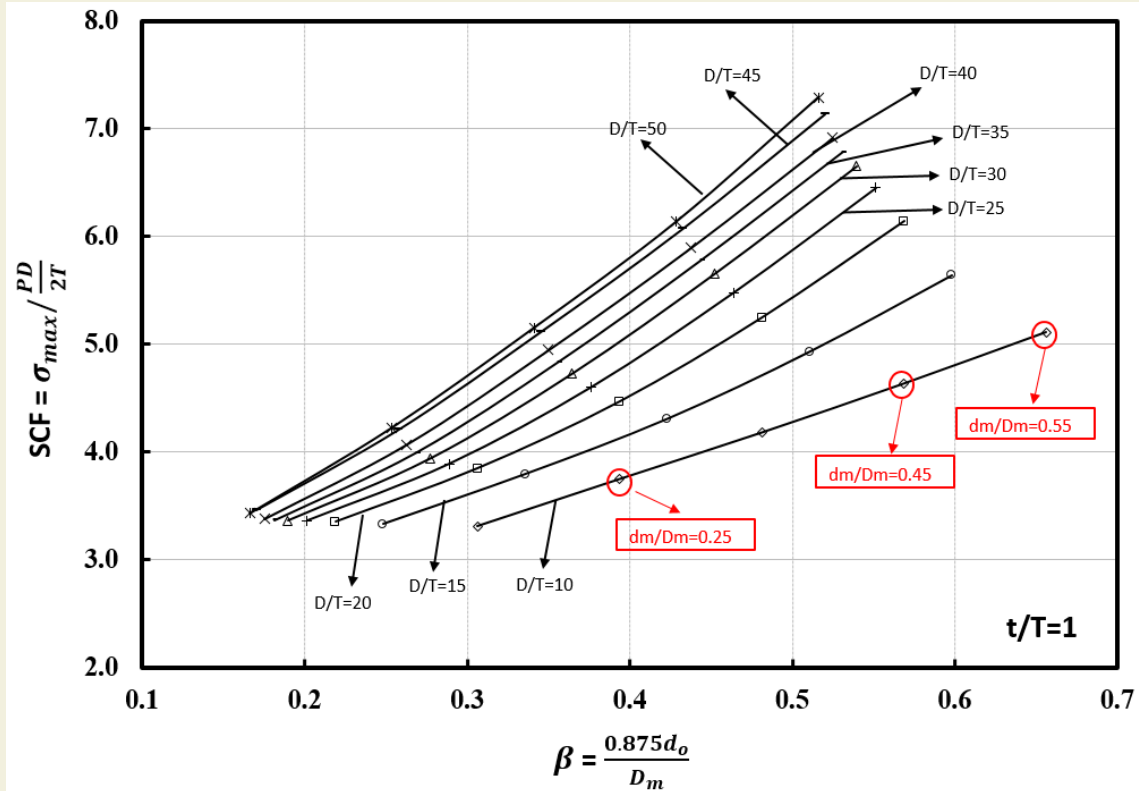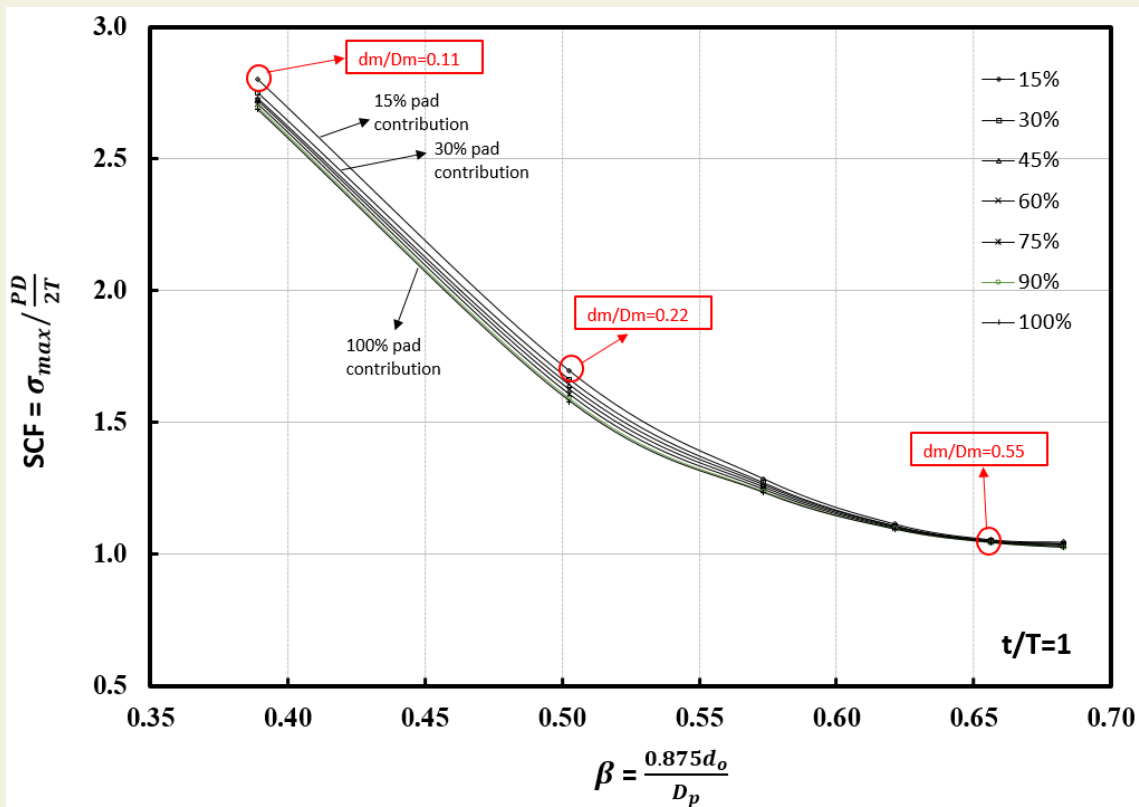

Figure 1. SCF Distribution for Nozzle/Cylinder Connection Under Internal Pressure – Without Pad Reinforcement (1st scenario)

When the t/T = 0.15 curve, in which SCF changes the least, the difference in the maximum SCF value is 21%. This difference occurs between the cases D/T=10 and D/T=50 where the first and last points are represented. When the t/T=0.55 situation, where the difference in the maximum SCF value is observed, is examined, it is seen that the proportional difference reaches 47%. In other words, it can be said that an approximately 3.5 times increase in t/T value corresponds to a 125% increase in SCF values.

For another case where the effect of the internal pressure

on the SCF distribution is examined, the D/T ratio is obtained from 10 to 50 with an increase of 5 units. By increasing the shell diameter (D) at a constant shell thickness (T), 9 different D/T values are created. Each D/T value represents a curve. These curves are formed by the parameter of dm/Dm. The dm/Dm changes are marked on the D/T=10 curve and all design curves are plotted in Figure 4. The t/T value was equal to 1 in all analyses. As shown in Figure 4, Although the nozzle diameter tends to increase at the same rate as the shell diameter, the change in SCF does not show the same trend. In the

Figure 2. SCF Distribution for Nozzle/Cylinder Connection Under Internal Pressure – Without Pad Reinforcement (2nd scenario)

Figure 3. SCF Distribution for Nozzle/Cylinder Connection Under Internal Pressure – Without Pad Reinforcement (3rd scenario) (t/T = dm/Dm)

case of this increase in dm/Dm of 0.15, it is just about 3% at its maximum point, and in the case of an increase in dm/Dm of 0.55, it is roughly 30%. All these results show that the larger the nozzle diameter, the linearly similar increase in SCF values.

2.2. Design Curve Generation for Nozzle-Cylinder Junction Under Internal Pressure Loading - Pad Reinforcement Effect

Reinforcement plate (pad) applications are one of the most effective ways to minimize the high stresses that

Figure 4. SCF Distribution for Nozzle/Cylinder Connection Under Internal Pressure – Without Pad Reinforcement (4th scenario) (t/T = 1)

Figure .5 SCF Distribution for Nozzle/Cylinder Connection Under Internal Pressure – With Pad Reinforcement (1st scenario) (t/T = 1)

occur in pressure vessel problems. This application is conducted by adding additional material to the joint areas. In this section, it is discussed how the reinforcement plates added to the nozzle/cylinder connection regions will affect the Stress Intensity Factor magnitudes. In his paper, Stikvoort [19] presented a study of the effect of the geometric gap between a cylindrical or spherical shell and a reinforcement pad on the stress concentration near the nozzle penetration when the pressure vessel is subjected to internal pressure. The mentioned study is important for the stress magnitudes occurring between the nozzle and the reinforcement area. However, the focal point here is the maximum stress on the entire system, and this region occurs at the crotch corner. For this reason, the gaps between the pad and the main vessel are ignored and it is considered to be an integrated assembly.

First, a model with a constant t/T ratio of 1 is considered, and the pad thickness (Tp) is increased at regular intervals. Also, the dm/Dm ratio is increased by 0.11 with each step starting from 0.11 to 0.66. Here, the shell diameter (Dm) is fixed. The main variable is the nozzle diameter (dm). In Figure 5, generated curves are displayed.

Another scenario is that the pad reinforcement is the key variable in this case, so the attachment parameter - β is modified to account for the diameter of the pad. The new expression is;

$$\beta = \frac{0.875d_o}{D_p}$$

Equation 2

As seen in Figure 5, it can be said that pad reinforcement is more effective in reducing stress as the dm/Dm ratio

decreases, that is, the smaller the nozzle opening. This SCF change ratio remains below 1% after 0.44 dm/Dm. However, when dm/Dm is 0.11 the SCF difference shows a 4.21% decrease at the maximum point.

Increasing the pad thickness in an equivalent manner is one of the main variables that influence the effect of pad contribution on SCF change. Varying the pad diameter (Dp) is the other variable. Five different Dp/dm ratios are determined for each curve generation (1.25, 1.5, 1.75, 2.0, and 2.25) to observe the effect of this variable. During the analysis, the pad diameter (Dp) is increased at constant intervals while the nozzle diameter (dm) remains constant. The results are indicated in Figure 6.

Given that both the opening of the nozzle as well as the outside dimensions of the main cylinder do not change, it is clear that changing the pad diameter has a significant impact on the SCF as well. An increase in pad diameter of approximately two times will result in a decrease in SCF values of approximately 80% if Dp/dm = 1.25 is compared with Dp/dm = 2.25. A decrease in S.C.F values is also achieved by increasing pad thickness, in line with the previous graph. With a clearer expression, an 85% pad contribution will increase S.C.F by over 13% on average.

In this section, the effects of reinforcement plate application under various parameters were examined and design curves were created. Based on these results, it has been shown that pad reinforcement ratio and pad diameter have positive effects on reducing the stress concentration factor. However, it has been shown in the curves obtained that the reinforcement plate application will not
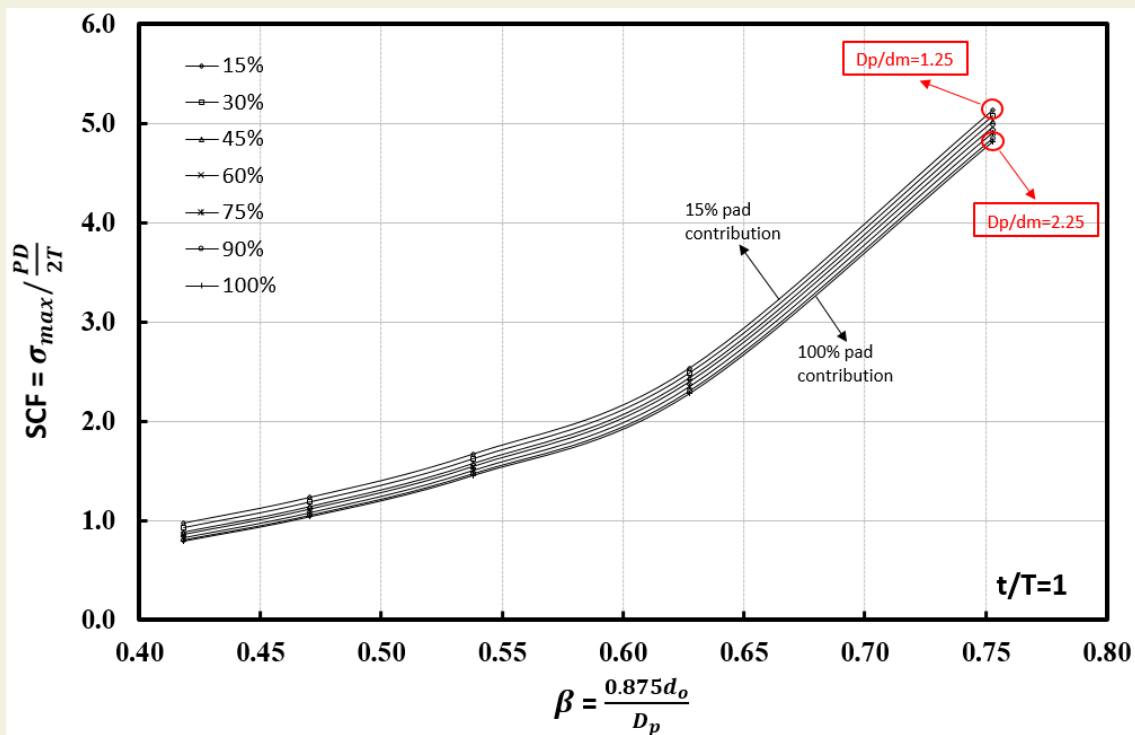

Figure 6. SCF Distribution for Nozzle/Cylinder Connection Under Internal Pressure – Without Pad Reinforcement (2nd scenario) (t/T = 1)

provide the desired performance if the nozzle opening is too large (especially if the d/D value is 0.5 and above). In such cases, it is stated that the pad diameter can be increased together with the pad thickness and the SCF could be reduced.

2.3. Design Curve Generation for Nozzle-Cylinder Junction Under External Local Loads

Following the above studies, the maximum stresses and stress concentration factors related to external local loadings are now determined. Thereafter, by using a suitable attachment parameter, design curves related to external loads are established. Since the stress results depending on the direction of the force will differ for the same load magnitudes in external local loadings, the SCF expression has been rearranged in Equation 3.

$$ \text{SCF} = \sigma_{max} \Big/ \frac{V_i}{2\pi R t}, \ (i = x, y, z) \quad \textbf{Equation 3} $$

In that formula, Vx, Vy, and Vz denote the shear force in the axial direction, the shear force applied in the longitudinal direction, and the tensile force, respectively. The aforementioned local loads are illustrated in Figure 7.

For all problems to which external loading will be applied, the mentioned loading conditions are exactly met. The di/Di ratio is the main parameter for all analyses. Design curves are created for 11 different ratios of that parameter. Here, for the di/Di parameter, it should be noted additionally, the value of Di is constant in all cases. That means the size of the main shell does not change. In
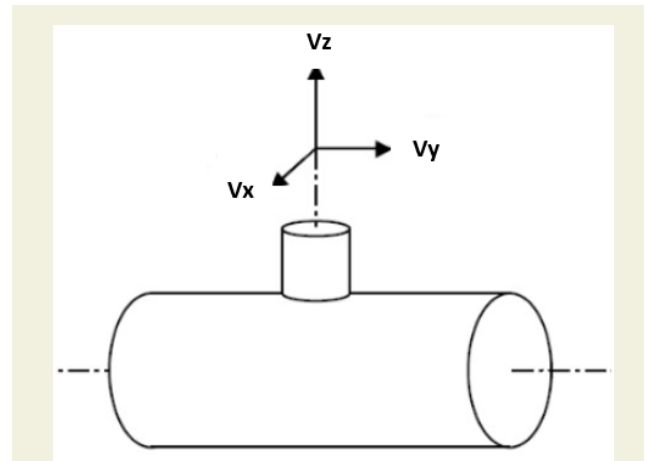
Figure. 7 Loading states for nozzle/cylinder connections.

contrast, the nozzle inner diameter - di is increased with each step. Also, another parameter used to create the design curves is t/T. The t/T ratio is obtained for 10 different points in increments of 0.2 from 0.2 to 2.0. Choosing these variables in the design curve graph has the purpose of providing the possibility to examine the diameter and thickness of the nozzle and cylinder during the same parametric study, which directly affects the maximum stress that will be imposed on the structure.

The generated design curves are shown are demonstrated in Figure 8, Figure 9, and Figure 10.

As the t value increases up to the di/Di = 0.38 curve in Figure 8, the SCF values decrease almost linearly. It is
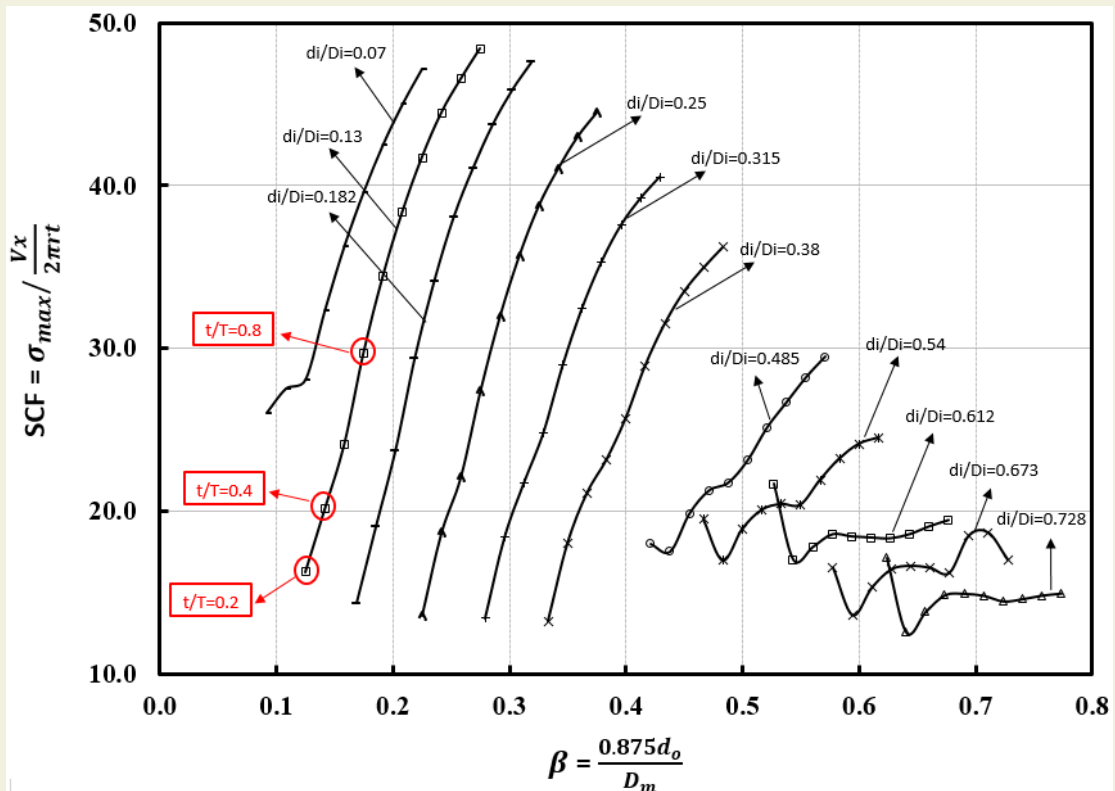
Figure. 8 SCF Distribution for Nozzle/Cylinder Connection Under External Loads (Vx)

also striking that the SCF is remarkably high at the t/T=0.2 point. This point is also the di/Di = 0.485 point, i.e., the nozzle radius is almost half the size of the cylinder radius. This shows that the increased shell diameter increases the stress magnitude and at this point, the nozzle wall thickness - t cannot meet the maximum stress. For this reason, the t/T=0.2 point for this Figure is the most striking point in the design curves obtained. It is also noted that the maximum SCF obtained for the same

t/T decreases with increasing nozzle inner diameters, and the wall thickness effect almost disappears.

When the cases where the Vy force is applied in Figure 9 are examined, it is seen that the interpretations that can be made for Vx in Figure 8 will be mostly similar. The progression of the curves, though, follows a similar trending pattern, especially after the di/Di=0.425 curve, which is quite remarkable. On the contrary, in the case
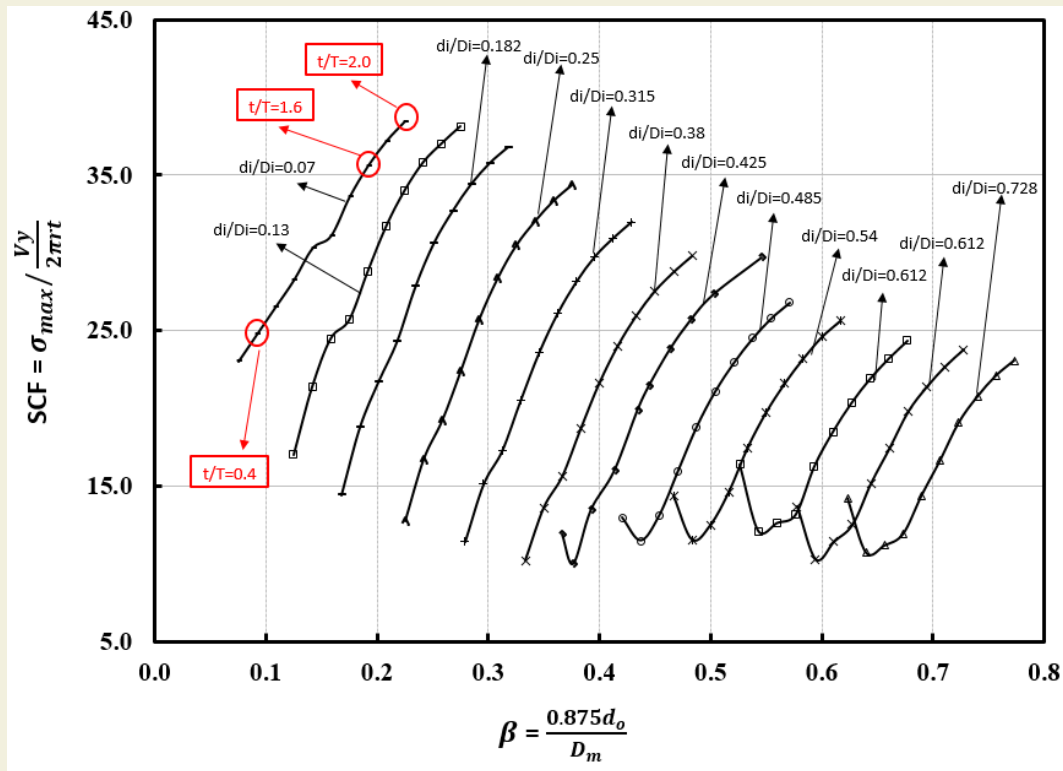
Figure 9. SCF Distribution for Nozzle/Cylinder Connection Under External Loads (Vy)
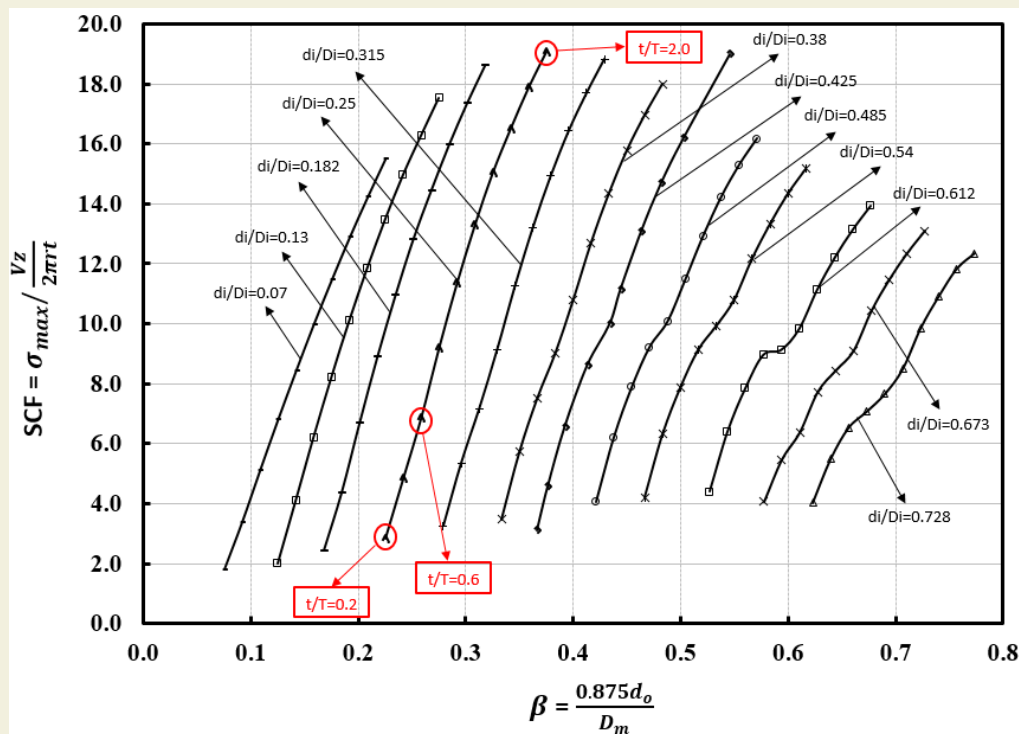
Figure 10. SCF Distribution for Nozzle/Cylinder Connection Under External Loads (Vz)

of t/T=0.2, the nozzle wall thickness is not able to meet the loads on the structure, and there is too much stress observed on the wall. Additionally, it is worth noting that if Vx loading is performed, SCF values tend to be 15% higher on average compared to Vy loading. As a result, the system is often subjected to greater force in the X direction than in the longitudinal direction when applying axial loading.

The case of loading in the Z direction (tensile load) is the last loading condition to be examined. The outcomes are displayed in Figure 10. The SCF will increase in value if t is increased as it is in any other external load when each curve is examined separately.

3. Conclusions

It is concluded that the maximum stresses calculated by FEA and SCF are obtained for the cylinder/cylinder joints under the influence of internal pressure and external local loads. From this, different parametric approaches and loading conditions were applied to the basic dimensions of geometry. There were also a number of design curves for cylinder-to-cylinder connections created. In all cases where design curves have been obtained, it can be seen that pressure and external loads are both responsible for a non-linear relation between load and stress. It is also of significance to note that the analysis made in this case, and the curves obtained, are only applicable to loads that operate in a one-way direction (tensile, longitudinal, and axial loading separately, etc.). In conclusion, this paper provides designers and researchers with useful guidelines for calculating parameters related to thickness and diameter under external load and internal pressure conditions.

In conclude, it is exceedingly difficult to define a single formulation for the obtained design curves due to the fact that they contain a complex number of variables and parameters. As such, by using the approach presented herein, by combining appropriate parameters, equations suitable for finite element analysis can be developed in future studies.

References

[1] Leckie, F. A., & Penny, R. K. (1963). Stress Concentration Factors for the Stresses at Nozzle Intersections in Pressure Vessels (Welding Research Council Bulletin 90).

[2] Spence, J., & Tooth, A. S. (Eds.). (2012). Pressure vessel design: concepts and principles.

[3] Kharat, A. R., Kamble, S. B., Patil, A. V., & Burse, I. D. (2016). comparative study of different approaches to estimate SCF in pressure vessel opening. Int. J. of Mechanical Engineering and Technology, 7: 142-155.

[4] Money, H. A. (1968, January). Designing flush cylinder-to-cylinder intersections to withstand pressure. In Mechanical Engineering 90(11): 74.

[5] Moffat, D. G., Mwenifumbo, J. A. M., Xu, S. H., & Mistry, J. (1991). Effective stress factors for piping branch junctions due to internal pressure and external moment loads. The Journal of Strain Analysis for Engineering Design, 26(2): 85-101.

[6] Moffat, D. G., Mistry, J., & Moore, S. E. (1999). Effective stress factor correlation equations for piping branch junctions under internal pressure loading. Journal of Pressure Vessel Technolology, 121(2): 121-126
https://doi.org/10.1115/1.2883674

[7] Mershon, J. L. (1987). Local Stresses in Cylindrical Shells due to External Loadings on Nozzles? Supplement to WRC Bulletin No. 107 (Revision 1). WRC Bulletin.

[8] Lind, N. C. (1968, January). Approximate stress-concentration analysis for pressurized branch pipe connections. In Mechanical Engineering 90(3): 78

[9] Decock, J. (1975). Reinforcement method of openings in cylindrical pressure vessels subjected to internal pressure. Weld. Res. Abroad, 21(9): 9-36.

[10] Kihiu, J. M., Rading, G. O., & Mutuli, S. M. (2007). Universal SCFs and optimal chamfering in cross-bored cylinders. International journal of pressure vessels and piping, 84(6): 396-404.

[11] Mukhtar, F. M., & Al-Gahtani, H. J. (2019). Comprehensive Evaluation of SCF for Spherical Pressure Vessels Intersected by Radial Cylindrical Nozzles. International Journal of Steel Structures, 19: 1911-1929.

[12] Gerdeen, J. C. (1972). Analysis of stress concentrations in thick cylinders with sideholes and crossholes. Journal of Manufacturing Science and Engineering, 94(3): 815-824

[13] Nziu, P. K., & Masu, L. M. (2019). Offsetting of circular cross bore effects on elastic pressurized thick cylinders. International journal of mechanical and production engineering research and development, 9: 71-82.

[14] Makulsawatudom, P., Mackenzie, D., & Hamilton, R. (2004). Stress concentration at crossholes in thick cylindrical vessels. The Journal of Strain Analysis for Engineering Design, 39(5): 471-481.

[15] Kharat, A., & Kulkarni, V. V. (2013). Stress concentration at openings in pressure vessels-A review. International Journal of Innovative Research in Science, Engineering and Technology, 2(3): 670-678.

[16] Bozkurt, M. (2022). Towards a unified design-by-analysis solution to pressure vessel nozzle-shell junctions under combined loading, PhD, University of Strathclyde Engineering, UK

[17] Bozkurt, M., Nash, D., & Uzzaman, A. (2021). A comparison of stress analysis and limit analysis approaches for single and multiple nozzle combinations in cylindrical pressure vessels. International Journal of Pressure Vessels and Piping, 194: 104563.

[18] Bozkurt, M., Nash, D., & Uzzaman, A. (2020, October). Effect of the internal pressure and external loads on nozzles in cylindrical vessel. In IOP Conference Series: Materials Science and Engineering, 938(1): 012007.

[19] Stikvoort, W. (2021). Effectiveness of reinforcement plates pertaining to pressure equipment. American Journal of Engineering Research (AJER), 10(8): 127-146.

4. APPENDIX

Notation

d_i: nozzle inner diameter

d_o: nozzle outer diameter

d_m: nozzle mean diameter

D_i: shell inner diameter

D_o: shell outer diameter

D_m: shell mean diameter

D_p: pad diameter

FEA: Finite Element Analysis

FEM: Finite Element Modelling

SCF: Stress Concentration Factor

t: nozzle thickness

T: shell thickness

β: attachment parameter

Optimizing printing parameters for enhanced mechanical properties of 3D printed PLA octet lattice structures

Oğuz Tunçel[1*]

[1]Siirt University, Engineering Faculty, Mechanical Engineering Department, Siirt, Türkiye

Orcid: O. Tunçel (0000-0002-6886-6367)

Abstract: 3D printers, known as one of the rapid prototyping methods, are used in research and academic studies as well as industry. This technology makes it easy and fast to produce a preliminary prototype of a design. This study explores the impact of printing parameters on the mechanical properties of 3D-printed octet lattice structures using PLA material. Focused on optimizing layer thickness, print speed, and infill density, the study employed Taguchi methodology. Compressive strength and strength per mass were the key metrics analyzed. The optimized parameters, determined as 0.2 mm layer thickness, 90 mm/s print speed, and 100% infill density, significantly enhanced compressive strength. Infill density emerged as the most influential factor, contributing to 82.75% of the overall variation. A robust predictive model was developed, achieving a 92.06% accuracy in estimating compressive strength per mass values. These findings provide crucial guidelines for manufacturing high-strength, lightweight PLA octet lattice structures, vital in industries like aerospace and automotive. This study advances additive manufacturing, opening avenues for further research in diverse lattice structures and materials.

Keywords: Fdm, pla, octet lattice, compression strength, Taguchi, ANOVA

1. Introduction

Additive manufacturing (AM) is a versatile industrial manufacturing technique that can produce products in a three-dimensional (3D) structure according to a predetermined design. It is the process of producing the structure layer by layer. These technologies have a lot of potential for generating efficient structural parts, complicated geometries, and small parts, and they have a lot of potential uses in aerospace, defense, automotive, electronics, tool and die making, energy, and biomedical [1,2]. Fused deposition modeling (FDM) is an important AM method with advantages such as ease of application, low machine and consumable cost, durable part production, and easy replacement of the filament used as consumable [3,4]. FDM is a widely used extrusion technique in which the material is heated, melted, and deposited layer by layer through a nozzle. Normally, the nozzle has horizontal movement capability, while the build platform moves vertically after the completion of each new layer. In certain FDM technologies, the nozzle can move both horizontally and vertically [5,6].

AM enables the fabrication of complicated three-dimensional lattice structures with precise control over the cell, support, and overall structure dimensions and configuration [7]. Lattice structures are designed and manufactured to offer specific properties such as strength, shock absorption, acoustic or visual damping, heat transfer, and thermal insulation, thanks to their lightweight. With additive manufacturing, trusses are produced as lattice structures that provide building units with a predefined design [8]. The cellular unit structure significantly influences the mechanical behavior of truss constructions [9]. Lattice structures can be applied in car bumpers and airplane wings that require energy absorption or wherever a high strength-to-weight ratio is needed [10].

The octet-truss lattice is a highly effective support structure for integrating structure and function because of its inherent porous qualities and remarkable load-bearing capability [11]. The octet-truss truss structure is characterized by a unit cell with 12 equal nodal connections and is typically stress-dominated. These structures are widely used in aerospace, automotive, and medical industries. They can, for example, replace foam materials in lightweight structures such as sandwich panels and offer higher strength-to-density ratios than flexural lattices [12]. The octet truss lattice structure has the potential for an alternative application to foams or honeycomb cellular materials [13].

Literature studies on the compressive strength of FDM-fabricated lattice structures are given below. Rahman et al. [14] achieved optimal results by combining 0.1 mm layer thickness, 205°C printing temperature, 50 mm/s printing speed, and 60°C bed temperature. These parameters yielded the maximum modulus of elasticity and compressive strength, showcasing the significant impact of manufacturing settings on PLA lattice cubic structures in biomedical applications. Dong et al. [15] optimized FDM process parameters for lattice structures using the manufacturable element concept. Layer thickness (0.2 mm, 245°C nozzle, 600 mm/min, 0% fan speed) proved most advantageous for horizontal struts. In contrast, inclined struts were optimized with a layer thickness of 0.1 mm, a nozzle temperature of 255°C, a printing speed of 1200 mm/min, and a fan speed of 50%. Their approach improved mechanical performance, emphasizing the significance of specific parameters for different structural features. Future research will explore the impact of dynamic process parameters on lattice structure quality in FDM fabrication. Dixit and Jain [16] optimized fused filament fabrication process parameters for lattice structures using the Taguchi method with TPU and PLA materials. They determined the optimal combination as 0.1 mm layer thickness, 100% infill density, and 40 mm/s printing speed, maximizing compressive strength. Liu et al. [17] enhanced the FDM technique by introducing a snap-fitting method for fabricating PLA plus BCC lattice structures. Relative densities of 2.1% to 8.3% were achieved, showing significant improvements: 37.6%–65.3% in peak strengths, 11.4%–39.6% in compressive moduli, and 67%–270% in energy absorption per unit volume compared to conventional FDM structures. The method also offered superior surface quality and printing efficiency. Analytical models considering node volume accurately predicted mechanical properties. This innovative approach can extend to other additive manufacturing technologies like PolyJet. Emir et al. [18] studied the load behaviors of octet-truss lattice structures produced via FDM with varied transition geometries. Compression tests and FEM analyses revealed transition geometry's crucial role in deformation patterns and stress distributions. Structures lacking transitions exhibited plastic deformation at low-stress levels, while transitioned geometries experienced plastic deformation at higher stresses. Deformation areas in straight and inclined transitions were smaller, emphasizing the importance of transition design. Stretch-dominated deformation, impacting lattice strength under load, was consistent across all structures. Zisopol et al. [19] conducted a study on PLA lattice structures through FDM, employing various filling patterns, including octet. The triangle pattern exhibited 98.98% accuracy and 57.70% deformation, reaching a maximum compressive force of 87.32 kN. The octet pattern, along with others, was examined in the research. The optimization of use value to production cost was achieved, emphasizing the economic importance of cubic subdivision and the technical feasibility of octet structures.

Optimizing printing parameters is essential as it directly affects the mechanical properties of the produced part. This study optimized additive manufacturing parameters for superior compressive strength in PLA octet-truss lattice structures. The findings contribute valuable insights for enhancing lattice structures' mechanical properties, emphasizing parameter optimization's importance in additive manufacturing processes. Future research could explore applying similar optimization techniques for different lattice structures and materials, further advancing
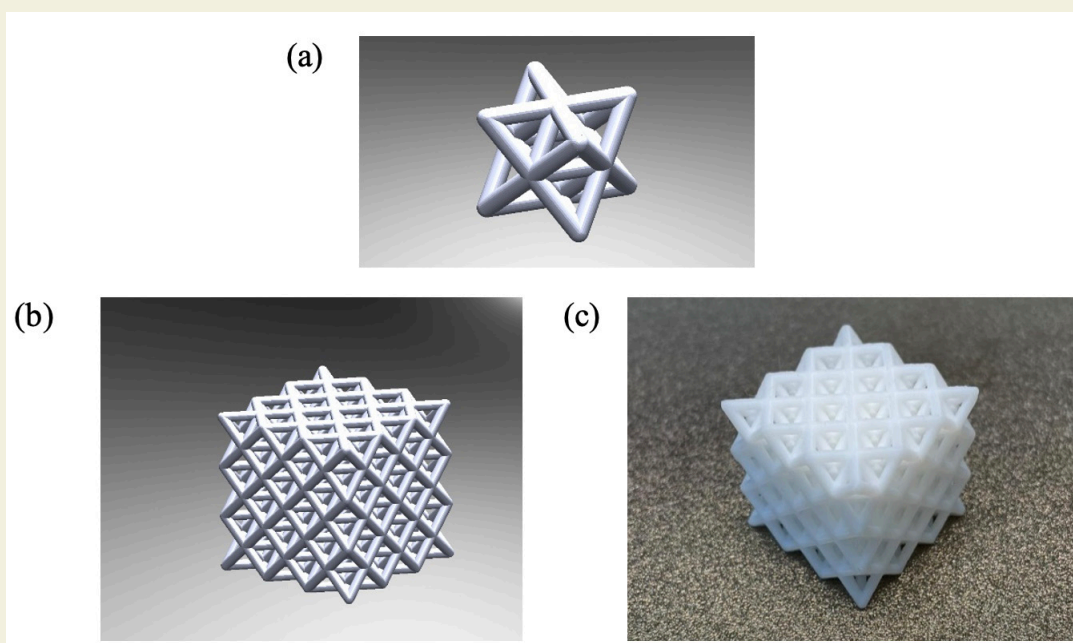
Figure 1. The experimental sample having octet-truss lattice structure (a) Octet-truss unit cell,

(b) Solidworks drawing of octet-truss compression specimen consisting of 3x3x3 unit cells, (c) An example of a sample printed with a 3D printer

the field of additive manufacturing.

2. Material and Method

This study used poly(lactic acid) PLA filament as the experimental material. PLA is an organic biopolymer and thermoplastic produced from corn starch and sugar cane [20]. Therefore, it is not harmful to human health. The filament used is Creality brand, white, and 1.75 mm thick. It has 1.24 g/cm³ density, 51 MPa tensile, 86 MPa compression, and 10.5 J impact strength. For compression tests, specimens consisting of cubic octet-truss lattice structures with dimensions of 30 mm x 30 mm x 30 mm are shown in Figure 1 [21,22]. The unit lattice structure has dimensions of 10 mm x 10 mm x 10 mm and a circular cross-section with a strut diameter of 1.75 mm (Figure 1a) [18]. The drawing of the printed specimen consisting of 3x3x3 unit cells for a total of 27 unit cells using the Solidworks 2020 program is shown in Figure 1b. An example of a sample printed with a 3D printer is shown in Figure 1c. As shown in Figure 1b in the Solidworks 2020 drawing program, the sample CAD file prepared in STL format was transferred to the Cura 5.4.0 program for parameter entries. Thanks to this program, the drawing is converted into G codes that the 3D printer can recognize. There is also the flexibility to change the parameters that affect the print quality as much as the printer's capacity allows.

Minitab 20.3 program was used to create the experimental design. The experimental design was performed utilizing the Taguchi methodology. The parameter changes were related to the defined output value of strength per unit mass. The experiments were designed with three different parameters and three levels. With the full factorial design, 3^3 total 27 experiments should be performed, while Taguchi L9 design was selected, and 9 experiments were used to reach the optimum output. The printing parameters and levels are given in Table 1, and the Taguchi L9 experimental design is given in Table 2. Printing processes were carried out using the Creality brand Ender 3S-1 Pro 3D printer. The masses of the test samples were measured after 3D printing using an analytical scale. The scale used is Shimadzu brand and can measure with an accuracy of 1 in 10000 grams. Taguchi analyses were performed using the larger is better approach using the equation in Equation 1 [23,24]. By means of tables created using signal-to-noise ratios (S/N ratio), the optimum output level for each parameter was selected, and Taguchi results were predicted. The effects of the parameters on the output were determined by analysis of variance (ANOVA). Thanks to ANOVA, we can see the percentage contribution of each parameter to the output. To support the ANOVA analysis, a Pareto Chart is also used to show whether the contribution of the parameters to output is significant or insignificant [25]. In addition, the relationship between output and input parameters was equated by creating a linear regression equation. Such equations allow us to obtain results for intermediate values of the parameters. Finally, the accuracy of the data obtained

from the equation was compared with the consistency of the experimental results.

**Table 1.** Print parameters and levels

Parameters	Unit	Level 1	Level 2	Level 3	Output
Layer thickness	(mm)	0.10	0.20	0.30	Strength per mass (MPa/g)
Print speed	(mm/s)	30	60	90	
Infill density	(%)	60	80	100	

$$\frac{S}{N_{max}} = -10 log \left(\frac{1}{n} \sum_{i=1}^{n} \frac{1}{y_i^2} \right) \qquad (1)$$

Table 2. Three parameters three level Taguchi L9 orthogonal experiment design

No	Layer thickness (mm)	Print speed (mm/s)	Infill density (%)
1	0.1	30	60
2	0.1	60	80
3	0.1	90	100
4	0.2	30	80
5	0.2	60	100
6	0.2	90	60
7	0.3	30	100
8	0.3	60	60
9	0.3	90	80

Three samples were 3D printed for each experimental group and subjected to compression tests using the UTEST brand tensile-compression device. These tests were carried out at room temperature, with a constant feed rate of 1 mm/min [26]. The experimentally obtained results were averaged from the three specimens in each group, and standard deviations were considered to ensure accuracy. Figure 2 is an image of a specimen after compression testing.
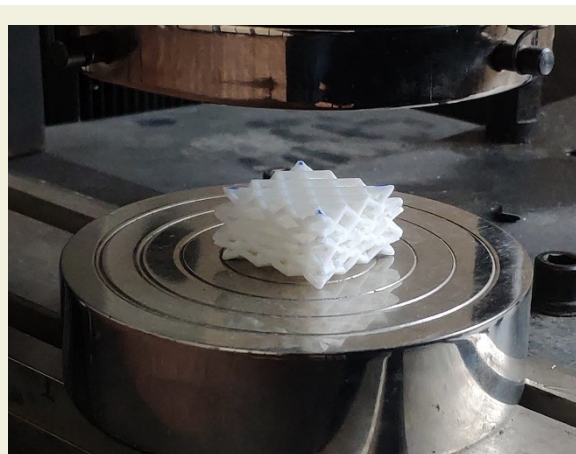
Figure 2. The image of a specimen subjected to compression test

3. Results and Discussion

The strength and strength per mass values obtained from the compression test are given in Table 3. According to Table 3, the highest compressive strength was obtained as 7.93 MPa in sample 3. The sample with the lowest compressive strength, sample 1, has a compressive strength of 4.62 MPa. The obtained strength values in this study were divided based on sample masses to assess the correlation between parameter variations and compressive strength more precisely [27–29]. The lowest strength per mass value was 0.472 MPa/g for sample 1, while the highest strength per mass value was 0.637 MPa/g for sample 3. The strength per mass value obtained in sample code 3 is 35% higher than that of sample code 1. When Table 3 is analyzed, it is seen that the infill density parameter is effective on the output. When considering the S/N ratios calculated as a result of Taguchi analysis, it is seen that the lowest value is in the sample coded 1 (-6.521), and the highest value is in the sample coded 3 (-3.917) (Table 3).

Table 3. Compression values with the calculated S/N ratios

No	Strength (MPa)	Mass (g)	Strength per mass (MPa/g)	Standard deviation	S/N ratio
1	4.62	9.79	0.472	0.011	-6.521
2	6.49	11.24	0.577	0.011	-4.776
3	7.93	12.45	0.637	0.028	-3.917
4	6.18	11.22	0.551	0.017	-5.177
5	7.92	12.49	0.634	0.028	-3.958
6	5.01	9.73	0.515	0.013	-5.764
7	7.07	12.50	0.565	0.008	-4.959
8	4.66	9.78	0.476	0.011	-6.448
9	6.20	11.22	0.552	0.020	-5.161

The S/N ratios response table generated from Taguchi analysis shows the S/N ratios for each level value of the parameters (Table 4). In the table, S/N values with high S/N ratios in each parameter maximize the output [30]. In this case, the 2nd, 3rd, and 3rd levels of layer thickness, print speed and, infill density parameters are effective on

strength per mass, respectively. According to Table 4, in order to reach the optimum output, manufacturing should be done with 0.2 mm layer thickness, 90 mm/s, and 100% infill density parameters. The higher the delta value, the higher the order of influence of the parameters on the output. When Table 4 is analyzed, the order of the effect of the parameters on the output is filling density, printing speed, and layer thickness.

Table 4. Response table for the S/N ratios of the strength per mass values (S/N: Larger is better)

Level	Layer thickness (mm)	Print speed (mm/s)	Infill density (%)
1	-5.072	-5.552	-6.244
2	-4.966*	-5.061	-5.038
3	-5.523	-4.947*	-4.278*
Delta	0.556	0.605	1.966
Rank	3	2	1

*Optimum level

The main effects plot for S/N ratios is given in Figure 3. Here, parameter levels above the mean line indicate that they are sufficient for the desired output levels [31]. 0.1-0.2 mm for layer thickness, 60-90 mm/s for print speed, and 80-100% for infill density are the parameter levels that will provide above-average strength per mass results. The points enclosed in red circles in Figure 3 also indicate the optimum parameter levels.

Table 5 displays the outcomes of the analysis of variance (ANOVA) for the parameter variations within the specified ranges investigated in the study. At the same time, Figure 4 illustrates the percentage contributions of these parameters to strength per mass. Analyses were performed at a 95% confidence level. When the P-value in Table 5 is less than 0.05, the parameters affect on the output [32]. In this case, the table shows that all three parameters affect on strength per mass. The highest contribution to strength per mass is infill density, which is 82.75%. The parameter with the second highest contribu-
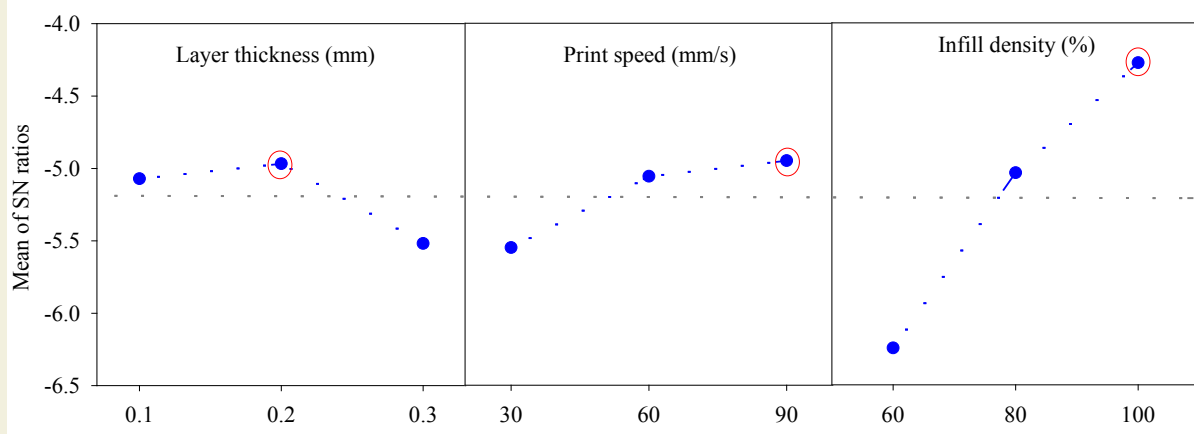

Figure 3. S/N ratio graph of parameters for strength per mass values

**Table 5.** Analysis of variance (ANOVA) results for strength per mass values

Source	(DoF)	Seq SS	Contribution (%)	F-Value	P-Value
Layer thickness (mm)	2	0.002215	7.97	235.98	0.0042
Print speed (mm/s)	2	0.002616	9.25	273.79	0.0036
Infill density (%)	2	0.023395	82.75	2448.30	0.0004
Error	2	0.000010	0.03	---	---
Total	8	0.028276	100	---	---

tion is the print speed, with 9.25%, while layer thickness has the lowest contribution, with 7.97%. The error rate in the study is very low (0.03%). The R^2 value obtained according to the model is 99.97%.
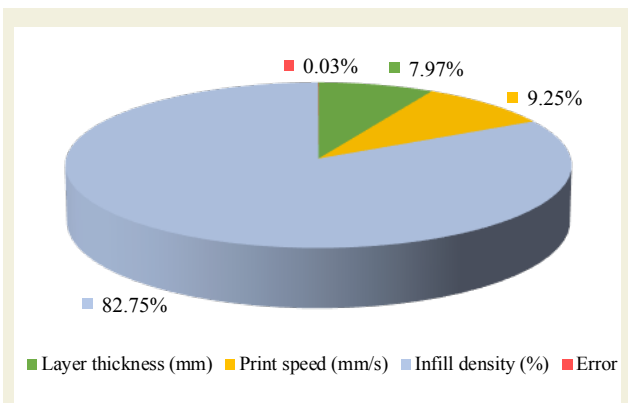
Figure 4. Effect of parameters on strength per mass as a percentage

The Pareto chart in Figure 5 shows the effect levels of the parameters. Parameters with a standardized effect value above the reference line (2.571) are shown as effective. In this case, infill density and print speed parameters are more effective. The standardized effect value of infill density is remarkable. The values obtained in the parato chart graph are consistent with the ANOVA table in Table 5.
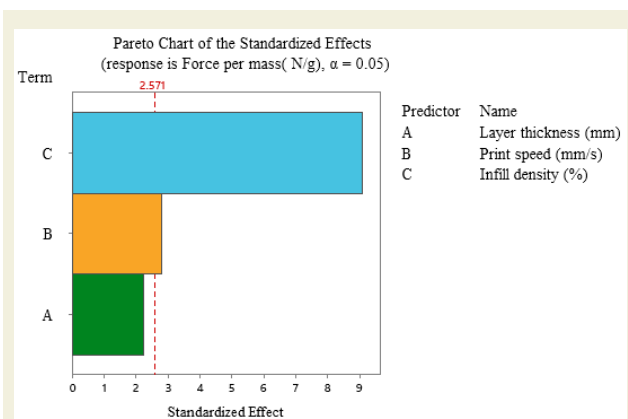
Figure 5. Pareto chart showing the effects of the parameters

According to Table 4 and Figure 3, the highest strength per mass output parameters were 0.2 mm layer thickness, 90 mm/s print speed, and 100% infill density. When predicted in the Minitab program with these parameter levels, the result was -3.818 for the S/N ratio and 0.640 MPa/g for predicted strength per mass (Table 6). According to the experimental result, the value per mass was 0.643. The error rate between the predicted and experimentally obtained values is as low as 0.47%. According to the results in Table 3, the highest strength per mass value was 0.637 MPa/g in sample 3. The value of 0.643 MPa/g obtained in the sample created with the optimum parameters is 0.94% higher than that of 0.637 MPa/g obtained in the initial design.

Table 6. Predicted optimum value and validation of experiment result

Optimum Level: 233	Predicted Value (MPa/g)	Experimental Result (MPa/g)
	0.640	0.643
Prediction Error (%)	0.47	

A linear regression equation was created to predict the change in strength per mass with the evolution of parameter change (Table 7). This equation also provides results for parameter levels or combinations not in the design. The R^2 value of the equation is also as high as 92.06%.

Figure 6 compares the predicted strength per mass values with the individual strength per mass results. A comparison of the predictions and results in Figure 6 shows that an efficient analysis is obtained from results close to the regression line. Most points fell within the 95% confidence interval. The R^2 (R-sq) value of the linear regression model obtained for these comparisons, such as those shown in Figure 6, was calculated at 95%.
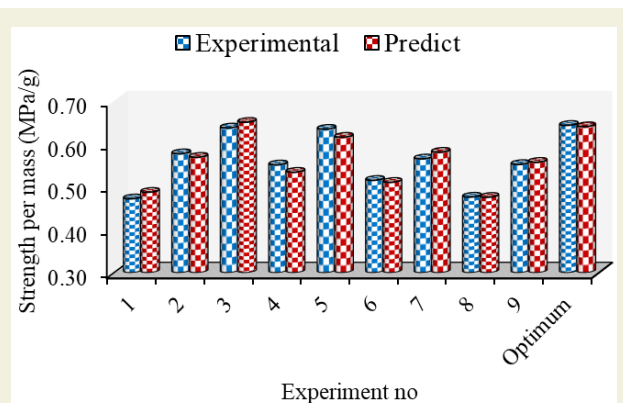
Figure 7 shows the experimental strength per mass results and the predicted strength per mass values according to the equation in Table 7. As seen in Figure 7, the strongly predicted data matched well with the obtained results. This showed that the equation with an R^2 value of 92.06% made high predictions.

Table 7. Linear regression equation for prediction of strength per mass values (MPa/g)

Strength per mass (MPa/g) = 0.2965-0.1550*Layer thickness +0.000644*Print speed+0.003108*Infill density
R-sq= 92.06%
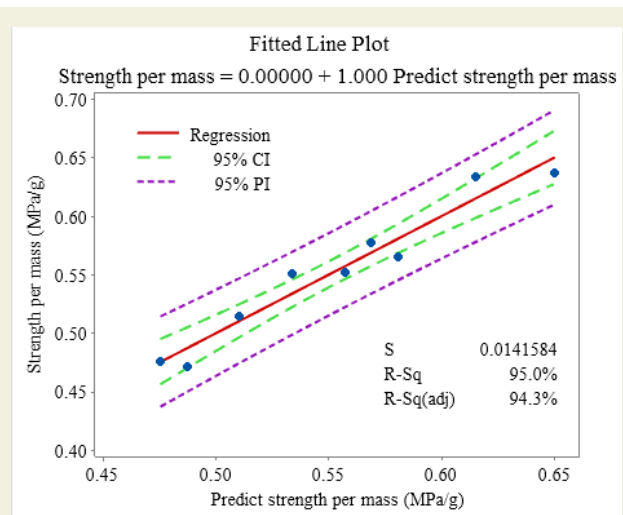
Figure 6. Predicted compression values compared with experimental results for compression per mass values

Figure 7. Predicted versus experimental results for strength per mass values

4. Conclusions

This study investigated the effect of printing parameters on the mechanical properties of 3D-printed octet lattice structures using PLA material. The Taguchi methodology was employed to optimize the printing parameters: layer thickness, print speed, and infill density. The compressive strength and strength per mass values were used as the leading indicators to evaluate the performance of the lattice structures. The results of the study revealed the following key findings:

- Through Taguchi analysis, the optimized printing parameters for superior compressive strength were determined to be 0.2 mm layer thickness, 90 mm/s print speed, and 100% infill density.

- The study highlighted the significant influence of infill density on the strength per mass of PLA octet lattice structures, contributing to 82.75% of the overall variation.

- A high level of accuracy was achieved in predicting the compressive strength per mass values using the optimized parameters, with an error rate of only 0.47%. Also, the developed linear regression equation demonstrated a strong predictive capability with an R-squared value of 92.06%.

- The optimized parameters and the predictive model can serve as valuable guidelines for manufacturing PLA octet lattice structures with enhanced mechanical properties. These structures find applications in various industries, including aerospace, automotive, and medical fields, where lightweight components with high strength-to-density ratios are essential.

- Future research could explore applying similar optimization techniques for different lattice structures and materials, expanding the scope of additive manufacturing in producing efficient and lightweight components for diverse applications.

In conclusion, this study contributes valuable insights into optimizing 3D printing parameters for enhancing the mechanical properties of lattice structures, paving the way for advancements in additive manufacturing technologies and their industrial applications.

References

[1] Vijayakumar, M.D., Palaniyappan, S., Veeman, D., Tamilselvan, M., (2023). Process Optimization of Hexagonally Structured Polyethylene Terephthalate Glycol and Carbon Fiber Composite with Added Shell Walls. Journal of Materials Engineering and Performance. 32(14): 6434–47. doi: 10.1007/s11665-022-07572-z.

[2] Di Angelo, L., Di Stefano, P., Dolatnezhadsomarin, A., Guardiani, E., Khorram, E., (2020). A reliable build orientation optimization method in additive manufacturing: the application to FDM technology. International Journal of Advanced Manufacturing Technology. 108(1–2): 263–76. doi: 10.1007/s00170-020-05359-x.

[3] Stephen Oluwashola Akande., (2015). Dimensional Accuracy and Surface Finish Optimization of Fused Deposition Modelling Parts using Desirability Function Analysis. International Journal of Engineering Research And. V4(04). doi: 10.17577/ijert-v4is040393.

[4] Kamer, M.S., Temiz, Ş., Yaykaşli, H., Kaya, A., Akay, O., (2022). Effect of Printing Speed on Fdm 3D-Printed Pla Samples Produced Using Different Two Printers. International Journal of 3D Printing Technologies and Digital Industry. 6(3): 438–48. doi: 10.46519/ij3dptdi.1088805.

[5] Tagliaferri, V., Trovalusci, F., Guarino, S., Venettacci, S., (2019). Environmental and economic analysis of FDM, SLS and MJF additive manufacturing technologies. Materials. 12(24). doi: 10.3390/ma1224161.

[6] Do an, O., Kamer, M.S., (2023). Experimental investigation of the creep behavior of test specimens manufactured with fused filament fabrication using different manufacturing parameters. Journal of the Faculty of Engineering and Architecture of Gazi University. 38(3): 1839–48. doi: 10.17341/gazimmfd.1122973.

[7] Silva, R.G., Estay, C.S., Pavez, G.M., Viñuela, J.Z., Torres, M.J.,

(2021). Influence of geometric and manufacturing parameters on the compressive behavior of 3d printed polymer lattice structures. Materials. 14(6). doi: 10.3390/ma14061462.

[8] Ali, H.M.A., Abdi, M., Sun, Y., (2022). Insight into the mechanical properties of 3D printed strut-based lattice structures. Progress in Additive Manufacturing. (0123456789). doi: 10.1007/s40964-022-00365-9.

[9] Qin, D., Sang, L., Zhang, Z., Lai, S., Zhao, Y., (2022). Compression Performance and Deformation Behavior of 3D-Printed PLA-Based Lattice Structures. Polymers. 14(5). doi: 10.3390/polym14051062.

[10] Zare Shiadehi, J., Zolfaghari, A., (2023). Design parameters of a Kagome lattice structure constructed by fused deposition modeling: a response surface methodology study. Iranian Polymer Journal (English Edition). 32(9): 1089–100. doi: 10.1007/s13726-023-01196-3.

[11] He, W., Luo, W., Zhang, J., Wang, Z., (2023). Investigation on the fracture behavior of octet-truss lattice based on the experiments and numerical simulations. Theoretical and Applied Fracture Mechanics. 125(April): 103918. doi: 10.1016/j.tafmec.2023.103918.

[12] Li, Y., Gu, H., Pavier, M., Coules, H., (2020). Compressive behaviours of octet-truss lattices. Proceedings of the Institution of Mechanical Engineers, Part C: Journal of Mechanical Engineering Science. 234(16): 3257–69. doi: 10.1177/0954406220913586.

[13] Song, J., Zhou, W., Wang, Y., Fan, R., Wang, Y., Chen, J., et al., (2019). Octet-truss cellular materials for improved mechanical properties and specific energy absorption. Materials and Design. 173: 107773. doi: 10.1016/j.matdes.2019.107773.

[14] Rahman, M.M., Sultana, J., Rayhan, S. Bin., Ahmed, A., (2023). Optimization of FDM manufacturing parameters for the compressive behavior of cubic lattice cores: an experimental approach by Taguchi method. International Journal of Advanced Manufacturing Technology.: 1329–43. doi: 10.1007/s00170-023-12342-9.

[15] Dong, G., Wijaya, G., Tang, Y., Zhao, Y.F., (2018). Optimizing process parameters of fused deposition modeling by Taguchi method for the fabrication of lattice structures. Additive Manufacturing. 19: 62–72. doi: 10.1016/j.addma.2017.11.004.

[16] Dixit, N., Jain, P.K., (2022). Effect of Fused Filament Fabrication Process Parameters on Compressive Strength of Thermoplastic Polyurethane and Polylactic Acid Lattice Structures. Journal of Materials Engineering and Performance. 31(7): 5973–82. doi: 10.1007/s11665-022-06664-0.

[17] Liu, W., Song, H., Wang, Z., Wang, J., Huang, C., (2019). Improving mechanical performance of fused deposition modeling lattice structures by a snap-fitting method. Materials and Design. 181: 108065. doi: 10.1016/j.matdes.2019.108065.

[18] Emir, E., Bahçe, E., Uysal, A., (2021). Effect of Octet-Truss Lattice Transition Geometries on Mechanical Properties. Journal of Materials Engineering and Performance. 30(12): 9370–6. doi: 10.1007/s11665-021-06096-2.

[19] Zisopol, D.G., Tănase, M., Portoacă, A.I., (2023). Innovative Strategies for Technical-Economical Optimization of FDM Production. Polymers. 15(18): 3787. doi: 10.3390/polym15183787.

[20] Jayasekara, T., Wickrama Surendra, Y., Rathnayake, M., (2022). Polylactic Acid Pellets Production from Corn and Sugarcane Molasses: Process Simulation for Scaled-Up Processing and Comparative Life Cycle Analysis. Journal of Polymers and the Environment. 30(11): 4590–604. doi: 10.1007/s10924-022-02535-w.

[21] Mora, S., Pugno, N.M., Misseroni, D., (2022). 3D printed architected lattice structures by material jetting. Materials Today. 59(October): 107–32. doi: 10.1016/j.mattod.2022.05.008.

[22] Raz, K., Chval, Z., Sedlacek, F., (2020). Compressive strength prediction of quad-diametral lattice structures. Key Engineering Materials. 847 KEM: 69–74. doi: 10.4028/www.scientific.net/KEM.847.69.

[23] Almetwally, A.A., (2020). Multi-objective Optimization of Woven Fabric Parameters Using Taguchi–Grey Relational Analysis. Journal of Natural Fibers. 17(10): 1468–78. doi: 10.1080/15440478.2019.1579156.

[24] Jagatheesan, K., Babu, K., (2023). Taguchi optimization of minimum quantity lubrication turning of AISI-4320 steel using biochar nanofluid. Biomass Conversion and Biorefinery. 13(2): 927–34. doi: 10.1007/s13399-020-01111-3.

[25] Abdulredha, M.M., Hussain, S.A., Abdullah, L.C., (2020). Optimization of the demulsification of water in oil emulsion via non-ionic surfactant by the response surface methods. Journal of Petroleum Science and Engineering. 184(July 2019): 106463. doi: 10.1016/j.petrol.2019.106463.

[26] Bouteldja, A., Louar, M.A., Hemmouche, L., Gilson, L., Miranda-Vicario, A., Rabet, L., (2023). Experimental investigation of the quasi-static and dynamic compressive behavior of polymer-based 3D-printed lattice structures. International Journal of Impact Engineering. 180(May): 104640. doi: 10.1016/j.ijimpeng.2023.104640.

[27] Almesmari, A., Sheikh-Ahmad, J., Jarrar, F, Bojanampati, S., (2023). Optimizing the specific mechanical properties of lattice structures fabricated by material extrusion additive manufacturing. Journal of Materials Research and Technology. 22: 1821–38. doi: 10.1016/j.jmrt.2022.12.024.

[28] Galeta, T., Raos, P., Stojšić, J., Pakši, I., (2016). Influence of structure on mechanical properties of 3D printed objects. Procedia Engineering. 149(June): 100–4. doi: 10.1016/j.proeng.2016.06.644.

[29] Sood, M., Wu, C., (2023). Influence of 3D printed structures on energy absorption 17(4): 390–405.

[30] Hikmat, M., Rostam, S., Ahmed, Y.M., (2021). Investigation of tensile property-based Taguchi method of PLA parts fabricated by FDM 3D printing technology. Results in Engineering. 11: 100264. doi: 10.1016/j.rineng.2021.100264.

[31] Ahmad, M.N., Ishak, M.R., Mohammad Taha, M., Mustapha, F., Leman, Z., Anak Lukista, D.D., et al., (2022). Application of Taguchi Method to Optimize the Parameter of Fused Deposition Modeling (FDM) Using Oil Palm Fiber Reinforced Thermoplastic Composites. Polymers. 14(11). doi: 10.3390/polym14112140.

[32] Wankhede, V., Jagetiya, D., Joshi, A., Chaudhari, R., (2019). Experimental investigation of FDM process parameters using Taguchi analysis. Materials Today: Proceedings. 27: 2117–20. doi: 10.1016/j.matpr.2019.09.078.

Structural and topology optimization of steel construction profiles in solar energy systems

Cengiz Bayram[1*], Ercan Köse[2]

[1]MEB Information Technologies Teacher, Gaziantep, Turkey.
[2]Electrical-Electronics Engineering Department, Tarsus University, 33400 Tarsus, Turkey

Orcid: C. Bayram (0000-0003-0150-377X), E. Köse (0000-0001-9814-6339)

Abstract: In recent years, significant investments have been made for Solar Power Plant (SPP) plants in many countries. The installation costs of SPP plants are quite high. This situation increases the amortization period of investments. Lowering these costs during the installation phase will pave the way for more investments. One of the most important cost items of SPP is steel construction costs. In this study, we aim it to reduce the cost by designing the best performance product by reducing the weight of C profiles, one of the steel constructions used during the installation of solar panels, with shape and topology methods. The calculated weight gain for the optimized model was 7,732 kg, derived from the difference between the initial weight of 60,800 kg/m and the optimized weight of 53,068 kg/m. This represents a percentage gain of 12.717%. The results got show that shape and topological optimization can provide significant gains in terms of cost.

Keywords: Solar Energy Systems, Structural and Topology Optimization, Steel Construction Profiles, Weight Reduction, Manufacturing Engineering

1. Intorduction

With the advancement of production technologies in the manufacturing sector, the product design stages have become crucial in reducing the weight of elements affecting material selection and total weight without compromising the product's functionality. This is significant not only from a cost perspective for manufacturers but also in providing ergonomic usage for end-users and making substantial contributions to the ecosystem.

In recent times, with the widespread adoption of solar energy facilities, reducing installation costs has become a critical focus area. Factors like angle, height, wind speed, precipitation in winter, and surface contamination affect the manufacturing of solar energy facilities. Manufacturers, aware of the potential cost increase, strive to address this through various methods and techniques, such as optimization methods. Academic studies have showed the application of optimization methods in this context.

Yang and Chuang introduced the Density Method in 1993 [1]. Another method, the Homogenization Method, was proposed by Bendsoe and Kikuchi in 1998 [2]. The finite element solver Optistruct solves optimization problems using the known density method for material distribution [3]. They conducted tests on designed components to identify critical areas. They perform topolo- gy optimization to enhance fatigue life [4]. Reducing the weight of parts in vehicles will contribute to reducing the total vehicle weight. Reducing vehicle total weight is a critical parameter for structural engineering applications that reduce fuel consumption [5]. Furthermore, the determination of areas to be emptied with different geometric shapes on a part is significant, considering their relationship with other assembled components. Therefore, the location of critical stress points is vital, enabling the determination and optimization of motor, suspension, transmission, and other component mounting locations [4, 6, 7].

In order to get high-strength materials without changing the dimensions of the product to be optimized, they extract the areas are extracted from specific regions, saving time and providing a lower-cost and faster solution. Solidworks® Simulation program is used for topology optimization to achieve this [8]. The aim of topology optimization is to find the most suitable material distribution that maximizes rigidity [9].

Today, more advanced techniques are used, and it can apply finite element methods to complex problems. Optimization is a tool used to maximize the benefit of a structure under a specific aim. In structural optimization, the "best structural design" is selected in three categories: Size Optimization, Shape Optimization, and Topology

Optimization. Topology optimization aims to find the best material distribution in a given structure, primarily managed because of weight savings. There are many applications [10, 11 12]. While shape and size optimization methods are intriguing, topology optimization focuses on optimizing the thickness and boundaries of parts to get a design that maximizes the use of the entire geometry area [13]. Structural topology optimization aims to prevent the use of unnecessary material and to create a structure that will best transfer loads to supports. It is used to get a system structure that meets design constraints as effectively as possible. Thus, topology optimization aims to create a structure with the minimum weight of the part and maximum strength [14].

Topology optimization seeks the most suitable configuration for structural optimization [15]. Using solid modeling and finite element analysis of these models in a computer environment reduces the cost of previous designs and significantly reduces the number of tests. The analysis of the tram's crash attenuating structure resulted in a lightweight design [16].

Topology optimization, which allows for the design of lightweight parts by distributing materials appropriately while maintaining the part's function in manufacturing technologies, is an effective method in the manufacturing sector [17].

In this comprehensive study, the weight of C-profiles, integral to steel constructions for solar panel installations, underwent optimization through shape and topology methods, with the dual objectives of enhancing performance and minimizing costs. The rigorous application of shape optimization involved refining geometric configurations for optimal load distribution, while topology optimization strategically redistributed material to improve mechanical properties and reduce unnecessary weight. The outcomes revealed a significant effectiveness in achieving these goals, showcasing superior performance metrics in the optimized C-profile designs. Beyond structural enhancements, the resultant weight reduction not only contributes to increased efficiency but also aligns with the broader aim of cost-effectiveness in solar panel installations. This research not only advances the understanding of optimizing steel constructions for renewable energy infrastructure, but also lays the groundwork for future innovations in the field, emphasizing the role of innovative engineering in fostering sustainability and economic viability.

2. Material and Method

In this study, we have targeted the optimization of the final product using shape, structural, and topology methods. The optimization objectives are shown in Figure 1. The initial problems are shown at left hand side and the optimal solutions are shown at the right-hand side. To examine structural and topological optimization for the optimization objectives, it is necessary.
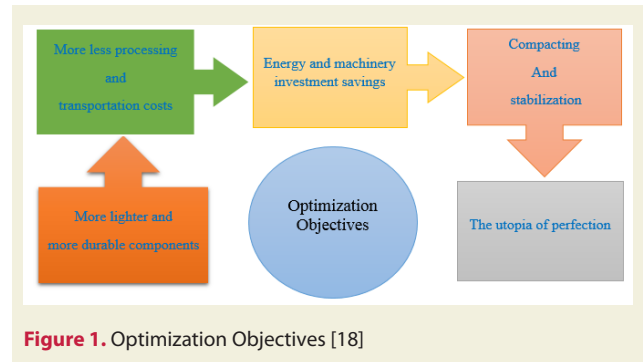
Figure 1. Optimization Objectives [18]

2.1. Structural Optimization

As shown in Figure 2, Structural Optimization encompasses various optimization types, including size, shape, topology, and topography optimization. Size optimization focuses on optimizing the profiles in the design, shape optimization targets the optimal designs for radii and holes, topology optimization aims to achieve the most suitable material distribution within the design volume, and topography optimization is used to get the best designs on sheet metal plates.
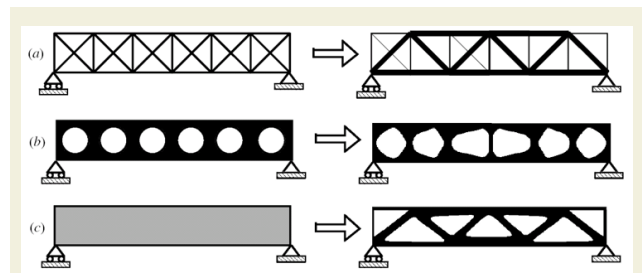
Figure 2. Structural Optimization, a) Sizing optimisation, b) Shape and c) Topology optimisation[10].

2.2. Topology Optimization

Under the specified constraints and objectives, achieving the most suitable material distribution, getting the best design, and creating high-quality and high-performance products are the preferred optimization method in the additive manufacturing sectors.

When establishing the optimization implementation processes, they conducted the analyses based on predetermined objectives to determine the steps to be taken, the techniques and methods to be used, and the materials to be developed in line with the defined goals.

2.3. Optimization and Optimization Processes

The process of creating the best-performing product by subjecting the existing product to forces under certain conditions, after determining the sensitivity of the lower and upper constraints, with a focus on reducing both material selection and total mass before delivering the product to the user.

Optimization can contribute in three ways: contributions to manufacturers, contributions to users, and con-

tributions to the environment.

Through optimization, selecting the right materials for research and development activities, reducing the total weight through light weighting efforts, and contributing to the lifespan of machines used in manufacturing technologies can provide advantages to manufacturers from a cost perspective. The performance product got through optimization can offer comfort to the end user. The optimized design product, by influencing the correct processing of resources and reducing the emission of toxic gases into the environment, contributes to the preservation of the natural environment.

2.3.1 Creation of Content

They showed the general stages of content creation in Figure 4. While determining our content; we examined scientific articles on weight reduction. In the articles reviewed, experience gained in how optimization studies were created using shape, structural and topology methods. In line with these, we have transferred solar panels to the optimum designs of the constructions.

In this study, we have developed an optimal process to reduce the steel construction installation costs of SPP. We give these process stages given in Figure 3.

2.3.2 Material Development

In this study, we have designed 52 models created with galvanized steel material in three dimensions using Solidworks solid modeling software. In each of the 4 C-profiles in the models, we used 20 circular geometric shapes for hollowing, with the condition that their positions remained fixed. This resulted in 80 circular forms across the 4 C-profiles. Starting with a minimum diameter of 1mm, the diameter increased incrementally, reaching a maximum diameter of 99 mm in each case, aiming to reduce the total weight. Each time, a total force of 1920 N applied, and the physical behavior of the C-profiles under force analyzed using the Solidworks Simulation program and illustrated with graphs.

2.3.3 Modeling and Analysis in Optimization

Using software in manufacturing technologies provides designers with multiple options. As technology advances, designers can create innovative designs. They can analyze the created models with simulation software, and it can document multiple analysis results of the product in reports. By examining the analysis results, the designer can identify and review any errors compared to reference models gained through experience. Afterward, necessary interventions can be made to design variables to improve the final performance product. It showed the Optimization Algorithm used in product development in Figure 5. We can group optimization terms under four headings: constraints, design variables, optimization area, and performance product determination.

2.3.3.1 Constraints

The models to be subjected to analysis are considered under specific loads and constraints, with the reference models being the models without any constraints, i.e., the initial version of the model, the model with lower constraints, and the model with upper constraints. The ability of other design variables to respond to these reference models is then evaluated. In the model with lower constraints, the smallest diameter circular sections (Q=1 mm) to be removed from the areas subjected to optimization are shown in Figure 6. In the model with upper constraints, the smallest diameter circular sections to be removed from the areas subjected to optimization (Q=99 mm) are shown in Figure 7.
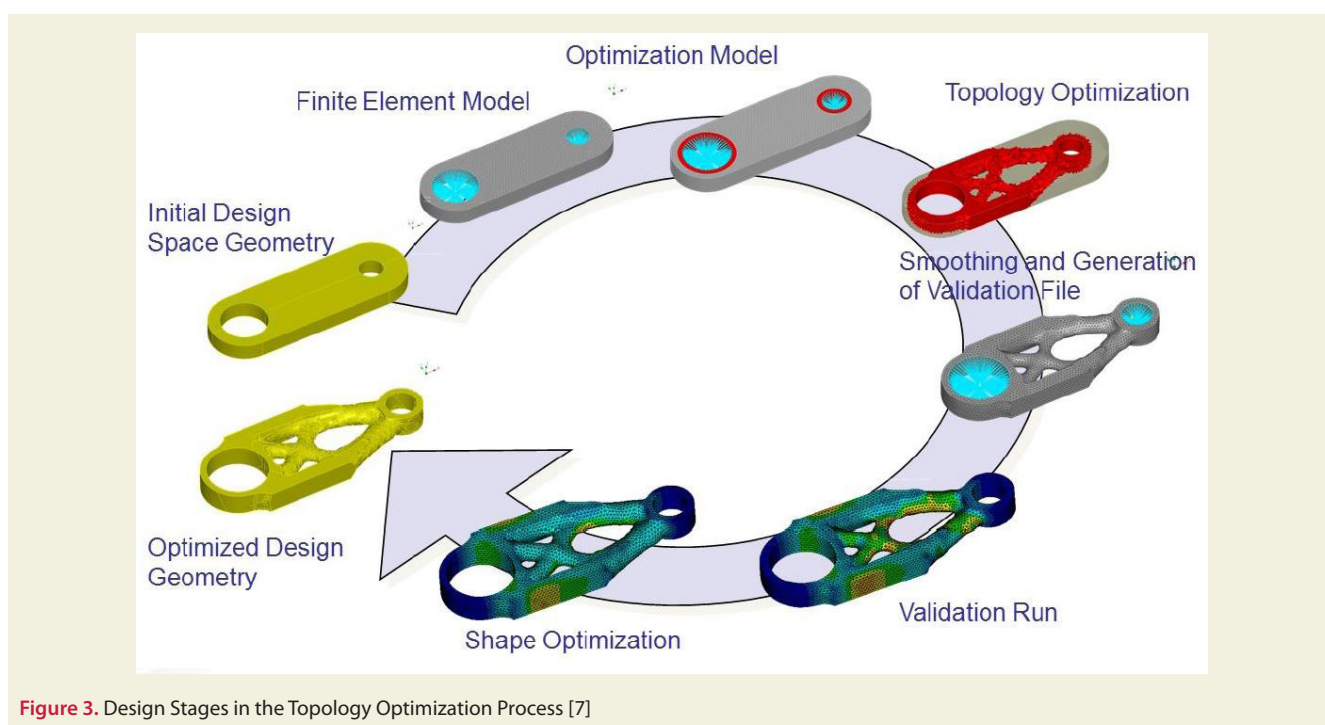
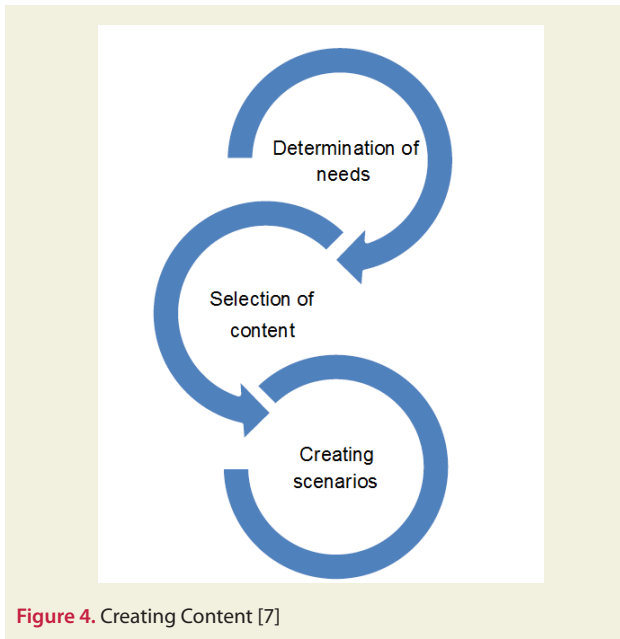**Figure 3.** Design Stages in the Topology Optimization Process [7]

Figure 4. Creating Content [7]

2.3.3.2 Design Variables

Design variables are parameters that can be modified beyond the material selection or fixed loads, different from the reference models. In the case of solar panels, the material used is galvanized steel, and the variable parameters are the diameters of the circular cutouts in the C-profiles. Apart from the models with lower and upper constraints, the circular sections to be removed from the areas subjected to optimization range from a diameter of (Q=2 mm) to a diameter of (Q=98 mm).

2.3.3.3 Optimization Area

The areas where topology optimization will be applied based on changing parameters, excluding the boundaries

that the design cannot respond to, are the optimization areas. These areas are shown in Figure 8.

2.3.3.4 Determination of Performance Product

The manufacturer can optimize the production technologies to obtain the best product, also known as the optimal product or performance product that can provide the desired response to the manufacturer, user, and the environment based on the analysis results while considering the comfort desired by the user.

2.3.3.5 Objective Function

It is expressed as the ultimate goal of the optimization process. For example, it can provide advantages such as user comfort, cost advantage for the manufacturer, and environmental friendliness. It is defined as f(x); the objective function. The type of the objective function depends on the nature of the problem.

Details of the processing stages of the selected sample part are shown in Figure 9.

2.3.3.6 Application of the Method

A general optimization problem can be defined as making an f(x) function, dependent on the variable x and subject to constraints, as small or as large as possible [19].

Where x represents a design vector consisting of a series of variables in the design process, known as an n-dimensional vector. f(x) is defined as the objective function.

Shown in Equations (1) and (2) and represent inequality and equality constraints, respectively. These design constraints are the requirements that must be met to obtain an acceptable design. In a general Topology Optimiza-
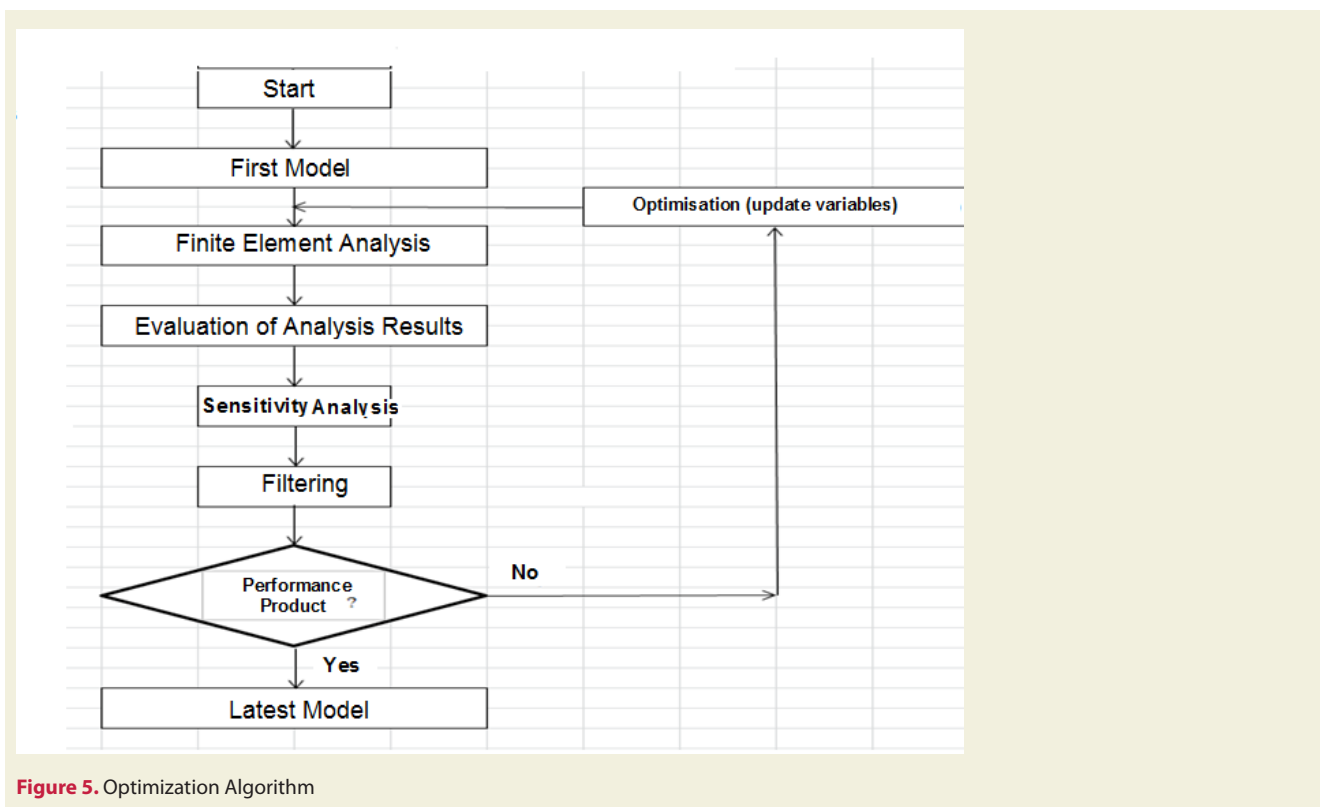
Figure 5. Optimization Algorithm

tion problem statement, for each finite element produced during the network generation phase (*i*), a design variable (ηi) is assigned, which is an internal pseudo-density of the model. The pseudo-density ranges from "0" to "1",

where $\eta i = 0$ represents material to be removed from the design, and $\eta i = 1$ represents material to be retained in the design [19].

Figure 6. Lower Constraint Will Apply "Model-Q-1"

Figure 7. Upper Restriction Will Apply "Model-Q-99"

Figure 8. Areas to be subjected to optimisation in the models
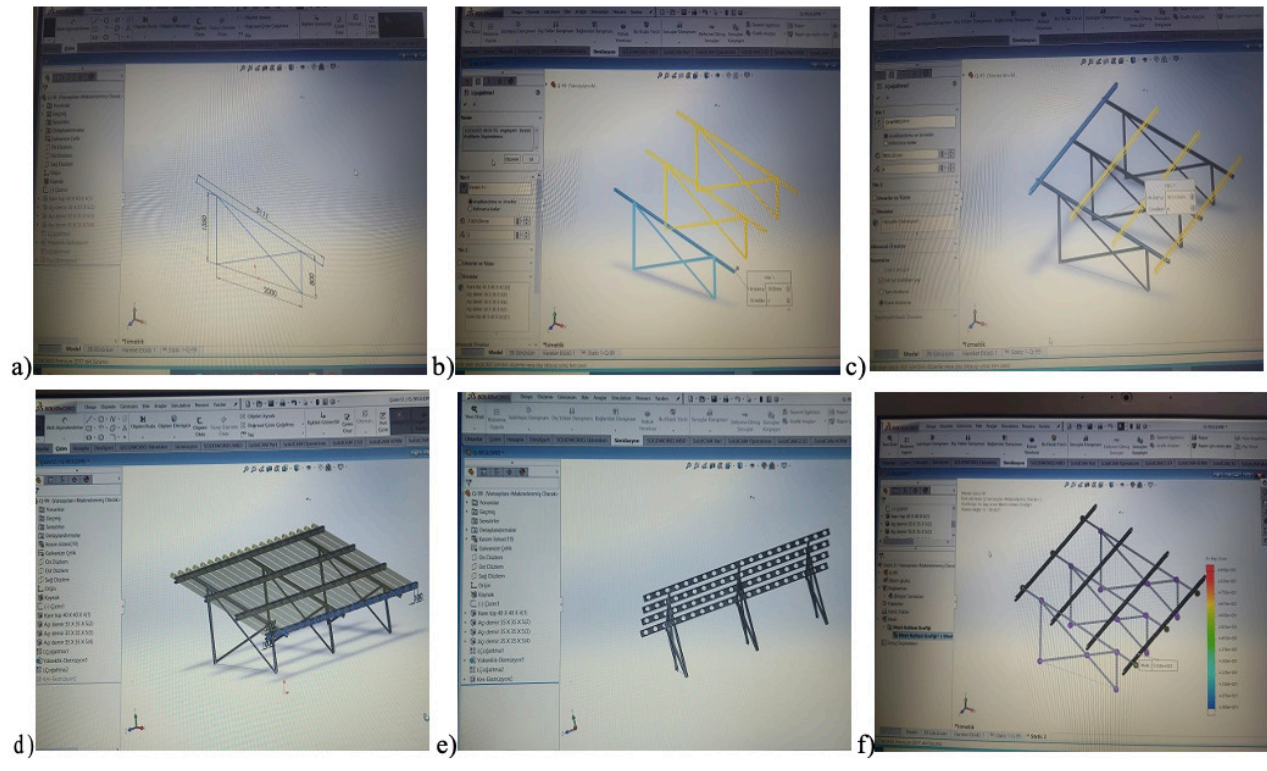
Figure 9. Selected sample part Selected sample part; a) Drawing the bottom profiles, b) Creating the bottom profiles, c) Placing the C profiles, d) Determination of the areas to be emptied from C profiles, e) Emptied version of the design, f) Creating the mesh structure of the design.

$$1 < g_j(x) < 100 \qquad j = 2,4,6, \dots ,99,9 \tag{1}$$

upper restriction diameter (Q=99mm) was taken.

$$1 < l_j(x) =< 100 \qquad j = 0.1, 0.2, \dots ,1 \tag{2}$$

$l_j(x)$ lower restriction diameter (Q=1mm) shown in equation (3) was taken.

$$l_j(x) = 0 \qquad j = 0 \tag{3}$$

The initial diameter of the model (Q = 0 mm) was taken.

The Topology Optimization method can also be expressed as follows:

$f(\eta_i)$ function is the smallest / is about to become the greatest value of making,

$$1 < \eta_i(x) < 1 \quad i = 1,2,4,6, \dots ,N; \; g_{aj} < g_j < g_{uj}$$

$$j = 1,2,3,4, \dots ,M \tag{4}$$

In the equations (4); N = number of finite elements, M = number of constraints, g_j = calculated constraint value g_{aj} and g_{uj} = are defined as lower and upper constraint limits [19].

2.3.3.7 Perspective Rear Views of Models with appling Lower Constraint

2.3.3.8 Finite Element Analysis

Finite Element Method, helps the designer to form an idea about the behavior of the model formed by the combination of all the parts that make up the design, against certain forces and strains, before production.

Meshing

It is a critical step for the analysis of models. The length, tolerance and on-site mesh control of the part ensure that the features of the product to be produced in the process of production technologies are shown in detail in the technical specifications. Mesh control; It allows specifying different element sizes for nodes, vertices, surfaces, and edges [20].

3. Results and Discussion

3.1. Profiles' Weight and Cost Calculations

A total of 52 CAD model designs were created in line with the content. The designed CAD models are subjected to finite element analysis in the Solidworks® Simulation program using a mixed curvature-based mesh structure. For each model in accordance with the prepared scenarios, results in the form of Static Node Stress, Static Tension, Static Displacement, and Safety Factors were obtained in graphical format. Table 1 below compiles the dimensions of solar panels commonly used in residential and commercial areas. The first noticeable aspect in the table with average measurements is the direct proportionality between the number of cells and panel dimensions. It can be observed that 72-cell panels are approximately 33 cm longer than 60-cell panels [21].

Figure 10. Model-Q-1

Figure 11. Model-Q-40
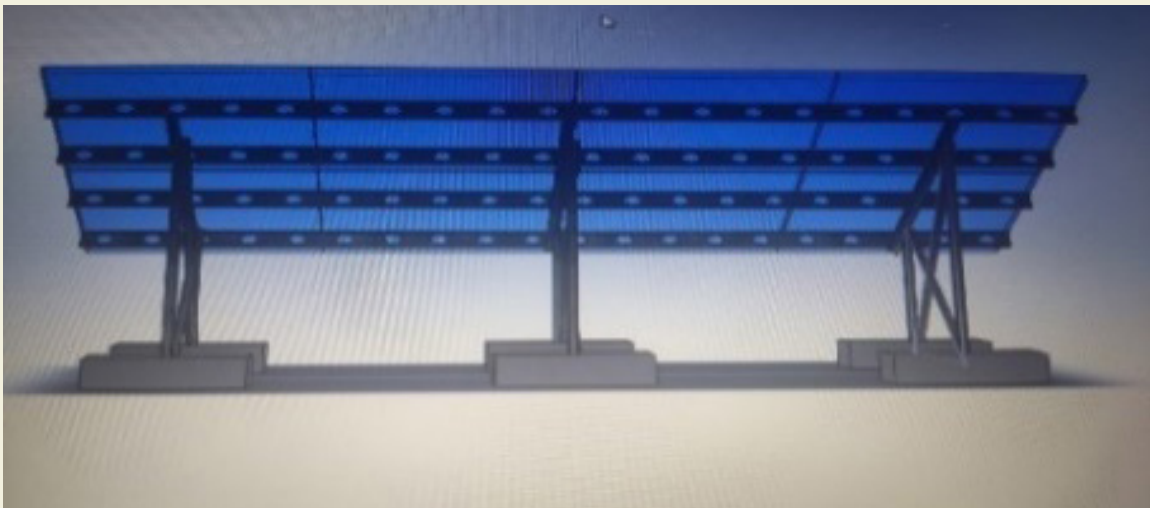
Figure 12. Model-Q-70

Table 1. Dimensions of solar panels used in residential and commercial areas [21].

Panel Properties	Residential	Commercial
Number of Cells	60	72
Average Height (cm)	165	198
Average Width (cm)	100	100
Average Thickness	3,5-5	3,5-5

Solar panel calculation for home; Approximately 20 panels are used for a 6kW system. The system to be installed will be approximately 8.5 meters wide and 4 metres long. In total, it will cover an area close to 33 square meters [21].

The weights of some panels are given in Table 2. While a panel with a power of 275 W weighs 20 kg, a panel with a power of 320 W weighs 19 kg [21].

Table 2. Weights of Solar Panels Used in Residential and Commercial Areas [21].

Brand	Watt	Type	Number of Cell	Weight (kg)
Elin Plus	320	Monocrystalline	60	19
Elin Plus	320	Monocrystalline	60	19
Alfasolar	275	Polycrystalline	60	20
Alfasolar	325	Monocrystalline	60	20
Jinko	405	Mono Perc	Half Cell-144	22,5
Elin Plus	395	Monocrystalline	72	22,5
Alfasolar	400	Monocrystalline	72	24

In this study, the dimensions of commercially installed solar energy panels are used. Dimensions, weights and properties of a panel used in the models;

Width=1000 mm, Length= 1980 mm, Brand=Alfasolar,
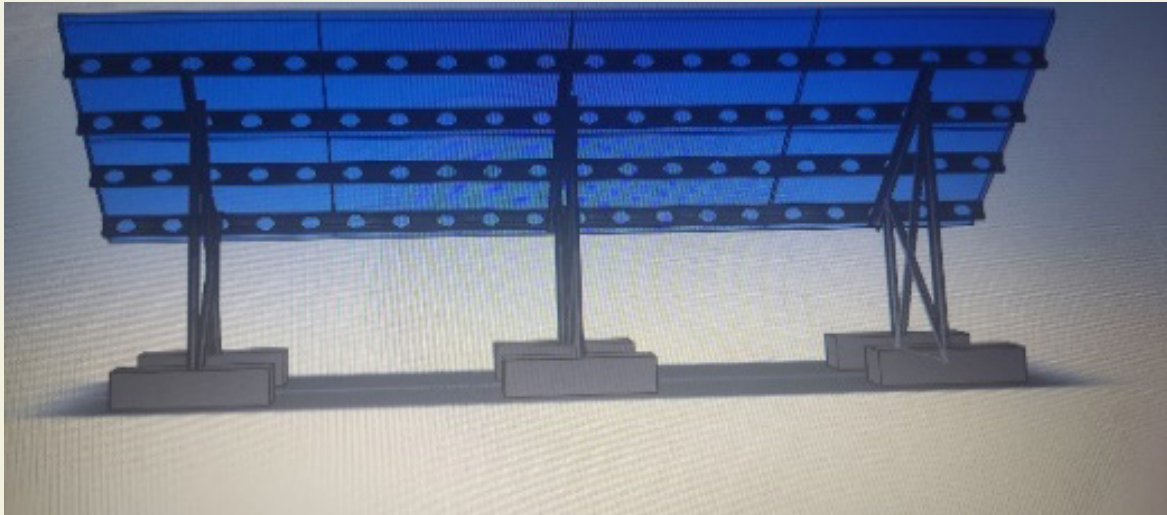
Figure 13. Model-Q-90
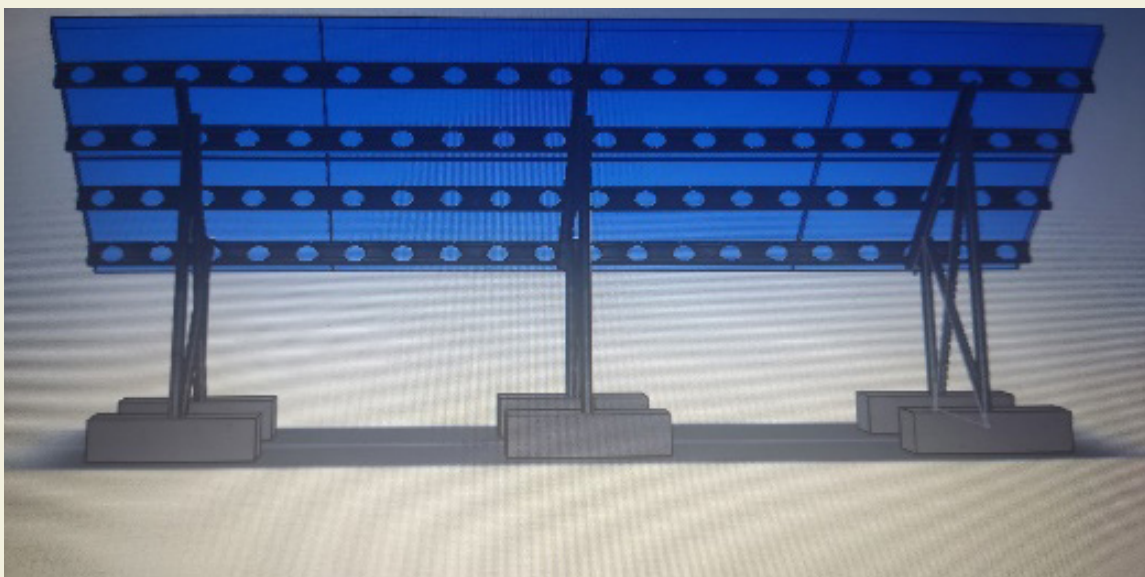
Figure 14. Model-Q-99

Type: Monocrystalline, Number of cells=72, Weight=24 kg, Total Weight = 24×8= 192 kg (Figure 15 and 16).

Force applied for analysis; 1 kg = 10 N

Applied force = (Total weight) × (Newton in kg) = 192 × (10 N) = 1920 N

3.2 C Profiles Weight Calculation

The properties of Profile C used in the model are given in Table 3. 20 circular forms will be cut from 1 C profile used in the model. A total of 80 circular forms will be cut from 4 C profiles used in the model (Figure 17 and 18).

In the proposed model, 4 C profiles were utilized with a total weight of 60,800 kg/m and a combined length of 16,000 mm, equivalent to 16 meters. Following optimization, the weight of the refined model (Figure 10-14), designated as "Model-Q-90," was determined to be 63,068 kg/m. Consequently, the calculated weight gain for the optimized model was 7,732 kg, derived from the difference between the initial weight of 60,800 kg/m and the optimized weight of 53,068 kg/m. This represents a percentage gain of 12.717%. The optimization process resulted in a notable improvement, enhancing the efficiency and performance of the model.

Table 3. Specifications of Profile C used in the model

Parameter	Specifications Values
Material Type	Dip galvanised steel
Size	4000 mm
Width	250 mm
Thickness	2 mm
Material Specific Gravity	7,6 gr. / cm^3
Size 1000 mm Weight of profile C	3,80 kg/m
Weight of 4000 mm C profile used	15,200 kg/m
Weight of 4 pieces of 4000 mm C profile used in the model	4×15,200 = 60,800 kg/m

3.3 Reduced Graph of Weights of Models

Proposed Model "Model-Q-90" Result Graph

Model-Q-90 static node stress, static strain, static displacement, and safety factor result graphs, along with the maximum and minimum values for each graph, are shown in Figure 19. As the diameters of the circles to be removed from the areas subjected to optimization in the C-profiles, one of the model components, increase, and the total weight of the model decreases. As the diameters of the circles to be removed from the areas subjected to
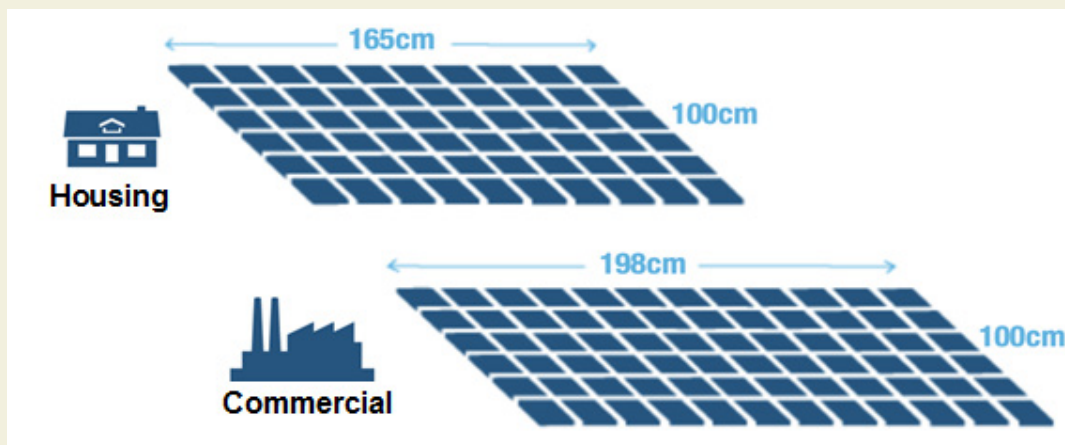
Figure 15. Dimensions of solar Panel Used in residential and commercial areas [21].
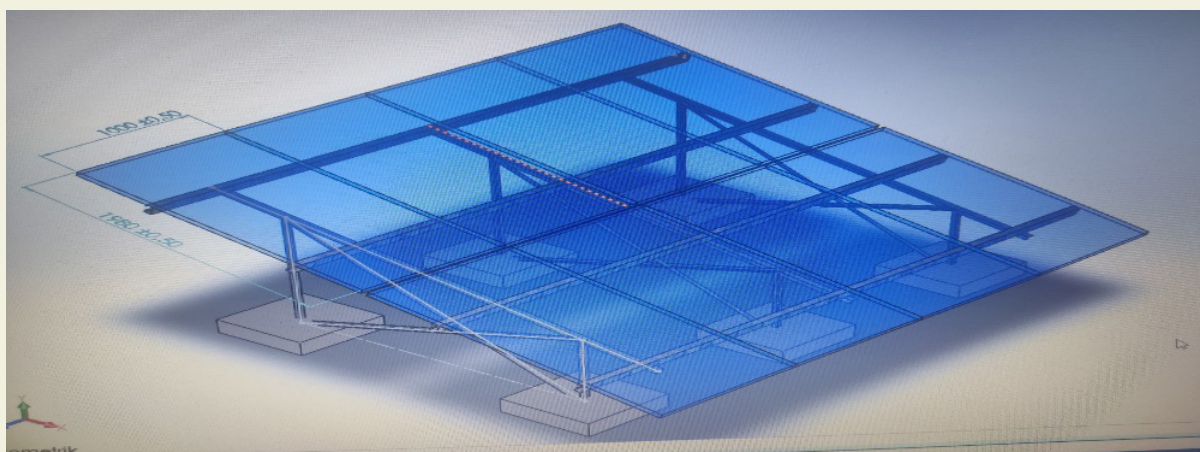
Figure 16. Dimensions of preferred solar panels in a selected model
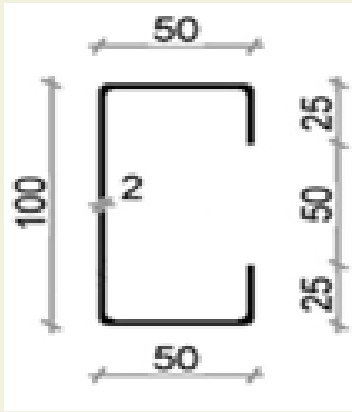
Figure 17. Dimensions of Dip Galvanised Steel with C Profile Structure [22]

optimization in the C-profiles, one of the model components, increase, stress at the static node points, i.e., the junction points of the elements, increases because the load is more pronounced at these node points. As the diameters of the circles to be removed from the areas subjected to optimization in the C-profiles, one of the model components, increase, static strain is generated and generally increases due to the logic of pixels exposed to load from the remaining areas, causing points to push against each other. As the diameters of the circles to be removed from the areas subjected to optimization in the C-profiles, one of the model components, increase, static displacements also generally increase due to the logic of pixels exposed to load from the remaining areas, causing points to push against each other, resulting in horizon-
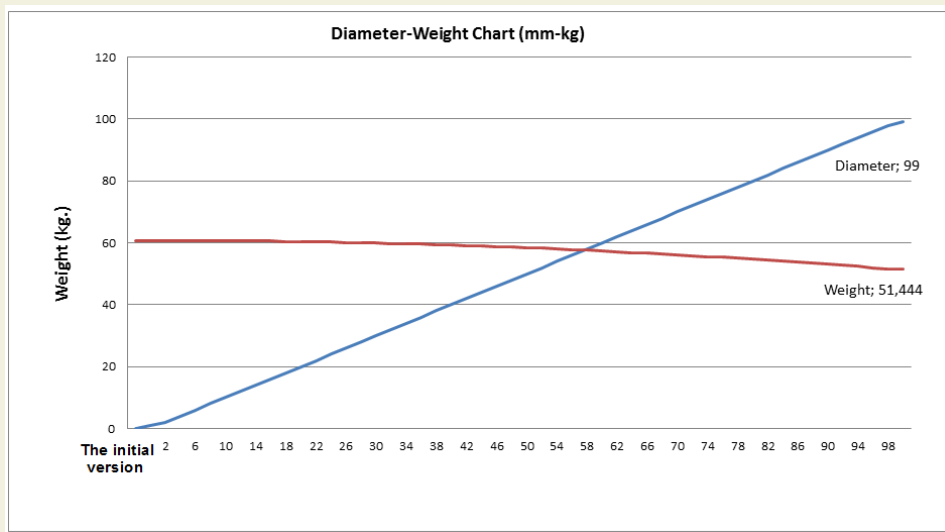
Figure 18. Reduced Weights of the Models
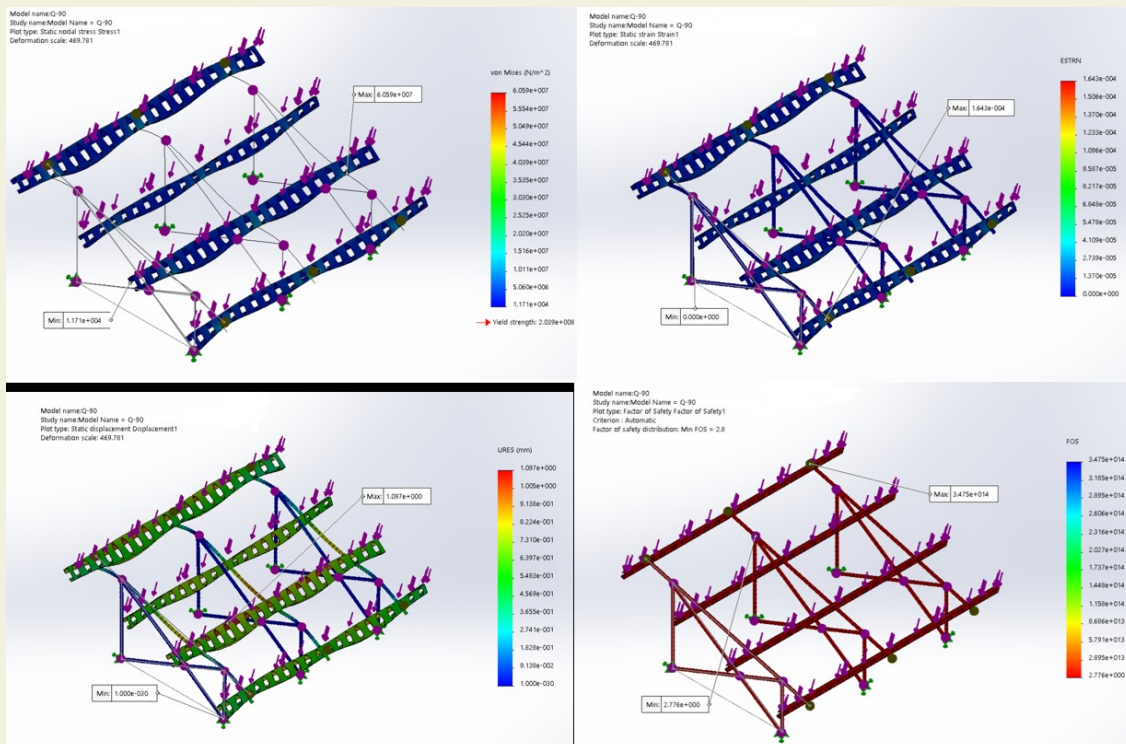
Figure 19. Proposed model "Model-Q-90" result graphs

tal displacements in the direction of the applied force on the component axis. As the diameters of the circles to be removed from the areas subjected to optimization in the C-profiles, one of the model components, increase, the safety factor generally decreases as the remaining areas are exposed to load. When the applied force on the models is reduced, the safety factor also increases. As the diameters of the circles to be removed from the areas subjected to optimization in the C-profiles, one of the model components, increase, deformations generally decrease as the area exposed to load decreases.

4. Conclusion

In this study, the structural and topological optimization methods were used to reduce the weights of C-profiles in steel construction solar panels. Initial model, models with lower constraints, and models with upper constraints considered as references based on experience, and other models treated as design variables. We conducted finite element analysis under an objective function to reduce their weights. The results, including Static Node Stress, Static Tension, Static Displacement, and Safety Factors, for the 52 models analyzed using finite element analysis were graphically presented, and we showed the maximum values in tables. This study has shown that optimization of models based on an objective function can contribute significantly to reducing their weights and costs, and design-based methods can be utilized during the installation of solar power plants. It emphasizes the applicability of design-based methods in the installation phase of solar power plants, affirming the potential for enhanced efficiency and cost-effectiveness in solar energy infrastructure.

Reference

[1] Yang, R.J., Chuang, C.H. (1993). Optimal topology design using lineer programming. Structural Optimization. 68: 265-290.

[2] Bendsoe, M.P., Kikuchi, N. (1988). Generating optimal topologies in structural design using a homogenization method. Computational Methods Application Mechanics Engineering, 71(2): 197-224.

[3] Albak, E.İ. (2019). Optimum Design of Brake Pedal Using Topology Optimization Method Intended for Weight Reduction on The Formula SAE Car. International Journal of Engineering Research and Development, 11(1): 328 – 334.

[4] Şen, Ş., Yaşar, M., Koçar, O. (2018). Stress Distribution Analysis and Topology Optimization for Semi-Trailer. Karaelmas Science and Engineering Journal, 8(1): 309-316.

[5] Doğru, M.H. (2019). Topology optimization of truck chassis under multi loading conditions. El-Cezeri, 6(3): 856-867.

[6] Rajappan, R., Vivekanandhan, M. (2013). Static and modal analysis of chassis by using FEA. International Journal of Engineering and Science, 2(2): 63-73.

[7] Kahraman, F., Küçük, M. (2020). A Research on Weight Reduction Application with Topology Optimization in the Automotive Industry. European Journal of Science and Technology, 20: 623-631.

[8] Özsoy, K., Şentürk, E., Aydoğan, D., Korucu, Ö.E. (2020). Topology Optimization For 3D Printer Technology: A Study On The N95 Mask, Turkish Journal of Nature and Science, 9(Special Issue): 152-159.

[9] Topaç, M.M., Özmen, B., Deryal, U., Selbes, O. (2019). Design of an Independent Suspension for a Special Type Semi-Trailer: Conceptual Design Studies. Journal of Polytechnic, 22 (1): 95-102.

[10] Bendsoe, M. P., Sigmund, O. (2003). Topology optimization: theory, methods, and applications. Springer Science & Business Media.

[11] Duddeck, F. (2008). Multidisciplinary optimization of car bodies. Structural and Multidisciplinary Optimization, 35: 375-389.

[12] Volz, K.H., Zimmer, H. (2007) Optimizing Topology and Shape for Crashworthiness in Vehicle Product Development, IABC International Automotive Body Congress, Berlin.

[13] Yüksel, O. (2019). An overview on topology optimization methods employed in structural engineering. Kırklareli University Journal of Engineering and Science, 5(2): 159-175.

[14] Kazakis, G., Kanellopoulos, I., Sotiropoulos, S., Lagaros, N.D. (2017). Topology optimization aided structural design: Interpretation, computational aspects and 3D printing. Heliyon, 3(10), e00431.

[15] Mortazavi, A. (2019). The performance comparison of three metaheuristic algorithms on the size, layout and topology optimization of truss structures. Mugla Journal of Science and Technology, 5(2): 28-41.

[16] Dener, B. (2021). Reducing mass of collision absorber construction using structural optimization methods, PhD. Thesis, Bursa Uludag University, Bursa-Turkey.

[17] Top, N., Gökçe, H., Şahin, İ. (2019). Topology Optimization for Additive Manufacturing: An Application on Hand Brake Mechanism. Journal of Selcuk-Technic, 18(1): 1-13.

[18] Okudan, A., (2018, 6 Eylül). The information on Topoloji Optimizasyonu was obtained on August 9, 2020, from the following website: "https://tr.linkedin.com/pulse/topoloji-optimizasyonu-101-ahmet-okudan."

[19] Öğüçlü, Ö., Yıldırım, Ç.Y., Weight reduction application with topology optimization in recycling machines.

[20] SOLIDWORKS Web Help, <Help.solidworks.com>, January 16, 2023.

[21] Solaravm.com, <solaravm.com>, January 20, 2023.

[22] Solarcelik.com, <solarcelik.com/solar- steel-profiles-price-list >, January 17, 2023.

Investigation of the velocity, mach number, and turbulent parameters for different projectile rear geometry

Mehmet Hanifi Doğru[1*], İbrahim Göv[2]

[1] Department of Pilotage, Gaziantep University, Gaziantep, Türkiye.
[2] Department of Aeronautics and Astronautics Engineering, Gaziantep University, Gaziantep, Türkiye.

Orcid: M.H. Doğru (0000-0001-6038-8308), İ. Göv (0000-0002-5513-0158)

Abstract: A firearm projectile consists of four main parts. The end part of the cartridge is called the bullet (core). When the weapon is fired, the bullet (core) shoots towards the target. In the literature, there are studies examining projectile geometries in terms of projectile velocity, range, and impact factor. By redesigning the geometric features, the velocity and turbulence states of the projectile can be improved. Therefore, in this study, a projectile with different rear geometries is analyzed in terms of velocity, turbulence energy, and Mach number. For projectile rear geometry, Sharp, 45-degree, and curve rear geometries are analyzed. After the analysis, parameters such as velocity, turbulent energy, and Mach number were analyzed. The results were then compared with each other and the most effective geometry was obtained.

Keywords: projectile, rear geometry, velocity, turbulent energy.

1. Introduction

Turbulence energy and velocity distribution are investigated for three different projectile tip shapes with different tip geometries. The maximum velocity drop according to the projectile tip geometry was determined. It has been determined which geometry causes the maximum velocity decrease [1].

Ballistic impact performance was investigated for the different tip types of bullets. Impact energy, deformation, and stress parameters were analyzed and compared to each other [2].

Christman and Gehring conducted an experimental study on the effect of phases on crater dimensions. Steel and aluminum rods with different aspect ratios were impacted into different target materials at different impact velocities [3].

In the study conducted by Shokrieh and Javadpour, a constant thickness armor was investigated. This armor consists of two layers, kevlar and ceramic based. LsDyna was used to obtain the ballistic velocity limit and the optimum armor thickness was determined [4].

The study was carried out by Lecysyn et. al. to analyze the situations that can occur when a high-velocity projectile hits a tank filled with liquid. The authors focus on projectile target interactions and describe how the reduction of projectile velocity is related to the initial conditions of the target [5].

The boundary layer separation was investigated during flight time for supersonic bullets by Rausch et. al [6] and Srivastava [7]. The bullet flight stability was studied in terms of supersonic-boundary-layer separation.

A 155 mm standard bullet was utilized. For the aerodynamic-properties of the bullet, minimal wings were added to the bullet's shoulder to investigate the separation. Comparison and discussion were performed for the boundary layer structures and aerodynamic data by Ma et al [8].

The flow concept, which has induced shock, was investigated by Jiang et al [9] using a supersonic projectile traveling in tubes. This study is based on the investigation of numerical data obtained by Gupta et. al. when projectiles with different nose geometries impacted the target plate.

A pneumatic gun was used to shoot at different projectile velocities at different thicknesses of the target plate. At the end of the study, the effects of bullet nose geometry on the velocity and deformation of the target plate were obtained. With this information, the thickness of the plate was tried to be estimated. [10]

As a result of the literature review, it was determined that there are very few studies on the flow analysis of projectiles and almost no studies on the rear geometry of projectiles. Therefore, in this study, the effects of the rear geometries of the projectiles on the velocity, Mach number, and turbulence parameters of the projectile are investigated.

2. Methodology

The effect of the rear geometry of the projectile is investigated to compare turbulence energy, Mach number, and velocity distribution of the projectile. The study is performed by using different three rear shapes which are sharp, 45-degree, and Curve shapes as shown in Figure 1. For projectile geometry, a 50-caliber projectile is used. 500 m/s initial velocity is defined for the projectile [1].
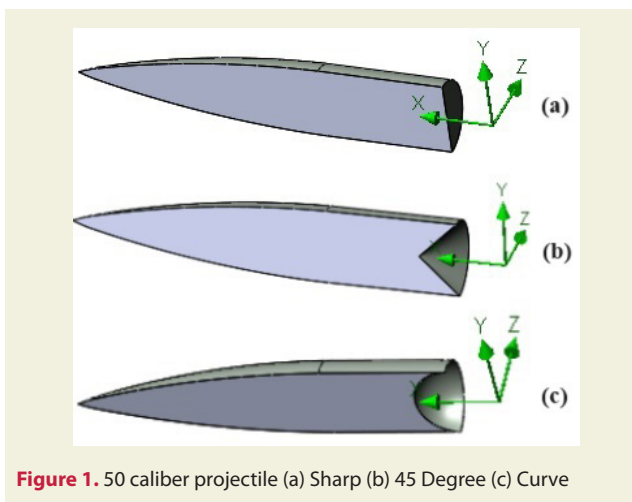
Figure 1. 50 caliber projectile (a) Sharp (b) 45 Degree (c) Curve

Turbulent energy, Mach number, and velocity of the projectile are achieved for each rear geometry at the end of the study.

Table 1. Dimensions of the flow domain

Axis	Dimension
X	0.5m
-X	0.3m
Y	0.15m
-Y	0.15m
Z	0.15m
-Z	0.15m

To perform this study, the SolidWorks flow simulation toolbox is used. The flow dimensions and view are given in Table 1 and Figure 2. For this flow analysis, external flow is used. In the computational domain, the distance -X is considered long in order to investigate the continuation of the backflow in more detail.

SolidWorks flow toolbox can be used for turbulent and laminar flows. Lam and Bremhorst proposed damping functions by using a modified k-ε turbulence model [11]. This describes transitional flows, turbulent, and laminar

homogeneous fluids consisting of the following turbulence conservation laws as given in equations 1-6.
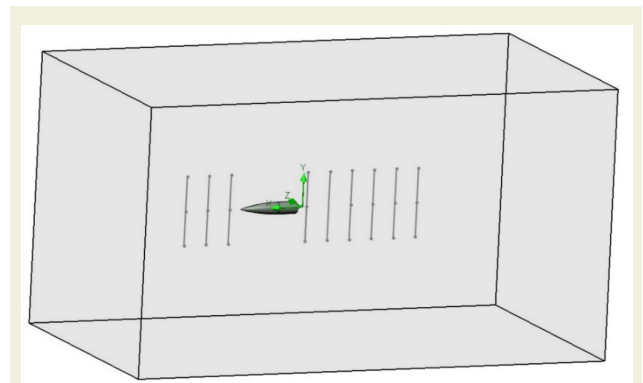
Figure 2. Flow domain view

$$\frac{\partial \rho k}{\partial t} + \frac{\partial \rho k u_i}{\partial x_i} = \frac{\partial}{\partial x_i}\left(\left(\mu + \frac{\mu_t}{\sigma_k}\right)\frac{\partial k}{\partial x_i}\right) + \tau_{ij}^R \frac{\partial u_i}{\partial x_j} - \rho\varepsilon + \mu_t P_B \quad (1)$$

$$\frac{\partial \rho \varepsilon}{\partial t} + \frac{\partial \rho \varepsilon u_i}{\partial x_i} = \frac{\partial}{\partial x_i}\left(\left(\mu + \frac{\mu_t}{\sigma_\varepsilon}\right)\frac{\partial \varepsilon}{\partial x_i}\right) + C_{\varepsilon 1}\frac{\varepsilon}{k}\left(\tau_{ij}^R \frac{\partial u_i}{\partial x_j} + C_B \mu_t P_B\right) - f_2 C_{\varepsilon 2} \quad (2)$$

$$\tau_{ij} = S_{ij} \quad (3)$$

$$\tau_{ij}^R = \mu_t S_{ij} - \frac{2}{3}\rho k \delta_{ij} \quad (4)$$

$$S_{ij} = \frac{\partial u_i}{\partial x_i} + \frac{\partial u_j}{\partial x_i} - \frac{2}{3}\delta_{ij}\frac{\partial u_k}{\partial x_k} \quad (5)$$

$$P_B = -\frac{g_i}{\sigma_B}\frac{1}{\rho}\frac{\partial \rho}{\partial x_i} \quad (6)$$

The mesh structure is created by using the unstructured mesh method as given in Figure 3. The optimum element number is obtained as 450000 elements according to the mesh accuracy study.
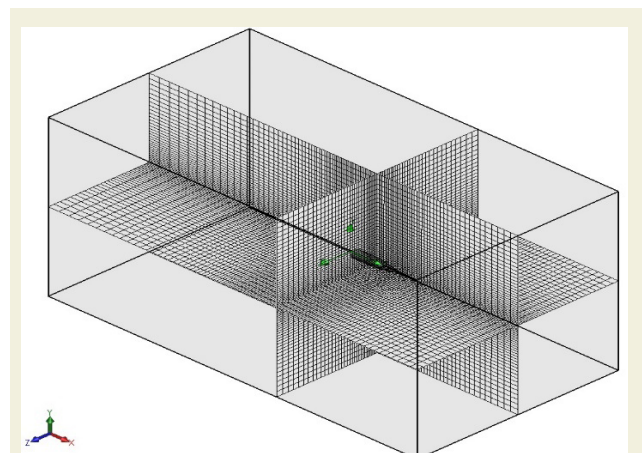

Figure 3. Mesh view of projectile

In the analysis, measurements were taken from different distances of the projectile within the computational domain as shown in Figure 4. In these measurements, velocity, Mach number, and turbulence parameters were obtained and information about the state of the flow was tried to be obtained.

Measurements were taken at -5D, -3D, and -D distances to determine whether there was any flow variation in the distance in front of the projectile tip.

3. Results and Discussions

3.1. Sharp Type Rear

Sharp-type rear geometry is analyzed in terms of the velocity distribution as given in Figure 5. The geometric information of the projectile is used as length is 64.63 mm and diameter is 13 mm for the projectile. 500 m/s initial velocity is defined for the projectile.
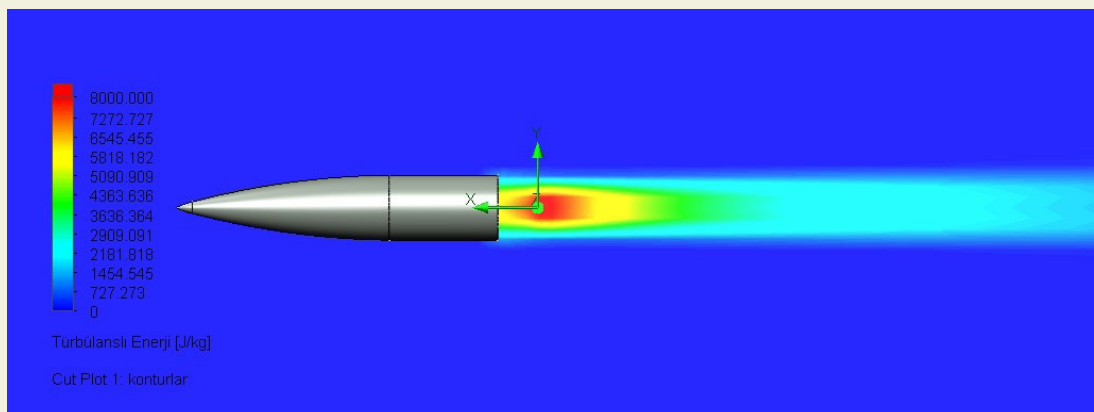
Figure 6 shows that the maximum velocity decrease is obtained at nearly 28 m/s in D measure after the rear of the projectile. It is observed that the speed decrease gradually decreases with increasing distance D.

Mach number is calculated according to the velocity of the projectile as nearly 1.45. Figure 7 and Figure 8 show that the maximum Mach number decrease is found as 0.087 in D measure after the rear of the projectile.

Mach number distribution is given in Figure 8 for all D measures.
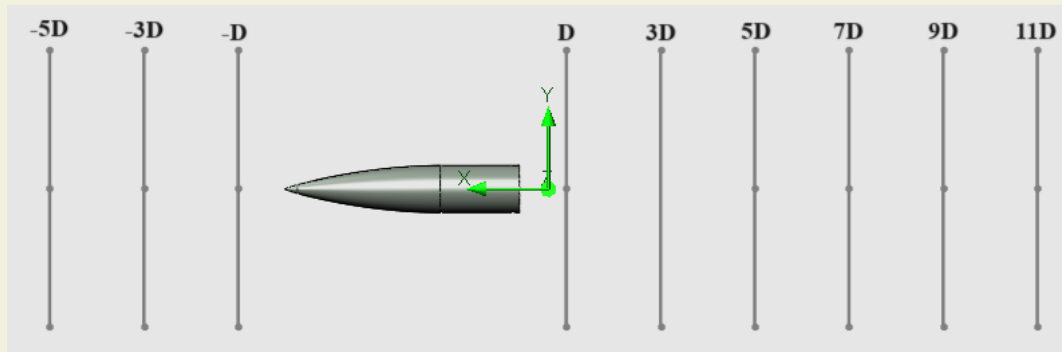
Figure 4. Measurement location for flow in the computational domain
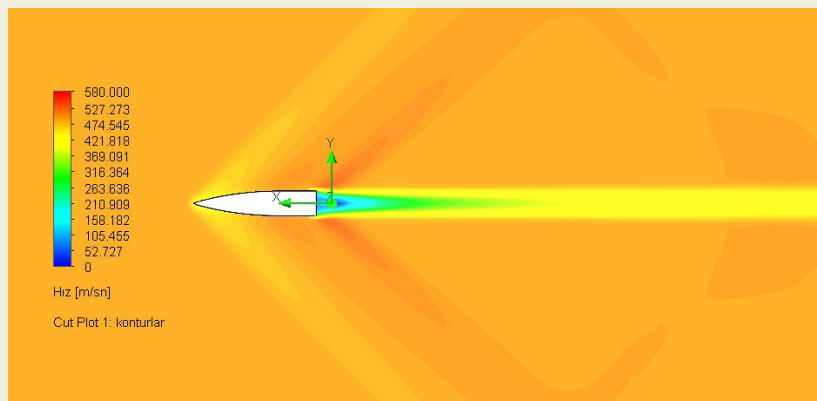
Figure 5. Sharp projectile velocity
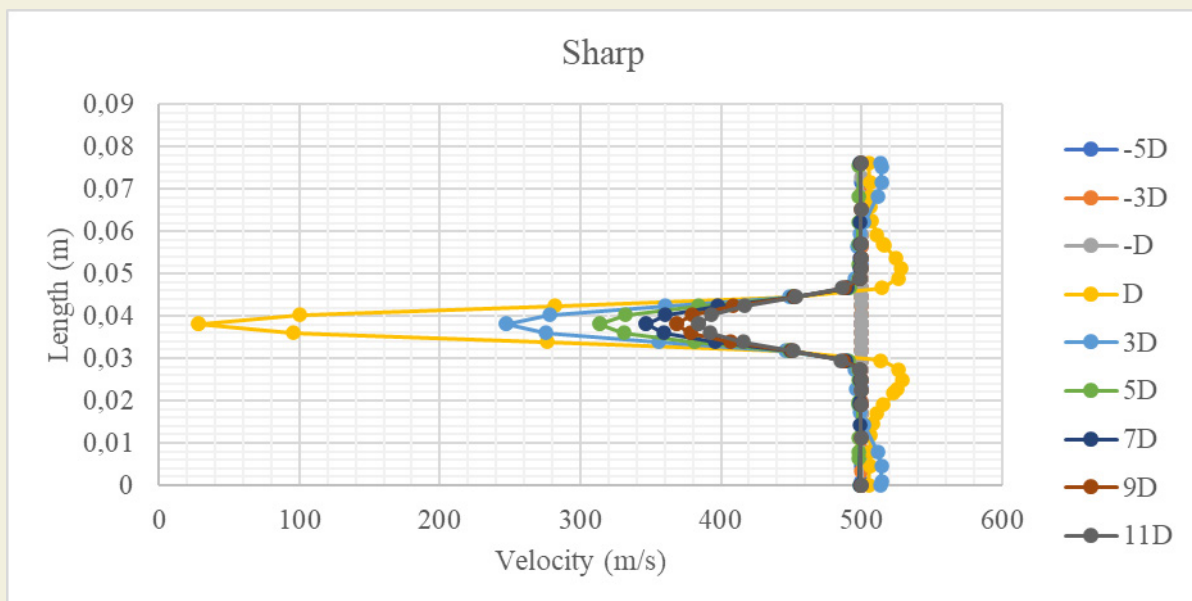
Figure 6. Sharp projectile velocity distribution according to D measure

Turbulent energy can be defined as the amount of energy per unit mass. Turbulent energy distribution on the projectile is given in Figure 9.

According to the geometric properties, the increment of the turbulent energy is found as 7599 J/kg for the sharp type of projectile on D measure as given in Figure 10.
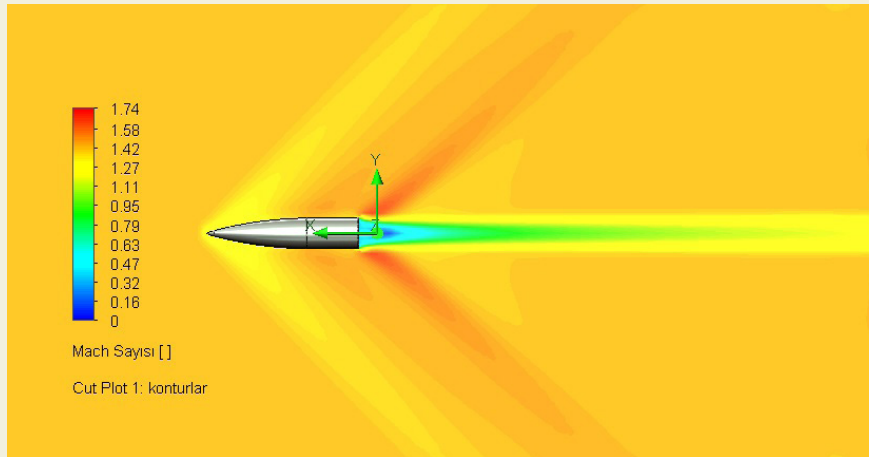
3.2. 45 Degree Rear Type

45-degree type rear geometry is analyzed in terms of the velocity distribution as given in Figure 11. 500 m/s initial velocity is defined for the projectile. In the analyses performed, the most appropriate geometry between sharp and curve is considered to be 45 degrees and this geometry was used for comparison.
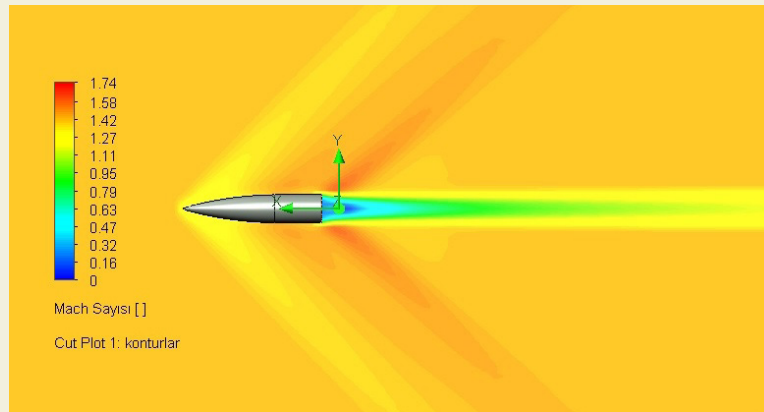
Figure 7. Sharp projectile Mach number
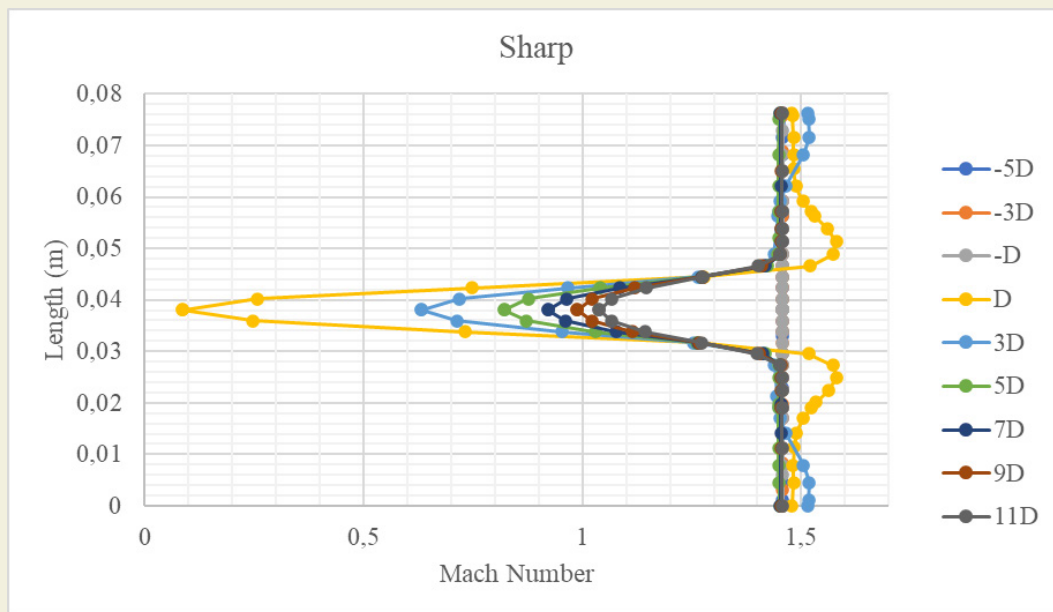
Figure 8. Sharp projectile Mach number distribution according to D measure

Figure 9. Sharp projectile turbulent energy

Figure 12 shows that the maximum velocity decrease is obtained at nearly 26 m/s in D measure after the rear of the 45-degree projectile. It is observed that the speed decrease gradually decreases with increasing distance D.

Figure 13 and Figure 14 show that the maximum Mach
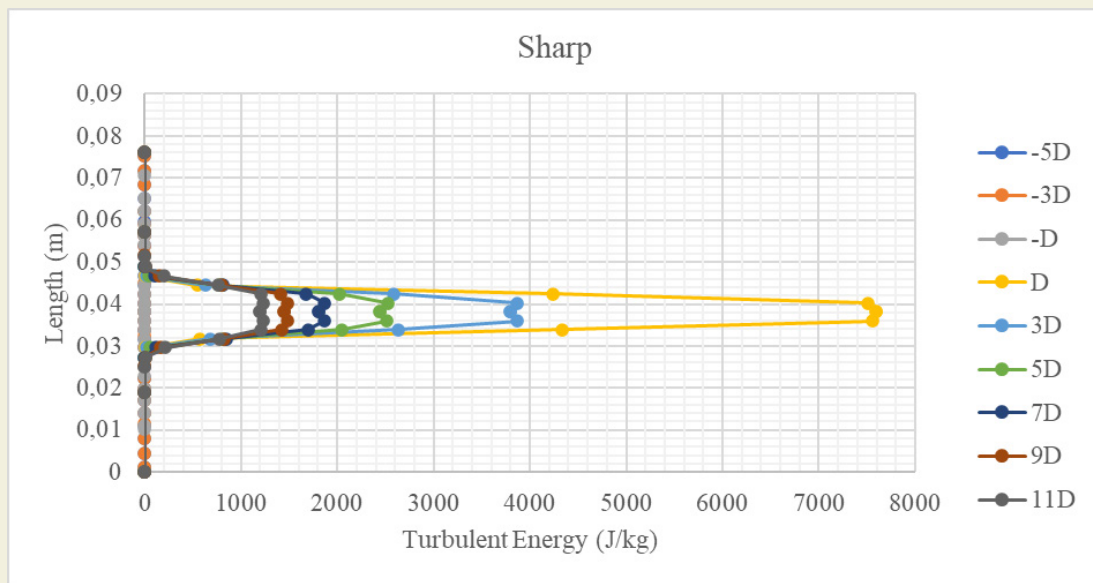
Figure 10. Sharp projectile turbulent energy distribution according to D measure
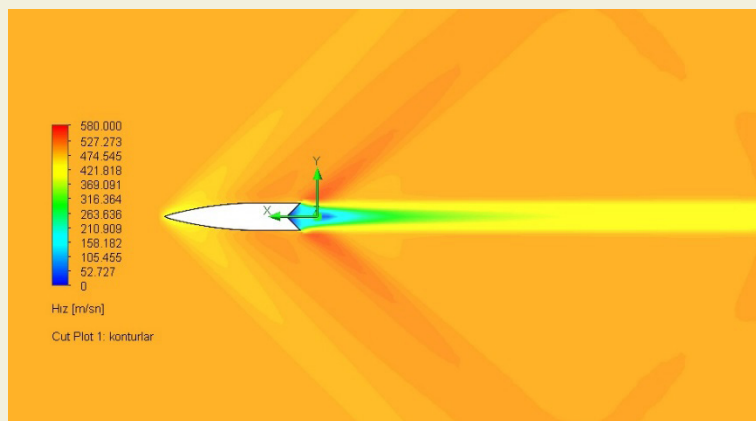
Figure 11. 45 Degree projectile velocity
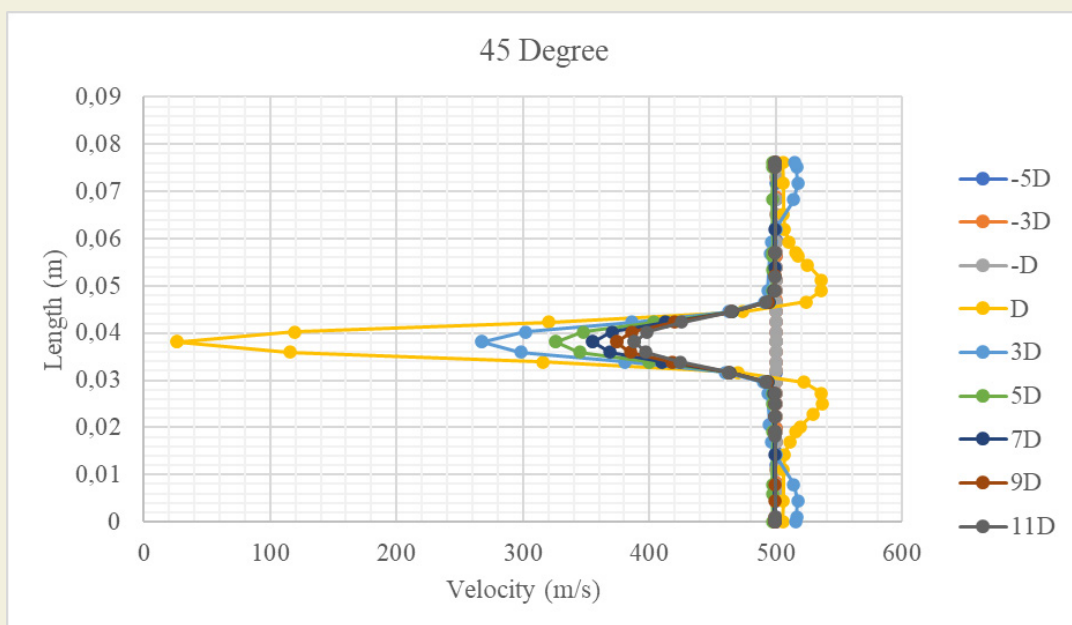
Figure 12. 45 Degree projectile velocity distribution according to D measure

number decrease is found as 0.098 in D measure after the rear of the 45 Degree projectile.

Mach number distribution is given for 45 Degree projectile in Figure 14 for all D measures.

Turbulent energy distribution on 45 Degree projectile is given in Figure 15. According to the geometric properties, the increment of the turbulent energy is found as 7643 J/kg for 45 45-degree type of projectile on D measure as given in Figure 16.

Figure 13. 45 Degree projectile Mach number
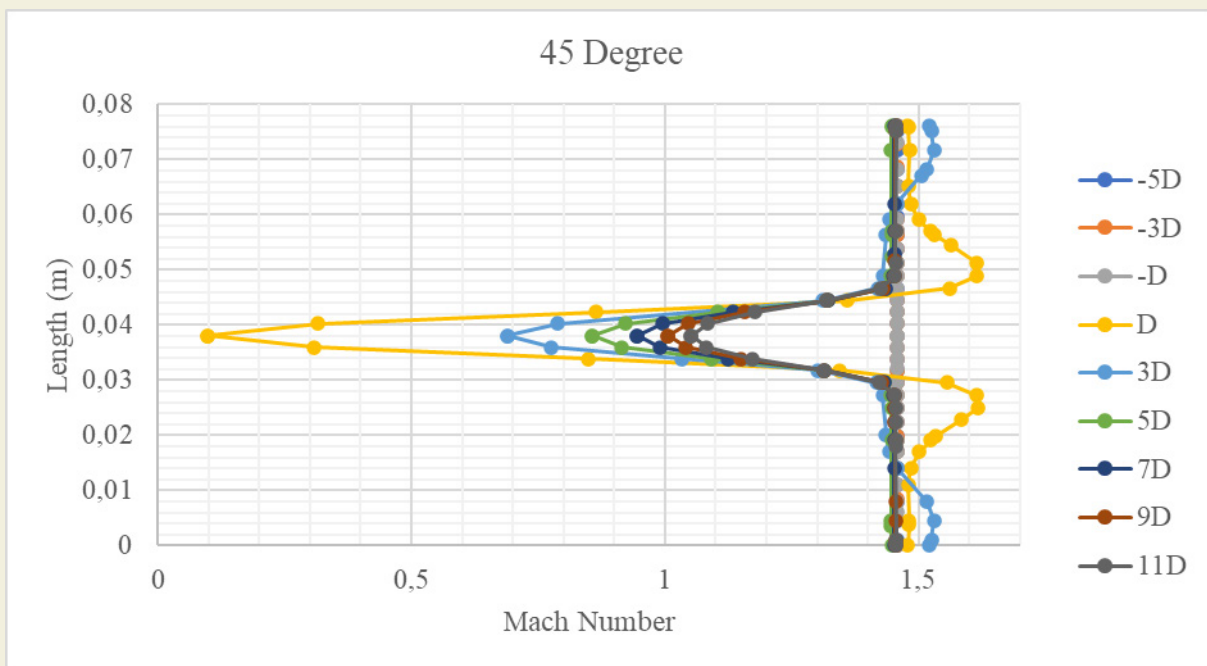
Figure 14. 45 Degree projectile Mach number distribution according to D measure
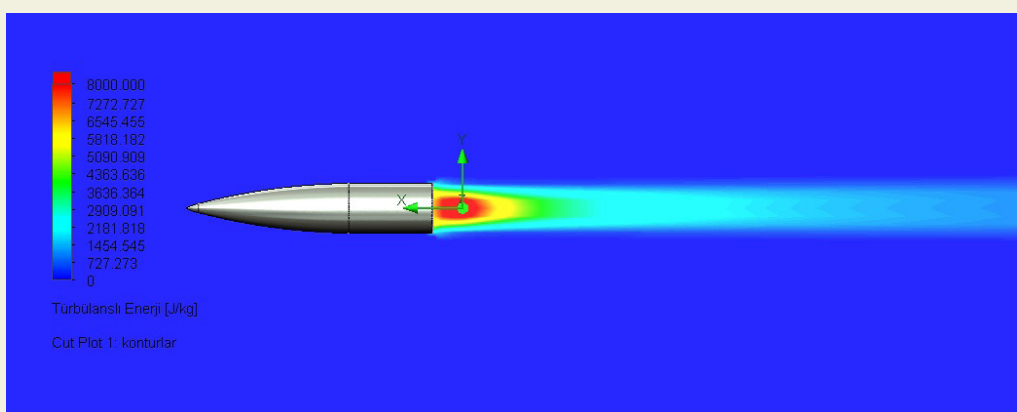
Figure 15. 45 Degree projectile turbulent energy

3.3. Curve Rear Type

Curve-type rear geometry is analyzed in terms of the velocity distribution as given in Figure 17. 500 m/s initial velocity is defined for the projectile.

Figure 18 shows that the maximum velocity decrease is obtained at nearly 45 m/s in D measure after the rear of the curve projectile. It is observed that the speed decrease gradually decreases with increasing distance D.
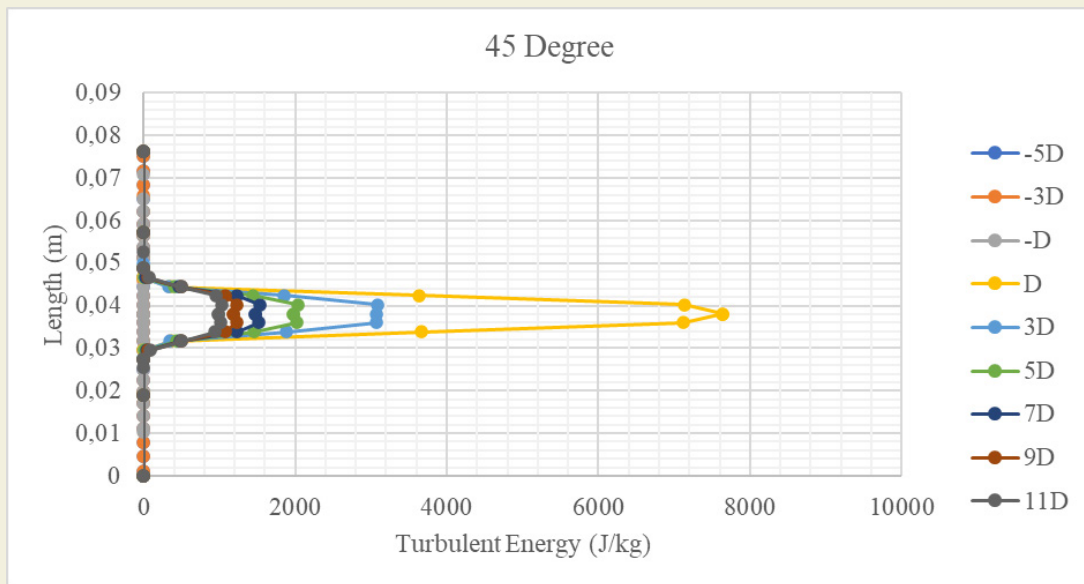

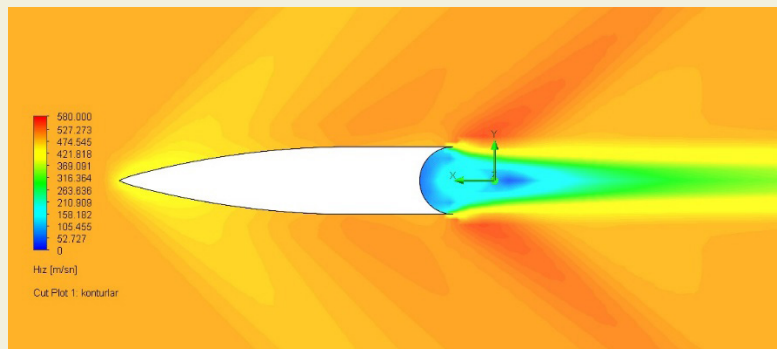**Figure 16.** 45 Degree projectile turbulent energy distribution according to D measure

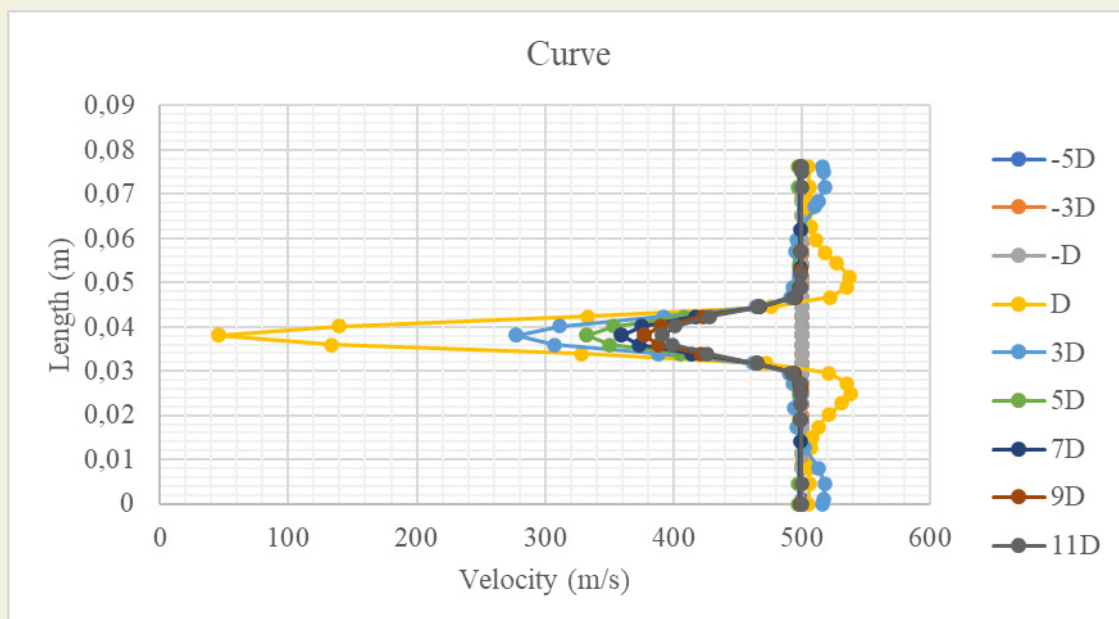**Figure 17.** Curve projectile velocity

Figure 18. Curve projectile velocity distribution according to D measure

Mach number distribution of curve type projectile is given in Figure 20 for all D measures.

Figure 19 and Figure 20 show that the maximum Mach number decrease is found as 0.133 in D measure after the rear of the curve type projectile.

Turbulent energy distribution on the curve projectile is given in Figure 21.

According to the geometric properties, the increment of the turbulent energy is found as 7936 J/kg for the curve type of projectile on D measure as given in Figure 22.

4. Conclusions

In this study, a projectile with different rear geometries is analyzed in terms of velocity, turbulence energy, and Mach number. For projectile rear geometry, Sharp,
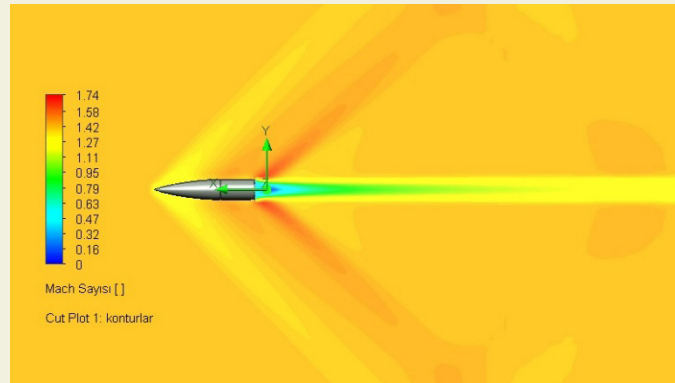

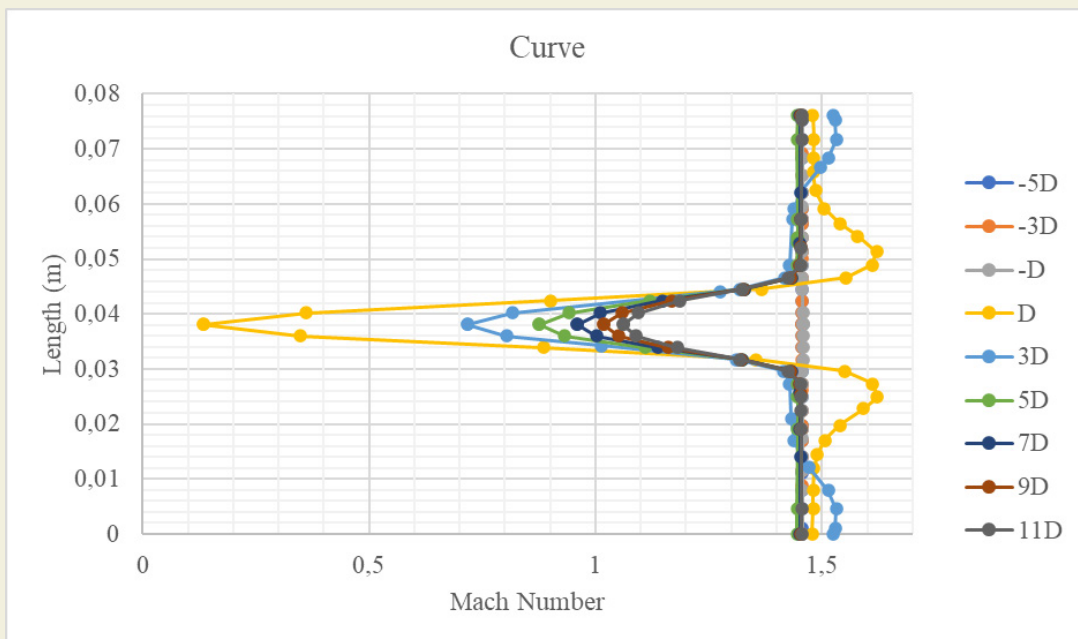**Figure 19.** Curve projectile Mach number

Figure 20. Curve projectile Mach number distribution according to D measure
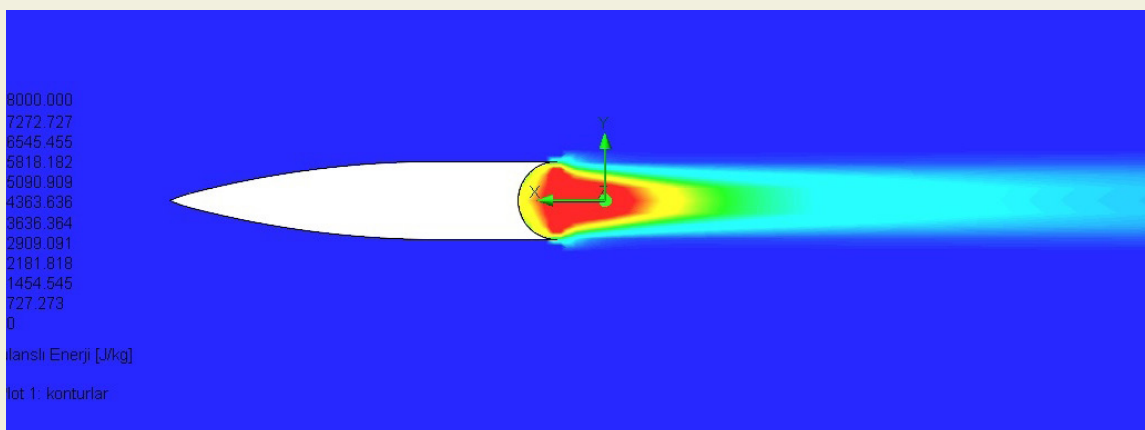

Figure 21. Curve projectile turbulent energy

45-degree, and curve rear geometries are analyzed. After the analysis, parameters such as velocity, turbulent energy, and Mach number were analyzed.

Minimum velocity, minimum Mach number, and maximum turbulent energy values are obtained according to change in D for sharp type projectile as given in Table 2.

Since it was found that there were no significant changes in the measurements taken at the rear of the bullet after the 11D distance, the measurements taken after the 11D distance were not included in the study.

Minimum velocity, minimum Mach number, and maximum turbulent energy values are obtained according to change in D for 45 Degree type projectile as given in Table 3.

Minimum velocity, minimum Mach number, and maxi-

mum turbulent energy values are obtained according to change in D for curve type projectile as given in Table 4.

As a result of the measurements taken at different D distances, it was determined that the maximum speed decrease was at D distance. When a comparison is made according to different back geometries (Figure 23), the velocity decrease obtained in the 45-degree projectile is 42% compared to the curve projectile, and the velocity decrease in the sharp projectile is 38% compared to the curve projectile.

As a result of the measurements taken at different D distances, it was determined that the maximum Mach number decrease was at D distance. When a comparison is made according to different back geometries (Figure 24), the Mach number decrease obtained in the 45-degree projectile is 26% compared to the curve projectile and
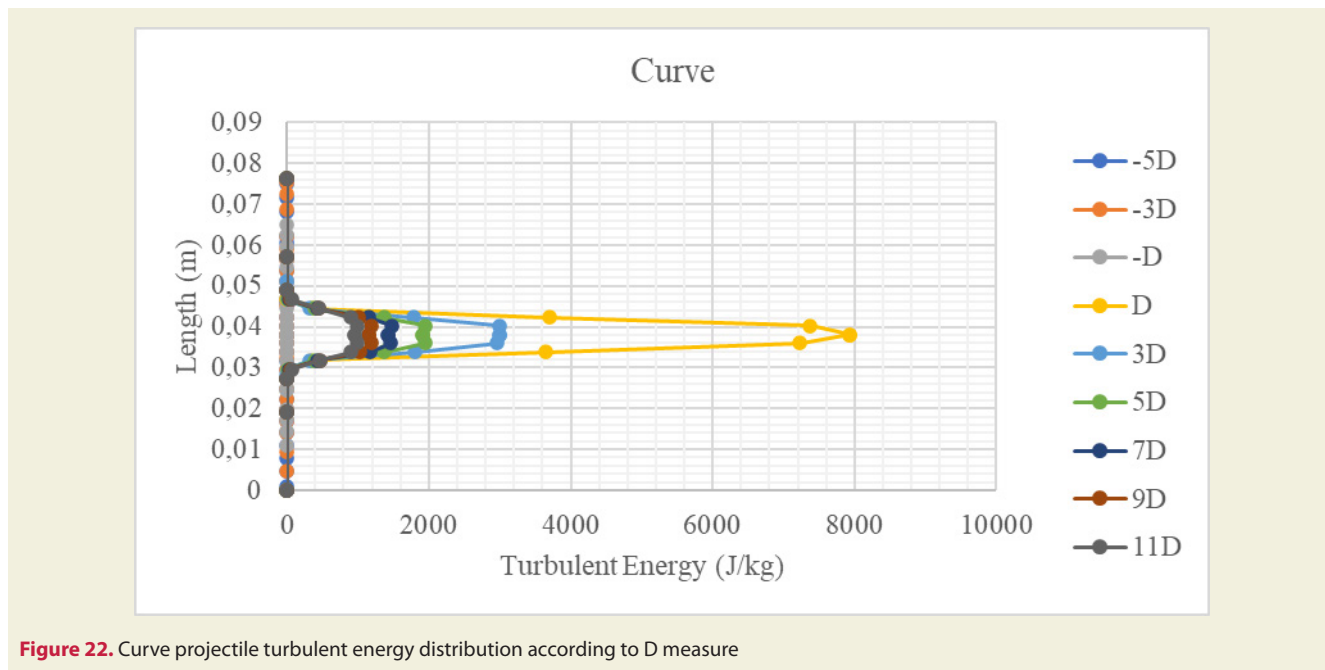

Figure 22. Curve projectile turbulent energy distribution according to D measure

Table 2. Sharp-type projectile aerodynamic parameters according to change in D

Shap Projectile Type	-5D	-3D	-D	D	3D	5D	7D	9D	11D
Min Velocity	500	500	499.97	28.49	247	313	346	368	384
Min Mach Number	1.457	1.457	1.456	0.087	0.632	0.821	0.922	0.986	1.039
Max Turbulent Energy	0.319	0.308	0.298	7599	3869	2519	1872	1488	1232

Table 3. 45 Degree type projectile aerodynamic parameters according to change in D

45 Degree Projectile Type	-5D	-3D	-D	D	3D	5D	7D	9D	11D
Min Velocity	500	500	499.97	26.62	267	325	354	373	388
Min Mach Number	1.457	1.457	1.456	0.098	0.688	0.857	0.946	1.01	1.051
Max Turbulent Energy	0.319	0.308	0.298	7643	3079	2030	1531	1233	1031

Table 4. Curve type projectile aerodynamic parameters according to change in D

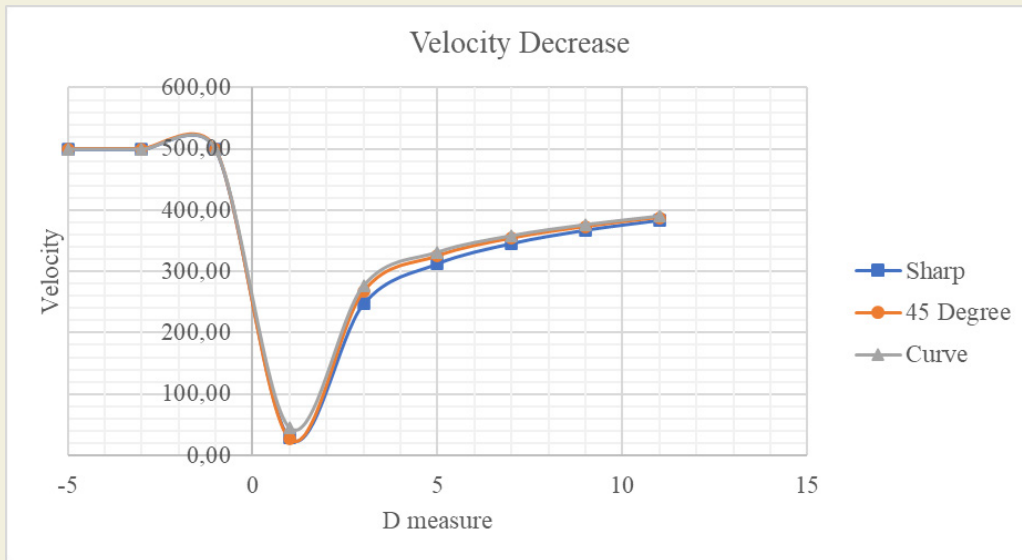| Curve Projectile Type	-5D	-3D	-D	D	3D	5D	7D	9D	11D
Min Velocity	500	500	499.97	45.49	277	332	359	377	391
Min Mach Number	1.457	1.457	1.456	0.133	0.717	0.877	0.960	1.02	1.061
Max Turbulent Energy	0.319	0.308	0.298	7936	3002	1952	1470	1184	989

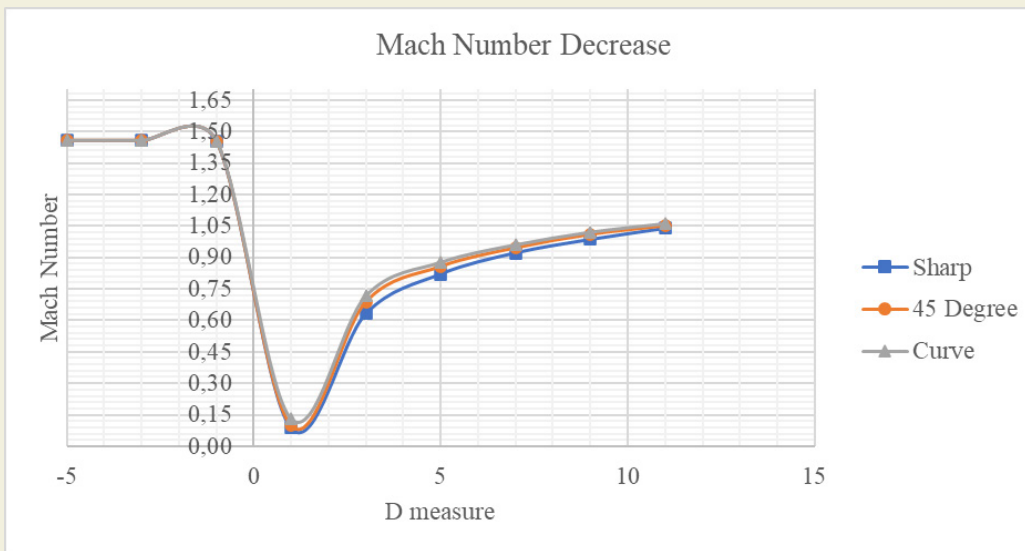**Figure 23.** Comparison velocity decrease for different type of projectile

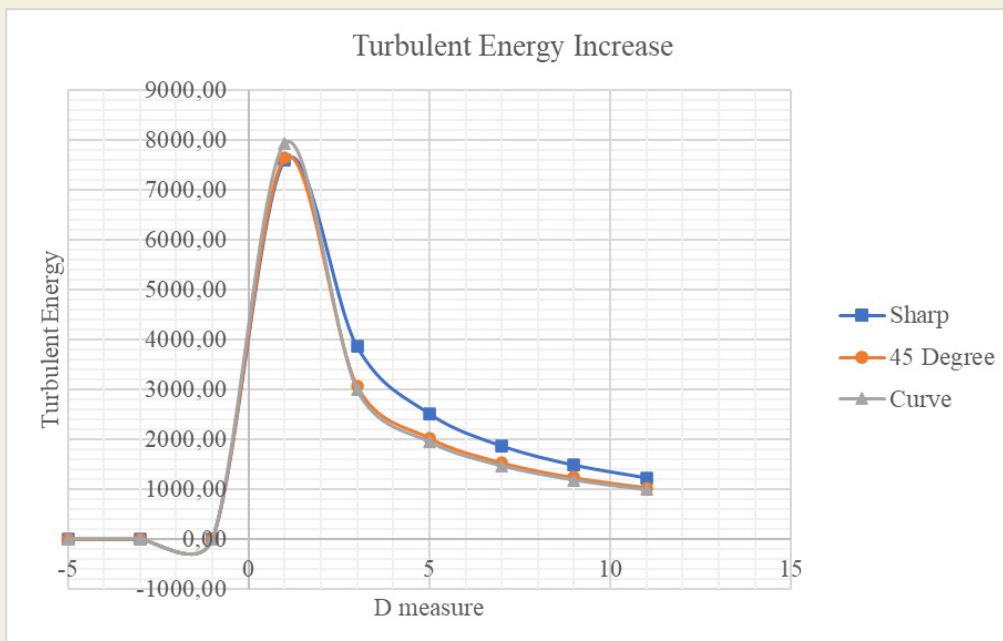**Figure 24.** Comparison Mach number decrease for different types of projectiles

Figure 25. Comparison turbulent energy increase for different types of projectile

the Mach number decrease in the sharp projectile is 34%

As a result of the measurements taken at different D distances, it was determined that the turbulence energy was highest at D distance. When a comparison was made according to different back geometries, it was determined that the most intense turbulence energy occurred in the

compared to the curve projectile.

curve projectile with 7936 J/kg. The turbulence intensity obtained in the curve projectile was 3.7% higher than the 45-degree projectile and 4.2% higher than the sharp projectile as shown in Figure 25.

References

[1] Doğru, M. H. (2017). Investigation of Velocity Distribution and Turbulent Energy for the Different Tip Shaped Projectiles. Çukurova University Journal of the Faculty of Engineering and Architecture, 32(3), 39-46. DOI: 10.21605/cukurovaummfd.357183

[2] Subaşı, M., Doğru, M. H., Yeter, E., & Yılmaz, N. F. (2020). Investigation of The Bullet Impact Energy Performance According to Variable Tip Geometry. The International Journal of Materials and Engineering Technology, 3(1), 10-15.

[3] Christman, D. R., & Gehring, J. W. (1966). Analysis of high-velocity projectile penetration mechanics. Journal of Applied Physics, 37(4), 1579-1587. DOI: 10.1063/1.1708570

[4] Shokrieh, M. M., & Javadpour, G. H. (2008). Penetration analysis of a projectile in ceramic composite armor. Composite structures, 82(2), 269-276. DOI: 10.1016/j.compstruct.2007.01.023

[5] Lecysyn, N., Dandrieux, A., Heymes, F., Slangen, P., Munier, L., Lapebie, E., ... & Dusserre, G. (2008). Preliminary study of ballistic impact on an industrial tank: Projectile velocity decay. Journal of Loss Prevention in the Process Industries, 21(6),627-634. DOI: 10.1016/j.jlp.2008.06.006

[6] Rausch J., Roberts B. (1975). Reaction Control System Aerodynamic Interaction Effects on Space Shuttle Orbiter, Journal of Spacecraft and Rockets, 12, 660-666. DOI: 10.2514/3.57032

[7] Srivastava B. (1998). Aerodynamic Performance of Supersonic Missile Body-and Wing Tip-Mounted Lateral Jets, Journal of Spacecraft and Rockets, 35, 278-286. DOI: 10.2514/2.3352

[8] Ma J., Chen Z-h., Huang Z-g., Gao J-g., Zhao Q. (2016). Investigation on the Flow Control of Micro-Vanes on a Supersonic Spinning Projectile, Defence Technology, 12, 227-233. DOI: 10.1016/j.dt.2016.01.008

[9] Jiang Z, Huang Y, Takayama K. (2004). Shocked Flows Induced by Supersonic Projectiles Moving in Tubes, Computers & fluids, 33, 953-966. DOI: 10.1016/S0045-7930(03)00041-0

[10] Gupta, N. K., Iqbal, M. A., & Sekhon, G. S. (2007). Effect of projectile nose shape, impact velocity and target thickness on deformation behavior of aluminum plates. International Journal of Solids and Structures, 44(10), 3411-3439. DOI: 10.1016/j.ijsolstr.2006.09.034

[11] Lam, C.K.G. and Bremhorst, K.A. (1981). Modified Form of Model for Predicting Wall Turbulence, ASME Journal of Fluids Engineering, Vol.103, pp. 456-460. DOI: 10.1115/1.3240815